Akihiro Abe · Kwang–Sup Lee
L. Leibler · Shiro Kobayashi
Editors

Controlled Polymerization and Polymeric Structures

Flow Microreactor Polymerization, Micelles Kinetics, Polypeptide Ordering, Light Emitting Nanostructures

Springer

259
Advances in Polymer Science

Aims and Scope

The series *Advances in Polymer Science* presents critical reviews of the present and future trends in polymer and biopolymer science. It covers all areas of research in polymer and biopolymer science including chemistry, physical chemistry, physics, material science.

The thematic volumes are addressed to scientists, whether at universities or in industry, who wish to keep abreast of the important advances in the covered topics.

Advances in Polymer Science enjoys a longstanding tradition and good reputation in its community. Each volume is dedicated to a current topic, and each review critically surveys one aspect of that topic, to place it within the context of the volume. The volumes typically summarize the significant developments of the last 5 to 10 years and discuss them critically, presenting selected examples, explaining and illustrating the important principles, and bringing together many important references of primary literature. On that basis, future research directions in the area can be discussed.

Advances in Polymer Science volumes thus are important references for polymer scientists, or scientists interested in polymer science - as an introduction to a neighboring field, or as a compilation of detailed information for the specialist.

Review articles for the individual volumes are invited by the volume editors. Single contributions can be specially commissioned.

Publisher's Note

The present volume of *Advances in Polymer Science* is a collection of substantial review articles on interesting and valuable subjects from different areas of Polymer Science. The volume was not originally planned as a topical volume. The articles were invited and reviewed by the Series Editors of *Advances in Polymer Science* on an independent basis. The collected articles were put together for publication by the publisher.

Tobias N. Wassermann
Publishing Editor, Springer

Akihiro Abe · Kwang-Sup Lee · L. Leibler ·
Shiro Kobayashi

Editors

Controlled Polymerization and Polymeric Structures

Flow Microreactor Polymerization, Micelles
Kinetics, Polypeptide Ordering, Light
Emitting Nanostructures

With contributions by

C. Cai · Y.K. Hong · J. Joo · S.H. Lee · J. Lin · R. Lund ·
A. Nagaki · D.H. Park · D. Richter · L. Willner ·
J.-i. Yoshida · W. Zhu · Z. Zhuang

Springer

Editors

Akihiro Abe
Department of Industrial Chemistry
Tokyo Institute of Polytechnics
Atsugi, Japan

Kwang-Sup Lee
Department of Macromolecular Science
Hannam University
Daejeon, Korea
Republic of (South Korea)

L. Leibler
Matière Molle et Chimie
Ecole Supérieure de Physique et Chimie I
Paris, France

Shiro Kobayashi
Kyoto Institute of Technology R & D Center
 for Bio-based Materials
Kyoto, Japan

Contents

Controlled Polymerization in Flow Microreactor Systems

Aiichiro Nagaki and Jun-ichi Yoshida

Abstract Flow microreactors are expected to make a revolutionary change in chemical synthesis in various fields of polymer synthesis. In fact, extensive studies on cationic polymerization, anionic polymerization, radical polymerization, coordination polymerization, polycondensation, and ring-opening polymerization using flow microreactor systems have opened new possibilities in polymer chemistry and the polymer industry. This article provides, in a concise form, a current overall picture of polymerization using flow microreactors.

Contents

A. Nagaki and J.-i. Yoshida (✉)
Department of Synthetic and Biological Chemistry, Graduate School of Engineering,
Kyoto University, Nishikyo-ku, Kyoto 615-8510, Japan
e-mail: yoshida@sbchem.kyoto-u.ac.jp

1 Introduction

Microtechnology is no longer the field of electronics, but is now moving into many different areas of science and engineering, including mechanics, optics, and fluids, because it provides better efficiencies while also answering the demands of society for conservation of resources and energy. Following remarkable advances in microfabrication technology, microtechnology has been used in the field of chemistry since the 1990s. Microdevices that are used for chemical reactions are called microreactors and are reactors with micrometer-sized channels in which chemical reactions are carried out.

Microreactors are normally set up as flow-type reactors (flow microreactors) with a continuous flow of a solution through the reaction chamber. Nowadays, chemical synthesis in flow microreactors is receiving significant research interest from both academia and industry [1–24]. Recent investigations have revealed significant features of flow microreactor systems involving fast mixing, stemming from short diffusion paths and fast heat transfer by virtue of high surface-to-volume ratios, which are advantageous for increasing the selectivity of chemical reactions [25–28]. Short residence time in a microchannel is beneficial for controlling highly reactive intermediates [29–45]. By taking advantages of such features of flow microreactor systems, various chemical reactions for organic synthesis have been developed [46–56].

Polymerization reactions that convert small molecules into macromolecules by repeating chemical reactions are a fascinating field in the application of flow microreactors. Extensive studies on cationic polymerization, anionic polymerization, radical polymerization, coordination polymerization, polycondensation, and ring-opening polymerization using flow microreactor systems have been carried out so far. Reviews on various polymerization methods in microreactors have been reported by Hessel et al., Wilms et al., Steinbacher and Mcquade, and Bally et al. [57–61]. The main objective of this article is to provide, in a concise form, a current overall picture of polymerization using flow microreactors, especially from the viewpoint of industrial applications. Because of space limitations, polymer particle synthesis will not be discussed here. Serra and Chang have published an excellent review on synthesis of polymer particles with an improved control of their sizes, size distributions, morphologies, and compositions using microreactors [62].

1.1 Characteristic Features of Flow Microreactors

Flow microreactors can influence the very essence of chemical reactions because of the following characteristic features derived from their small size and flow nature:

1. *Fast mixing* [63, 64]: Many chemical reactions involve combining two substances, and for this reason mixing to achieve homogeneity in solution is very important, especially for fast reactions. Mixing occurs due to molecular
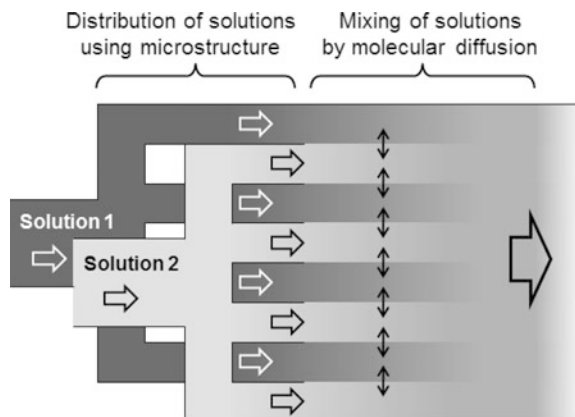
Fig. 1 Working principles of a multilamination-type micromixer

diffusion. According to the theory of molecular diffusion, the time needed for molecular diffusion is proportional to the square of the length of the diffusion path. Therefore, the marked shortening of the diffusion path in a microreactor results in a mixing speed that is unobtainable in a macroreactor. The working principle of a typical micromixer (i.e., a multilamination-type micromixer [65]) is shown in Fig. 1. The solutions to be mixed are distributed into several segments of flows of small width by using the microstructure. Mixing takes place through the interfaces of the segments of flow by virtue of the short diffusion path.

2. *Temperature control*: Heat is transferred between the interior and exterior of a reactor via the reactor surface according to the theory of heat transfer. Therefore, area per unit volume of the reactor is a crucial factor for heat transfer. Generally, volume is equal to the length cubed, and surface area is equal to length squared. When the length is shortened, the surface-to-volume ratio increases. Thus, a feature of microspaces compared to macrospaces is that they have larger surface-to-volume ratios (Fig. 2). Because microreactors have a greater surface area per unit volume than macroreactors, heat transfer occurs rapidly in a flow microreactor, enabling fast cooling and heating and, hence, precise temperature control.

   Another characteristic feature of microreactors derived from their much greater surface-to-volume ratios is that they make phase-boundary reactions such as gas–liquid, liquid–liquid, or solid–liquid reactions more efficient. This feature of flow microreactors is also advantageous for photochemical [66–75] and electrochemical [76–86] reactions, which have received significant attention from the viewpoint of environmentally benign syntheses.

3. *Residence time control*: The length of time that the solution remains inside the reactor is called the residence time. In flow reactors, the residence time increases with the length of the channel and decreases with the flow speed. In flow microreactors, the residence time can be greatly reduced by shortening the length of the microchannels. This feature of flow microreactors is extremely

Size	1/100
Surface area	1/10,000
Volume	1/1,000,000
Surface / Volume	100
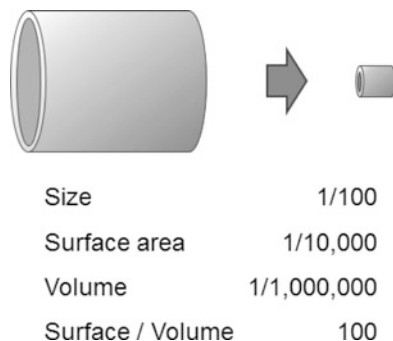
Fig. 2 Numerical aspects of decreasing size
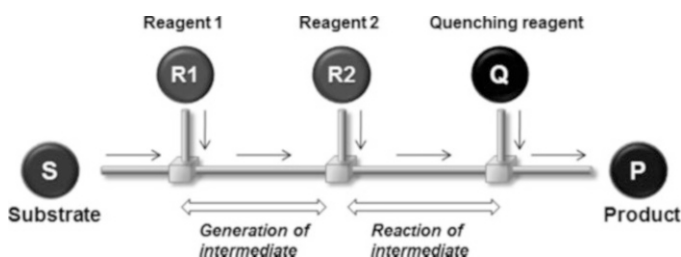
Fig. 3 Principle of generation and reaction of unstable short-lived reactive intermediates based on residence time control in a flow microreactor

useful in controlling reactions involving unstable short-lived reactive intermediates. Unstable reactive species can be transferred to another location to be used in the next reaction before they decompose (Fig. 3). By taking advantage of this feature, chemical transformations that are very difficult or impossible in macroreactors can be achieved in microreactors [87–90].

1.2 Cationic Polymerization

1.2.1 Basic Principles of Cationic Polymerization of Vinyl Monomers

Cationic polymerization [91, 92] is one of the most fundamental methods of synthesizing polymers. Although there are several types of cationic polymerization, the most important is cationic polymerization of vinyl monomers having a cation stabilizing group (Y) (Scheme 1).

The initiation usually involves the addition of a cationic species (A^+) to a vinyl monomer to produce a carbocationic intermediate associated with a counter anion (X^-), which is derived from the initiator. In general, proton acids or carbocations generated from their precursors by acid-promoted ionization reactions [93–95], are
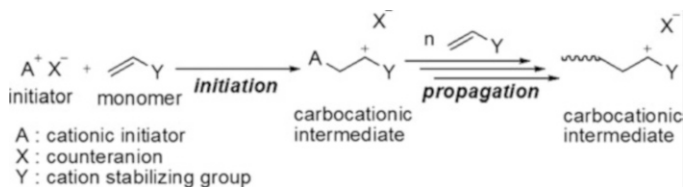
Scheme 1 Cationic polymerization of vinyl monomers
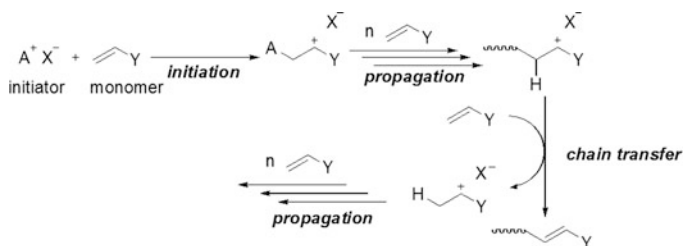
Scheme 2 Chain transfer as a side reaction in cationic polymerization of vinyl monomers

used as initiators. The carbocationic intermediate thus obtained adds to another molecule of the monomer to give the next carbocationic intermediate, which adds to another monomer (propagation step). The carbocationic intermediates are usually highly reactive and unstable. They undergo a number of side reactions such as chain transfer and termination. Chain transfer to monomer is the most problematic with regards control of molecular weight and molecular weight distribution. Namely, the β-proton of the carbocationic intermediate is inherently acidic because of the positive charge on the carbon. On the other hand, monomers used in cationic polymerization are inherently nucleophilic or basic. Therefore, the proton abstraction from the carbocationic intermediate by the monomer is inevitable and very difficult to suppress (Scheme 2).

1.2.2 Controlled/Living Cationic Polymerization of Vinyl Monomers Based on Cation Stabilization

One of the most important breakthroughs in cationic polymerization is the discovery of living cationic polymerization. The inherent and serious drawback of cationic vinyl polymerization is instability of the carbocationic intermediates, which causes the chain transfer leading to the formation of polymers of broad molecular weight distribution. Higashimura, Sawamoto, and coworkers proposed and verified experimentally that living cationic polymerization can be attained by stabilizing the carbocationic intermediate by nucleophilic interaction with a suitably nucleophilic counter anion or an externally added Lewis base (B) (Scheme 3) [96–98].
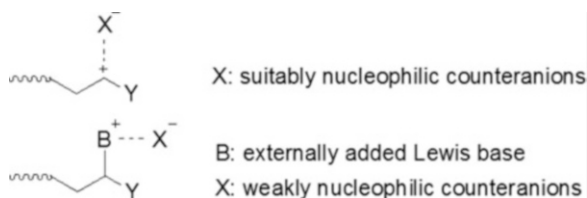
Scheme 3 Stabilization of the carbocationic intermediate by nucleophilic interaction with a suitably nucleophilic counteranion or an externally added Lewis base
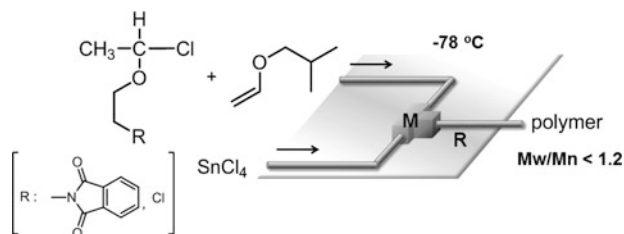
Fig. 4 Flow microreactor system for controlled/living cationic polymerization of vinyl ether initiated by SnCl$_4$. *M* interdigital multilamination micromixer, *R* microtube reactor

In both methods the positive charge of the carbocationic center is reduced and thereby the acidity of the β-proton is reduced to suppress the chain transfer. As a result, good molecular weight control and molecular weight distribution control are attained. On the basis of the principles, a number of initiating systems have been developed for living cationic polymerization [99].

1.2.3 Controlled/Living Cationic Polymerization of Vinyl Ethers Based on Cation Stabilization Using Flow Microreactor Systems [100]

Living cationic polymerization of vinyl ethers initiated by the SnCl$_4$/RCl catalytic system can be carried out in a continuous microreactor system consisting of a interdigital mutilamination micromixer (channel width = 40 μm) and a microtube reactor (Fig. 4). A solution of a monomer and an initiator's precursor is mixed with a solution of SnCl$_4$ using the micromixer at −78°C and the resulting mixture allowed to react in the microtube reactor at the same temperature. For example, isobutyl vinyl ether (IBVE) can be polymerized using functionalized initiators to obtain end-functionalized polymers of narrow molecular weight distribution (weight-average molecular weight/number-average molecular weight, $M_w/M_n < 1.2$). Block copolymerization of IBVE and *n*-butyl vinyl ether (NBVE) can also be successfully achieved using a microreactor system consisting of two micromixers and two microtube reactors to obtain the corresponding copolymer of narrow molecular weight distribution ($M_w/M_n < 1.3$).
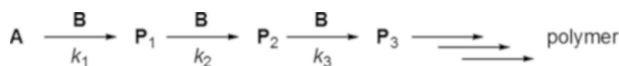
Scheme 4 Polymerization as a competitive consecutive reaction

1.2.4 Controlled/Living Cationic Polymerization of Vinyl Ethers Without Stabilizing Carbocationic Intermediates Using Flow Microreactor Systems

One of the major drawbacks of the controlled/living cationic polymerization based on stabilization of the carbocationic intermediates is slow propagation. Because the concentration of the active propagating species is very low because of the equilibrium between active species and dormant species, overall polymerization reactions are much slower than those without the equilibrium. Another important drawback of the controlled/living polymerization is the use of additives such as Lewis bases. Such additives remain in polymer products and are generally rather difficult to remove from the polymer products.

Recently, it has been demonstrated that good control of molecular weight and molecular weight distribution can be attained by using microreactor systems without stabilizing the carbocationic intermediates. The concept of this new technology (flow-microreactor-system-controlled polymerization) is described in the following section.

Concept of Flow-Microreactor-System-Controlled Polymerization Technology

Control of molecular weight and molecular weight distribution in polymerization can be seen as control of competitive consecutive reactions as shown in Scheme 4, where A is an initiator and B is a monomer.

In the first step, initiator (A) reacts with monomer (B) to produce the first carbocationic intermediate P_1. In the second step, P_1 reacts with another monomer to produce the second carbocationic intermediate P_2. Further reactions lead to polymer formation. If the initiation step to give P_1 is faster than the propagation steps, there is a chance to obtain good molecular weight control and molecular weight distribution control based on monomer/initiator ratios. However, this is the case only when the reactions are slower than the mixing and the reactions proceed in a homogeneous solution. If reactions are faster than mixing, a significant amount of P_2 (and P_n, where $n > 2$) is formed before initiator A is consumed, even if $k_1 \gg k_2$. In this case, it is meaningless to define concentrations of A and B based on the total volume of the solution because the solution is not homogeneous and the product selectivity is not determined by kinetics. This problem is similar to the problem of disguised chemical selectivity for competitive consecutive reactions [101] and can be solved by extremely fast micromixing. In fact, the enhancement of product selectivity of competitive consecutive reactions [102] such as Friedel–Crafts reactions [103, 104], [4+2] cycloaddition reactions [105, 106],

lithiation of dibromobiaryls [107–110], iodination of aromatic compounds [111, 112], and the reaction of a Grignard reagent with $B(OMe)_3$ [113] by virtue of extremely fast micromixing using flow microreactor systems has been reported. These successful results suggest the possibility of molecular weight and molecular weight distribution control by using flow microreactor systems.

In flow-microreactor-system-controlled polymerization, extremely fast mixing of an initiator solution and a monomer solution leads to selective initiation. Propagation proceeds on the basis of the monomer/initiator ratio under homogeneous conditions, and therefore polymers are obtained with good control of molecular weight and molecular weight distribution. Minimization of local deviations in temperature by fast heat transfer through the wall of a microreactor by virtue of the high surface-to-volume ratios is also important because polymerization processes are usually highly exothermic.

"Cation Pool"-Initiated Polymerization of Vinyl Ethers Using Flow Microreactor Systems

Flow-microreactor-system-controlled cationic polymerization requires extremely reactive initiators, and highly reactive organic cations can serve as effective initiators for this method. Usually, organic cations such as carbenium ions and onium ions are generated by an acid-promoted reversible process from their precursors. Yoshida and coworkers have developed the "cation pool" method [114, 115] in which organic cations are generated irreversibly by low temperature electrolysis and are accumulated in relatively high concentration in the absence of nucleophiles. N-acyliminium ions [116], alkoxycarbenium ions [117–121], diarylcarbenium ions [122, 123], and glycosyl triflate [124] have been generated and accumulated by this method. Yoshida and coworkers reported that N-acyliminium ion pools serve as extremely reactive initiators for cationic polymerization in flow microreactors [116].

A pool of an N-acyliminium ions is generated by low-temperature electrochemical oxidation of its precursor, a α-silyl-substituted N-acylamine. Cationic polymerization of NBVE using the N-acyliminium ion as an initiator in a conventional batch reactor gives the polymer in a quantitative yield after quenching with i-Pr_2NH/CH_2Cl_2, but the molecular weight distribution is broad (M_n = 5,700, M_w/M_n = 2.56). The reverse addition sequence (the N-acyliminium ion to the monomer) gives rise to a similar molecular weight distribution (quantitative yield, M_n = 13,100, M_w/M_n = 2.25). The simultaneous addition of a monomer solution and a solution of the N-acyliminium ion does not improve the molecular weight distribution control (quantitative yield, M_n = 24,500, M_w/M_n = 2.43). The molecular weight, however, strongly depends upon the method of mixing because the rate of the polymerization is so fast. In contrast, the use of a flow microreactor system consisting of two micromixers (M1 and M2) and two microtube reactors (R1 and R2) shown in Fig. 5 leads to excellent control of molecular weight and its distribution (M_n = 6,700, M_w/M_n = 1.14) [125]. Solutions of N-acyliminium ion (because the yield of N-acyliminium ion from precursor is estimated to be about 80% based on the
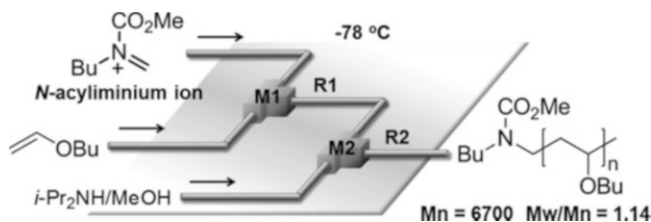
Fig. 5 Flow microreactor system for polymerization of vinyl ether initiated by *N*-acyliminium ion (cation pool). *M1*, *M2* micromixers; *R1*, *R2* microtube reactors

Table 1 Cationic polymerization of NBVE initiated by *N*-acyliminium ion using a flow microreactor system

Run	Monomer (equiv.)	Flow rate (mL/min)	Temperature (°C)	M_n	M_w/M_n
1	10	5.0	−78	1,500	1.40
2	25	5.0	−78	2,900	1.26
3	35	5.0	−78	4,400	1.17
4	50	5.0	−78	6,700	1.14
5	50	3.0	−78	5,600	1.35
6	50	1.0	−78	6,200	2.84
7	50	5.0	−48	8,200	1.30
8	50	5.0	−27	5,500	1.34
9	50	5.0	0	6,500	1.61

reactions with various nucleophiles, 1.2 equiv. of precursor is used when 1.0 equiv. of *N*-acyliminium ion is needed for polymerization) and NBVE are introduced to M1 by the syringe pump technique at −78°C. Then, the reaction mixture is introduced to a microtube reactor (R1 in Fig. 5) ($\phi = 1.0$ mm, 10 cm), in which the polymerization takes place. In the final stage, *i*-Pr$_2$NH/CH$_2$Cl$_2$ is introduced at M2 to quench the polymerization. The polymerization takes place quite effectively and is complete within the residence time of 0.05 s to give the polymer with narrow molecular weight distribution ($M_n = 6,700$, $M_w/M_n = 1.14$). The molecular weight can be controlled by changing the monomer/initiator ratio. The molecular weight (M_n) increases linearly with the amount of NBVE, indicating that chain transfer reactions do not play a significant role in this system.

The effect of the flow rate on molecular weight distribution (Table 1, runs 4–6) indicates the importance of mixing, because it is known that mixing efficiency decreases with a decrease in the flow rate in the micromixer [65]. Reaction temperature is also important for controlling molecular weight distribution, as demonstrated by an increase in M_w/M_n with an increase in temperature (runs 4 and 7–9). A high level of molecular weight control can also be achieved by control of the initiation process by fast micromixing. Precise control of polymerization temperature also seems to be responsible for the remarkable control.

The polymer end is "living" within the residence time of 0.5 s at −78°C, and can be effectively trapped by allyltrimethylsilane. Moreover, the "cation pool"-initiated
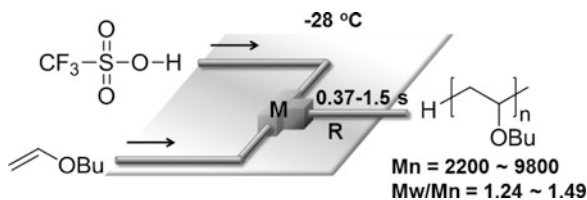
Fig. 6 Flow microreactor system for polymerization of vinyl ethers initiated by TfOH. *M* T-shaped micromixer, *R* microtube reactor

polymerization using a microreactor system can be applied to other vinyl ethers such as IBVE and *tert*-butyl vinyl ether (TBVE) to obtain the corresponding polymers (M_w/M_n of 1.12 for IBVE and 1.50 for TBVE), though the corresponding polymerization using batch macroreactors results in much poorer molecular weight distribution control (M_w/M_n of 4.31 for IBVE and 2.29 for TBVE).

Brønsted-Acid-Initiated Polymerization of Vinyl Ethers Using Flow Microreactor Systems

Proton addition is one of the most simple and straightforward methods for the initiation of cationic polymerization. Brønsted acids are effective for this purpose. However, if we use a weak Brønsted acid, i.e., a conjugate acid of a strong nucleophilic anion, the addition of a Lewis acid is necessary to establish a reversible activation of a covalent end group for effective propagation. On the other hand, if we use a strong Brønsted acid, i.e., a conjugate acid of an extremely weak nucleophilic anion, the addition of a Lewis base is required to stabilize the carbocationic propagating polymer ends [98]. In the absence of a Lewis base, highly ionic polymer ends are too reactive and participate in transfer reactions by loss of β-protons, leading to a very broad molecular weight distribution.

Trifluoromethanesulfonic acid (TfOH) is an effective initiator for cationic polymerization. For example, TfOH-initiated polymerization of IBVE in 1,2-dichloroethane using a batch macroreactor [126] is complete within 10 s at −25°C. The molecular weight distribution is, however, rather broad and ranges from 2.73 to 4.71, presumably because of chain transfer reactions due to high reactivity of the polymer ends. By employing flow microreactor systems consisting of a T-shaped micromixer and a microtube reactor, however, cationic polymerization using a strong Brønsted acid such as TfOH can be accomplished in a highly controlled manner without adding a Lewis base (Fig. 6) [127]. The polymerization is complete within the residence time of 0.37–1.5 s at −25°C (almost quantitative yields). The degree of molecular weight distribution control strongly depends on the inner diameter of the mixer and the flow rate, as depicted in Table 2. M_w/M_n decreased with a decrease in the mixer inner diameter, presumably because faster mixing is achieved by a mixer of smaller diameter. M_w/M_n also decreases with an increase in the flow rate, probably because the increase in flow rate enhanced the mixing efficiency. High level of

Table 2 TfOH-initiated polymerization of isobutyl vinyl ether (IBVE) in a microreactor system

| T-shaped inner diameter (µm) | Flow rate (mL/min) | | M_n | M_w/M_n |
	NBVE	TfOH		
250	2	2	2,900	2.30
	3	3	2,400	2.34
	4	4	1,600	1.61
	5	5	1,500	1.22
	6	6	1,500	1.22
	7	7	1,500	1.19
	8	8	1,500	1.22
500	5	5	2,000	2.54
	6	6	1,500	1.82
	7	7	1,400	1.67
800	6	6	2,500	2.27
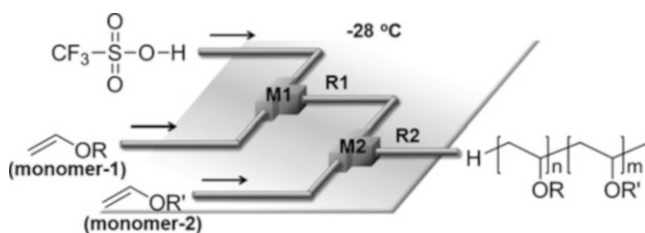
Fig. 7 Flow microreactor system for block copolymerization of vinyl ether initiated by TfOH. *M1*, *M2* micromixers; *R1*, *R2* microtube reactors

molecular weight distribution control can be attained even at $-25°C$. It is important to note that very low temperatures such as $-78°C$, which might be an obstacle to industrial-scale applications, are not required.

One of the advantages of controlled/living polymerization is that the method allows flexible synthesis of structurally defined block copolymers composed of different monomers, offering greater opportunities for synthesis of organic materials with interesting properties.

An example of microreactor systems for block copolymerization is shown in Fig. 7. The first monomer IBVE is mixed with TfOH in the first micromixer (M1). Introduction of the second monomer (NBVE or EVE) at the second micromixer M2 results in the formation of the polymer of higher molecular weight with narrow molecular weight distribution [128]. Block copolymerization can be carried out with any combination and with either order of monomer addition, as shown in Table 3, demonstrating that the present method serves as a flexible method for the synthesis of block copolymers. Therefore, flow-microreactor-system-controlled polymerization can serve as a powerful method for synthesis of structurally well-defined polymers and copolymers in industry.

Table 3 Block polymerization of vinyl ether initiated by TfOH using the flow microreactor system

Monomer-1	Monomer-2	M_n	M_w/M_n
IBVE	–	1,500	1.18
IBVE	NBVE	2,300	1.43
IBVE	EVE	2,400	1.54
NBVE	–	1,000	1.24
NBVE	IBVE	1,700	1.45
NBVE	EVE	1,900	1.55
EVE	–	860	1.16
EVE	IBVE	2,100	1.54
EVE	NBVE	2,100	1.41
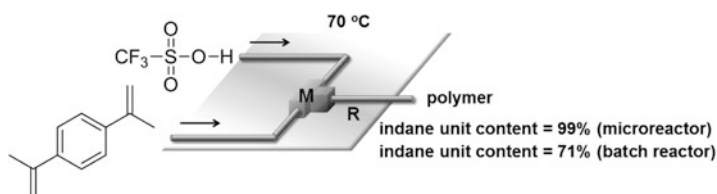
Fig. 8 Flow microreactor system for cationic polymerization of 1,4-diisopropenylbenzene initiated by TfOH. *M* T-shaped micromixer, *R* microtube reactor

1.2.5 Cationic Polymerization of Diisopropenylbenzenes Using Flow Microreactor Systems

Polyindanes have received significant research interest because of their remarkable thermal resistance. Extensive work on the synthesis of 1,1,3-trimethyl-substituted polyindanes by cationic polymerization of 1,4-diisopropenylbenzenes and their thermal properties has carried out by Nuyken and coworkers [129, 130]. The polymers of high indane-unit content serve as useful materials because of their high thermal resistance and low dielectric constants. The use of flow microreactor systems is effective for increasing the indane-unit content. In fact, indane-unit content (99%) was much higher in the flow microreactor system than that (71%) for the batch macrosystem under similar conditions (70°C, [1,4-diisopropenylbenzene] = 0.1 M, [TfOH] = 2 M) (Fig. 8) [131]. The characteristic features of flow microreactor systems including fast mixing and uniformity of the temperature seem to be responsible.

1.3   Anionic Polymerization

1.3.1   Controlled/Living Anionic Polymerization of Vinyl Monomers

Living anionic polymerizations have received significant attention since Michael Szwarc's first report in 1956 [132]. Anionic polymerization [133–137] serves as an important and powerful method for macromolecular engineering, permitting the preparation of highly defined block copolymers, star polymers, and further complex architectures, because the anionic polymer ends are living even in the absence of a capping agent [138, 139]. In fact, the anionic growing polymer ends (usually organolithium species) can be utilized for end-functionalization reactions with various electrophiles and block copolymerization with other monomers. A major drawback of conventional anionic polymerization in polar solvents in batch macroreactors is the requirement for low temperatures, such as $-78°C$ [140]. Such a requirement causes severe limitations in the use of this highly useful polymerization in industry. Using nonpolar solvents, the polymerization can be conducted at higher temperatures, but much longer reaction time is needed for completion. It is also problematic that the use of individually manufactured laboratory equipment is frequently necessary.

Kinetic studies on anionic polymerization in a continuous flow mode have also been reported by Szwarc and coworkers [141, 142], Schulz and coworkers [141, 142], and Muller and coworkers [143, 144]. However, preparative anionic polymerizations in continuous flow mode have not been studied until recently.

1.3.2   Controlled/Living Anionic Polymerization of Styrenes

Anionic polymerization of styrenes is a highly useful technique for the synthesis of polystyrenes with precisely adjustable molecular weights and molecular weight distributions and is applied for the synthesis of structurally well-defined polymers such as end-functionalized polymers and block copolymers.

Controlled/Living Anionic Polymerization of Styrenes in Polar Solvent Using Flow Microreactor Systems [145]

In a conventional anionic polymerization of styrenes in polar solvents in a batch macroreactor, major drawbacks include the requirement of low temperature such as $-78°C$. In contrast, Nagaki et al. reported that controlled anionic polymerization of styrene can be conducted under easily accessible conditions such as $0°C$ in a polar solvent using a flow microreactor to obtain the polystyrene with narrower molecular weight distribution (M_n = 1,200–20,000, M_w/M_n = 1.09–1.13) (Fig. 9) [146]. Moreover, the molecular weight can be easily controlled by changing the flow rates of monomer and initiator solutions. Furthermore, these methods can be
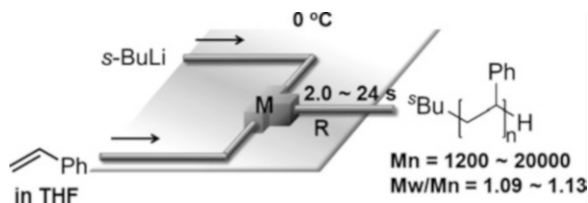
Fig. 9 Flow microreactor system for anionic polymerization of styrene in THF. *M* T-shaped micromixer, *R* microtube reactor

applied to styrene derivatives having silyl, methoxy, alkynyl, and alkylthio groups on the benzene ring. Wurm et al. also reported the anionic polymerization of styrene at 20°C using a flow microreactor [147]. Polystyrenes in a broad range of molecular weight with a narrow molecular weight distribution can be obtained within several seconds ($M_n = 1,700$–70,000, $M_w/M_n = 1.09$–1.41). It should be noted that strict dryness of the apparatus and high vacuum techniques is needed in the classical batch methods but that such experimental effort can be significant reduced by using flow microreactors. Residual impurities and moisture can be removed by purging the reactor with solutions of a monomer and an initiator before a solution of the desired polymer product is collected at the outlet of flow microreactors.

Integration of chemical reactions enhances the power and speed of organic and polymer synthesis, and recently it has been recognized that flow microreactors enable space-integration of reactions [148–153]. On the basis of livingness of the polymer end, structurally well-defined polymers such as end-functionalized polymers and block copolymers can be synthesized using integrated flow microreactor systems consisting of two micromixers and two microtube reactors. For example, functionalization of a living polymer end using chlorosilanes such as chlorotrimethylsilane and chlorodimethylvinylsilane is effectively achieved by using integrated flow microreactor systems to obtain polystyrenes bearing the silyl group at the terminal. Block copolymerization can also be achieved using the integrated flow microreactor system at 0°C and 24°C to obtain structurally defined block copolymers composed of two different styrenes in quantitative yields (Fig. 10).

End-functionalization with epoxides is also popular because epoxides have high reactivity toward nucleophiles by virtue of ring strain. Use of functionalized epoxides enables a further transformation after deprotection. For example, polymerization of styrene followed by end-functionalization with the various glycidyl ethers having acetal structures such as ethoxy ethyl glycidyl ether (EEGE), 1,2-isopropylidene glyceryl glycidyl ether (IGG), and *trans*-2-phenyl-1,3-dioxane glycidyl ether (PDGE) can be accomplished using a flow microreactor system (Fig. 11) [154]. The acetal and ketal protecting groups in the glycidyl ethers are stable toward the highly reactive carbanionic living polymer ends but they can be easily cleaved under acidic conditions to afford multihydroxyl end-functionalized polymers (Fig. 12).

Fig. 10 Integrated flow microreactor system for anionic block copolymerization of styrenes in THF. *M1*, *M2* micromixers; *R1*, *R2* microtube reactors

Fig. 11 Flow microreactor system for anionic polymerization of styrene in THF initiated by *s*-BuLi and subsequent functionalization reaction with epoxides. *M1*, *M2* micromixers; *R1*, *R2* microtube reactors

Fig. 12 Synthesis of multihydroxyl end-functionalized polystyrenes

Fig. 13 Integrated flow microreactor system for the synthesis of block copolymers having two different polymer chains on a silicon core. *M1, M2, M3, M4* T-shaped micromixers; *R1, R2, R3, R4* microtube reactors

The syntheses of various branched polymers with complex architectures such as star polymers and dendrimer-like star-branched polymers using living anionic polymerization have been studied extensively. These branched polymers have attracted much attention from theoretical, synthetic, and practical viewpoints because of their unique and interesting properties in solution, melt, and solid states. Block copolymers having different polymer chains on a core are especially interesting. To synthesize such a structure, selective 1:1 reaction of a living polymer chain and a poly-functional core molecule is essential in the first step. In a conventional batch macroreactor, an excess amount of polyfunctional core should be used to obtain the monosubstituted compound selectively [155–157]. This requirement is problematic because an excess amount of functional core should remain unchanged in the first step and, therefore, it should be removed before proceeding to the second step. The use of a flow microreactor system serves as a powerful method for solving this problem (disguised chemical selectivity [102–113]). As shown in Fig. 13, the end functionalization with 1 equiv. of dichlorodimethylsilane leads to selective formation of a product having a single polymer chain on silicon ($M_n = 1,400$, $M_w/M_n = 1.13$), although use of a batch macroreactor leads to lower controllability ($M_n = 1,300$, $M_w/M_n = 1.21$). Extremely fast 1:1 micromixing of the living polymer chain and dichlorodimethylsilane enables the selective introduction of a single polymer chain into silicon. Therefore, the subsequent reaction with another living polymer chain using an integrated flow microreactor system gives block copolymers having two different polymer chains on a silicon core. The chlorosilane having a single polymer chain can be used for the subsequent reaction with alcohols and Grignard reagents.
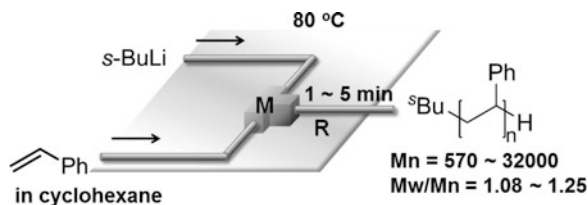
Fig. 14 Flow microreactor system for anionic polymerization of styrene in cyclohexane at 80°C initiated by s-BuLi. *M* T-shaped micromixer; *R* microtube reactor
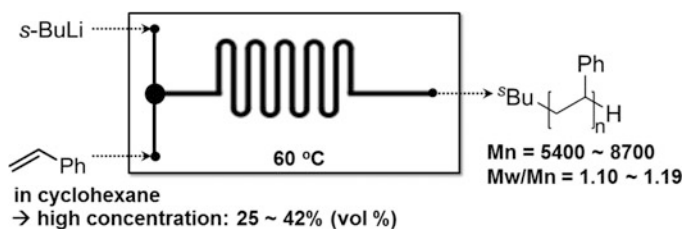
Fig. 15 Aluminum-polyimide microfluidic device for anionic polymerization of styrene initiated by s-BuLi in cyclohexane at high concentrations at 60°C

Controlled/Living Anionic Polymerization of Styrenes in Nonpolar Solvent Using Flow Microreactor Systems

Anionic polymerization of styrenes can be conducted in nonpolar solvents at room temperature in a batch macroreactor. However, much longer reaction time is needed for completion. It is also important to carry out the polymerization with <20% by volume of styrene because the reactions with >20% by volume of styrene may result in a rapid increase in reaction temperature, potentially causing danger. The use of a flow microreactor is effective for solving the problem. In fact, controlled anionic polymerization of styrene initiated by s-BuLi in cyclohexane as a nonpolar solvent can be conducted at 80°C by using a flow microreactor system to obtain polystyrenes in quantitative yields within 1–5 min (Fig. 14). The controlled polymerization of styrene in cyclohexane under high monomer concentration (25–42% by volume of styrene) at 60°C can be achieved by using an aluminum-polyimide microfluidic device (Fig. 15) [158]. Moreover, the molecular weight distribution of polymers is influence by the channel patterns (i.e., straight, periodically pinched, obtuse zigzag, and acute zigzag channels).

1.3.3 Controlled/Living Anionic Polymerization of Alkyl Methacrylates Using Flow Microreactor Systems

Synthesis of poly(alkyl methacrylate)s with well-defined structures has received significant research interest because of the versatility of these materials as plastics, adhesives, and elastomers containing a number of different reactive functions.

Fig. 16 Flow microreactor system for anionic polymerization of alkyl methacrylates initiated by 1,1-diphenylhexyllithium. *M1*, *M2* T-shaped micromixers; *R1*, *R2* microtube reactors

The use of living anionic polymerization of alkyl methacrylates is very popular for this purpose. Living anionic polymerization of alkyl methacrylates does not need a capping agent and therefore is very fast compared to living radical polymerization. However, synthesis of poly(alkyl methacrylate)s via anionic polymerization using a conventional batch macroreactor should be carried out at low temperatures such as $-78°C$ to obtain polymers of narrow molecular-weight distribution [159, 160]. The requirement of such low temperatures causes several limitations in the use of this highly useful polymerization in industry. However, if the problem is solved, living anionic polymerization of alkyl methacrylate could serve as a powerful method for synthesis of poly(alkyl methacrylate)s.

Controlled anionic polymerization of alkyl methacrylates initiated by 1,1-diphenylhexyllithium using a flow microreactor gives the corresponding poly (alkyl methacrylate)s with high level of control of molecular weight under easily accessible temperatures compared with conventional batch macropolymerization, e.g., $-28°C$ for methyl methacrylate (MMA) ($M_w/M_n = 1.16$), $0°C$ for butyl methacrylate (BuMA) ($M_w/M_n = 1.24$), and $24°C$ for *tert*-butyl methacrylate (*t*-BuMA) ($M_w/M_n = 1.12$). Precise control of the reaction temperature and fast mixing of a monomer and an initiator seem to be responsible (Fig. 16) [161].

The livingness of the reactive carbanionic polymer end is important for producing end-functionalized polymers and block copolymers. The livingness of the polymer end in a flow microreactor system can be verified as shown in Fig. 17. Solutions of an alkyl methacrylate and of 1,1-diphenylhexyllithium are mixed in the first micromixer (M1 in Fig. 17) and the polymerization is carried out in the first microtube reactor (R1 in Fig. 17). Then, a solution of the same monomer is introduced at the second micromixer (M2), which is connected to the second microtube reactor (R2) where the sequential polymerization takes place. By changing the length of R1 with a fixed flow rate, the effect of the residence time in R1 can be examined. The M_n increases by the addition of the second monomer solution. However, an increase in the residence time in R1 causes an increase in the M_w/M_n, presumably because of decomposition of the polymer end (Fig. 18). By choosing an appropriate residence time in R1 (2.95 s for MMA; 0.825 s for BuMA), the sequential polymerization can be
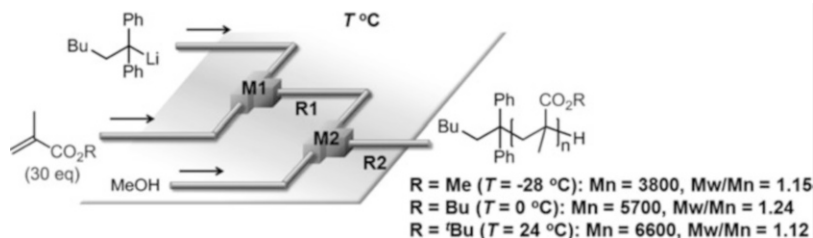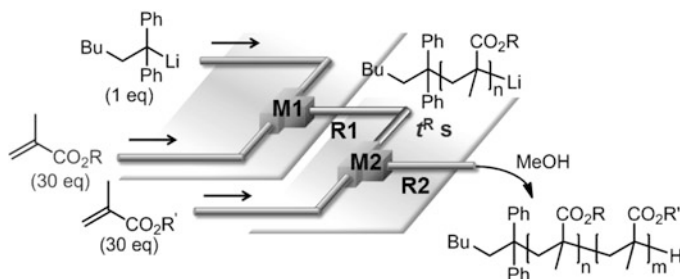
Fig. 17 Integrated flow microreactor system for the sequential anionic polymerization of alkyl methacrylates initiated by 1,1-diphenylhexyllithium. *M1*, *M2* T-shaped micromixers; *R1*, *R2* microtube reactors
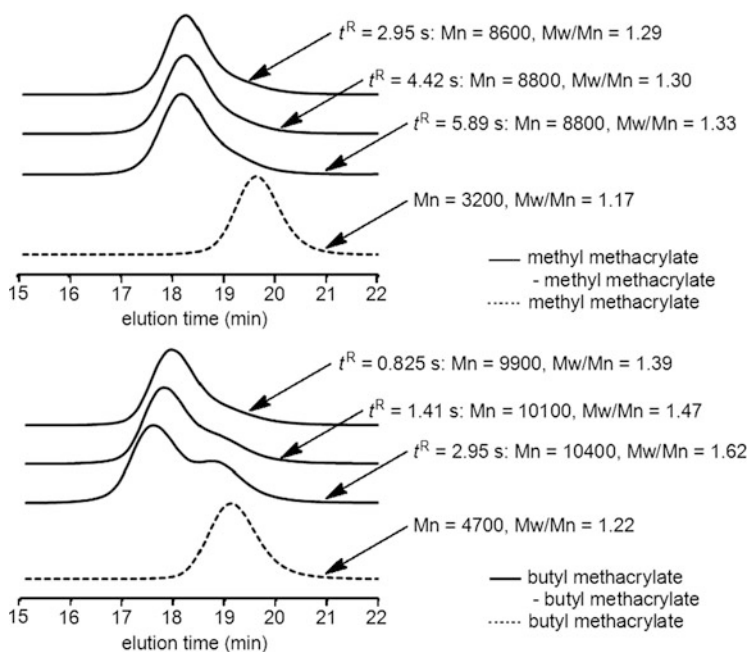
Fig. 18 Size-exclusion chromatography traces of polymers obtained in the integrated flow microreactor system. Effect of residence time on the molecular weight distribution for (**a**) methyl methacrylate–methyl methacrylate, and (**b**) butyl methacrylate–butyl methacrylate

successfully carried out without significant decomposition of the living polymer end [162]. The polymer chain end is living within such residence times. Moreover, the subsequent reaction of the living polymer end with a different alkyl methacrylate leads to the formation of a block copolymer having narrow molecular-weight distribution (Table 4).

Table 4 Block copolymerization of alkyl methacrylates initiated by 1,1-diphenylhexyllithium using the integrated flow microreactor system

Monomer-1	Monomer-2	M_n	M_w/M_n
MMA	–	3,200	1.17
MMA	MMA	8,600	1.29
BuMA	–	4,700	1.22
BuMA	BuMA	9,900	1.39
BuMA	^{t}BuMA	9,000	1.31
^{t}BuMA	–	5,300	1.13
^{t}BuMA	^{t}BuMA	10,000	1.13
^{t}BuMA	BuMA	9,500	1.16
^{t}BuMA	MMA	8,400	1.15

R = Me (T = -28 °C): Mn = 9000, Mw/Mn = 1.30
R = Bu (T = 0 °C): Mn = 12200, Mw/Mn = 1.55
R = ^{t}Bu (T = 24 °C): Mn = 9200, Mw/Mn = 1.19
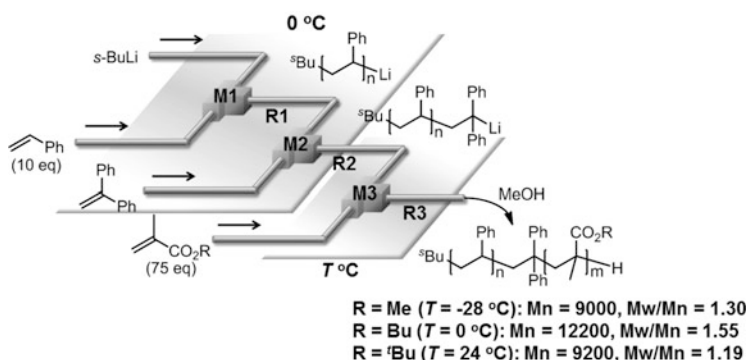
Fig. 19 Integrated flow microreactor system for the anionic block copolymerization of styrene and alkyl methacrylates initiated by *s*-BuLi. *M1*, *M2*, *M3* T-shaped micromixers; *R1*, *R2*, *R3* microtube reactors

1.3.4 Controlled/Living Anionic Block Copolymerization of Styrenes and Alkyl Methacrylates Using Integrated Flow Microreactor Systems

As mentioned above, flow microreactors are effective for accomplishing the controlled anionic polymerization of styrenes and alkyl methacrylates. A high level of molecular weight distribution control can be achieved under easily accessible conditions such as 24°C to −28°C by virtue of the characteristic features of flow microreactors, which include fast mixing, fast heat transfer, and precise residence time control. Another advantage of flow-microreactor-controlled polymerization is easy modulation of flow microreactors to integrate polymerization reactions. In fact, by using integrated flow microreactor systems, the polystyrene living polymer end, which is produced by butyllithium-initiated anionic polymerization of styrene, can be effectively trapped with 1,1-diphenylethylene, and the resulting organolithium species can be used as a macro-initiator for anionic polymerization of alkyl methacrylates. Therefore, styrene–alkyl methacrylate diblock copolymers can be synthesized with a high level of molecular weight distribution control at easily accessible temperatures such as 24°C to −28°C (Fig. 19) [163]. Moreover, triblock

copolymers can be also synthesized by sequential introduction of styrene and two different alkyl methacrylates in a similar manner (styrene–t-BuMA–MMA triblock copolymer, $M_n = 8{,}800$, $M_w/M_n = 1.23$; styrene–t-BuMA–butyl methacrylate triblock copolymer, $M_n = 9{,}000$, $M_w/M_n = 1.35$).

1.4 Radical Polymerization

1.4.1 Free-Radical Polymerization Using Flow Microreactor Systems

Free-radical polymerization is an important process for the industrial synthesis of macromolecules because free radicals are compatible with a wide variety of functional groups that do not survive in ionic and metal-catalyzed polymerizations [164]. Because free-radical polymerization is usually highly exothermic, a precise temperature control is essential for performing free-radical polymerization in a highly controlled manner. Therefore, the polymerization in a conventional batch macroreactor often suffers from a low level of molecular weight distribution control because of inefficient heat removal and the lack of homogeneity of the reaction temperature. Therefore, the controllability of the reaction temperature is a major concern in free-radical polymerization from the viewpoint of industrial applications. As a matter of fact, heat removal capacity is often a limiting factor in polymerizations in batch macroreactors. Therefore, the advantage of flow microreactors for radical polymerization is obvious because they enable fast heat transfer.

Iwasaki and Yoshida reported the free-radical polymerization of various monomers using flow microreactor systems. Polymerization of butyl acrylate (BA) gives a polymer of much smaller M_w/M_n than that obtained with a batch macroreactor because of a much higher heat-removal efficiency in the flow microreactor (Fig. 20) [165]. For the polymerization of benzyl methacrylate (nBMA) and MMA, the effect of the flow microreactor on molecular weight distribution control is smaller than for BA. For the polymerization of vinyl benzoate (VBz) and styrene, no appreciable effect is observed. The tendency indicates that the flow microreactor is quite effective for highly exothermic polymerization such as that of BA, but not so effective for less exothermic polymerizations. Similar results on the polymerization of styrene have been reported by Leveson et al. [166]. Moreover, a microchemical pilot plant for radical polymerization of MMA has been built by numbering-up (i.e., scaling up by parallel operation of a number of units) eight microtube reactors (vide infra) [167].

The effects of mixing in radical polymerization of MMA are interesting [168]. The use of a 5 mm static mixer leads to fouling in the reactor. In contrast, the use of an interdigital multilamination micromixer with 36 lamellae of 25 μm thickness results in a reduction in fouling. This numbering-up approach enables production of 2,000 tons per year without the fouling problem [169].
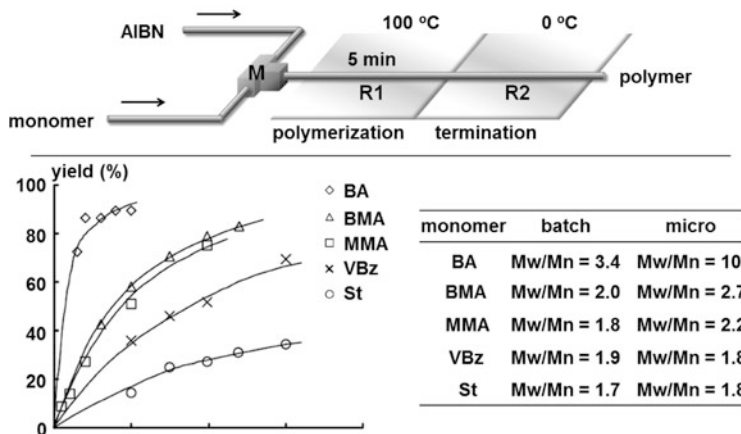
Fig. 20 Flow microreactor system for the free-radical polymerization initiated by AIBN and relative rate of the polymerization in the flow microreactor. *M* T-shaped micromixer; *R1*, *R2* microtube reactors

Serra and coworkers studied the outstanding effect of mixing on conversion, molecular weight and polydispersity in free-radical polymerizations of styrene by a numerical simulation using different micromixer geometries [170, 171].

Latex production by miniemulsion polymerizations [172–174] in continuous tubular reactors has also been reported by McKenna and coworkers [175].

1.4.2 Living Radical Polymerization Using Flow Microreactor Systems

The major drawbacks of free-radical polymerization are the low controllability of macromolecular structures and the broad molecular weight distribution of the resulting polymers. Living radical polymerization [176–180] has been developed to overcome the problem. Because more than 50% of polymers are produced via free-radical processes in industry, living radical polymerization offers a possible way to synthesize polymers of narrow molecular weight distribution [181]. Various methods including atom transfer radical polymerization (ATRP) [182–187], reversible addition–fragmentation chain transfer radical polymerization (RAFT) [188–190], nitroxide-mediated radical polymerization (NMP) [191–193], organoiodine-mediated radical polymerization (IRP) [194], cobalt-mediated polymerization [195] and organotellurium-, antimony-, or bismuth-mediated living radical polymerization (TERP) [196–201] have been developed for conducting living radical polymerization.
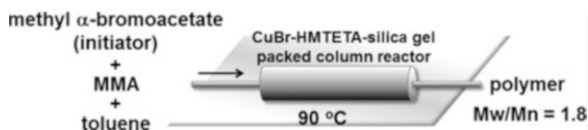
Fig. 21 CuBr-HMTETA-silica gel packed column reactor for the ATRP of MMA initiated by methyl α-bromoacetate
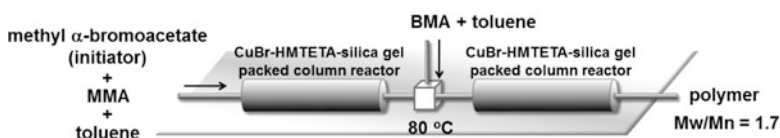
Fig. 22 CuBr-HMTETA-silica gel packed column reactor for the atom transfer radical block copolymerization of MMA with butyl methacrylate (nBMA) initiated by methyl α-bromoacetate

ATRP Using Flow Microreactor Systems

ATRP [182–187] is one of the most extensively studied living radical polymerizations because of its simplicity and broad applicability, and serves as a method for synthesizing previously inaccessible well-defined nanostructured polymeric materials [202]. One of the main drawbacks of this process is low catalytic efficiency and deep color of the final product. In general, the use of 0.1–1% catalyst results in the formation of the colored polymer containing the residual catalyst. Therefore, after polymerization, additional purification by passing the solution through silica gel or alumina gel is needed to remove the catalyst from product. A possible solution to this problem is the use of supported catalysts.

A continuous column reactor packed with silica-gel-supported CuBr-HMTETA catalyst for ATRP of MMA exhibits high catalyst retention, high catalytic activity, and good stability up to 100 h (Fig. 21). Moreover, the product solution is colorless [203]. In addition, the molecular weight of the resulting PMMA can be controlled by simply changing the flow rate of MMA. The polymerization in the reactor is first order with respect to monomer concentration, which is typical for ATRP processes. However, the polydispersity index (M_n/M_w) for the resulting polymer is about 1.8, which is larger than that for the polymer prepared using the same supported catalyst in batch (about 1.1). This is presumably because back-mixing in the column and trapping of polymer chains in the silica gel pores take place. The system in which two column reactors are connected in series has been developed and applied to block copolymerization of MMA with nBMA (Fig. 22) [204].

A photopolymerized microfluidic device consisting of two inlets, active mixing chamber containing a magnetic stir bar, a single reaction channel (500 μm × 600 μm), and one outlet has been used for ATRP reaction of 2-hydroxypropyl methacrylate (HPMA) initiated by methyl 2-bromopropionate (Fig. 23) [205]. The molecular weight can be controlled by changing the residence time at the different flow rates (Table 5). The kinetics and polymer properties are similar to those for the batch reactions reported in the literature [206]. Furthermore, a block copolymer poly
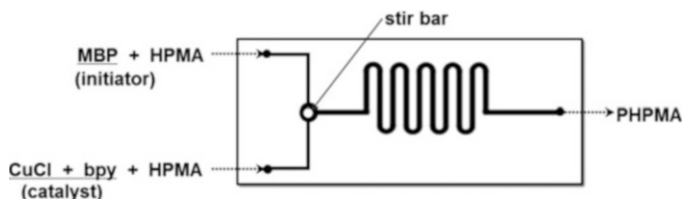
Fig. 23 Microfluidic device for the synthesis of poly(2-hydroxypropyl methacrylate) (PHPMA) using a MBP initiator

Table 5 Microchannel polymerization of HPMA at different pumping rates and initiator concentrations

[MBP]/[HPMA]	Pump rate (µL/h)	Residence time (h)	Conversion (%)	M_n	M_w/M_n
1:40	50	2.00	92	6,240	1.21
	150	0.67	74	5,560	1.19
	300	0.33	47	3,950	1.26
	400	0.25	29	3,300	1.27
	500	0.20	17	2,770	1.32
1:100	50	2.00	62	12,740	1.26
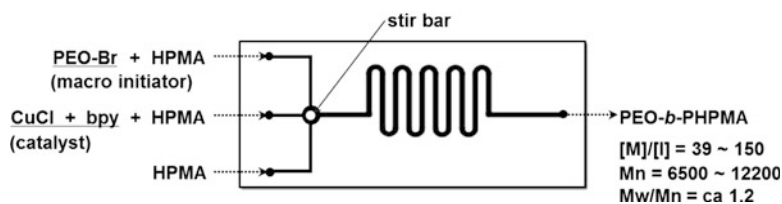
Fig. 24 Microfluidic device for the synthesis of poly(ethylene oxide-*block*-2-hydroxypropyl methacrylate) (PEO-*b*-PHPMA) using a PEO macroinitiator

(ethylene oxide-*block*-2-hydroxypropyl methacrylate) (PEO-*b*-PHPMA) can be prepared by the copolymerization of HPMA with a PEO macroinitiator, prepared by reaction of the terminal hydroxy group of the PEO-OH with a twofold molar excess of 2-bromoisobutyryl bromide and triethylamine (Fig. 24). The stoichiometry of the reactants can be easily changed by varying relative flow rates [207].

RAFT Polymerization Using Flow Microreactor Systems

RAFT [188–190] is known for its compatibility with a wide range of monomers, temperature, and impurities, as compared to other living radical polymerizations such as ATRP and NMP.

RAFT polymerization in miniemulsion has been carried out in a tubular reactor. Emulsion is prepared in a batch reactor using sodium dodecyl sulfate (SDS, surfactant), Triton X-405 (surfactant), styrene (monomer), hexadecane
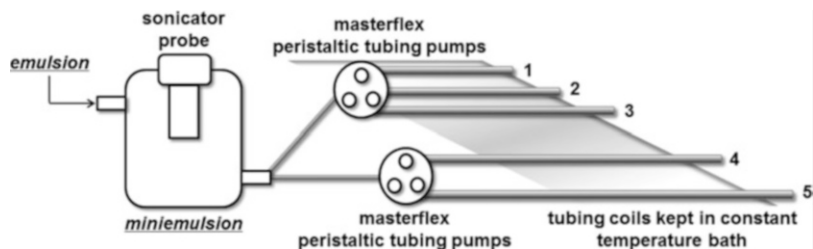
Fig. 25 Multitubule reactor for RAFT polymerizations using continuous miniemulsion
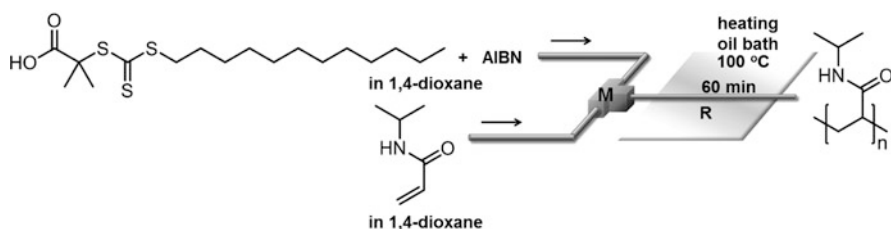
Fig. 26 Continuous flow reactor for the reversible addition–fragmentation chain transfer radical polymerization. *M* micromixer, *R* microtube reactor

(costabilizer), and 1-phenylethyl phenyldithioacetate (PEPDTA, RAFT agent), and is pumped into a continuous sonication vessel to obtain a miniemulsion (Fig. 25) [208]. The miniemulsion is introduced into tube reactors where the polymerization takes place. Kinetically, the polymerization in the tube reactor behaves similarly to the batch polymerization. However, the tubular reactor produces polymer with a slightly higher molecular weight distribution than that for polymer produced in a batch reactor, presumably because back-mixing or axial dispersion effects in the tubular reactor broaden the residence time distribution of particles within the reactor. These systems can be extended for the synthesis of block copolymer of polystyrene and poly(butyl acrylate) [209].

RAFT polymerizations of *N*-isopropylacrylamide (NIPAM) as monomer and a trithiocarbonate as chain transfer agent have been carried out using a flow microreactor under homogeneous conditions (Fig. 26) [210]. In a flow process, an increase in the inner diameter of the tube results in slightly lower conversions and wider molecular weight distributions. Polymerization rates in a flow microreactor are considerably higher than those of batch polymerization because of uniform heating (Table 6).

RAFT polymerizations of various monomers including acrylamides, acrylates, and vinyl acetate have been studied by Hornung et al. [211]. Polymers of narrow molecular weight distribution and average molecular weights similar to those of batch polymerizations were obtained on a multigram scale.

Table 6 Conversion of the RAFT polymerization and poly(nisopropylacrylamide) (PNIPAM) properties after 60 min at 90°C

Method	Heating method	Conversion (%)	M_n	M_w/M_n
Flow	Oil bath	88	21,500	1.15
Flow	Oil bath	78	17,200	1.31
Flow	Oil bath	79	20,000	1.31
Batch	Oil bath	40	13,400	1.12
Batch	Microwave	85	19,400	1.16
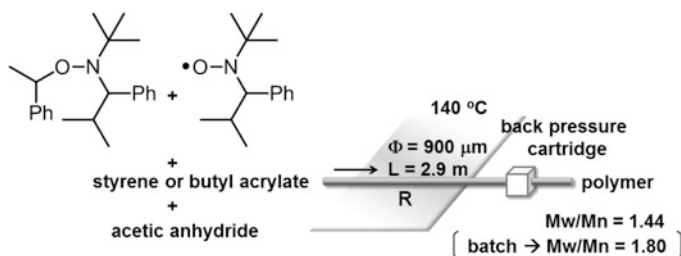
Fig. 27 Continuous flow microreactor system for nitroxide-mediated radical polymerization (NMP) of poly(styrene) or poly(*n*-butyl acrylate). *R* microtube reactor

NMP Using Flow Microreactor Systems

NMP [191–193] can be applied to a wide range of monomers such as styrenes, acrylates, acrylamides, acrylonitrile, and 1,3-dienes. Acyclic nitroxides such as 2,2,5-trimethyl-4-phenyl-3-azahexane-3-nitroxide (TIPNO) or *N*-*tert*-butyl-*N*-(1-diethyl phosphono-2,2-dimethylpropyl) nitroxide (DEPN) enables the reversible termination of the growing polymer chains.

NMP of styrene and *n*-butyl acrylate at 140°C has been performed in a continuous-flow microtubular reactor (Fig. 27) consisting of a stainless steel tube reactor and a back-pressure cartridge [212]. In the case of styrene polymerization, there is no difference between batch reactors and flow microreactors. However, for *n*-butyl acrylate, a better control of the polymerization has been observed in the flow microreactor (M_w/M_n of 1.80 for the batch reactor and 1.44 for the flow microreactor). Moreover, consumption of the monomer is much faster using the flow microreactor (Fig. 28).

NMP of styrene in a miniemulsion can be also performed in a tubular reactor [213]. In the first step, a macroinitiator is prepared by bulk polymerization in a batch reactor and the subsequent miniemulsion polymerization is carried out in a tubular reactor. The polymerization kinetics in the tubular reactor are similar to those in a batch reactor. It is also noteworthy that both preparation of a macroinitiator and a miniemulsion polymerization can be achieved in a continuous tubular reactor to obtain polystyrene-*block*-poly(butyl acrylate) diblock and polystyrene-*block*-poly(butyl acrylate)-*block*-polystyrene triblock copolymers [214].
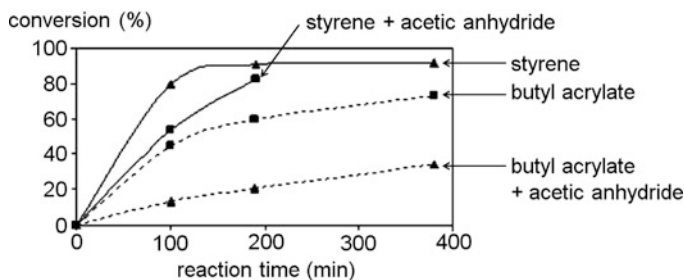
Fig. 28 Conversion versus reaction time of nitroxide-mediated radical polymerization of styrene and *n*-butyl acrylate without or with acetic anhydride
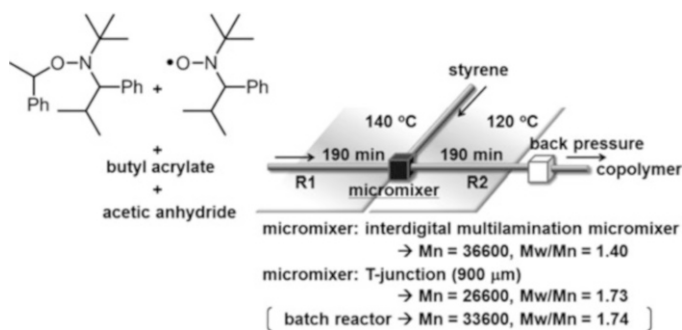
Fig. 29 Continuous flow microreactor system for nitroxide-mediated radical block copolymerization of *n*-butyl acrylate and styrene. *R1*, *R2* microtube reactor

Continuous nitroxide-mediated block copolymerization of *n*-butyl acrylate (first monomer) and styrene (second monomer) can be performed using two serial 900-μm inner diameter stainless steel microtube reactors (Fig. 29) [215]. For the second polymerization process, the influence of mixing was examined by changing micromixers. The use of a high-pressure interdigital multilamination micromixer (HPIMM) provided by the Institut für Mikrotechnik Mainz (Mainz, Germany), can significantly reduce the polydispersity index ($M_w/M_n = 1.36$, 120°C) compared with that obtained in a batch macroreactor ($M_w/M_n = 1.74$, 120°C). Efficient mixing of a viscous solution of poly(*n*-butyl acrylate) and a solution of styrene by virtue of small diffusion paths caused by small lamination widths seems to be responsible. Conversions, molecular weights, and molecular weight distributions are significantly influenced by the nature of the micromixer [216]. The results obtained with three micromixers, i.e. two HPIMMs with different lamination widths and a slit plate micromixer (LH2) manufactured by Ehrfeld Mikrotechnik BTS (Wendelsheim, Germany) are summarized in Table 7. Molecular weight distribution and molecular weight strongly depend on the factor F, given by $F = 1/N(W_C + W_L)$ where N is the number of channels per inlet, W_C is the channel width, and W_L is the slit or aperture width. The relationship between molecular

Table 7 Interdigital multilamination micromixer characteristics

Micromixer	HPIMM		LH2
	ML45	ML20	ML50
Number of channels per inlet, N	16	15	10
Channel width, W_C (μm)	45	20	50
microstructure thickness (μm)	250	100	300
Slit or aperture width, W_L (μm)	60	60	50
Form factor, F (mm^{-1})	0.59	0.83	1.0
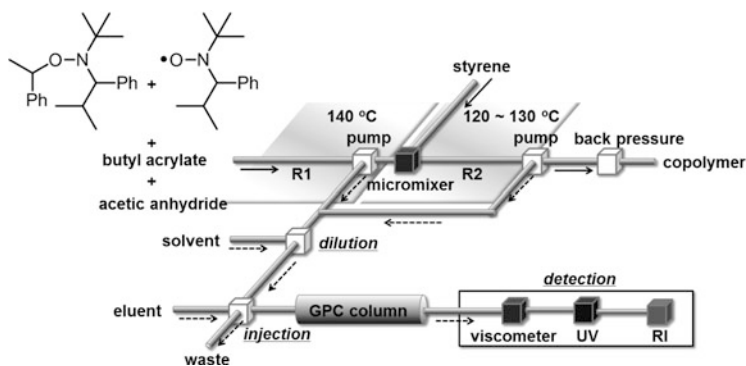
Fig. 30 Continuous online rapid size-exclusion chromatography monitoring of polymerizations (CORSEMP) system for nitroxide-mediated radical block copolymerization of *n*-butyl acrylate and styrene

weight distribution or molecular weight and F is linear, enabling prediction of copolymer features.

Recently, Ryu, Studer and colleagues also reported the use of highly sterically hindered amines [217, 218] for the NMP of styrene and butyl acrylate in a flow microreactor [219]. The polymerization in the flow microreactor is faster than that in the batch system, although polymers with slightly smaller molecular are obtained in flow.

In general, gel permeation chromatography (GPC) is used to characterized polymers. However, sample preparation and analysis requires a long time. The integration of a flow microreactor with analytical devices to monitor the progress of polymerization in real time allows fast screening and optimization. For example, the continuous online rapid size-exclusion chromatography monitoring of polymerizations (CORSEMP) system has been developed by Serra, Hadziioannou and coworkers [220]. The system consists of automatic samplings, dilutions, and injections every 12 min for monitoring of polymer synthesis in continuous flow (Fig. 30). In addition, this system also includes a viscometer, refractive index and UV detectors, and GPC to determine the molecular weights and molecular weight distributions. The nitroxide-mediated block copolymerization of *n*-butyl acrylate and styrene can be monitored in "near real-time" with good accuracy and
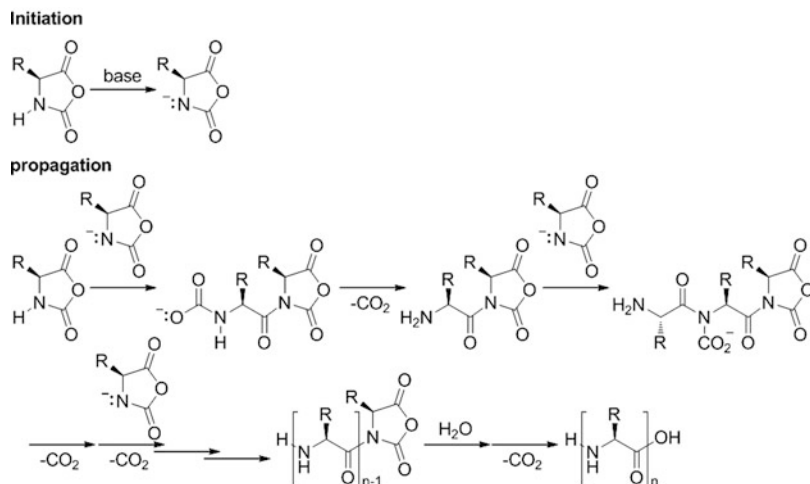
Fig. 31 Mechanism of polymerization of amino acid *N*-carboxyanhydride (NCA) initiated by a base

repeatability. Very recently, bifurcation analysis and grade transition dynamic optimization for NMP of styrene in a tubular reactor have been demonstrated by Flores-Tlacuahuac and coworkers [221, 222].

1.5 Ring-Opening Polymerization Using Flow Microreactor Systems

Ring-opening polymerization is categorized as chain-growth polymerization in which the terminal end of a polymer acts as a reactive center [223]. The reaction of cyclic compounds with a polymer end causes cleavage of the ring and repetition of this process leads to the formation of high molecular weight polymers. The synthesis of polyamides from lactams, polyesters from lactones, and polyethers from cyclic ethers have been widely used.

The most popular approach for the synthesis of polyamides from amino acids [224] is the amino acid *N*-carboxyanhydride (NCA) method (Fig. 31) [225]. The initiation with a base such as a tertiary amine is followed by the reaction of another NCA molecule with the resulting activated NCA anion to produce a dimer with an electrophilic *N*-acyl NCA end group and a nucleophilic carbamate group. Then, *N*-carbamic acid is detached as carbon dioxide during the propagation reaction. It is known that deprotonation of NCA and attack of the NCA anion are relatively fast [226]. Therefore, it is important to control these steps. However, in conventional batch systems, control of polymerization is difficult due to local concentration gradients. In contrast, flow microreactor systems enable such control (Fig. 32) [227]. For example, polymerization of *N*-benzyloxycarbonyl-L-lysine using a flow
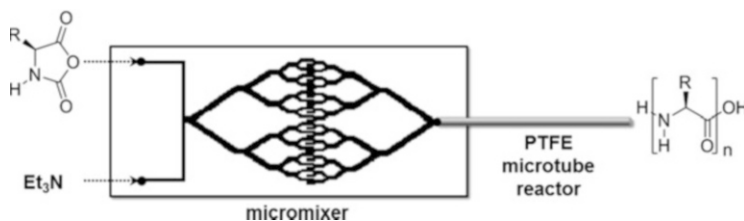
Fig. 32 Flow microreactor system consisting of a polydimethylsiloxane (PDMS) multilayered laminar micromixer and PTFE microtubes for polymerization of amino acid *N*-carboxyanhydride (NCA) initiated by triethylamine

Table 8 Comparison of polymer properties

Polymer	System	M_n	M_w/M_n
Poly(Glu)	Batch	40,200	1.56
	Microreactor	40,000	1.17
Copoly(Lys-Ala)	Batch	17,700	2.56
	Microreactor	18,800	1.64
Copoly(Lys-Leu)	Batch	18,100	2.13
	Microreactor	19,200	1.54

microreactor system consisting of a polydimethylsiloxane-based multilamination mixer and a PTFE microtube leads to narrower molecular weight distribution (M_w/M_n of about 1.2 for the flow reactor and 1.5 for the batch reactor), although molecular weights are similar (flow M_n of about 20,000 for the flow reactor and about 18,000 for the batch reactor) [228]. The use of a simple T-shaped connector as a mixer leads to broader molecular weight distribution, indicating the importance of fast micromixing. This flow microreactor system can be applied to the polymerization and copolymerization of other amino acid NCAs to obtain poly(Glu), copoly (Lys-Ala) and copoly(Lys-Leu) of narrower molecular weight distribution than those obtained from the batch reactor (Table 8).

A silicon-glass-based flow microreactor system that is suitable for long periods of use has been developed and applied to the polymerization of amino acid NCAs [229]. The flow microreactor exhibits excellent controllability of the molecular weight distribution. Moreover, a single flow microreactor can produce 100 mg/min of copoly(Lys-Leu). This means that more than 200 g of copoly(Lys-Leu) acids can be produced in 2 months.

Hyperbranched polymers have attracted much attention because these polymers exhibit different characteristic features, such as a lower viscosity, higher solubility, and higher amount of terminal groups, compared with those of the corresponding linear polymers. Such polymers can be prepared by ring-opening multibranching polymerization. Hyperbranched polyglycerols are popular because they have a large number of hydroxyl groups and exhibit excellent biocompatibility [230]. A continuous micromixer-assisted flow process for the synthesis of hyperbranched polyglycerol by ring-opening multibranching polymerization of glycidol was
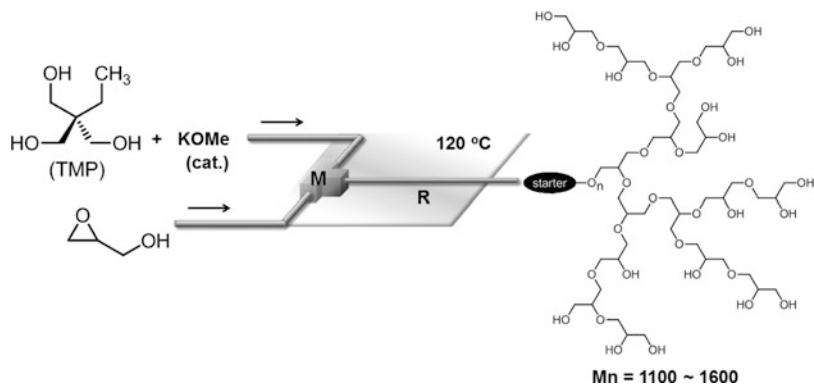
Fig. 33 Flow microreactor for synthesis of hyperbranched polyglycerol by ring-opening multibranching polymerization of glycidol. *M* micromixer

demonstrated by Wilms et al. [231] (Fig. 33). The polymerization was carried out in the presence of trimethylol propane (TMP) as a multifunctional initiator and potassium methoxide, which are necessary for deprotonation of 10% of the hydroxyl groups to obtain well-defined hyperbranched polyglycerols with molecular weights up to 1,000 g/mol. However, higher flow rates result in the partial formation of high molecular weight products, probably because of the formation of "hot spots" where the polymerization proceeds much faster.

The continuous-flow microwave-assisted polymerization of 2-ethyl-2-oxazoline was reported by Paulus et al. [232]. The flow process overcomes the problems associated with scale-up of the batch process, including safety issues.

1.6 Polycondensation Using Flow Microreactor Systems

Polycondensation reactions are important processes for the synthesis of polyesters, polycarbonates, polyamides, and polysiloxanes [233]. Polycondensation reaction is classified into a step-growth polymerization, which involves a stepwise covalent-bond-forming reaction between functional groups of two monomers, between a functional group of a monomer and a polymer end, or between functional groups of two polymer ends. Because the propagating polymers and monomer do not contain an active species (such as cations, radicals, or anions), the polymer chains reach moderately high molecular weight even at very high conversion. Therefore, in principle, it is difficult to control molecular weight and molecular weight distribution precisely.

Polycondensation of 4,4'-oxydianiline (ODA) and isophthaloyl dichloride (IPA) followed by terminal modification has been carried out in a flow microreactor system (Fig. 34) [234]. The polymerization in the flow microreactor is faster than that in the batch system. A higher mixing efficiency of monomer seems to be responsible for the faster reaction. It is also important to note that the molecular
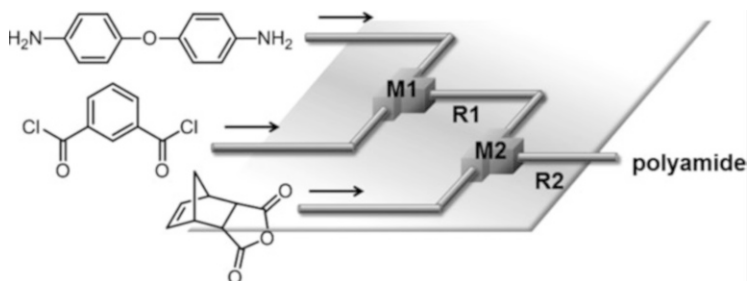
Fig. 34 Flow microreactor system for polycondensation of 4,4'-oxydianiline (ODA) and isophthaloyl dichloride (IPA) followed by terminal modification. *M1*, *M2* micromixers; *R1*, *R2* microtube reactors
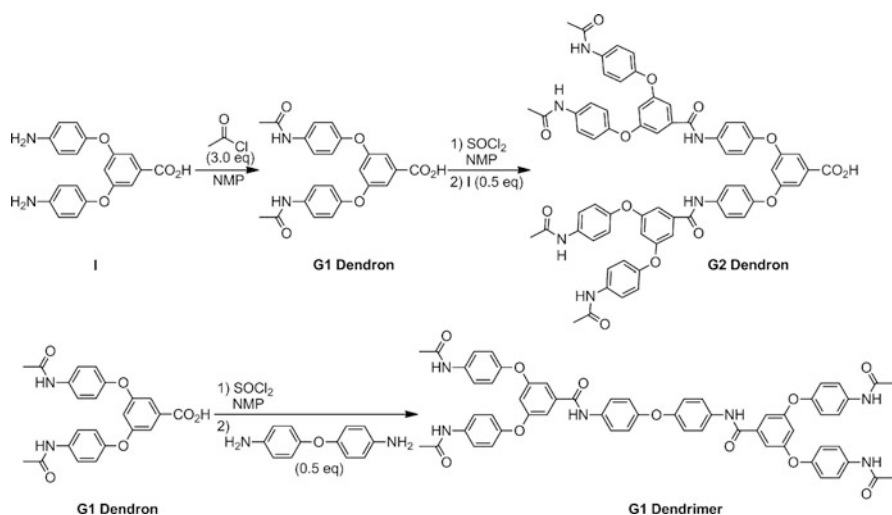
Fig. 35 Reactions of the convergent synthesis of polyamide dendrons and dendrimers

weight distribution of the polymer obtained in the flow is slightly narrower than that obtained in batch. Precise control of reaction temperature in the microreactor seems to be responsible.

Dendrimers, which have a highly branched 3D structure, provide a high degree of surface functionality and versatility. Polycondensation reactions are widely used for synthesizing various dendrimers. The synthesis of polyamide dendrons (G1 dendron, G2 dendron) and a dendrimer (G1 dendrimer) as shown in Fig. 35 has been carried out using flow microreactors [235]. The use of flow microreactors enables significant reduction in reaction time. In addition, the reaction can be performed at a constant temperature such as 30°C in flow, whereas a low temperature such as 0°C is necessary for the first mixing to avoid side reactions in batch. Moreover, polyamide dendrons can be deposited onto the functionalized glass surface through amide bond formation in flow.
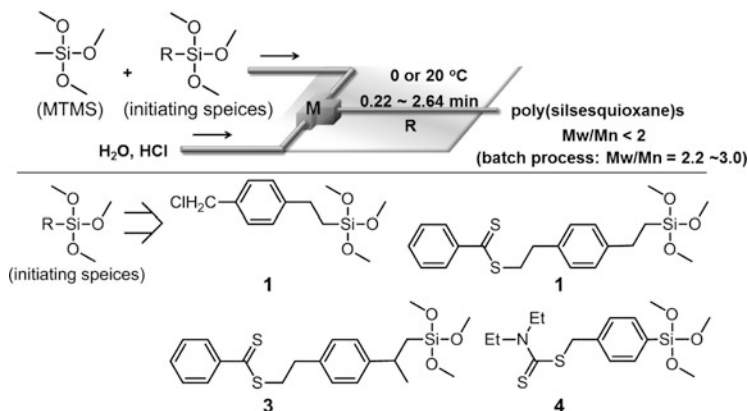
Fig. 36 Flow microreactor system for polycondensation reactions of trialkoxysilanes. *M* micromixer, *R* microtube reactor

By polycondensation of trifunctional silanols, it is possible to prepare poly (silsesquioxane)s, which emerge as materials for various applications ranging from low dielectric constant materials [236] to flame-retardant material [237]. The polycondensation reaction of methyltrimethoxysilane (MTMS) and various trimethoxysilanes involving initiators *p*-(chloromethyl)phenylethyltrimethoxysilane (**1**), dithiobenzoic acid benzyl-(4-ethyltrimethoxysilyl) ester (**2**), dithiobenzoic acid 1-ethylphenyl-4-(ethyltrimethoxysilyl) ester (**3**), and *N*,*N*-diethyldithiocarbamoy-lethylphenyl(trimethoxy)silane (**4**) [238, 239] can be successfully achieved in a microreactor to obtain the corresponding poly(silsesquioxane)s (Fig. 36) [240]. The yields are significantly higher than those in batch. The polydispersity indexes can be smaller than 2, whereas they are usually between 2.2 and 3 in batch. Moreover, molecular weights, which range from 1,900 to 11,000, can be controlled by changing the residence time (Table 9).

1.7 Ziegler–Natta Polymerization Using Flow Microreactor Systems

Ziegler–Natta polymerization [241, 242] is an important method of vinyl polymeri-zation because it allows synthesis of polymers of specific tacticity. As reported by Santos and Metzger, Ziegler–Natta polymerization can be carried out in a flow microreactor system coupled directly to the electrospray ionization (ESI) source of a quadrupole time-of-flight (Q-TOF) mass spectrometer (Fig. 37) [243]. In the first micromixer (M1), a catalyst (Cp_2ZrCl_2/MAO) and a monomer solution are mixed continuously to initiate the polymerization. The polymerization occurs in a microtube reactor. The solution thus obtained is introduced to the second micromixer (M2), where the polymerization is quenched by acetonitrile. The quenched solution is fed directly into the ESI source. The transient cationic species

Table 9 Molecular weight and molecular weight distribution obtained in microreactor synthesis

Initiator	Temperature (°C)	Residence time (min)	M_n	M_w/M_n
1	0	0.22	1,900	1.47
	0	0.66	3,450	1.49
	0	1.32	4,350	1.50
	0	1.98	6,250	1.54
	0	2.64	8,400	1.59
1	20	0.22	2,700	1.71
	20	2.64	9,550	1.93
2	0	0.22	2,100	1.46
	0	2.64	8,200	1.69
2	20	0.22	3,200	1.79
	20	2.64	9,700	1.87
3	0	0.22	2,200	1.53
	0	2.64	8,900	1.65
3	20	0.22	3,400	1.71
	20	2.64	10,100	1.92
4	0	0.22	2,250	1.39
	0	2.64	8,100	1.61
4	20	0.22	3,700	1.87
	20	2.64	11,000	1.95
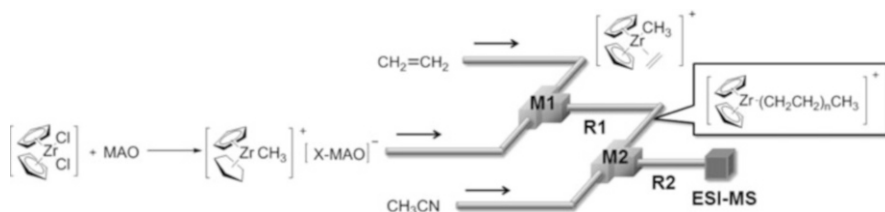
Fig. 37 Flow microreactor system for Ziegler–Natta polymerization

can be characterized by mass spectrometry. This is the first case where an alkyl zirconium cation intermediate in the homogeneous Ziegler–Natta polymerization of ethylene has been detected directly.

1.8 Fabrication of Polymeric Structures Inside Microchannels Using Fluid Flow

1.8.1 Polymerization on the Surface of Microchannels

Surface-initiated polymerization is an attractive method for fabrication of microfluidic devices [244–247]. For example, Xu et al. reported surface-initiated ATRP inside microchannels to produce flat gradient and patterned surfaces [248].
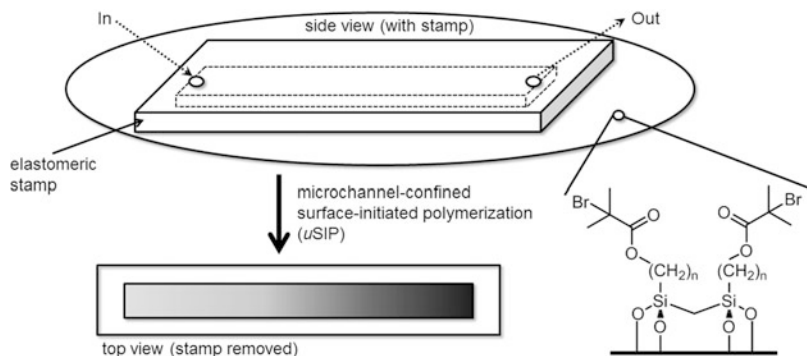
Fig. 38 Microchannel-confined surface-initiated polymerization (μSIP)
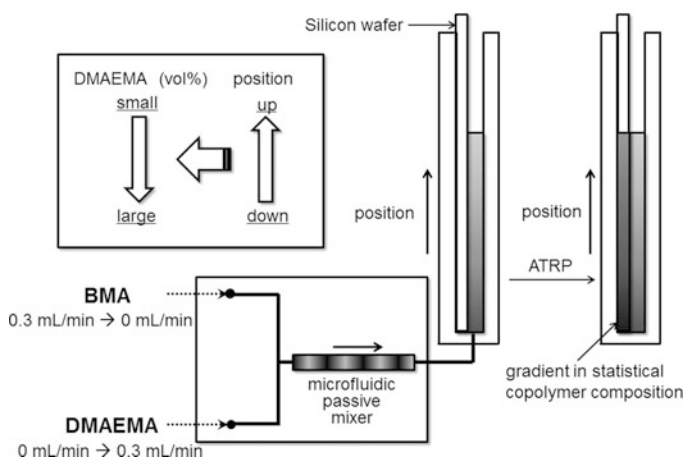
Fig. 39 Setup used for the patterning of a surface with a statistical-copolymer-brush gradient

A solution of 2-hydroxyethyl methacrylate (HEMA) is introduced into the microchannel (300 mm × 8 mm × 4.5 cm), which was manufactured on a silicon wafer and functionalized with initiator-functionalized self-assembled monolayer (Fig. 38). A polymer gradient is created inside the microchannel so that the thickness of the polymer brush decreases linearly from the inlet to the outlet.

A microfluidic system can be applied to generate complex gradient solutions [249–251]. The generation of a solution gradient in a microfluidic passive mixer [252] has been used to synthesize a surface-grafted statistical-copolymer-brush composition gradient via surface-initiated ATRP (Fig. 39) [253]. Using surface-initiated polymerization, the monomer solution gradient of *n*BMA and 2-(*N,N*-dimethylamino) ethyl methacrylate (DMAEMA) was applied to synthesize a statistical-copolymer-brush composition gradient. Burdick et al. also reported a similar approach to fabrication of photo-crosslinked hydrogels with gradients of immobilized molecules and crosslinking densities using a microfluidics–photopolymerization process [254].
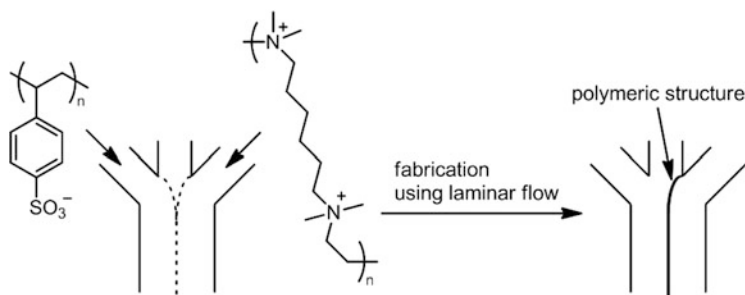
Fig. 40 Polymeric structure deposited on glass at the laminar flow interface of two solutions of poly(sodium 4-styrenesulfonate) and hexadimethrine bromide

1.8.2 Fabrication of Polymer Membranes Inside Microchannels

Characteristic features of controlled laminar flow in microfluidics devices have been utilized in many applications such as diffusion-based separation and detection, solvent extraction, mixing, and hydrodynamic focusing [255, 256].

A method of microfabrication based on multicomponent laminar flow inside microchannels was developed by Whitesides, Kenis and colleagues [257, 258]. Laminar streams of solutions enable a reaction at the interface between streams to make membranes inside the microchannel. For example, the reaction at the interface between two aqueous phases containing the oppositely charged polymers poly (sodium 4-styrenesulfonate) and hexadimethrine bromide flowing laminarly in parallel produces a polymeric structure (membrane) deposited on glass at the laminar flow interface (Fig. 40).

Zhao et al. demonstrated the formation of a laminar flow interface of immiscible liquids in a microchannel using partial chemical modification of the channel surface [259]. Synthesis of a polyamide nylon membrane by an interfacial polycondensation reaction of adipoyl chloride in 1,2-dichloroethane and hexamethylenediamine in water can be achieved in the cross-junction of the microchannel. Hiamoto et al. also demonstrated design and synthesis of nylon polyamide membrane structures by an interfacial polycondensation reaction of adipoyl chloride in 1,2-dichloroethane and hexamethylenediamine in water (Fig. 41) [260]. Uozumi and coworkers also reported that catalytic membrane-installed microchannel devices prepared from linear polymer ligands and palladium complexes could be applied to Suzuki–Miyaura coupling reaction, oxidative cyclization of alkenols, allylic arylation, and hydrodehalogenation [261–265]. In addition, the influence of microfluidic device geometry and flow rate on membrance formation by the interfacial polymerization was also demonstrated by Gargiuli et al. [266].

Single and parallel dual-membrane structures are successfully prepared by using multilayer flow such as organic/aqueous two-layer flow and organic/aqueous/organic three-layer flow inside a microchannel, and this method can be applied to the preparation of surface-modified polymer membranes (Fig. 42). For example, horseradish peroxidase is immobilized on one side of the membrane surface, and this enzyme-modified membrane realizes substrate permeation and a subsequent reaction.
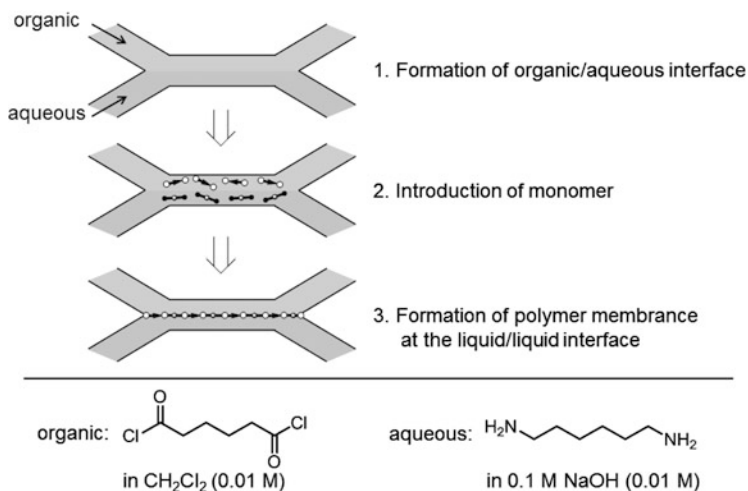
Fig. 41 Polymer membrane formation under organic/aqueous two-phase flow in an X-shaped microchannel
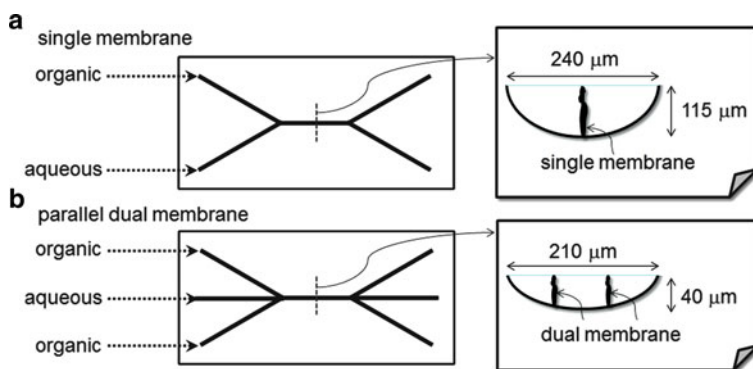
Fig. 42 Channel patterns and cross-sectional views of the nylon membrane prepared inside a microchannel. (**a**) Single membrane formed under organic/aqueous two-layer flow. (**b**) Parallel dual membranes formed under organic/aqueous/organic three-layer flow

Protein-polymeric membrane in a microchannel is prepared by using a concentric laminar flow (Fig. 43) [267]. Crosslinking condensation of a crosslinked enzyme aggregate (CLEA) [268] with aldehyde groups, which react with amino groups of the enzyme, in a concentric laminar flow results in the formation of a cylindrical enzyme-polymerized membrane on the inner wall of the microtube. The use of this technology for membrane formation in a microchannel can be extended to a broad range of functional proteins.
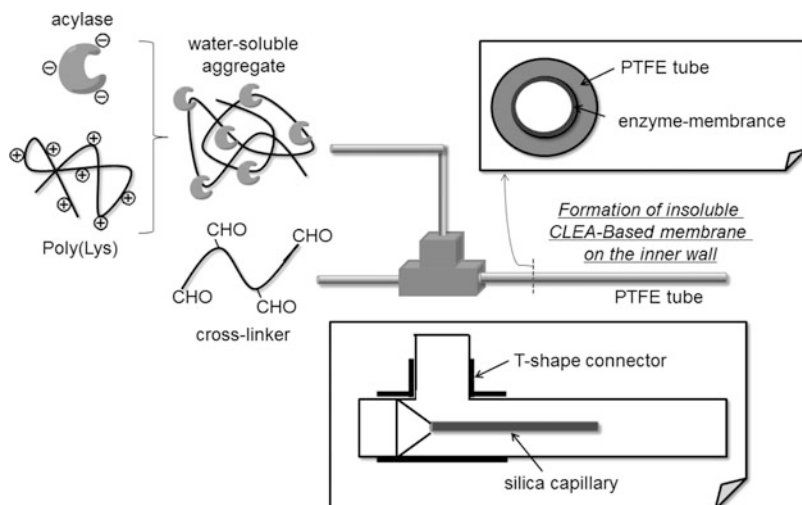
Fig. 43 Procedure for preparation of enzyme-membrane in a microtube
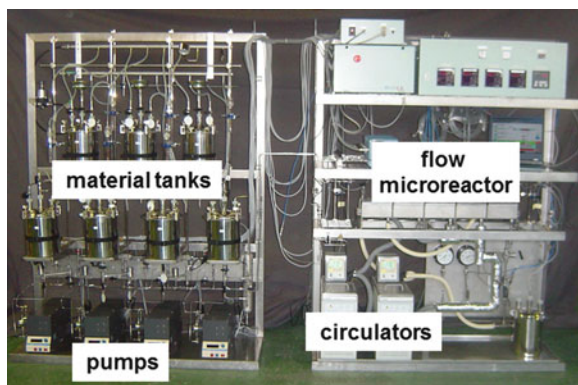
Fig. 44 Pilot plant for radical polymerization

1.9 Industrial Applications

It is easily anticipated that flow microreactors can enjoy industrial applications by virtue of inherent advantages based on their microstructure and flow nature. Significant progress in flow-microreactor-system-controlled polymerization to obtain structurally well-defined polymers has already been made to meet the demands of the chemical industry. The lack of need for cryogenic conditions for anionic polymerizations may enable commercial production. Some pilot plants have already been built and tested to examine the feasibility and durability of polymerization in flow microreactors. For example, a microchemical pilot plant

for radical polymerization of MMA has been built by numbering-up eight microtube reactors, which can be operated continuously for 6 days to produce 4.0 kg of the polymer, indicating that flow microreactor systems can be used for industrial production of polymers (Fig. 44) [167]. The information accumulated in laboratories and pilot plants should enable the development of this field to realize commercial plants for making polymers in the future.

1.10 Conclusion

The examples shown in this review article demonstrate that a variety of methods for polymer synthesis have been developed in flow microreactors. Continuous flow synthesis enables serial combinatorial synthesis, in which a variety of polymers can be synthesized in a sequential way using a single flow reactor with a flow switch. Space integration, which enables the synthesis of structurally well-defined polymers without isolating living polymer ends, also enhances the power and speed of polymer synthesis. Because several test plants for continuous production have already been built, there is no doubt that flow microreactors can contribute to polymer production in industry.

In conclusion, continuous flow polymer synthesis will be an indispensable technology for laboratory research and production in industry. Various methods for polymer synthesis by virtue of the characteristic features of flow microreactors will be developed, and they will work together to help meet the demanding expectations of polymer chemistry in the future.

References

1. Hessel V, Hardt S, Löwe H (2004) Chemical micro process engineering. Wiley, Weinheim
2. Wirth T (2008) Microreactors in organic synthesis and catalysis. Wiley, Weinheim
3. Hessel V, Renken A, Schouten JC et al (2009) Micro process engineering. Wiley, Weinheim
4. Watts P, Wiles C (2011) Micro reaction technology in organic synthesis. CRC, New York
5. Fletcher PDI, Haswell SJ, Pombo-Villar E et al (2002) Micro reactors: principles and applications in organic synthesis. Tetrahedron 58:4735–4757
6. Jähnisch K, Hessel V, Löwe H et al (2004) Chemistry in microstructured reactors. Angew Chem Int Ed 43:406–446
7. Kiwi-Minsker L, Renken A (2005) Microstructured reactors for catalytic reactions. Catal Today 110:2–14
8. Doku GN, Verboom W, Reinhoudt DN et al (2005) On-microchip multiphase chemistry – a review of microreactor design principles and reagent contacting modes. Tetrahedron 61:2733–2742
9. Watts P, Haswell SJ (2005) The application of micro reactors for organic synthesis. Chem Soc Rev 34:235–246
10. Geyer K, Codee JDC, Seeberger PH (2006) Microreactors as tools for synthetic chemists-the chemists' round-bottomed flask of the 21st century? Chem Eur J 12:8434–8442
11. Whitesides G (2006) The origins and the future of microfluidics. Nature 442:368–373

12. deMello AJ (2006) Control and detection of chemical reactions in microfluidic systems. Nature 442:394–402
13. Song H, Chen DL, Ismagilov RF (2006) Reactions in droplets in microfluidic channels. Angew Chem Int Ed 45:7336–7356
14. Kobayashi J, Mori Y, Kobayashi S (2006) Multiphase organic synthesis in microchannel reactors. Chem Asian J 1:22–35
15. Brivio M, Verboom W, Reinhoudt DN (2006) Miniaturized continuous flow reaction vessels: influence on chemical reactions. Lab Chip 6:329–344
16. Mason BP, Price KE, Steinbacher JL et al (2007) Greener approaches to organic synthesis using microreactor technology. Chem Rev 107:2300–2318
17. Ahmed-Omer B, Brandtand JC, Wirth T (2007) Advanced organic synthesis using microreactor technology. Org Biomol Chem 5:733–740
18. Watts P, Wiles C (2007) Recent advances in synthetic micro reaction technology. Chem Commun 443–467
19. Fukuyama T, Rahman MT, Sato M et al (2008) Adventures in inner space: microflow systems for practical organic synthesis. Synlett 151–163
20. Lin W, Wang Y, Wang S et al (2009) Integrated microfluidic reactors. Nano Today 4:470–481
21. McMullen JP, Jensen KF (2010) Integrated microreactors for reaction automation: new approaches to reaction development. Annu Rev Anal Chem 3:19–42
22. Ley SV (2010) The changing face of organic synthesis. Tetrahedron 66:6270–6292
23. Webb D, Jamison TF (2010) Continuous flow multi-step organic synthesis. Chem Sci 1:675–680
24. Yoshida J, Kim H, Nagaki A (2011) Green and sustainable chemical synthesis using flow microreactors. ChemSusChem 4:331–340
25. Chambers RD, Holling D, Spink RCH et al (2001) Elemental fluorine. Part 13. Gas-liquid thin film microreactors for selective direct fluorination. Lab Chip 1:132–137
26. Jähnisch K, Baerns M, Hessel V et al (2000) Direct fluorination of toluene using elemental fluorine in gas/liquid microreactors. J Fluor Chem 105:117–123
27. Ducry L, Roberge DM (2005) Controlled autocatalytic nitration of phenol in a microreactor. Angew Chem Int Ed 44:7972–7975
28. Wakami H, Yoshida J (2005) Grignard exchange reaction using a microflow system: from bench to pilot plan. Org Process Res Dev 9:787–791
29. Usutani H, Tomida Y, Nagaki A et al (2007) Generation and reactions of o-bromophenyllithium without benzyne formation using a microreactor. J Am Chem Soc 129:3046–3047
30. Nagaki A, Tomida Y, Usutani H et al (2007) Integrated micro flow synthesis based on sequential Br-Li exchange reactions of p-, m-, and o-dibromobenzenes. Chem Asian J 2:1513–1523
31. Nagaki A, Kim H, Yoshida J (2008) Aryllithium compounds bearing alkoxycarbonyl groups. Generation and reactions using a microflow system. Angew Chem Int Ed 47:7833–7836
32. Nagaki A, Takizawa E, Yoshida J (2009) Oxiranyl anion methodology using microflow systems. J Am Chem Soc 131:1654–1655
33. Nagaki A, Kim H, Yoshida J (2009) Nitro-substituted aryl lithium compounds in microreactor synthesis: switch between kinetic and thermodynamic control. Angew Chem Int Ed 48:8063–8065
34. Tomida Y, Nagaki A, Yoshida J (2009) Carbolithiation of conjugated enynes with aryllithiums in microflow system and applications to synthesis of allenylsilanes. Org Lett 11:3614–3617
35. Nagaki A, Takizawa E, Yoshida J (2009) Generation and reactions of α-silyloxiranyllithium in a microreactor. Chem Lett 38:486–487
36. Nagaki A, Takizawa E, Yoshida J (2009) Generations and reactions of N-tert-butylsulfonyl-aziridinyllithiums using microreactors. Chem Lett 38:1060–1061

37. Nagaki A, Kim H, Matsuo C et al (2010) Generation and reaction of cyano-substituted aryllithium compounds using microreactors. Org Biomol Chem 8:1212–1217
38. Nagaki A, Kim H, Moriwaki Y et al (2010) A flow microreactor system enables organolithium reactions without protecting alkoxycarbonyl groups. Chem Eur J 16:11167–11177
39. Nagaki A, Takizawa E, Yoshida J (2010) Generation and reactions of oxiranyllithiums by use of a flow microreactor system. Chem Eur J 16:14149–14158
40. Tomida Y, Nagaki A, Yoshida J (2011) Asymmetric carbolithiation of conjugated enynes: a flow microreactor enables the use of configurationally unstable intermediates before they epimerize. J Am Chem Soc 133:3744–3747
41. Kim H, Nagaki A, Yoshida J (2011) A flow-microreactor approach to protecting-group-free synthesis using organolithium compounds. Nat Commun 2:264
42. Nagaki A, Yamada S, Doi M et al (2011) Flow microreactor synthesis of disubstituted pyridines from dibromopyridines via Br/Li exchange without using cryogenic conditions. Green Chem 13:1110–1113
43. Nagaki A, Tokuoka S, Yamada S et al (2011) Perfluoroalkylation in flow microreactors: generation of perfluoroalkyllithiums in the presence and absence of electrophiles. Org Biomol Chem 9:7559–7563
44. Asai T, Takata A, Nagaki A et al (2012) Practical synthesis of photochromic diarylethenes in integrated flow microreactor. ChemSusChem 5:339–350
45. Nagaki A, Matsuo C, Kim S et al (2012) Lithiation of 1,2-dichloroethene in flow microreactors: versatile synthesis of alkenes and alkynes by precise residence-time control. Angew Chem Int Ed 51:3245–3248
46. He P, Watts P, Marken F et al (2006) Self-supported and clean one-step cathodic coupling of ... Derivatives in a micro flow reactor. Angew Chem Int Ed 45:4146–4149
47. Tanaka K, Motomatsu S, Koyama K et al (2007) Large-scale synthesis of immunoactivating natural product, pristane, by continuous microfluidic dehydration as the key step. Org Lett 9:299–302
48. Sahoo HR, Kralj JG, Jensen KF (2007) Multi-step continuous flow microchemical synthesis involving multiple reactions and separations. Angew Chem Int Ed 46:5704–5708
49. Hornung CH, Mackley MR, Baxendale IR et al (2007) A microcapillary flow disc reactor for organic synthesis. Org Process Res Dev 11:399–405
50. Fukuyama T, Kobayashi M, Rahman MT et al (2008) Spurring radical reactions of organic halides with tin hydride and TTMSS using microreactors. Org Lett 10:533–536
51. Tricotet T, O'Shea DF (2010) Automated generation and reactions of 3-hydroxymethylindoles in continuous-flow microreactors. Chem Eur J 16:6678–6686
52. Browne DL, Baumann M, Harji BH et al (2011) A new enabling technology for convenient laboratory scale continuous flow processing at low temperatures. Org Lett 13:3312–3315
53. Carter CF, Lange H, Sakai D et al (2011) Diastereoselective chain elongation reactions using microreactors for application in complex molecule assembly. Chem Eur J 17:3398–3405
54. Zaborenko N, Bedore MW, Jamison TF et al (2011) Kinetic and scale-up investigations of epoxide aminolysis in microreactors at high temperatures and pressures. Org Process Res Dev 15:131–139
55. Noël T, Kuhn S, Musachio AJ et al (2011) Suzuki–Miyaura cross-coupling reactions in flow: multistep synthesis enabled by a microfluidic extraction. Angew Chem Int Ed 50:5943–5946
56. Gutierrez AC, Jamison TF (2011) Continuous photochemical generation of catalytically active [CpRu]$^+$ complexes from CpRu(η^6-C$_6$H$_6$)PF$_6$. Org Lett 13:6414–6417
57. Hessel V, Serra C, Löwe H et al (2005) Polymerisationen in mikrostrukturierten reaktoren: ein überblick. Chem Ing Technol 77:1693–1714
58. Steinbacher JL, Mcquade DT (2006) Polymer chemistry in flow: new polymers, beads, capsules, and fibers. J Polym Sci A Polym Chem 44:6505–6533

59. Wilms D, Klos J, Frey H (2008) Microstructured reactors for polymer synthesis: a renaissance of continuous flow processes for tailor-made macromolecules? Macromol Chem Phys 209:343–356
60. Bally F, Serra CA, Hessel V et al (2010) Homogeneous polymerization: benefits brought by microprocess technologies to the synthesis and production of polymers. Macromol React Eng 4:543–561
61. Bally F, Serra CA, Hessel V et al (2011) Micromixer-assisted polymerization processes. Chem Eng Sci 66:1449–1462
62. Serra CA, Chang Z (2008) Microfluidic-assisted synthesis of polymer particles. Chem Eng Technol 31:1099–1115
63. Kakuta M, Bessoth FG, Manz A (2001) Microfabricated devices for fluid mixing and their application for chemical synthesis. Chem Rec 1:395–405
64. Hessel V, Löwe H, Schönfeld F (2005) Micromixers – a review on passive and active mixing principles. Chem Eng Sci 60:2479–2501
65. Ehrfeld W, Golbig K, Hessel V et al (1999) Characterization of mixing in micromixers by a test reaction: single mixing unites and mixer arrays. Ind Eng Chem Res 38:1075–1082
66. Lu H, Schmidt MA, Jensen KF (2001) Photochemical reactions and on-line UV detection in microfabricated reactors. Lab Chip 1:22–28
67. Ueno K, Kitagawa F, Kitamura N (2002) Photocyanation of pyrene across an oil/water interface in a polymer microchannel. Lab Chip 2:231–234
68. Fukuyama T, Hino Y, Kamata N et al (2004) Quick execution of [2+2] type photochemical cycloaddition reaction by continuous flow system using a glass-made microreactor. Chem Lett 33:1430–1431
69. Maeda H, Mukae H, Mizuno K (2005) Enhanced efficiency and regioselectivity of intramolecular (2π+2π) photocycloaddition of 1-cyanonaphthalene derivative using microreactors. Chem Lett 34:66–67
70. Jähnisch K, Dingerdissen U (2005) For an example of endoperoxide quenching in a continuous flow system. Chem Eng Technol 28:426–427
71. Hook BD, Dohle W, Hirst PR et al (2005) A practical flow reactor for continuous organic photochemistry. J Org Chem 70:7558–7564
72. Matsushita Y, Kumada S, Wakabayashi K et al (2006) Photocatalytic reduction in microreactors. Chem Lett 35:410–411
73. Sugimoto A, Sumino Y, Takagi M et al (2006) High throughput evaluation of the production of substituted acetylenes by the Sonogashira reaction followed by the Mizoroki–Heck reaction in ionic liquids, in situ, using a novel array reactor. Tetrahedron Lett 47:6197–6200
74. Matsushita Y, Ohba N, Suzuki T et al (2008) Photocatalytic reduction of CO_2 in a photocatalytic microreactor under gas-liquid-solid multiphase-flow condition excited by 365-nm UV-LEDs. Catal Today 132:153–158
75. Horie T, Sumino M, Tanaka T et al (2010) Photodimerization of maleic anhydride in a microreactor without clogging. Org Process Res Dev 14:405–410
76. Yoshida J, Kataoka K, Horcajada R et al (2008) Modern strategies in electroorganic synthesis. Chem Rev 108:2265–2299
77. Yoshida J (2009) Organic electrochemistry, microreactors, and their synergy. ECS Interface, Summer 40–45
78. Löwe H, Ehrfeld W (1999) State-of-the-art in microreaction technology: concepts, manufacturing and applications. Electrochim Acta 44:3679–3689
79. Suga S, Okajima M, Fujiwara K et al (2001) "Cation flow" method. A new approach to conventional and combinatorial organic syntheses using electrochemical microflow systems. J Am Chem Soc 123:7941–7942
80. Kupper M, Hessel V, Löwe H et al (2003) Micro reactor for electroorganic synthesis in the simulated moving bed-reaction and separation environment. Electrochim Acta 48:2889–2896
81. Paddon CA, Pritchard GJ, Thiemann T et al (2002) Paired electrosynthesis: micro-flow cell processes with and without added electrolyte. Electrochem Commun 4:825–831

82. Horii D, Atobe M, Fuchigami T et al (2005) Self-supported paired electrosynthesis of 2,5-dimethoxy-2,5-dihydrofuran using a thin layer flow cell without intentionally added supporting electrolyte. Electrochem Commun 7:35–39

83. Horcajada R, Okajima M, Suga S et al (2005) Microflow electroorganic synthesis without supporting electrolyte. Chem Commun 1303–1305

84. Suga S, Okajima M, Fujiwara K et al (2005) Electrochemical combinatorial organic syntheses using micro flow systems. QSAR Comb Sci 24:728–741

85. Horii D, Atobe M, Fuchigami T et al (2006) Self-supported methoxylation and acetoxylation electrosynthesis using a simple thin-layer flow cell. J Electrochem Soc 153:D143–D147

86. Horii D, Fuchigami T, Atobe M (2007) A new approach to anodic substitution reaction using parallel laminar flow in a micro-flow reactor. J Am Chem Soc 129:11692–11693

87. Yoshida J (2008) Flash chemistry. Fast organic synthesis in microsystems. Wiley-Blackwell, Hoboken

88. Yoshida J (2010) Flash chemistry: flow microreactor synthesis based on high-resolution reaction time control. Chem Rec 10:332–341

89. Yoshida J, Nagaki A, Yamada T (2008) Flash chemistry: fast chemical synthesis by using microreactors. Chem Eur J 14:7450–7459

90. Yoshida J (2005) Flash chemistry using electrochemical method and microsystems. Chem Commun 4509–4516

91. Higashimura T (1971) Cationic polymerization. Kagaku Dojin, Kyoto

92. Matyjaszewski K, Sawamoto M (1996) In: Matyjaszewski K (ed) Cationic polymerizations. Dekker, New York

93. Prakash GKS, Schleyer PVR (1997) Stable carbocation chemistry. Wiley Interscience, New York

94. Olah GA (1995) My search for carbocations and their role in chemistry (Nobel lecture). Angew Chem Int Ed 34:1393–1405

95. Olah GA (2001) 100 years of carbocations and their significance in chemistry. J Org Chem 66:5943–5957

96. Miyamoto M, Sawamoto M, Higashimura T (1984) Living polymerization of isobutyl vinyl ether with the hydrogen iodide/iodine initiating system. Macromolecules 17:265–268

97. Aoshima S, Higashimura T (1989) Living cationic polymerization of vinyl monomers by organoaluminum halides. Living polymerization of isobutyl vinyl ether by $EtA1C1_2$ in the presence of ester additives. Macromolecules 22:1009–1013

98. Kishimoto Y, Aoshima S, Higashimura T (1989) Living cationic polymerization of vinyl monomers by organoaluminum halides. Polymerization of isobutyl vinyl ether by $EtA1C1_2$ in the presence of ether additives. Macromolecules 22:3877–3882

99. Puskas JE, Kaszas J (2000) Living carbocationic polymerization of resonance-stabilized monomers. Prog Polym Sci 25:403–452

100. Inagaki N, Ando T, Sawamoto M et al (2004) Living cationic polymerization with micromixer: syntheses of end-functinalized polymers and multiblock copolymer. Polym Repr Jpn 53:2416–2417

101. Rys P (1976) Disguised chemical selectivities. Acc Chem Res 10:345–351

102. Yoshida J, Nagaki A, Iwasaki T et al (2005) Enhancement of chemical selectivity by microreactors. Chem Eng Technol 3:259–266

103. Nagaki A, Togai M, Suga S et al (2005) Control of extremely fast competitve consecutive reactions using micromixing. J Am Chem Soc 127:11666–11675

104. Suga S, Nagaki A, Yoshida J (2003) Highly selective Friedel–Crafts monoalkylation using micromixing. Chem Commun 354–355

105. Suga S, Nagaki A, Tsutsui Y et al (2003) "N-Acyliminium ion pool" as hetero diene in [4+2] cycloaddition reaction. Org Lett 5:945–949

106. Suga S, Tsutsui Y, Nagaki A et al (2005) Cycloaddition of "N-acyliminium ion pool" with carbon-carbon multiple bond. Bull Chem Soc Jpn 78:1206–1217

107. Nagaki A, Takabayashi N, Tomida Y et al (2008) Synthesis of unsymmetrical biaryls by means of mono-selective reaction of polyhaloarenes using integrated microflow system. Org Lett 18:3937–3940
108. Nagaki A, Takabayashi N, Tomida Y et al (2009) Synthesis of unsymmetrically substituted biaryls via sequential lithiation of dibromobiaryls using integrated microflow systems. Beilstein J Org Chem 5:16
109. Ishigaki Y, Suzuki T, Nishida J et al (2011) Hysteretic tricolor electrochromic systems based on the dynamic redox properties of unsymmetrically substituted dihydrophenanthrenes and biphenyl-2,2′-diyl dications: efficient precursor synthesis by a flow microreactor method. Materials 4:1906–1926
110. Suzuki T, Uchimura Y, Ishigaki Y et al (2012) Non-additive substituent effects on expanding prestrained C–C bond in crystal: X-ray analyses on unsymmetrically substituted tetraaryl-pyracenes prepared by a flow microreactor method. Chem Lett 41:541–543
111. Midorikawa K, Suga S, Yoshida J (2006) Selective monoiodination of aromatic compounds with electrochemically generated I^+ using micromixing. Chem Commun 3794–3796
112. Kataoka K, Hagiwara Y, Midorikawa K et al (2008) Practical electrochemical iodination of aromatic compounds. Org Process Res Dev 12:1130–1136
113. Hessel V, Hofmann C, Löwe H et al (2004) Selectivity gains and energy savings for the industrial phenyl boronic acid process using micromixer/tubular reactors. Org Process Res Dev 8:511–523
114. Yoshida J, Suga S, Suzuki S et al (1999) Direct oxidative carbon-carbon bond formation using the "cation pool" method. Generation of iminium cation pools and their reaction with carbon nucleophiles. J Am Chem Soc 121:9546–9549
115. Yoshida J, Suga S (2002) Basic concepts of "cation pool" and "cation flow" methods and their applications in conventional and combinatorial organic synthesis. Chem Eur J 8:2650–2658
116. Suga S, Nishida T, Yamada D et al (2004) Three-component coupling based on the "cation pool" method. J Am Chem Soc 126:14338–14339
117. Suga S, Suzuki S, Yamamoto A et al (2000) Electrooxidative generation and accumulation of alkoxycarbenium ions and their reactions with carbon nucleophiles. J Am Chem Soc 122:10244–10245
118. Suga S, Matsumoto K, Ueoka K et al (2006) Indirect cation pool method. Rapid generation of alkoxycarbenium ion pools from thioacetals. J Am Chem Soc 128:7710–7711
119. Suzuki S, Matsumoto K, Kawamura K et al (2004) Generation of alkoxycarbenium ion pools from thioacetals and applications to glycosylation chemistry. Org Lett 6:3755–3758
120. Okajima M, Suga S, Itami K et al (2005) "Cation pool" method based on C–C bond dissociation. Effective generation of monocations and dications. J Am Chem Soc 127:6930–6931
121. Saito K, Ueoka K, Matsumoto K et al (2011) Indirect cation flow method. Flash generation of alkoxycarbenium ions and studies on stability of glycosyl cations. Angew Chem Int Ed 50:5153–5156
122. Okajima M, Soga K, Nokami T et al (2006) Oxidative generation of diarylcarbenium ion pools. Org Lett 8:5005–5007
123. Okajima M, Soga K, Watanabe T et al (2009) Generation of diarylcarbenium ion pools via electrochemical C–H bond dissociation. Bull Chem Soc Jpn 82:594–599
124. Nokami T, Shibuya A, Tsuyama H et al (2007) Electrochemical generarion of glycosyl triflate pools. J Am Chem Soc 129:10922–10928
125. Nagaki A, Kawamura K, Suga S et al (2004) "Cation pool" initiated controlled/living polymerization using microsystems. J Am Chem Soc 126:14702–14703
126. Cho CG, Feit BA, Webster OW (1990) Cationic polymerization of isobutyl vinyl ether: livingness enhancement by dialkyl sulfide. Macromolecules 23:1918–1923
127. Iwasaki T, Nagaki A, Yoshida J (2007) Microsystem controlled cationic polymerization of vinyl ethers initiated by CF_3SO_3H. Chem Commun 1263–1265

128. Nagaki A, Iwasaki T, Kawamura K et al (2008) Microflow system controlled carbocationic polymerization of vinyl ethers. Chem Asian J 3:1558–1567
129. Dittmer T, Gruber F, Nuyken O (1989) Cationic polymerization of bis(1-alkylvinyl)benzenes and related monomers – structure elucidation of 1,1,3-trimetnyl substituted polyindane. Makromol Chem 190:1755–1770
130. Dittmer T, Gruber F, Nuyken O (1989) Cationic polymerization of bis(1-alkylvinyl)benzenes and related monomers – controlled syntheses of 1,1,3-trimetnyl substitued polyindanes. Makromol Chem 190:1771–1790
131. Iwasaki T, Yoshida J (2007) CF_3SO_3H initiated cationic polymerization of diisopropenyl-benzenes in macrobatch and microflow systems. Macromol Rapid Commun 28:1219–1224
132. Szwarc M (1956) Living polymers. Nature 178:1168–1169
133. Hsieh HL, Quirk RP (1996) Anionic polymerization: principles and practical applications. Dekker, New York
134. Jagur-grodzinski J (2002) Functional polymers by living anionic polymerization. J Polym Sci A Polym Chem 40:2116–2133
135. Hong K, Uhrig D, Mays JW (1999) Living anionic polymerization. Curr Opin Solid State Mater Sci 4:531
136. Hirao A, Loykulnant S, Ishizone T (2002) Recent advance in living anionic polymerization of functionalized styrene derivatives. Prog Polym Sci 27:1399–1471
137. Hadjichristidis N, Pitsikalis M, Pispas S et al (2001) Polymers with complex architecture by living anionic polymerization. Chem Rev 101:3747–3792
138. Frechet JMJ (1994) Functional polymers and dendrimers: reactivity, molecular architecture, and interfacial energy. Science 263:1710–1715
139. Percec V (2001) Frontiers in polymer chemistry. Chem Rev 101(12):3579–3580
140. Jagur-Grodzinski J (2006) Living and controlled polymerization: synthesis, characterization, and properties of the respective polymers and copolymers. NOVA, New York
141. Bhattacharyya DN, Lee CL, Smid J et al (1965) J Phys Chem 69:612
142. Figini RV, Hostalka H, Hurm K et al (1965) Z Phys Chem 45:269
143. Baskaran D, Müller AHE (1997) Kinetic investigation on metal free anionic polymerization of methyl methacrylate using tetraphenylphosphonium as the counterion in tetrahydrofuran. Macromolecules 30:1869–1874
144. Hofe T, Maurer A, Müller AHE (1998) GIT Labor Fahz 42:1127
145. Tonhauser C, Frey H (2010) A road less traveled to functional polymers: epoxide termination in living carbanionic polymer synthesis. Macromol Rapid Commun 31:1938–1947
146. Nagaki A, Tomida Y, Yoshida J (2008) Microflow system controlled anionic polymerization of styrenes. Macromolecules 41:6322–6330
147. Wurm F, Wilms D, Klos J et al (2008) Carbanions on trap – living anionic polymerization in a microstructured reactor. Macromol Chem Phys 209:1106–1114
148. Yoshida J, Saito K, Nokami T et al (2011) Space integration of reactions: an approach to increase capability of organic synthesis. Synlett 9:1189–1194
149. Suga S, Yamada D, Yoshida J (2010) Cationic three-component coupling involving an optically active enamine derivative. From time integration to space integration of reactions. Chem Lett 39:404–405
150. Nagaki A, Kenmoku A, Moriwaki Y et al (2010) Cross-coupling in a flow microreactor. Space integration of lithiation and Murahashi coupling. Angew Chem Int Ed 49:7543–7547
151. Nagaki A, Uesugi Y, Tomida Y et al (2011) Homocoupling of aryl halides in flow: space integration of lithiation and $FeCl_3$ promoted homocoupling. Beilstein J Org Chem 7:1064–1069
152. Nagaki A, Imai K, Kim H et al (2011) Flash synthesis of TAC-101 and its analogues from 1,3,5-tribromobenzene using integrated flow microreactor systems. RSC Adv 1:758–760
153. Nagaki A, Moriwaki Y, Haraki S et al (2012) Cross-coupling of aryllithiums with aryl and vinyl halides in flow microreactors. Chem Asian J 7:1061–1068

154. Tonhauser C, Wilms D, Wurm F et al (2010) Multihydroxyl-functional polystyrenes in continuous flow. Macromolecules 43:5582–5588
155. Pennisi RW, Fetters LJ (1988) Preparation of asymmetric three-arm polybutadiene and polystyrene stars. Macromolecules 21:1094–1099
156. Iatrou H, Hadjichristidis N (1992) Synthesis of a model 3-miktoarm star terpolymer. Macromolecules 25:4649–4651
157. Rózga-Wijas K, Chojnowski J, Fortuniak W et al (2003) Branched functionalised polysiloxane–silica hybrids for immobilisation of catalysts. J Mater Chem 13:2301–2310
158. Iida K, Chastek TQ, Beers KL et al (2009) Living anionic polymerization using a microfluidic reactor. Lab Chip 9:339–345
159. Zune C, Jérôme R (1999) Anionic polymerization of methacrylic monomers: characterization of the propagating species. Prog Polym Sci 24:631–664
160. Baskaran D (2003) Strategic developments in living anionic polymerization of alkyl (meth) acrylates. Prog Polym Sci 28:521–581
161. Nagaki A, Tomida Y, Miyazaki A et al (2009) Microflow system controlled anionic polymerization of MMA. Macromolecules 42:4384–4387
162. Nagaki A, Miyazaki A, Tomida Y et al (2011) Anionic polymerization of alkyl methacrylates using flow microreactor systems. Chem Eng J 167:548–555
163. Nagaki A, Miyazaki A, Yoshida J (2010) Synthesis of polystyrenes-poly(alkyl methacrylates) block copolymers via anionic polymerization using an integrated flow microreactor system. Macromolecules 43:8424–8429
164. Matyjaszewski K, Davis TP (2002) Handbook of radical polymerization. Wiley, New York
165. Iwasaki T, Yoshida J (2005) Free radical polymerization in microreactors. Significant improvement in molecular weight distribution control. Macromolecules 38:1159–1163
166. Leveson P, Dunk WAE, Jachuck RJ (2004) Investigation of shear effects on styrene free radical polymerization using a narrow channel reactor. J Appl Polym Sci 94:1365–1369
167. Iwasaki T, Kawano N, Yoshida J (2006) Radical polymerization using micro flow system. Numbering-up of microreactors and continuous operation. Org Process Res Dev 10:1126–1131
168. Bayer T, Pysall D, Wachsen O (2000) Micro mixing effects in continuous radical polymerization. In: Ehrfeld W (ed) Proceedings 3rd international conference on microreaction technology. Springer, Berlin, pp 165–170
169. Axiva GmbH, Pysall D, Wachsen O et al (1999) Method and device for continuous production of polymers. Patent WO/1999/054362
170. Serra C, Sary N, Schlatter G et al (2005) Numerical simulation of polymerization in interdigital multilamination micromixers. Lab Chip 5:966–973
171. Serra C, Schlatter G, Sary N et al (2007) Free radical polymerization in multilaminated microreactors: 2D and 3D multiphysics CFD modelling. Microfluid Nanofluid 3:451–461
172. Rollin AL, Patterson I, Huneault R et al (1977) The effect of flow regime on the continuous emulsion polymerization of styrene in a tubular reactor. Can J Chem Eng 55:565–571
173. Dalpe J, Bataille P (1989) Loop polymerization of vinyl acetate. J Appl Polym Sci 38:2237–2244
174. Abad C, de la Cal JC, Asua JM (1995) Start-up procedures in the emulsion copolymerization of vinyl esters in a continuous loop reactor. Polymer 36:4293–4299
175. Ouzine K, Graillat C, McKenna T (2004) Continuous tubular reactors for latex production: conventional emulsion and miniemulsion polymerizations. J Appl Polym Sci 91:2195–2207
176. Matyjaszewski K, Davis TP (2002) Handbook of radical polymerization. Wiley-Interscience, New York
177. Moad G, Solomon DH (2006) The chemistry of radical polymerization. Elsevier, Amsterdam
178. Braunecke WA, Matyjaszewski K (2007) Controlled/living radical polymerization: features, developments, and perspectives. Prog Polym Sci 32:93–146
179. Matyjaszewski K (1998) Controlled radical polymerization, vol 685. American Chemical Society, Washington

180. Matyjaszewski K (2000) Controlled/living radical polymerization: progress in ATRP, NMP, and RAFT, vol 768. American Chemical Society, Washington
181. Otsu T (2000) Iniferter concept and living radical polymerization. J Polym Sci Polym Chem 38:2121–2136
182. Matyjaszewski K, Xia J (2001) Atom transfer radical polymerization. Chem Rev 101:2921–2990
183. Ouchi M, Terashima T, Sawamoto M (2008) Precision control of radical polymerization via transition metal catalysis: from dormant species to designed catalysts for precision functional polymers. Acc Chem Res 41:1120–1132
184. Kamigaito M, Ando T, Sawamoto M (2001) Metal-catalyzed living radical polymerization. Chem Rev 101:3689–3746
185. Wang J, Matyjaszewski K (1995) Controlled/"living" radical polymerization. Halogen atom transfer radical polymerization promoted by a Cu(I)/Cu(II) redox process. Macromolecules 28:7901–7910
186. Wang J, Matyjaszewski K (1995) Atom transfer radical polymerization in the presence of transition metal complexes. J Am Chem Soc 117:5614–5615
187. Kato M, Kamigaito M, Sawamoto M et al (1995) Polymerization of methyl methacrylate with the carbon tetrachloride/dichlorotris-(triphenylphosphine)ruthenium(II)/methylaluminum bis (2,6-di-*tert*-butylphenoxide) initiating system: possibility of living radical polymerization. Macromolecules 28:1721–1723
188. Moad G, Rizzardo E, Thang SH (2008) Radical addition-fragmentation chemistry in polymer synthesis. Polymer 49:1079–1131
189. Löwe AB, McCormick CL (2007) Reversible addition-fragmentation chain transfer (RAFT) radical polymerization and the synthesis of water-soluble (co)polymers under homogeneous conditions in organic and aqueous media. Prog Polym Sci 32:283–351
190. Chiefari J, Chong YKB, Ercole F et al (1998) Living free-radical polymerization by reversible addition-fragmentation. Chain transfer: the RAFT process. Macromolecules 31:5559–5562
191. Hawker CJ, Bosman AW, Harth E (2001) New polymer synthesis by nitroxide mediated living radical polymerizations. Chem Rev 101:3661–3688
192. Studer A (2004) Tin-free radical chemistry using the persistent radical effect: alkoxyamine isomerization, addition reactions and polymerizations. Chem Soc Rev 33:267–273
193. Grubbs RB (2011) Nitroxide-mediated radical polymerization: limitations and versatility. Polym Rev 51:104–137
194. David G, Boyer C, Tonnar J, Ameduri B et al (2006) Use of iodocompounds in radical polymerization. Chem Rev 106:3936–3962
195. Poli R (2006) Relationship between one-electron transition-metal reactivity and radical polymerization processes. Angew Chem Int Ed 45:5058–5070
196. Yamago S (2009) Precision polymer synthesis by degenerative transfer controlled/living radical polymerization using organotellurium, organostibine, and organobismuthine chain transfer agents. Chem Rev 109:5051–5068
197. Yamago S (2006) The development of organotellurium-mediated and organostibine-mediated living radical polymerization reactions. J Polym Sci A Polym Chem 44:1–12
198. Goto A, Kwak Y, Fukuda T et al (2003) Mechanism-based invention of high-speed living radical polymerization using organotellurium compounds and azo-initiators. J Am Chem Soc 125:8720–8721
199. Yamago S, Iida K, Yoshida J (2002) Organotellurium compounds as novel initiators for controlled/living radical polymerizations. Synthesis of functionalized polystyrenes and end-group modifications. J Am Chem Soc 124:2874–2875
200. Kwak Y, Goto A, Fukuda T et al (2006) A systematic study on activation processes in organotellurium-mediated living radical polymerizations (TERPs) of styrene, methyl methacrylate, methyl acrylate, and vinyl acetate. Macromolecules 39:4671–4679
201. Yamago S, Iida K, Yoshida J (2002) Synthesis of poly(meth)acrylate derivatives and their di- and triblock copolymers. J Am Chem Soc 124:13666–13667

202. Matyjaszewski K (1997) Controlled radical polymerization, ACS Symposium Series, vol 685. American Chemical Society, Washington
203. Shen Y, Zhu S, Pelton R (2000) Packed column reactor for continuous atom transfer radical polymerization: methyl methacrylate polymerization using silica gel supported catalyst. Macromol Rapid Commun 21:956–959
204. Shen Y, Zhu S (2002) Continuous atom transfer radical block copolymerization of methacrylates. AIChE J 48:2609–2619
205. Wu T, Mei Y, Cabral JT et al (2004) A new synthetic method for controlled polymerization using a microfluidic system. J Am Chem Soc 126:9880–9881
206. Save M, Weaver JVM, Armes SP et al (2002) Atom transfer radical polymerization of hydroxy-functional methacrylates at ambient temperature: comparison of glycerol monomethacrylate with 2-hydroxypropyl methacrylate. Macromolecules 35:1152–1159
207. Wu T, Mei Y, Xu C et al (2005) Block copolymer PEO-b-PHPMA synthesis using controlled radical polymerization on a chip. Macromol Rapid Commun 26:1037–1042
208. Russum JP, Jones CW, Schork FJ (2004) Continuous reversible addition-fragmentation chain transfer polymerization in miniemulsion utilizing a multi-tube reaction system. Macromol Rapid Commun 25:1064–1068
209. Russum JP, Jones CW, Schork FJ (2005) Continuous living polymerization in miniemulsion using reversible addition fragmentation chain transfer (RAFT) in a tubular reactor. Ind Eng Chem Res 44:2484–2493
210. Diehl C, Laurino P, Azzouz N et al (2010) Accelerated continuous flow RAFT polymerization. Macromolecules 43:10311–10314
211. Hornung CH, Guerrero-Sanchez C, Brasholz M et al (2011) Controlled RAFT polymerization in a continuous flow microreactor. Org Process Res Dev 15:593–601
212. Rosenfeld C, Serra C, Brochon C et al (2007) High-temperature nitroxide-mediated radical polymerization in a continuous microtube reactor: towards a better control of the polymerization reaction. Chem Eng Sci 62:5245–5250
213. Enright TE, Cunningham MF, Keoshkerian B (2005) Nitroxide-mediated polymerization of styrene in a continuous tubular reactor. Macromol Rapid Commun 26:221–225
214. Enright TE, Cunningham MF, Keoshkerian B (2010) Nitroxide-mediated bulk and miniemulsion polymerization in a continuous tubular reactor: synthesis of homo-, di- and triblock copolymers. Macromol React Eng 4:186–196
215. Rosenfeld C, Serra C, Brochon C et al (2008) Use of micromixers to control the molecular weight distribution in continuous two-stage nitroxide-mediated copolymerizations. Chem Eng J 135S:S242–S246
216. Rosenfeld C, Serra C, Brochon C et al (2008) Influence of micromixer characteristics on polydispersity index of block copolymers synthesized in continuous flow microreactors. Lab Chip 8:1682–1687
217. Miele S, Nesvadba P, Studer A (2009) 1-*tert*-Butyl-3,3,5,5-tetraalkyl-2-piperazinon-4-oxyls: highly efficient nitroxides for controlled radical polymerization. Macromolecules 42:2419–2427
218. Knoop CA, Studer A (2003) Hydroxy- and silyloxy-substituted TEMPO derivatives for the living free-radical polymerization of styrene and n-butyl acrylate: synthesis, kinetics, and mechanistic studies. J Am Chem Soc 125:16327–16333
219. Fukuyama T, Kajihara Y, Ryu I et al (2012) Nitroxide-mediated polymerization of styrene, butyl acrylate, or methyl methacrylate by microflow reactor technology. Synthesis 44:2555–2559
220. Rosenfeld C, Serra C, O'Donohue S et al (2007) Continuous online rapid size exclusion chromatography monitoring of polymerizations – CORSEMP. Macromol React Eng 1:547–552
221. Zitlalpopoca-Soriano AG, Vivaldo-Lima E, Flores-Tlacuahuac A (2010) Bifurcation analysis of a tubular reactor for nitroxide-mediated radical polymerization of styrene. Macromol React Eng 4:599–612

222. Zitlalpopoca-Soriano AG, Vivaldo-Lima E, Flores-Tlacuahuac A (2010) Grade transition dynamic optimization of the living nitroxide-mediated radical polymerization of styrene in a tubular reactor. Macromol React Eng 4:516–533
223. Stridsberg KM, Ryner M, Albertsson AC (2002) Controlled ring opening polymerization: polymers with controlled architecture. In: Albertsson AC (ed) Advances in polymers science. Springer, Berlin
224. Sanda F, Endo T (1999) Syntheses and functions of polymers based on amino acids. Macromol Chem Phys 200:2651–2661
225. Deming TJ (2000) Living polymerization of α-amino acid-N-carboxyanhydrides. J Polym Sci A Polym Chem 38:3011–3018
226. Bamfold CH, Block H (1961) The initiation step in the polymerization of N-carboxy α-amino acid anhydrides. J Chem Soc IV:4989–4991
227. Honda T, Miyazaki M, Nakamura H et al (2005) Controllable polymerization of N-carboxy anhydrides in a microreaction system. Lab Chip 5:812–818
228. Yamaguchi Y, Ogino K, Yamashita K et al (2004) Rapid micromixing based on multilayer laminar flows. J Chem Eng Jpn 37:1265–1270
229. Miyazaki M, Honda T, Nakamura H et al (2007) Development of a microreactor for amino acid polymerization. Chem Eng Technol 30:300–304
230. Kainthan RK, Janzen J, Levin E et al (2006) Biocompatibility testing of branched and linear polyglycidol. Biomacromolecules 7:703–709
231. Wilms D, Nieberle J, Klos J et al (2007) Synthesis of hyperbranched polyglycerol in a continuous flow microreactor. Chem Eng Technol 30:1519–1524
232. Paulus RM, Erdmenger T, Becer CR et al (2007) Scale-up of microwave-assisted polymerizations in continuous-flow mode: cationic ring-opening polymerization of 2-ethyl-2-oxazoline. Macromol Rapid Commun 28:484–491
233. Rogers ME, Long TE, Turner SR (2003) Introduction to synthetic methods in step-growth polymers. In: Rogers ME, Long TE (eds) Synthetic methods in step-growth polymers. Wiley, Chichester, pp 1–16
234. Kuboyama T, Yoshida J (2005) Synthesis of terminally modified polymer with a micromixer. In: Proceedings of the 8th topical conference on microreaction technology. American Institute of Chemical Engineers, New York, 132d
235. Liu S, Chang CH (2007) High rate convergent synthesis and deposition of polyamide dendrimers using a continuous-flow microreactor. Chem Eng Technol 30:334–340
236. Miller RD (1999) In search of low-k dielectrics. Science 286:421–423
237. Chiang CL, Ma CCM (2003) Synthesis, characterization and properties of novolac ladder-like polysilsesquioxanes containing phosphorus. J Polym Sci A Polym Chem 41:1371–1379
238. Kessler D, Theato P (2008) Synthesis of functional inorganic-organic hybrid polymers based on poly(silsesquioxanes) and their thin film properties. Macromolecules 41:5237–5244
239. de Boer B, Simon HK, Werts MPL et al (2000) "Living" free radical photopolymerization initiated from surface-grafted iniferter monolayers. Macromolecules 33:349–356
240. Kessler D, Löwe H, Theato P (2009) Synthesis of defined poly(silsesquioxane)s: fast poly-condensation of trialkoxysilanes in a continuous-flow microreactor. Macromol Chem Phys 210:807–813
241. Andresen A, Cordes HG, Herwig H et al (1976) Influence of long-chain branching on the viscoelastic properties of low-density polyethylenes. Angew Chem Int Ed 15:630–632
242. Sinn H, Kaminsky W, Vollmer HJ et al (1980) Living polymers on polymerization with extremely productive Ziegler catalysts. Angew Chem Int Ed 19:390–392
243. Santos LS, Metzger JO (2006) Study of homogeneously catalyzed Ziegler-Natta polymeriza-tion of ethene by ESI-MS. Angew Chem Int Ed 45:977–981
244. Luo N, Hutchinson JB, Anseth KS et al (2002) Integrated surface modification of fully polymeric microfluidic devices using living radical photopolymerization chemistry. J Polym Sci A Polym Chem 40:1885–1891
245. Luo N, Metters AT, Hutchison JB et al (2003) Methacrylated photoiniferter as a chemical basis for microlithography: micropatterning based on photografting polymerization. Macromolecules 36:6739–6745

246. Hutchison JB, Haraldsson KT, Good BT et al (2004) Robust polymer microfluidic device fabrication via contact liquid photolithographic polymerization (CLiPP). Lab Chip 4:658–662
247. Simms HM, Brotherton CM, Good BT et al (2005) In situ fabrication of macroporous polymer networks within microfluidic devices by living radical photopolymerization and leaching. Lab Chip 5:151–157
248. Xu C, Wu T, Drain CM et al (2005) Microchannel confined surface-initiated polymerization. Macromolecules 38:6–8
249. Jeon NL, Dertinger SKW, Chiu DT et al (2000) Generation of solution and surface gradients using microfluidic systems. Langmuir 16:8311–8316
250. Dertinger SKW, Chiu DT, Jeon NL et al (2001) Generation of gradients having complex shapes using microfluidic networks. Anal Chem 73:1240–1246
251. Jiang X, Xu Q, Dertinger SKW et al (2005) A general method for patterning gradients of biomolecules on surfaces using microfluidic networks. Anal Chem 77:2338–2347
252. Stroock A, Dertinger SKW, Ajdari A et al (2002) Chaotic mixer for microchannels. Science 295:647–651
253. Xu C, Barnes SE, Wu T et al (2006) Solution and surface composition gradients via microfluidic confinement: fabrication of a statistical-copolymer-brush composition gradient. Adv Mater 18:1427–1430
254. Burdick JA, Khademhosseini A, Langer R (2004) Fabrication of gradient hydrogels using a microfluidics/photopolymerization process. Langmuir 20:5153–5156
255. Atencia J, Beebe DJ (2005) Controlled microfluidic interfaces. Nature 437:648–655
256. Weigl BH, Yager P (1999) Microfluidic diffusion-based separation and detection. Science 283:346–347
257. Kenis PJA, Ismagilov RF, Whitesides GM (1999) Microfabrication inside capillaries using multiphase laminar flow patterning. Science 285:83–85
258. Kenis PJA, Ismagilov RF, Takayama S et al (2000) Fabrication inside microchannels using fluid flow. Acc Chem Res 33:841–847
259. Zhao B, Viernes NOL, Moore JS et al (2002) Control and applications of immiscible liquids in microchannels. J Am Chem Soc 124:5284–5285
260. Hisamoto H, Shimizu Y, Uchiyama K et al (2003) Chemicofunctional membrane for integrated chemical processes on a microchip. Anal Chem 75:350–354
261. Uozumi Y, Yamada YMA, Beppu T et al (2006) Instantaneous carbon–carbon bond formation using a microchannel reactor with a catalytic membrane. J Am Chem Soc 128:15994–15995
262. Yamada YMA, Torii K, Uozumi Y (2009) Oxidative cyclization of alkenols with oxone using a miniflow reactor. Beilstein J Org Chem 5:18
263. Yamada YMA, Watanabe T, Torii K et al (2009) Catalytic membrane-installed microchannel reactors for one-second allylic arylation. Chem Commun 5594–5596
264. Yamada YMA, Watanabe T, Torii K et al (2010) Palladium membrane-installed microchannel devices for instantaneous Suzuki–Miyaura cross-coupling. Chem Eur J 16:11311–11319
265. Yamada YMA, Watanabe T, Ohno A et al (2012) Development of polymeric palladium-nanoparticle membrane-installed microflow devices and their application in hydrodehalogenation. ChemSusChem 5:293–299
266. Gargiuli J, Shapiro E, Gulhane H et al (2006) Microfluidic systems for in situ formation of nylon 6,6 membranes. J Membr Sci 282:257–265
267. Honda T, Miyazaki M, Nakamura H et al (2006) Facile preparation of an enzyme-immobilized microreactor using a cross-linking enzyme membrane on a microchannel surface. Adv Synth Catal 348:2163–2171
268. Cao L, Langen L, Sheldon RA (2003) Immobilised enzymes: carrier-bound or carrier-free? Curr Opin Biotechnol 14:387–394

Kinetics of Block Copolymer Micelles Studied by Small-Angle Scattering Methods

Reidar Lund, Lutz Willner, and Dieter Richter

Abstract This article reviews recent progress in studying the kinetics of block copolymer micellar systems by time-resolved small angle scattering techniques. The review includes an overview of the theoretical background concerning block copolymer micellar structure and kinetics, with a clear distinction between equilibrium and non-equilibrium processes. Basic principles of both static and time-resolved small-angle X-ray and neutron scattering (TR-SAXS and TR-SANS) techniques are summarized, with a special emphasis on the characterization of block copolymer micellar systems. In particular, the principle of SANS in combination with hydrogen/ deuterium (H/D) contrast variation for the determination of chain exchange under equilibrium conditions is highlighted. In the experimental part, we first review results on equilibrium kinetics obtained within the last decade by the TR-SANS/H/D labeling technique. In general, the experimental results strongly indicate that the component exchange between different micelles proceeds via the exchange of single unimers. In agreement with the theoretical prediction, chain expulsion is the rate-determining step. The corresponding activation energy is mainly governed by the interfacial tension and the length of the insoluble block, which determine the exchange rate with a double exponential dependence. Thus, due to this extremely strong dependence, even synthetic polymers with modest chain length distribution show a logarithmic time dependence instead of the theoretically expected single exponential decay. In the second part, the kinetic results obtained under non-equilibrium conditions, i.e., relaxation processes obtained after perturbations from equilibrium, are reviewed. This part covers formation kinetics as well as reorganization and morphological transition kinetics. We present, as a special highlight, TR-SAXS

R. Lund (✉)
Department of Chemistry, University of Oslo, Postboks 1033 Blindern, 0315 Oslo, Norway
e-mail: reidar.lund@kjemi.uio.no

L. Willner (✉) and D. Richter
Jülich Centre for Neutron Science JCNS and Institute for Complex Systems ICS,
Forschungszentrum Jülich GmbH, 52425 Jülich, Germany
e-mail: l.willner@fz-juelich.de; d.richter@fz-juelich.de

measurements with millisecond resolution on the formation of star-like micelles after stopped-flow mixing of molecularly dissolved block copolymers with a selective solvent. The micellization process could be modelled as a nucleation & growth process with unimer exchange as the elemental mechanism. The resulting scenario could be described as a three step process that includes a fast nucleation event, a region of micellar growth, and a final equilibration to thermodynamically stable micelles. In summary, this review demonstrates the importance of small angle scattering techniques for studying fundamental aspects of kinetics in block copolymer micelles and in soft matter materials in general.

Keywords Block copolymer micelles · Contrast variation · Equilibrium and non-equilibrium kinetics · Morphology · Small-angle neutron and X-ray scattering · Time-resolved SAXS/SANS

Contents

Symbols

$\frac{\mathrm{d}\Sigma}{\mathrm{d}\Omega}$	Macroscopic differential scattering cross-section per unit volume in cm^{-1}
k_p^+	Rate constant for unimer insertion from micelle of size P
k_p^-	Rate constant for unimer expulsion from micelle of size P

$\lvert \mathbf{Q} \rvert = Q$	Scattering vector in Å^{-1}
A	Area
a	Elementary lattice size
$A(Q)$	Scattering amplitude in cm
A_2, A_3	Second and third virial coeffcient
b	Scattering length in cm
C_F, C_H	Numerical prefactors
d	Density in g/cm^3
D	Diffusion coefficient
d_f	Fractal dimension
E_a	Activation energy
F	Free energy
f	Ratio between degree of polymerization of soluble and insoluble block
F_{micelle}	The mixing term of free block copolymers and solvent
F_{mix}	Free energy of mixing
$G(P, \phi_1)$	Chemical potential
H/D	Hydrogen/deuterium
j_P	Flux of unimers to micelle of size P
k_B	Boltzmann constant: 1.38×10^{-23} J/K
L	Cylinder length in Å
l_i	Monomer segment length of block i
M_w	Weight average molecular weight in g/mole
$n(r)$	Density profile
N_A	Degree of polymerization of soluble block
N_{Avo}	Avogadro's number: 6.022×10^{23} mole^{-1}
N_B	Degree of polymerization of insoluble block
N_m	Total particle number
P	Micellar aggregation number
$P(Q)$	Form factor
$R(t)$	Relaxation function (TR-SANS)
R_c	Micellar core radius in Å
R_g	Radius of gyration
R_m	Total micellar radius in Å
s	Grafting density (area available per chain)
$S(Q)$	Structure factor
S_m	Translational entropy of micelles
t_{dead}	Dead time of mixing
v	Flory exponent
V_i	Volume of component i
V_s	Sample volume in cm^3
γ	Interfacial tension in mN/m
ζ	Fraction of block copolymer in the micellar state
η	Corona density
ξ	Blob radius/correlation length

ρ	Scattering length density in cm^{-2}
σ_{int}	Gaussian width of core–corona interface
σ_m	Smearing parameter for micellar radius
τ_1	Slow relaxation time (Aniansson and Wall)
τ_2	Fast relaxation time (Aniansson and Wall)
Φ_0	Solvent fraction in micellar core
ϕ_0	Total amphiphile volume fraction
ϕ_1	Unimer concentration
Φ_p	Concentration of micelle of size p
χ	Flory–Huggins interaction parameter

1 Introduction

Self-assembly is responsible for the formation of essential structures in nature, including lipid membranes and living cells. The resulting structures are formed as a consequence of a delicate balance between hydrophilic and hydrophobic contributions and/or enthalpic and entropic forces. Whereas the surface tension drives the formation of such systems, entropy and stochastic fluctuations try to rip the structures apart. This has important consequences. First of all, self-assembled structures are classified as soft materials meaning that the properties are rather susceptible to intensive parameters such as temperature and pressure and that the structures are easily perturbed and deformed by external fields. Secondly, they are intrinsically dynamic structures; both their formation and stability are potentially governed by their kinetics. Additionally, self-assembled systems are often only metastable, i.e., they are long-lived non-equilibrium structures. Whereas molecular thermodynamics can be used as a quantitative tool to predict structural parameters for systems in equilibrium, there is no general facile approach for non-equilibrium systems. A great challenge is therefore to understand the underlying physics and use this to understand the design rules for non-equilibrium structures. However, this requires advanced instrumentation tools capable of a full four-dimensional characterization of materials, i.e., providing full spatiotemporal information on the nanoscale.

Experimental observation of the kinetic processes of self-assembly is very challenging due to the wide range of time scales involved. Typically, a nucleation event takes place on a short time scale of the order of microseconds to milliseconds, which contrasts with the slower time scale for reorganization processes that can occur on time scales as slow as hours to years. Ideally, it is desirable to watch the structural evolution of the process to keep track of possible metastable intermediates, in analogy with what is commonly observed under chemical reactions. For this, time-resolved small-angle neutron and X-ray scattering (TR-SANS and TR-SAXS) techniques are ideal because the structure is encoded in the angular dependence of

the scattered intensity. In fact, with the advent of ever more powerful X-ray sources such as the third-generation synchrotrons, state-of-the-art SAXS gives access to spatiotemporal resolution of the order of only micro- to milliseconds up to hours, directly on the relevant length scales of about 1–100 nm. With more powerful neutron sources such as the high-flux reactor at Institut Laue Langevin (ILL), it is now also possible to access time scales down to about 100 ms with SANS. With even more powerful spallation sources such as the SNS, Oak Ridge in the USA and the future European Spallation Source (ESS) at Lund, Sweden, SANS is expected to catch up with the synchrotron and more easily give time resolutions approaching milliseconds and microseconds. Here in particular, neutron scattering will be useful as selective deuteration of molecules or parts of molecules, opening up many possibilities for contrast variation to label and highlight specific parts of the structure or to watch specific kinetic processes. In this review, we will focus on how these methods can be applied to investigate kinetics in micellar systems, in particular block copolymer systems.

Amphiphilic molecules such as surfactants and block copolymers containing hydrophobic (water-insoluble) and hydrophilic (water-soluble) parts, serve as simple synthetic model systems for understanding self-assembly. Micellization is a common self-assembly process whereby amphiphilic molecules spontaneously aggregate into various nanostructures that are usually of spherical, ellipsoidal, cylindrical, or vesicular shapes [1, 2]. These processes usually occur in selective solvents, i.e., solvents that are good for one part but poor for the other. Here, self-assembly is primarily driven by the incompatibility of the insoluble (hydrophobic or more generally "solvophobic") part with water or other solvents, and is mainly counteracted by repulsions or unfavorable configurations experienced in the swollen corona of the resulting micelles.

Block copolymer micelles are macromolecular analogues to ordinary surfactant micelles. These systems generally consist of two or more distinct types of polymeric blocks covalently linked together. Because of the wealth of possible combinations of chemistry and compositions of such polymers, the possibilities for tailoring self-assembly and resulting structures are virtually endless, leading to a wide range of applications. Common for micellization is that the aggregates are formed above a certain threshold concentration, called the critical micelle concentration (cmc). As block copolymers often contain large insoluble blocks, the cmc in these systems can be almost immeasurably small and micelles are spontaneously formed at almost any concentration in solvents where the interfacial tension is high, such as in water. An idealized example of how micelles are formed from block copolymers is shown in Fig. 1. Here, a sudden micellization is induced from a homogeneous solution of dissolved block copolymer chains by suddenly altering the conditions (change in solubility by addition of co-solvents, salts, etc.). This micelle formation process is a typical non-equilibrium kinetic process. Once micelles are formed, the classical view for micellar solutions is that the system attains its equilibrium by continuously exchanging the constituting chains. An example of such scenario is also shown in Fig. 1, where a single chain (unimer) is released and reabsorbed into the micelle. In much the same way as in chemical reactions, such a unimer exchange process is a
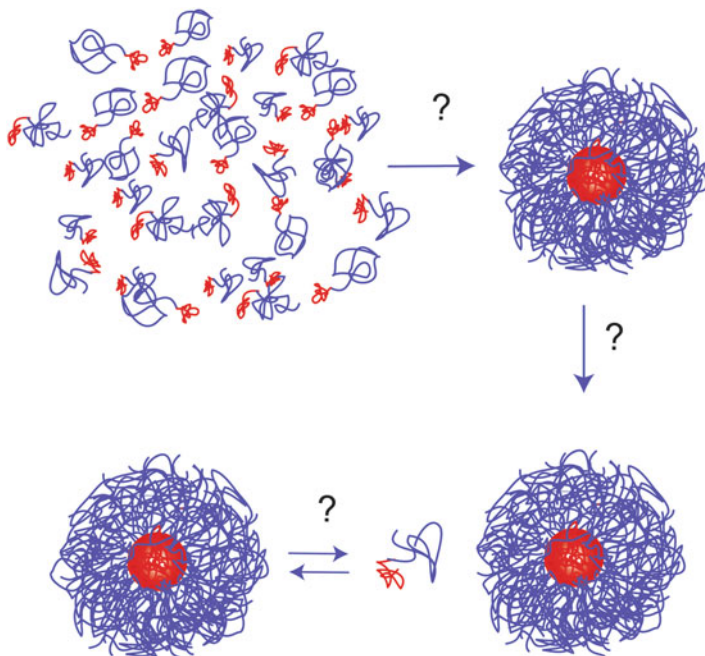
Fig. 1 Illustration of two kinetic processes in micellar systems. (*a*) Micelle formation, i.e., the kinetics associated with aggregation of single amphiphiles (unimers) into micelles and (*b*) the equilibrium kinetics characterizing a dynamic equilibrium of unimers exchanging between micelles

prerequisite for a dynamic equilibrium. However, for block copolymers characterized by a vanishingly small cmc, the question is: how can equilibrium be expected to be achieved?

As has been increasingly recognized over the last decade, block copolymer micelles are often characterized by exceedingly slow kinetics and, consequently, equilibrium is not necessarily achieved on a global scale. The system is then non-ergodic and the structure is thus generally path dependent, i.e., dependent on the sample preparation method [3–6]. This has significant implications in both nanotechnological and biomedical applications as the system is no longer just determined by thermodynamics (i.e., the global minimum in the parameter landscape), but rather by the kinetic pathways and the stability of the metastable state, in particular towards intramicellar reorganization processes. Recently, this property has been utilized to gain control over the nanostructures via kinetic control [5, 7–9] whereby the morphology and chemical composition can be manipulated via their non-equilibrium growth mechanism, etc. Kinetic control also represents a convenient methodology to use these "trapped" metastable states in order to create various non-equilibrium nanostructures that would otherwise not form under equilibrium conditions. While in equilibrium, most systems form either spherical, cylindrical, or vesicular structures; however, a notable computer simulation study [10] has shown that exotic (metastable) structures such as toroidal as well as intertwined and perforated shapes

can be formed in a simple A-B amphipihile system. Such structures are likely to be more long-lived in block copolymer systems due to their slower dynamics and kinetics. This opens up exciting possibilities for achieving well-defined intricate structures in simple two-component systems. However, in order to take full advantage of these possibilities, the kinetic pathways and the kinetics of block copolymer systems must be understood. On a more fundamental note, kinetic pathways in self-assembled systems and kinetic control are integral parts of the understanding and intelligent use of these materials in a nanotechnological setting. Their importance can be understood in much the same way as the importance of kinetics in chemical reactions and how an understanding of kinetics has helped design products and extended the use of both inorganic and organic chemistry in the twentieth century. Apart from kinetic control and manipulation of structures, kinetics is also essential in controlling the size and stability of nanoparticles formed by block copolymers for their use as, e.g., drug delivery systems [11] or in industrial applications as components of emulsions or non-foaming surfactant systems [12]. A great deal of effort must therefore be made towards studies assessing kinetic processes and in development of suitable experimental techniques.

Time resolved SAXS/SANS allow a structural observation of kinetic processes on the nanoscale (1–100 nm) on a time scale ranging from milliseconds to hours. This allows micellar kinetics to be followed in real time, giving direct structural information of the process and its evolution. Synchrotron SAXS can reach smaller time scales and exhibits better resolution compared to neutron-based methods. However, SANS offers the possibility for contrast variation via simple H/D exchange chemistry, which opens up a world of possibilities for the investigation of kinetics in soft matter systems, in particular transport and exchange processes that otherwise would be invisible in scattering experiments. As most of these techniques have become available over recent years with advancements in both instrumentation and sample environments, there is a need for an overview of the development and the possibilities that are now available in the field of soft matter in general and micellar systems in particular.

To this end, in this review we focus on the study of kinetic processes in micellar systems using time-resolved SAXS and SANS. Particular attention will be given to block copolymer systems and novel methodologies to study the kinetics using TR-SAXS or TR-SANS. Secondly, labeling experiments to study equilibrium kinetics using SANS will be thoroughly presented. While several related reviews have been presented [13–19], these contributions have been mostly devoted to low molecular weight surfactant systems and/or only focused on the general methodology of either SANS or SAXS. Here, we will give a thorough overview of results on block copolymer systems and show how both SAXS and SANS can be used as complementary methods to study kinetic processes in these systems. We will discuss both the strength and weaknesses of these methods and compare the results with investigations using other methods. Small-angle scattering methods are low-resolution methods that give ensemble averages over a large number of (most often orientational averaged) particles. The technique therefore requires a significant effort in data modeling and the development of methodology to analyze the data and thereby optimize the information content. Significant attention is therefore devoted to data modeling, in

particular with respect to time-resolved data and mechanistic models for kinetics. The fundamentals of scattering techniques and their application to micellar systems will be reviewed together with fundamentals of thermodynamics and kinetic models for block copolymer self-assembly. In the literature there is often an unclear terminology regarding the use of "kinetics of micelles". The terms "micelle dynamics" or "micelle kinetics" are often used for equilibrium kinetics (exchange kinetics), relaxation kinetics (micelle–micelle relaxation kinetics) and micellization kinetics (unimer–micelle transition). Here, we will attempt to clarify this subject and give a broader overview of the different processes encountered in micellar solutions. A particular focus will be on equilibrium kinetics and non-equilibrium micellization kinetics, although other processes will be covered as well.

2 Theoretical Background

In this section, we give a brief review of important selected theories for surfactant and block copolymer micelles. First, the classical thermodynamic theories covering both mean-field and scaling approaches are briefly reviewed before discussing kinetics. Classical theories for equilibrium and near-equilibrium surfactant and block copolymer micelle kinetics will be briefly reviewed before covering non-equilibrium kinetics in the final part.

2.1 Structure and Thermodynamics

The molecular organization and morphologies of micellar structures depend intimately on a delicate balance between hydrophobic and hydrophilic interactions as well as, if charges are present, electrostatic interactions. In addition, translational entropy may play an important role. Thermodynamics permits the determination of the structural micellar parameters, cmc (the concentration above which a significant aggregation occurs), micellar size distributions, etc. via molecular parameters. The earliest, most extensive descriptions of micellization were presented by Hill [20], who developed a molecular thermodynamic theory in which the individual micelles were considered as "small" phase-separated entities in equilibrium with other micelles, unimers, and solvent. This microscopic phase-separation picture was further developed by Hall and Pethica [21] and provides the most fundamental basis for many later developments. Tanford later made seminal contributions to an understanding of the effect of hydrophobicity and its driving force for micellization in aqueous solutions [22–24]. He showed that the hydrophobicity of hydrocarbons and organic molecules is mainly related to the entropy of water associated with hydrogen bonds.

In order to calculate the free energy of micellization accurately, one needs to take into account the enthalpic terms describing the interactions between the block copolymer and solvent, the free energy of the micelle (F_{micelle}), the mixing free energy (F_{mix}), as well as the translational entropy associated with micelles and free chains (S_{m}).

2.1.1 Mean-Field Theories

Mean-field theories are common in statistical physics and have been used to describe a wide range of phenomena ranging from magnetism to micelles. The common basis is the assumption that the local potential felt by all the neighboring particles is replaced by an effective field. The field is constant in time, isotropical and its strength depends on the number, coordination, and nature of its neighbors. This means that a multibody problem is reduced into effective interactions. In polymer physics, a familiar version is the Flory–Huggins solution theory whereby polymer segments are distributed together with the solvent molecules on a lattice. The thermodynamic properties can thereby be derived by calculating the distribution and resulting enthalpic interactions on such a lattice [25]. These ideas have been used by several authors to calculate the structural properties in micellar solutions [26–28].

A very complete and detailed model was presented by Leibler, Wheeler and Orland in the early 1980s [26]. The model uses a Flory–Huggins framework to calculate the mixing free energy and the free energy of the reference disordered state. The theory was originally developed for symmetric A-B type block copolymers (where A is the soluble block and B the insoluble block) in an A-homopolymer "solvent" and is thus restricted to a situation with no excluded volume effects in the corona ($\chi = 0.5$) (true mean field). Although the theory was originally formulated for symmetric block copolymers, Balsara and coworkers extended the theory for asymmetric B-A-B type systems and also considered "loops" in the corona [29]. Lund et al. later extended the model further to allow for a partial mixing between the B-type chain and a solvent for micelles in solutions [30]. As the model also applies relatively well for some block copolymer/solvent systems and provides a very useful starting point for discussing micellization theoretically, we will describe the theory in some detail.

Within this classical theory by Leibler and coworkers, the total free energy can be written as a sum of three contributions: the free energy of a micelle (F_{micelle}), the mixing term of free block copolymers and solvent (F_{mix}), and finally the entropic term (TS_{m}) describing the gas of micelles and block copolymers. In units per lattice site, this can be written as:

$$F_{\text{total}} = \frac{\phi_0 \zeta}{P \cdot N} \cdot F_{\text{micelle}} + F_{\text{mix}} - T S_{\text{m}} \tag{1}$$

where ζ is the fraction of block copolymers in the micellar state and ϕ_0 is the total volume fraction of block copolymers. P denotes the aggregation number (number of chains per micelle).

The individual terms can be written as:

$$F_{\text{mix}} = (1 - \xi \phi_0 \zeta) \left(\frac{\phi_1 \ln(\phi_1)}{N} + (1 - \phi_1) \frac{\ln(1 - \phi_1)}{N_{\text{s}}} + \chi \frac{\phi_1}{1+f} \cdot (1 - \phi_1/(1+f)) \right) \tag{2}$$

where N_s is the number of lattice points occupied by the solvent molecules and ϕ_1 the unimer volume fraction. Note that because ϕ_0 is typically 1% (dilute solution), this term is negligible in most practical situations. $\xi = (f + \eta)/[\eta(f + 1)]$; $N = N_A + N_B$ is the total number of polymer segments; $f = N_A/N_B$ the ratio of the repeat unit of the soluble, N_A, and insoluble block, N_B; η is the volume fraction of the A-polymer block in the corona; $\eta = PV_A/V_{corona}$ where V_A is the molecular volume of a single A-block; $V_{corona} = 4\pi/3\left(R_m^3 - R_c^3\right)$ is the volume of the corona; and R_c and R_m are the radii of core and micelle, respectively.

The translational entropy associated with the micelles and the unaggregated block copolymer chains can be written using the Flory–Huggins theory as:

$$S_m/k_B = -\left(\frac{\phi_0\zeta}{P\cdot N}\ln(\xi\,\phi_0\zeta) + \frac{1 - \xi\,\phi_0\zeta}{\xi\cdot P\cdot N}\ln(1 - \xi\,\phi_0\zeta)\right) \tag{3}$$

The micellar free energy, $F_{micelle}$, can be approximated to consist of mainly three terms:

$$F_{micelle} = F_{core} + F_{shell} + F_{int} \tag{4}$$

Within the classical Leibler, Orland, and Wheeler mean-field theory, the free energy is mainly dominated by the balance between stretching and swelling of the polymer chains and the interfacial energy. Here, the interactions between the coronal chains are assumed to be zero while the interactions between the two blocks are implicitly assumed to be equal to those between the solvent and insoluble B-block. Being a mean-field theory, no fluctuations are considered and the density of micelles is considered to be constant. Possible distribution in terms of the aggregation number is thereby neglected.

The free energy term of a micellar core consisting entirely of B-polymer segments can be written as:

$$F_{core} = \frac{3}{2}\cdot P\cdot\left(\frac{R_c^2}{N_B\cdot a^2} + \frac{N_B\cdot a^2}{R_c^2} - 2\right) \tag{5}$$

where a denotes the lattice size. However, in order to take into account swelling of the micellar core (i.e., when solvent molecules penetrate the core), one can modify the theory by introducing a Flory–Huggins expression describing the enthalpic and entropic interactions between the solvent molecules and the polymer segments within the core. This can be done by adding the term $F_{core}^{swollen}$ to Eq. 5 [30]:

$$F_{core}^{swollen} = F_{core} + \frac{4\pi R_c^3}{3\,a^3}\left(\Phi_0\cdot\frac{\ln(\phi_0)}{N_0} + \Phi_0\cdot(1 - \Phi_0)\cdot\chi\right) \tag{6}$$

where N_0 is the number of lattice sites occupied by a solvent molecule and Φ_0 is the fraction of solvent molecules in the core (homogeneously distributed).

The contribution from the shell consisting of A-block polymers with concentration η, homogeneously distributed in the radial direction, is written in the form:

$$F_{\text{shell}} = \frac{3}{2} \cdot P \cdot \left(\frac{R^2_{\text{corona}}}{N_B \cdot a^2} + \frac{N_B \cdot a^2}{R^2_{\text{corona}}} - 2 \right) + \frac{4\pi \left(R_m^3 - R_c^3\right)}{3a^3} \cdot \frac{(1-\eta)\ln(1-\eta)}{N_0} \quad (7)$$

The interfacial energy for a swollen core (assuming equal composition at surface and volume) may be written as:

$$F_{\text{int}} = \frac{4\pi R_c^2}{a^2} \gamma (1 - \Phi_0) \quad (8)$$

where $\gamma = \frac{k_B T}{a^2} \sqrt{\frac{\chi}{6}}$ is the interfacial tension and χ is the Flory–Huggins solubility parameter between A and B; in micellar solutions, between B and the solvent.

By minimizing the expressions above (Eq. 1) with respect to the independent parameters, the micellar parameters, including the cmc, for a given system can in principle be obtained.

In the case where interfacial energy (i.e. interfacial tension, γ) is large, then large micelles with only a very small fraction of unaggregated block copolymers are expected. Thus, the cmc (equal to ϕ_1 in equilibrium) is small and aggregation number $P \gg 1$, which in a dilute solution ($\phi_0 \approx 1\%$) leads to a negligible mixing free energy (i.e., F_{mix} and $S_m \approx 0$) and the total free energy of micellization is essentially given by the internal free energy of the micelle, F_{micelle}. This approximation is sometimes called the pseudo-phase approximation because physically this picture corresponds to a view in which the micelles constitute a thermodynamic "phase". However, since micelles are a sort of mesophase structure rather than a distinct state of matter, micellization is not called a phase transition. An extensive molecular thermodynamic mean-field theory has also been developed by Nagarayan (see, e.g., [31]) to calculate the micellar free energy in great detail. Quantitative predictions were made that gave reasonable agreement with experimental results in the case of polystyrene–polybutadiene (PS-PB) and polystyrene–polyisoprene (PS-PI) diblock copolymer systems. Mean-field approaches can be expected to work only for relatively homogeneous systems with weak interactions. A more recent example concerns PS-PB diblock copolymers in *n*-alkane solvents, which at room temperature are close to θ conditions [30]. It was shown that the structural properties measured by SANS, could be well described by the Leibler mean-field approach, provided that the swelling and penetration of solvent molecules into the micellar cores is included. In the case of polymeric systems that exhibit strong excluded volume interactions or repulsions, a mean-field approach is not appropriate.

2.1.2 Scaling Theories

For systems exhibiting strong excluded volume interactions, a mean-field approach is no longer realistic and spatial correlations must be taken into account. Although this is a notorious deep problem in theoretical statistical physics in general and polymers in particular, a relatively simple way of calculating free energies for micellar systems is represented by so-called "scaling theories", which have an origin in Kadanoff's approach and renormalization group theories developed to treat interactions in magnetic systems and critical phenomena [32, 33].

Scaling theory is a quite simple approach, which in the realm of polymer science was pioneered mainly by de Gennes [34]. Scaling theories apply a "coarse-grained" approach whereby the molecular details of the system is only indirectly considered using simplified geometrical descriptions. Complicated structural and thermodynamic features of polymeric systems are estimated using simple geometrical and physical arguments. Thereby, problems associated with mathematical complexities imposed by long-range excluded volume effects are partially circumvented. The central idea utilizes the fractal properties of polymeric chains and the scale invariance of such systems.[1] Introducing a characteristic length scale, ξ (the blob size), defined as regions of non-overlapping polymer segments, the polymer chains can be pictured as a "necklace" of connected "blobs". Inside the blobs, the potential of neighboring chains are not felt and the chains effectively behave as single isolated chains. The blob size scales as: [34]:

$$\xi \sim g^v \tag{9}$$

where v is the Flory exponent, taking the value 0.5 for a Gaussian chain and 0.588[2] for swollen chains [35]. g is the effective number of segments inside a blob. Furthermore, realizing that the blob size is defined by the fluctuations of the chain, the standard equipartition theorem in statistical physics suggests that its energy should be of the order of $k_B T$, where k_B is the Boltzmann constant. de Gennes further hypothesized that the free energy contribution of such a system can be calculated simply be counting the numbers of blobs and multiplying by $k_B T$. This can be called the de Gennes' $k_B T$ per blob recipe [34].

For block copolymer micelles there are many applications of such theories [36–42] generally using the pseudo-phase approximation.

We will first concentrate on the thermodynamics of spherical micelles that are generally formed for block copolymers having asymmetric compositions. Here, it is

---

[1] Renormalization group theory (see, e.g., [35]) lies at the heart of this theory, justifying the use of scaling laws in the asymptotic limit, i.e., for infinitely long polymer chains and for dilute solutions. For semidilute solutions, however, this criterion is not so crucial because the polymer chains are overlapping and many properties, e.g., osmotic pressure, are independent of the chain length.

[2] The fractal dimension d_f is given by $1/v \approx 1.7$ in this case, i.e., the chain is more extended than a Gaussian chain with $d_f = 2$. We also note here that the blob concept obviously only applies to systems with excluded volume effects, i.e., where $d_f < 2$.

possible to make several simplifications and consider limiting cases or classes of micelles. We will assume that the pseudo-phase approximation is fulfilled and that mixing entropy terms are negligible and can be ignored.

In all models (as for mean-field theories), the reduction of interfacial area upon micellization is considered to be the driving force for micellization. Thus, the interfacial tension is an important parameter. The interfacial free energy per chain of a spherical micelle (Eq. 8) can be written as:

$$F_{\text{int}} = \frac{4\pi R_{\text{c}}^2 \gamma}{P} \sim \ P^{-1/3}\gamma \tag{10}$$

where R_{c} is the micellar core radius and P is the aggregation number of the micelle that would scale with the volume, and thus $P \sim R_{\text{c}}^3$.

This term will favor micellar growth and, in the absence of other effects, lead to a macroscopic phase separation. However, in a real micellar system, growth will be primarily counteracted by a repulsion between the head groups or a finite extension of the surfactant tails. In polymeric systems, entropic contributions become dominant, e.g., stretching of chains. The major difference between the models is the way in which the counteracting free energy is calculated, in particular the free energy of the corona.

Within scaling theories, it is possible to distinguish three limiting cases for spherical polymeric micelles: crew-cut, intermediate and star-like micelles. For crew-cut micelles, characterized by having the number of repeat units of the B-block, N_{B}, much larger than of the soluble A-block, N_{A} (i.e. $N_{\text{A}} \ll N_{\text{B}}$), the free energy of the corona is assumed to be negligible compared with the stretching contribution in the core. As seen in Eq. 5, this contribution can be estimated from the rubber elasticity. Furthermore, ignoring prefactors and the finite extension of the chain, this can be simply written as:

$$F_{\text{core}} \sim \ \frac{R_{\text{c}}^2}{N_{\text{B}} l_{\text{B}}^2} \sim \ P^{2/3} \tag{11}$$

with l_{B}, the corresponding characteristic monomer length of the insoluble polymer B-block.

For the other two cases, it is assumed that the balancing free energy is determined by the free energy of the corona, which is calculated by assuming a flat core–corona interface for intermediate micelles (i.e., suitable when the B-block is relatively large) and a highly curved interface when $N_{\text{A}} \gg N_{\text{B}}$ for star-like micelles. Using the analogy to grafted polymer chains, the free energy of the corona can be calculated using the physics of polymer brushes [36–38, 41, 43].

This gives the following free energies of the corona:

$$F_{\text{corona}}/k_{\text{b}}T \sim \begin{cases} P^{1/2} \ln\left(N_{\text{A}}^{3/5} P^{-2/15} N_{\text{B}}^{-1/3}\right) & \text{Star-like} \\ P^{5/18} N_{\text{B}}^{-5/9} N_{\text{A}} & \text{Intermediate} \end{cases} \tag{12}$$

From this formalism, the dependence of the various micellar parameters on, for example, molecular weight, composition, interfacial tension, etc. can be estimated. The results seem to compare rather well with experimental data, see, e.g., [44, 45]. For example, for intermediate and star-like micelles, the aggregation number would scale as:

$$P_{\text{scaling}} \sim \begin{cases} \gamma^{6/5} N_B^{4/5} l_B^{12/5} & \text{Star-like} \\ \gamma^{18/11} N_B^2 N_A^{-18/11} l_A^{-30/11} l_B^{30/11} & \text{Intermediate} \end{cases} \tag{13}$$

2.1.3   Thermodynamics of Morphological Transitions

Under certain conditions, cylindrical micelles or even vesicles can be formed instead of spherical symmetric micelles. Cylindrical micelles are usually formed as a consequence of a delicate balance between the different terms, most notably governed by the chain stretching in the micellar core. Compared to spherical micelles, the core radius of a cylinder for an equivalent area or volume can easily be evaluated to be 2/3 smaller. Hence, in a cylindrical micelle, the amount of chain stretching is expected to be less pronounced than in a spherical one. On the other hand, chain interactions in the corona of a cylindrical micelle is expected to be more severe due to the smaller area available for each chain. All terms must thus be included and a more detailed thermodynamic evaluation should be performed. For vesicles, the bending modules is additionally expected to be important [46].

A very detailed and accurate theoretical description of the problem concerning the cylinder–sphere transition was made by Zhulina et al. [47].

For this approach, the same total free energy as in Eq. 4 was used. As before, the interface contribution can be calculated in a straightforward way and equals the area of the micellar core times the interfacial tension, γ:

$$F_{\text{int}} = \frac{A_j \cdot \gamma}{P \cdot k_B T} \begin{cases} A_j = 4\pi R_c^2 & \text{Spheres} \\ A_j = 2\pi R_c L & \text{Cylinders} \end{cases} \tag{14}$$

The aggregation number P can be related to other micellar parameters assuming a compact (solvent-free) core: $P = \pi R_c^2 L/(V_B/N_{\text{Avo}})$ and $P = 4\pi R_c^3/(3 \cdot V_B/N_{\text{Avo}})$ for cylinders and spheres, respectively. Here V_B is the molar volume of the insoluble B-block and N_{Avo} is Avagadro's number.

For the corona contribution, some care has to be taken. In order to calculate the free energy of this part, the number of blobs has to be calculated for each morphology, taking into account that the radial dependence of the density changes with the curvature. For a completely planar surface, de Gennes and Alexander [36, 37] showed that the blob size will be constant and scale by $\xi \approx s$, where s is the area available per chain. For a curved micellar core, the surface per corona chain will naturally increase

with the radial distance r away from the core $r > R_c$ and thus the area per chain will also be a function of r, i.e., $s = s(r)$.

Following the approach by Zhulina et al. [47], the energy density is thus $\Phi(r) = C_F \cdot k_B T / s(r)^{3/2}$ and the corona free energy per $k_B T$ can be calculated from $F_{\text{corona}} = \int_{R_c}^{R_m} \Phi(r)/k_B T s(r) dr = C_F \cdot \int_{R_c}^{R_m} s(r)^{-1/2} dr$. C_F is a numerical scaling factor of order unity.

The area per chain is found to have the following approximate form:

$$s(r) \begin{cases} s(r) = s_0 \left(\frac{r}{R_c}\right)^2 & \text{Spheres} \\ s(r) = s_0 \frac{r}{R_c} & \text{Cylinders} \end{cases} \tag{15}$$

These give the following results:

$$F_{\text{corona}} = C_F \int_{R_c}^{R_c+D} s(r)^{-1/2} dx; \begin{cases} s(r) = s_0 \left(\frac{r}{R_c}\right)^2 & \text{Spheres} \\ s(r) = s_0 \frac{r}{R_c} & \text{Cylinders} \end{cases} \tag{16}$$

where $s(r)$ is a function that describes the radial dependence of the grafting density, s (area available per chain), which on the core surface ($r = 0$) is equal to $s_0 = 4\pi R_c^2/P$ for spherical micelles and $s_0 = 2\pi R_c \times L/P$ for cylindrical micelles (where L is the cylinder length). After some calculus, Zhulina et al. showed that the analytical expressions of F_{corona} can be written as:

$$F_{\text{corona}} = \begin{cases} \frac{v C_F R_c}{\sqrt{s}} \ln\left(1 + \frac{l_A C_H N_A \left(s l_A^{-2}\right)^{(v-1)/2v}}{v R_c}\right) & \text{Spheres} \\ \frac{2 C_F R_c}{\sqrt{s}} \left[\left(1 + \frac{(1+v) \cdot l_A C_H N_A \left(s l_A^{-2}\right)^{(v-1)/2v}}{2 v R_c}\right)^{v/(v+1)} - 1\right] & \text{Cylinders} \end{cases} \tag{17}$$

Here C_F and C_H are numerical prefactors; l_B and l_A the effective segment lengths of insoluble and soluble blocks; N_B and N_A denote the respective number of repeat units; and v is the excluded volume parameter controlling the conformation of the chain. In a good solvent, v takes the well-known value 0.588.

F_{core} corresponds to the elastic energy associated with stretching the chains beyond their unperturbed end-to-end distance to the radius of the core. If this contribution is to be determined accurately, the fraction of chains needed to stretch must be evaluated. This was carefully worked out for various geometries by Semenov [39], who also calculated the fraction of chain-ends needed to effectively fill the core for each geometry. The results are:

$$F_{\text{core}} = k_j \cdot \frac{R_c^2}{R_{ee}^2}; \begin{cases} k_j = \frac{\pi^2}{16} & \text{Spheres} \\ k_j = \frac{3\pi^2}{80} & \text{Cylinders} \end{cases} \tag{18}$$

where R_c is the core radius and $R_{ee} \approx N_B^{1/2} l_B$ is the unperturbed (bulk) end-to-end distance of the core-forming polymer. The units are, as before, in $k_B T$. The total free energy can be found by summing Eqs. 14–18 according to Eq. 4 and the stability of sphere and cylinder can be estimated by the respective free energy. Minimalization with respect to the independent variables (P, R_m, etc.) will give the equilibrium values.

In a recent work on symmetric poly(ethylene-*alt*-propylene)–poly(ethylene oxide) (PEP-PEO) block copolymers in various *N,N*-dimethylformamide (DMF) and water mixtures, this model was used to analyze the structural data and the cylinder-to-sphere transition by minimizing the total free energy using Eq. 4 combined with Eqs. 14–18 above [48]. The values obtained by fitting the model after numerical minimization were in good accordance with the experimental data, and the resulting free energy profiles could describe the transition quite well. For transitions from cylinders to vesicles, a corresponding detailed thermodynamic model is yet to be presented and compared with experimental values. However, a useful compilation of theoretical considerations concerning the free energy contributions has been published [46].

2.2   Chain Exchange Kinetics in Equilibrium

Micelles can attain and maintain their global equilibrium by constantly redistributing their chains. This can predominantly occur via two main mechanisms[3]: unimer exchange and fusion/fission, as schematically illustrated in Fig. 2. These two mechanisms will be discussed in the context of different thermodynamic and kinetic models.

Exchange and relaxation kinetics of surfactant micelles are classical topics from the 1970s and 1980s [16, 50–54]. Because exchange kinetics are usually very fast for surfactant micelles, the process was more indirectly measured using a perturbation scheme like, e.g., temperature or pressure jumps. The relaxation to the new equilibrium is subsequently followed by light-scattering and other suitable methods. Such processes can be referred to as near-equilibrium relaxation kinetics and involve a transition from one micellar equilibrium to another mediated by a small change in the thermodynamic conditions. An illustration of such a process is depicted in Fig. 3.

As a consequence of available experimental data from relaxation experiments, most of the early theoretical work has been focused on this, in particular in the equilibrium regime where perturbations are small, which facilitates the treatment. Most notable is the work by Aniansson and Wall [54–56], valid for neutral surfactants, and that of Kahlweit [57], who also takes into account fusion of micelles

---

[3] Other mechanism such as concerted insertion, i.e., the scenario that two micelles exchange an unimer upon direct overlap [49], have also been proposed although these are expected to be less probable, at least for low concentrations.
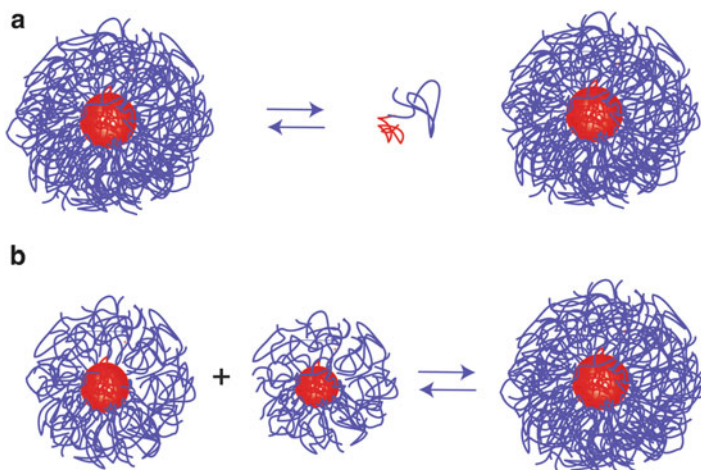
Fig. 2 Illustration of two important mechanisms involved in various kinetic processes in micellar systems. (**a**) Unimer exchange, single surfactant/block copolymer chains are interchanged one by one via the solvent medium. (**b**) Fusion/fission, where two micelles fuse or are fragmented to smaller micelles, respectively
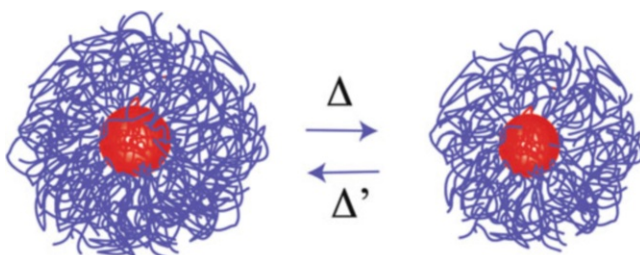
Fig. 3 Illustration of a relaxation process from one micellar equilibrium to another upon a small perturbation, Δ (the reverse perturbation, Δ') can either be due to a change in an intensive variable (temperature, pressure, electric field, etc.) or extensive variables such as pH, added salt, etc.

and the effect of charge screening. Here, we will focus on neutral systems where electrostatic effects are not relevant.

We will briefly review the available classical theories relevant to both surfactant and block copolymer micelle kinetics.

2.2.1 Aniansson and Wall Mechanism: Unimer Exchange and Linear Relaxation Experiments

The Aniansson and Wall theory (A-W theory) [55, 56] was developed for the near equilibrium relaxation kinetics of neutral low molecular weight micelles. It was

assumed that all changes in the association/dissociation involve individual unitary steps where only an exchange of one surfactant molecule is allowed at a time (Fig. 2a). This can be written as:

$$M_P + U \underset{k_p^-}{\overset{k_p^+}{\rightleftharpoons}} M_{P+1} \tag{19}$$

where U is the unimer, M_P is a micelle with aggregation number P, and k_p^+ and k_p^- are the corresponding rate constants for the insertion and expulsion. The corresponding rate equation is:

$$\frac{\mathrm{d}[U]}{\mathrm{d}t} = -k_p^+ [M_P][U] + k_p^- [M_{P+1}] \tag{20}$$

Using a system of rate equations constructed from the above mechanism, Aniansson and Wall showed that in a relaxation experiment close to equilibrium, in the linear regime, the relaxation is determined by two relaxation time constants. The first time constant characterizes the fast relaxation associated with a readjustment of the unimer concentration, without a change in the number density of micelles. As shown by Aniansson and Wall, this contribution depends on the expulsion rate constant, the width of the distribution of the micellar population, σ, and the fraction of unimers, X.

$$\frac{1}{\tau_1} = \frac{k_-}{\sigma^2} + \frac{k_-}{\langle P \rangle} \cdot X(1 + C_{\mathrm{dev}}) \tag{21}$$

where k_- is the expulsion rate constant for micelles at their equilibrium size (independent of P) and C_{dev} is a number that describes the relative deviation from equilibrium. For relaxation experiments performed in the linear regime (i.e. for very small perturbations), $C_{\mathrm{dev}} \approx 0$.

The second relaxation time τ_2, is related to a change in the number of micelles and is much slower because the surfactants have to be rearranged between the micelles in a cooperative fashion (formation/dissociation of micelles limited by unimer exchange). Again under the assumption of unimer exchange, this can be written as:

$$\frac{1}{\tau_2} = \frac{\langle P \rangle^2}{\phi_0} \frac{1}{R} \cdot \left(1 + \frac{\sigma^2}{\langle P \rangle}\right)^{-1} \tag{22}$$

where

$$\frac{1}{R} = \frac{1}{\Sigma_p k_p^- \cdot \phi_p} \tag{23}$$

The time scale of the first process is seen to decrease linearly with micellar density. The reason is that the larger the number of micelles, the more unimers are

consumed or expelled, which leads to a faster net growth or reduction of the micelles towards a new equilibrium. The second process is characterized by τ_2; however, it is expected to have a more complex concentration dependence. This comes from the fact that since the micelle equilibration only proceeds via unimer exchange, any intermediate metastable aggregates will consume unimers and hinder the formation of the final stable micellar state. The time scale thereby depends on the concentration and kinetics of all improper micelles ($P < P_{eq}$ or $P > P_{eq}$) and thus more than the width of the mean distribution. As seen in Eqs. 22–23, A-W theory predicts that the τ_2 increases with R, which characterizes the population and in some sense the lifetime of the improper (out of equilibrium) micelles as ϕ_0 is the total concentration. The quantity R thus depends on the thermodynamic stability and, hence, on the lifetime of improper, metastable micelles. This concentration dependence is thus difficult to predict because τ_2 depends on the concentration of the different types of micelles of size P, ϕ_p. This highlights the fact that micelle formation is an activated process because metastable micelles must dissolve by unimer expulsion before the equilibrium micelles can be formed. This issue will be discussed in more detail later when we return to non-equilibrium micellization kinetics in section 2.3.

Note that the A-W theory was derived under the assumption that the micellar size distribution is Gaussian, independent of concentration, and can be taken to be essentially the equilibrium distribution. Thus, in this linear relaxation process, the micellar population is imagined to be "shifted" to a new mean aggregation value.

The existence of two relaxation constants and the corresponding concentration dependence predicted by Aniansson and Wall has been well corroborated in many experiments, especially for surfactant systems with large hydrophobic tails, where the two processes can be observed more clearly [54]. It has been shown that for classical ionic surfactants $1/\tau_1$ shows a consistent increase with concentration, whereas the second process, characterized by τ_2, seems to first increase and then decrease again upon higher micelle concentration [51, 54]. This complex concentration dependence of τ_2 was later addressed in a work by Lessner and coworkers [52, 53] and attributed to previously ignored effects of charge screening, which can promote micellar fusion or fission [57]. This conclusion was based on temperature-jump experiments where the mechanism seemingly changed on going from low to high concentrations. Screening of the charges at high ionic strengths in ionic surfactants lowers the repulsion, facilitating fusion as an increasingly important exchange mechanism. Fusion/fission is in general expected to play more of a role in micellar systems with low repulsion, such as in nonionic micelles [58]. The relaxation time for the fusion/fission mechanism is expected to decrease with concentration, and a tentative description was given by Lessner et al. [53]. However, this does not seem to be strictly necessary to understand the experimental results because the A-W theory also predicts a complicated concentration dependence of τ_2 simply because metastable micelles restrict micellar growth by consuming and depleting unimers [54]. In any case, a complication for charged micelles, not considered in the original A-W theory, is the effect of co-solutes such as counter-ions accompanying the main surfactant chain. These ions will additionally affect the thermodynamics by lowering the cmc, which in turn leads

to slower τ_2 at higher concentrations (increasing ionic strengths). Some corrections along these lines, explicitly taking into account issues of charge screening, have been done by Kahlweit and coworkers [52, 53].

2.2.2 Rate Constants for Unimer Exchange in Equilibrium

Most of the experimental and theoretical work concerning kinetics of micellar systems in the 1970s and 1980s were concerned with the outcome of so-called linear relaxation experiments. There was also an attempt to relate the kinetics with the general diffusion in micellar systems [50]. NMR experiments as well as later experiments using fluorescence spectroscopy or neutron scattering are able to follow labeled entities and the signal is not related to changes in sizes and their distributions. For example, in temperature-jump experiments followed by light scattering, the changes in concentration and size of all micelles and unimers are monitored. A labeling experiment is thus "cleaner" and provides a more direct access to the rate constants. In addition, for neutron scattering, the structure can also be analyzed simultaneously with nanometer resolution. In the subsequent section, rate constants associated with micellar kinetics and their dependence on molecular parameters will be discussed.

2.2.3 Reaction-Limited Versus Diffusion-Limited Exchange Kinetics

The situation for low molecular weight surfactant micelles might be different to that for polymeric micelles. In the former case, the kinetics is close to being "diffusion-limited" [54], i.e., the diffusion of chains between the micellar droplets is comparable to the time scale of the expulsion/insertion process.

In general, exchange "reactions" should be analyzed with respect to both transport between micelles (diffusion) and expulsion/insertion. In complete analogy with chemical reaction kinetics known in physical chemistry (see, e.g., Atkins [59]) this can be formulated as:

$$M_P + U \underset{k_{-d}}{\overset{k_d}{\rightleftharpoons}} M_{P-U*} \underset{k_-}{\overset{k_+}{\rightleftharpoons}} M_{P+1} \tag{24}$$
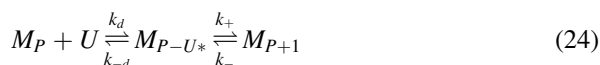
Here, the diffusion rate constant to (k_d) and from (k_{-d}) the micelle is included. The intermediate micelle–unimer complex (the fictive activated complex) is denoted as M_{P-U*}.

Assuming that the intermediate configuration is rare (low concentration of fictive reaction intermediate), one can assume $d[M_{P-U*}]/dt \approx 0$. This yields:

$$\frac{d[U]}{dt} = \left(\frac{k_d k_{-d}}{k_{-d} + k_+} - k_d \right) [M_P][U] + \frac{k_{-d} k_-}{k_{-d} + k_+} [M_{P+1}] \tag{25}$$

In general, the diffusion of single polymers in a low molecular weight solvent such as water is relatively fast, $D \approx 10^{-11}$ m^2/s and thus a typical distance of about 10 nm would be covered in a few microseconds. Hence, we can assume that $k_{-d} \gg k_+$, leading to the simple equation:

$$\frac{d[U]}{dt} \approx k_-[M_{P+1}] \tag{26}$$

Thus, this simple result suggests that the rate of unimer exchange is governed by the expulsion rate constant. We will see later that this approximation is indeed a good assumption when we compare with the proposed models for unimeric expulsion/insertion.

2.2.4 Exchange Kinetics in Surfactant Micelles

Given the central role of the expulsion rate constant for micellar stability, formation, and dissociation, it is essential to determine the physical governing factors and functional form. Aniansson and Wall based their calculations [54] on a general diffusion in an external potential. In this approach, the diffusion coefficient, $D(\mathbf{r})$ is dependent on the position, $\mathbf{r}$, due to the potential $V(\mathbf{r})$. In a sphero-symmetric system, we can imagine that the diffusion of a unimer only depends on the distance, r, from the origin and this problem can be summarized in a Einstein–Smoluchowski type equation:

$$J = -D(r) \left[\frac{\partial \phi(r)}{\partial r} + \frac{1}{k_B T} \frac{\partial V(r)}{\partial r} \phi(r) \right] \tag{27}$$

where $\phi(r)$ is the concentration at radius r and $V(r)$ is the corresponding potential. In order to solve Eq. 27 self-consistently, the potential, $V(r)$, must be specified. Aniansson and Wall considered a situation where the potential increases linearly with r until $V(\text{max}) = \varepsilon$ at $x = l_{\text{tail}}$ (i.e., when the surfactant tail is outside the micelle) where it drops to 0. This corresponds to the physical picture in which the surfactant is treated as a straight rod moving along its axis normal to the surface of the micelles. The motion is diffusive and affected by the interfacial (hydrophobic) energy, which increases linearly with the extent of diffusion out of the micelle. No interactions in the corona are considered. The equilibrium concentration of the segment would be $c(r) = c(0)\exp(-V(r)/k_B T)$. With these assumptions, Aniansson and Wall deduced for the expulsion rate constant:

$$k_- = P \frac{D_m}{l_r' l_0'} \exp(-\varepsilon/k_B T) \tag{28}$$

where l_r' and l_0' are two characteristic sizes related to the actual shape of the potential (both close to the unit length of the surfactant) and D_m is the free diffusion of the surfactant.

It is important to stress that the activation energy, ε, which is related to the surface energy of the exposed hydrocarbon part, is here expected to grow linearly with the length of surfactant:

$$\varepsilon \sim l_{tail} = N \cdot l_0 \tag{29}$$

where l_0 is the bond length. This is a consequence of the rather stiff nature of alkyl-chain-type surfactants and is equivalent to Tanford's classical results of the hydrophobic energy of alkyl chains, which have the form: $\varepsilon_H = \text{constant} + k_B T(N-1)$ [22–24]. This has important consequences for the kinetics, which we will come back to later (sections 4.3–4.6).

Halperin and Alexander extended the theory of the Aniansson and Wall approach to calculate the detailed rate constants and the associated activation energies for polymeric materials, i.e., block copolymer micelles. We briefly review the central results in the following section.

2.2.5 Exchange Kinetics in Block Copolymer Micelles: Halperin and Alexander Theory

The theory proposed by Halperin and Alexander (H-A theory) [60] is based on the structural scaling description of polymeric micelles outlined in Sect. 2.1.2. Using a combination of scaling theory and Kramers' rate theory for diffusion in an external potential [61], the expulsion rate for both "crew-cut" and "star-like" spherical micelles was derived. Moreover, Halperin and Alexander discussed different scenarios of chain exchange between micelles.

Hence, the most important process for the equilibrium kinetics is the unimer exchange mechanism which, as expected from the Aniansson–Wall scenario, is mainly governed by the expulsion rate constant. In the model of Halperin and Alexander this release of a single unimer from the micelle is pictured to go through two stages:

1. Ejection of the solvophobic part of the block copolymer to form a "bud" on the interface of the micellar core. Thereby, an extra area $\left(\approx l_B^2 N_B^{2/3} \right)$ is exposed to the solvent.
2. Diffusion of the whole block copolymer through the micellar corona.

Fig. 4 Illustration of the chain expulsion process of a single chain from a star-like micelle with core radius R_c and corona thickness D and a corresponding schematic free energy profile, $F(y)$, along the reaction coordinate. In the calculations given in the text the reference state is chosen according to $F(P + 1) \equiv 0$ so that $F^* = E_a$ for the expulsion process
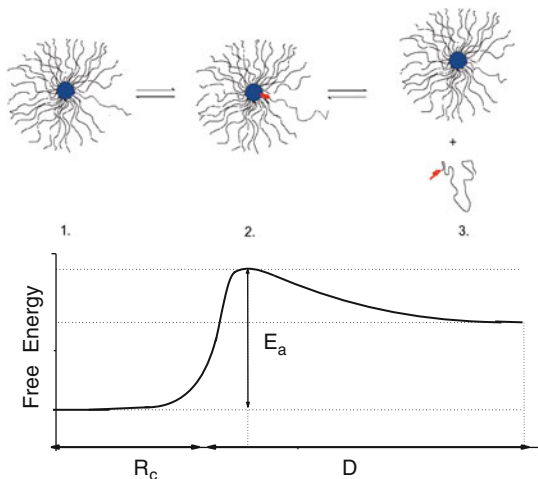
The corresponding free energy profile is shown in Fig. 4.

For one-dimensional stationary flow in a potential well, Kramers' rate theory gives the following expression for the outgoing flux, J:

$$J = -D \, \exp(-F(r)/k_B T) \frac{\partial}{\partial r} \phi(r) \, \exp(F(r)/k_B T) \tag{30}$$

where $F(y)$ is the free energy profile along the "reaction coordinate", y. As a polymer is expected to follow a curvilinear rather than a straight path, y is not necessarily the spatial coordinate r as for rod-like surfactants. $\phi(y)$ is the local polymer concentration of the diffusing block copolymer characterized by a typical diffusion coefficient D. Halperin and Alexander demonstrated that the flux could be rewritten as:

$$J \sim \exp(-F^*/k_B T) v_{\text{diffusion}} \tag{31}$$

where $v_{\text{diffusion}}$ is the chain velocity over the barrier and $F^* = F(y^*)$ is the maximum free energy. This is principally determined by the interfacial energy penalty due to the expelled B-blocks, i.e., $F^* \sim r_{\text{bud}}^2 \gamma \sim N_B^{2/3} l_B^2 \gamma$, with r_{bud} being the radius of the collapsed B-block.

For micelles with a thin corona, $N_B \ll N_A$, $v_{\text{diffusion}}$ is roughly determined by the time, τ_B, necessary to diffuse the length of its insoluble block, i.e., $\tau_B \sim N_B^{2/3}/D$. Assuming classical diffusion of polymer segments in homogeneous surroundings, Stoke–Einstein's law gives $D \sim 1/N_B^{1/3} l_B$ and $\tau_B \sim N_B^{2/3} l_B^2 / (N_B^{-1} l_B^{-1}) = N_B l_B^3 = v_B$ where v_B is the molecular volume of the B-block.

The above-mentioned expression is valid whenever the core is large compared to the corona. In the opposite limit, as in star-like micelles, the diffusion through the corona has to be considered instead. Using the Langevin equation to describe the

stochastic passage of the chain through the corona, Halperin and Alexander obtained for the characteristic velocity of diffusion through the corona $v_{\text{diffusion}} \sim L^{-2}P^{1/2} \sim N_{\text{B}}^{2/25}N_{\text{A}}^{-6/5}$.

Thus, the velocity of the block copolymers over the activation barrier is in the two limiting cases given by:

$$v_{\text{diffusion}} \sim \begin{cases} \frac{N_{\text{B}}^{1/3}l_{\text{B}}}{\tau_{\text{B}}} \sim N_{\text{B}}^{-2/3}, & N_{\text{B}} \gg N_{\text{A}} \\ L^{-2}P^{1/2} \sim N_{\text{B}}^{2/25}N_{\text{A}}^{-6/5}, & N_{\text{A}} \gg N_{\text{B}} \end{cases} \tag{32}$$

The expulsion rate can be obtained using $k_- = \exp(-F^*)v_{\text{diffusion}}/R_{\text{c}}$ and $k_- = \exp(-F^*)v_{\text{diffusion}}/L$ for crew-cut and star-like micelles, respectively. In this way, the following expressions are obtained:

$$k_- \sim \begin{cases} \exp\left(-N_{\text{B}}^{2/3}\,\gamma l_{\text{B}}^2/k_{\text{B}}T\right)N_{\text{B}}^{-4/3}, & N_{\text{B}} \gg N_{\text{A}} \\ \exp\left(-N_{\text{B}}^{2/3}\,\gamma l_{\text{B}}^2/k_{\text{B}}T\right)N_{\text{B}}^{-2/25}N_{\text{A}}^{-9/5}, & N_{\text{A}} \gg N_{\text{B}} \end{cases} \tag{33}$$

Thus, in all cases the activation energy has the form:

$$E_{\text{a}} \sim N_{\text{B}}^{2/3}\,\gamma l_{\text{B}}^2 \tag{34}$$

2.2.6 Modified Halperin and Alexander Theory

According to the H-A theory, the chain exchange is dominated by chain expulsion and follows a first-order kinetic process characterized by a single exponential:

$$R(t) = \exp(-k_-t) \tag{35}$$

with a rate constant of the Boltzmann/Arrhenius form $k = 1/\tau_0\exp(-E_{\text{a}}/k_{\text{B}}T)$, where τ_0 is a characteristic time. In this model, the activation energy, E_{a}, is given by the product of the interfacial area and the interfacial tension γ of the single (collapsed) B-block. In the original paper by Halperin and Alexander, this was written as $E_{\text{a}} = \gamma \cdot N_{\text{B}}^{2/3} \cdot l_{\text{B}}^2$, where N_{B} is the degree of polymerization of the insoluble block B and l_{B} the monomer length. However, as recently recognized [62, 63] this is only correct up to a prefactor (scaling law). In fact, if we assume that the hydrophobic part of the expelled chain is a compact globule, we can calculate the prefactor and Eq. 34 takes the form:

$$E_{\text{a}} = \gamma \cdot (\alpha 36\pi)^{1/3} \cdot (V_0)^{2/3} \cdot N_{\text{B}}^{2/3} \tag{36}$$

where V_0 is the monomer volume of the hydrophobic block.

Deviation from this conformation would give different prefactors and, importantly, a different N_B-dependence. In order to take this into account, we write the following for the rate constant:

$$k(N_B) = (1/\tau_0) \exp(-\alpha \cdot \gamma \cdot (36\pi)^{1/3} (V_0)^{2/3} N_B^\beta / k_B T) \qquad (37)$$

where β is a scaling exponent that is 2/3 for spherical globules and 1 in the case of linear chains where all segments are in contact with the solvent. Thus, we would expect an exponent that has the following validity range: $2/3 \leq \beta \leq 1$. α is a prefactor that, together with β, corrects for deviations from a spherical shape, and/or interpenetration of solvent. The prefactor α is more complicated to estimate as it would be associated to both a change in chain conformation and interactions between the hydrophobic part of the ejected bud and the corona. Prefactor α would also represent a general correction factor for entropic and enthalpic interactions with coronal chains.

2.2.7   Unimer Exchange Kinetics at Higher Concentrations: Effect of Osmotic Pressure

In a recent work, the original Halperin and Alexander model was, in light of new experimental data, extended for the case of high concentrations and particularly for the case of overlapping coronal A-chains [64]. As noted, Eq. 34 is only approximately correct and several corrections should be included. In particular, as is evident from Fig. 4, Eq. 34 does not give a complete description of the activation barrier. In addition to the surface free energy of the exposed insoluble B-block, the expulsion process involves interactions with the corona chains. The free energy of the "activated state" must therefore be calculated in more detail.

As noted by Halperin, the expulsion steps involve three additional free energy changes that should be included: (1) the free energy term ΔF_{ins} arising from the osmotic pressure "felt" by the expulsed B-bud when inserted into the semi-dilute concentration of A-chain; (2) the lowering of the surface free energy after losing one chain $(\Delta F \sim (P_{eq} - 1)^{3/2} - P_{eq}^{2/3})$; and (3) the increase in free energy of the corona (increased crowding) due to the small reduction of the core radius and small increase in curvature. For a system of star-like micelles, this leads to a term that scales as $\Delta F \sim \gamma^{2/5} N_B^{2/5}$ and thus imposes a correction to Eq. 34 according to:

$$E_{a,\phi} \sim N_B^{2/3} \gamma \left(1 + \gamma^{-2/5} N_B^{-4/15}\right) \qquad (38)$$

As discussed later, this might lead to an apparent modification of the prefactor of the activation energy seen in experiments (See sect. 4.5).

The osmotic insertion term ΔF_{ins} evidently changes with the corona density, which is a function of concentration, through screening effects or as an effect of

direct overlap of the corona belonging to two adjacent micelles. Alternatively, a similar effect can be induced by adding A-type homopolymers [64].

Halperin also considered the screening-induced growth of micelles that occurs when the repulsion within the corona decreases. In this case one can write:

$$E_{a,\phi} = E_a + \Delta F = N_B^{2/3}\gamma + R_c^{3/2}(\eta)N_B^{-1/2} \tag{39}$$

where the last term reflects the concentration-dependent corona density (η). Because the rate is sensitive to the exponential of this term, small variations are sufficient for a notable acceleration or deceleration.

2.2.8   Other Mechanisms for Chain Exchange: Fusion and Fission

So far, we have considered unimer exchange as the only (main) equilibration mechanism. However, other important mechanism may come into play. As depicted in Fig. 2, the most likely candidates are fusion and fission mechanisms:

$$M_i + M_j \rightleftharpoons M_{i+j} \tag{40}$$

The question is, however, with what probability does fusion or fission occur in comparison with unimer exchange, i.e., how important are they? Halperin and Alexander performed a rather straightforward calculation of the activation energy for fusion of two micelles of size P_1 and P_2 under the assumption that the corona free energy (star-like) of the micelle dominates. For star-like micelles they obtained:

$$E_a^{\text{fusion}}(P)/k_B T \sim \begin{cases} P^{3/2} & \text{for } P_1 \approx P_2 \approx P \\ P_1 \cdot P_2^{1/2} & \text{for } P_1 << P_2 \approx P \end{cases} \tag{41}$$

whereas for micelles with thin coronas:

$$E_a^{\text{fusion}}(P)/k_B T \sim \begin{cases} P^2 & \text{for } P_1 \approx P_2 \approx P \\ P_2^{2/9} & \text{for } P_1 = 1 << P_2 \approx P \end{cases} \tag{42}$$

As seen, the activation energy for fusion rapidly increases and grows to unfavorable values with increasing P. In comparison, fusion of dissimilar micelles is more probable. The most favored (lowest activation barrier), however, corresponds to the case where one of the fusing entities is a unimer. This corresponds to an insertion of a unimer into a micelle, which will have the following insertion rate constant:

$$k_+^p \sim \frac{1}{\tau_0} \exp(-\beta P^\alpha) \tag{43}$$

where τ_0 is a typical factor setting the time scale and $\alpha = 1/2$ and $2/9$ for a star-like and crew-cut micelles, respectively.

For micellar fission, the activation energy is given by the free energy difference: $F(P_1) + F(P_2) - F(P)$ for a micelle of size P splitting into two micelles of size P_1 and P_2. This gives:

$$E_a^{\text{fission}}(P)/k_B T = (36\pi)^{1/3} P^{2/3} \cdot N_B^{2/3} \frac{\gamma \cdot l_B^2}{k_B T} \left[x^{2/3} + (1-x)^{2/3} - 1 \right]$$

$$+ \frac{1}{2} \cdot P^{5/3} N_B^{-1/3} \left[x^{5/3} + (1-x)^{5/3} - 1 \right] - \frac{1}{6} \left[x \ln x + (1-x) \ln(1-x) \right] \quad (44)$$

where $x = \frac{P_1}{\langle P \rangle}$. Obviously, $P_2 = P - P_1$

As seen, the activation energy assumes rather big values for fission. The value, however, is greatly reduced for smaller x. For small x we can approximately write $E_a^{\text{fission}}(P) \sim P^{2/3}$ $N_B^{2/3} x^{2/3}$. Because x must be multiples i of P, one obtains $E_a^{\text{fission}}(P) \sim N_B^{2/3} i^{2/3}$. Hence, fission into a micelle of size $P - 1$ and a unimer ($i = 1$) has the smallest activation energy and thus the highest probability.

Hence, from these calculations it can be deduced that fusion/fission is not important for polymeric micelles because the associated activation energies are very large, especially when the corona is rather dense/extended. This is reasonable, at least in the case of star-like micelles or whenever the micelles are well-developed, i.e., at the end of the equilibration process or at equilibrium. However, this has been challenged in a more recent work by Dormidontova [65]. In this work, the theory was extended to also include nonlinear kinetics, e.g., the kinetics of micelle formation. In this respect, all relevant rate constants and the proper dependence on block copolymer characteristics, concentration, etc., were reconsidered and calculated in great detail by taking into account polymer-specific dynamics such as Reptation- and Rouse-like dynamics [66]. By using a full chemical reaction scheme (coupled reactions of all possible micellar sizes), the corresponding formation kinetics were simulated on the basis of the calculated rate constants. An important outcome of this work is that micellar fusion/fission is not negligible and plays an important role for the formation kinetics. This is particularly the case at short times where micelles tend to be less compact and more unstable.
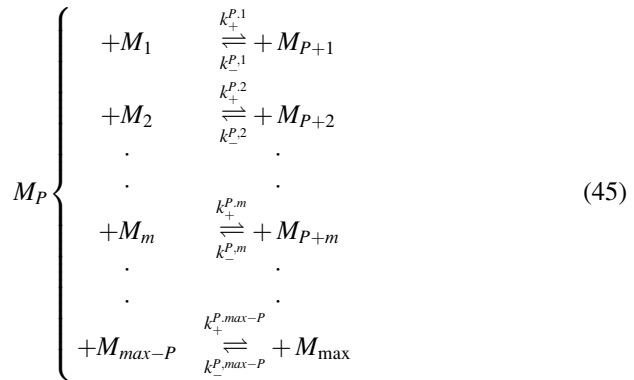
2.3 Non-equilibrium Micellization Kinetics

Contrary to the case of equilibrium kinetics, micellization of block copolymers proceeds from unimers and potentially involves any aggregate size up to or even above the equilibrium size. Hence, a theoretical treatment of the problem involves finding the concentration of the set of aggregates at all times: $\{\phi_1(t), \phi_2(t) \ldots \phi_n(t) \ldots \phi_{\max}(t)\}$. This is quite challenging task, for which the detailed mechanisms must be established and then all activation energies, rate constants, etc.

must be calculated. There are several approaches to this problem, which we will briefly go through in the next section.

2.3.1 Chemical Reaction Approach

A brute force method for calculation of the micellization kinetics is to treat the problem as series of chemical reactions. Such an approach has been developed extensively within chemical engineering to treat complex coupled reactions. For micelles, we can write the reaction scheme on the general form:

$$
M_P \begin{cases}
+M_1 & \overset{k_+^{P,1}}{\underset{k_-^{P,1}}{\rightleftharpoons}} +M_{P+1} \\[1ex]
+M_2 & \overset{k_+^{P,2}}{\underset{k_-^{P,2}}{\rightleftharpoons}} +M_{P+2} \\[1ex]
\quad \cdot & \qquad \cdot \\
\quad \cdot & \qquad \cdot \\
+M_m & \overset{k_+^{P,m}}{\underset{k_-^{P,m}}{\rightleftharpoons}} +M_{P+m} \\[1ex]
\quad \cdot & \qquad \cdot \\
\quad \cdot & \qquad \cdot \\
+M_{max-P} & \overset{k_+^{P,max-P}}{\underset{k_-^{P,max-P}}{\rightleftharpoons}} +M_{max}
\end{cases}
\tag{45}
$$

where P is aggregation number and $1 \leq P \leq \text{max} - P$ indicates the range in aggregation number. Here $k_-^{P,m}$ and $k_+^{P,m}$ are the rate constants for dissociation of two aggregates into sizes P and m and the inverse reaction, respectively.

The time evolution of the species are given by the resulting coupled differential equations:

$$
\frac{\partial \phi_P}{\partial t} = \left[\sum_m k_+^{P,m} \phi_P \cdot \phi_m - k_-^{P,m} \phi_{P+m} \right]
\tag{46}
$$

This set of differential equations must then be solved numerically in a computer program.

Utilizing this kind of scheme and a detailed energetic analysis of the rate constants, Dormidontova [65] obtained a full description of a typical micellization process for a system with $1 \leq P \leq 35$ with an equilibrium size P_{eq}. The results show that fusion/fission occurs, but mainly at short times.

While this approach is quite attractive from the point of view of versatility and flexibility, the main disadvantage is that this method is heavy and computationally very demanding.

2.3.2 Free Energy Landscape Formalism

The previous "brute force" method is rather ineffective as all "reactions" and species are treated equally, regardless of the probability of formation or the stability. It may very well be that most of the pathways are so improbable or so energy-costly that they can be completely ignored.

In another approach, the micellization can be seen as a journey on a multidimensional energy landscape (phase space, i.e., a space spanned by all parameters) towards an equilibrium state that represents a global minimum on the landscape. One can imagine that the most probable path corresponds to the path of minimal energy, which naturally introduces a constraint. Such an approach was recently used by Diamant and coworkers for surfactant micelles [67]. Here, we will briefly review a generic model for block copolymers.

The Theory of Nyrkova and Semenov

For block copolymer micelles, a conceptual model was developed by Nyrkova and Semenov [68] who considered the difference between the total free energy of a micelle compared with that of unimers:

$$F(P, \phi_1) = F_{\text{micelle}}(P) - P \cdot F_1 - (P - 1)\ln(\phi_1) \tag{47}$$

The concentration of a given aggregate is thereby determined by: $\phi_P = \phi_0 \exp[F(P,\phi_0)]$, where ϕ_1 is the concentration of unimers (at equilibrium $\phi_1 = $ cmc). In Fig. 5, the potential is plotted for some representative values (for details see [68]).

Nyrkova and Semenov further assumed that only unimer exchange is active (i.e., dominant). By considering the aggregation number as representative of the mean micellar size and the unimer concentration, the free energy landscape is reduced and solely spanned by these two variables. In this way, the path from single chains (unimers) to equilibrium micelles is naturally the path with minimal energy. The local minima along the path thus represent metastable micelles. These metastable micelles considerably slow down the growth to the equilibrium micellar state and can, in some cases, completely deplete unimers and arrest further growth. This makes micellization an activated process in the sense that there is a (collective) entropic and enthalpic barrier to overcome in order to form micelles from unimers. In the words of Nyrkova and Semenov: "The main point is that micelle formation and their relaxation are activation processes involving collective energy barriers which can be high enough to considerably slow down or even to virtually suppress certain channels of relaxation." These ideas are very similar to those presented earlier by Aniansson and Wall [54–56]. A very important contribution is thus the entropic barrier for micellization.

Fig. 5 The micellar free energy, $F(P,\phi_1)$ (in $k_B T$ units) versus the aggregation number plotted for different unimer concentrations. The curves were calculated using the typical potential: $F_{\text{micelle}}(P) = \gamma' P^{3/2} + \beta P^{2/3}$, with $\gamma' = 38$ and $\beta = 1.3$. Both the maximum, indicated by $F_a(\phi)$, and the minimum decrease rapidly with the unimer concentration ϕ_1
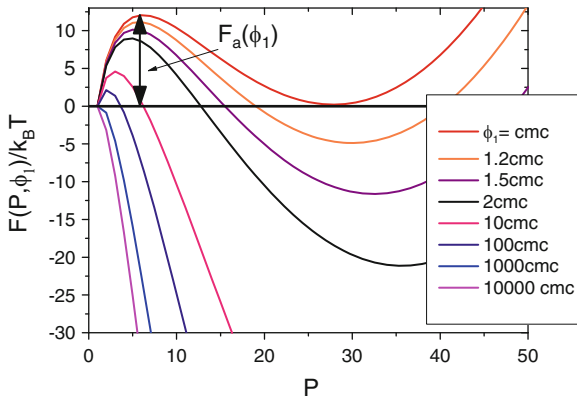
A typical time for micellization was found to be given by:

$$\tau_{\text{mic}} \sim \exp(F_a(\phi_1)) \tag{48}$$

where $F_a(\phi_1)$ is the height of the maximum of the $F(P,\phi_1)$. The values can be visualized more clearly in Fig. 5. This can be thought about as a barrier for micellization, similar to a nucleation barrier, that increases with decreasing ϕ_1, reflecting an increasing entropic barrier closer to equilibrium. At $\phi_1 = $ cmc, i.e., at equilibrium, the activation barrier scales with the interfacial tension and molecular weight: $F(P, \phi_1) \sim \gamma^{1.8} \cdot N_B^{1.2}$. This has the important consequence that the micellization time will be exceedingly long: the larger the polymer blocks and the higher the interfacial tension, the longer the equilibration of micelles will take. In a typical aqueous system with large $\gamma \approx 50$ mN/m, the micellization time can easily reach literally astronomical times scales, e.g., 10^{10} s [68]. The dependence on the unimer concentration is also tremendous. This is shown in Fig. 6.

As seen, the typical equilibration time rapidly reaches extremely large values. This inspired Nyrkova and Semenov to define an apparent critical micelle concentration, cmc_{app}, corresponding an equilibration time of 3,600 s (1 h), i.e., $\tau_{\text{mic}}(\text{cmc}_{\text{app}}) \equiv 3,600$ s. An important conclusion from this work is therefore that the measured cmc will always be much larger (in Fig. 6, by about a factor of 80–90) compared to the real cmc equilibrium value. A real cmc will not be measurable on a typical experimental time scale.[4]

In a given micellization process, $F_a(\phi_1)$ and of course also τ_{mic} will be time-dependent and lead to a broad distribution of relaxation times. Moreover, as $F_a(\phi_1)$ grows with time, the relaxation time becomes larger and the equilibration will slow down or even stop at longer times. However, in order to calculate this, the detailed time evolution needs to be developed. We show one example in the next section.

---

[4] Such a definition is equivalent to what is customary in glass physics, where the transition from an equilibrium liquid to a non-equilibrium supercooled liquid (a glass) is characterized by a glass transition temperature, T_g, which is typically defined as the temperature at which the α-relaxation time scale approaches a certain laboratory time scale, typically 100 s.
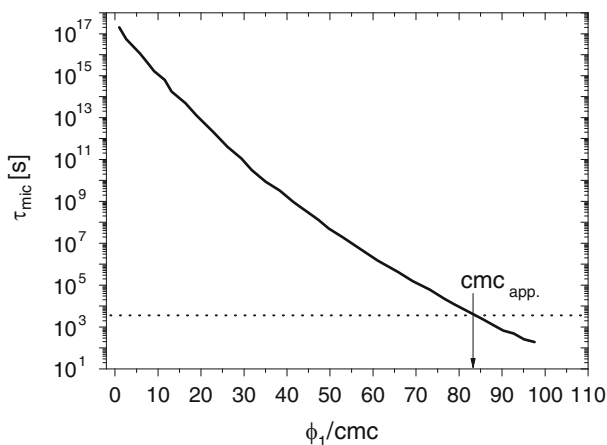
Fig. 6 Typical micellar equilibration time, τ_{mic}, as a function of the unimer concentration normalized by the equilibrium value (cmc). *Dotted horizontal line* corresponds to a time of 1 h and defines the apparent critical micelle concentration, cmc_{app}. Reproduced from [68]
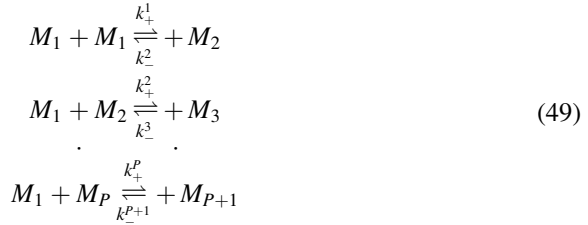
2.3.3 Nucleation and Growth Approach

Nucleation and growth theories constitute a very attractive methodology in solid state physics to describe phenomena related to phase transitions. In this view, a new phase is pictured as growing out from a small finite-sized droplet. Typical examples are liquid bubbles formed from a gaseous phase (e.g., rain droplets), gas bubbles forming under close-to-critical liquids (e.g., boiling water), or crystallization in amorphous liquids (e.g., in silica-based semiconductors or organic polymers) [69].

Although micellization is not strictly speaking a phase transition phenomenon, nucleation and growth can also be used here. The micelles are then seen as droplets that can only grow up to limited size and will form a new continuous body (new phase). The next section reviews an example of such an approach.

Micellization Kinetics as a Nucleation Process

Considering the results of Halperin and Alexander [60] and of Nyrkova and Semenov [68] presented above, fusion and fission events between polymeric micelles appear to be rather rare. In any case, unimer exchange will always be an important if not completely dominating mechanism as a consequence of the low activation barrier of the process compared to other mechanisms.

Ignoring fusion and fission, the reaction scheme in Eq. 45 can be greatly simplified and we can write:

$$
\begin{aligned}
M_1 + M_1 &\underset{k_-^2}{\overset{k_+^1}{\rightleftharpoons}} + M_2 \\
M_1 + M_2 &\underset{k_-^3}{\overset{k_+^2}{\rightleftharpoons}} + M_3 \\
\cdot\qquad&\qquad\cdot \\
M_1 + M_P &\underset{k_-^{P+1}}{\overset{k_+^P}{\rightleftharpoons}} + M_{P+1}
\end{aligned}
\tag{49}
$$

The growth rate of a given cluster of aggregation number P can be expressed via the flux, J_P, which describes the number created (or dissolved) per unit time and volume:

$$
J_P = k_+^P \phi_1 \phi_{P-1} - k_-^P \phi_P
\tag{50}
$$

In order to simplify these equations, the basic principle of microscopic reversibility introduced by Onsager in the 1930s can be evoked [70]. According to this principle, used to derive the reciprocal relations in non-equilibrium thermodynamics, there is a local reversibility of all (sub-)processes even though the system is out of equilibrium. Hence, applying this principle, which is strictly speaking only likely to be valid close to equilibrium, we can write:

$$
k_+^P \cdot \phi_P \cdot \phi_1 = k_-^{P+1} \cdot \phi_{P+1}
\tag{51}
$$

In other words, on a local scale the reaction is balanced, i.e., there is a microscopic reversibility. Note that this applies to locally defined variables and not to the mean (averaged) values. For an exchange-mediated growth process as we consider here, this means that the rate of individual unimer expulsion/insertion processes are much faster than the overall micelle formation.

Furthermore, the Boltzmann relation that describes the probability and stability of a given cluster can be used. From the theory of Nyrkova and Semenov this gives:

$$
\phi_P = \phi_1 \exp(-F(P, \phi_1))
\tag{52}
$$

where the chemical potential can be written as:

$$
G(P, \phi_1) = k_B T (F_{\text{micelle}}(P) - P \cdot F_1 - (P - 1) \cdot \ln(\phi_1))
\tag{53}
$$

Using Eqs. 52–53, one can eliminate one rate constant and express Eq. 50 in terms of the insertion rate constant k_+^p:

$$
j_{P+1} = k_+^P \phi_1 \left[\phi_P - \phi_{P+1} \exp(G(P + 1, \phi_1) - G(P, \phi_1)/k_B T) \right]
\tag{54}
$$

thus, the flux is only determined by k_+^p and the chemical potential by $G(P, \phi_1)$.

Equivalently, the same scenario can be expressed mathematically in terms of the expulsion rate constant, k_-^p, which gives:

$$j_{P+1} = k_-^P \left[\phi_p \exp -(G(P+1, \phi_1) - G(P, \phi_1)/k_{\mathrm{B}}T) - \phi_{P+1} \right] \qquad (55)$$

The whole evolution of the micellar ensemble is then unambiguously given by the generic system of differential equations:

$$\frac{\partial \phi_P}{\partial t} = j_P - j_{P+1} \qquad (56)$$

The stiff differential equation system can be solved numerically giving the concentration of the micellar entities/aggregates $\{\phi_1(t).....\phi_P(t)\}$ as a function of time. In Sect. 5.1.2, a comparison between the theory and experimental TR-SAXS results will be presented.

3 Experimental Techniques

In this section we will go through the relevant details concerning experimental techniques, restricting ourselves to SANS and SAXS methods. Other relevant methods such as fluorescence spectroscopy and light scattering techniques will not be covered as these are considered out of the scope of this review article. Rather, we intend to give an overview of modern methodologies related to small-angle neutron and X-ray scattering.

3.1 Small-Angle Scattering Methods

In this section, the principles of small angle scattering and in particular the applications to micellar systems are briefly reviewed. We will later focus on the unique possibilities for resolving kinetic processes. For a more thorough review on small angle scattering in general, we refer to the textbook edited by Lindner and Zemb [71] or the classical books by Guinier and Fournet [72] and by Feigin and Svergun [73]. Detailed review articles on scattering of block copolymer and surfactant micelles have been published by Pedersen [74, 75].

3.1.1 Basic Principles of SAXS and SANS

The main differences between neutron and X-rays as probes in scattering experiments lie in their interaction with matter and their energy. While X-rays interact strongly with electrons in the (most frequently) outer shell of the atom and scatter through electromagnetic interactions, neutrons penetrate the core of the atom and scatter by

very short-range nuclear interactions. The energy for typical "cold" neutrons ($\approx m$eV) differs strongly from that of typical X-rays ($\approx k$eV), i.e., by factor of $\approx 10^6$.

The consequence is first of all that the scattering amplitudes are completely different in X-ray and neutron scattering, i.e., neutrons and X-rays "see" matter differently. As a consequence of their interaction with matter, neutrons can distinguish between isotopes and render even light elements visible. This can be exploited very efficiently to perform "contrast variation" studies, which are one of the main strengths of neutron scattering, in particular for organic matter with abundant hydrogen content. Secondly, because of their energy, neutrons are more suitable to detect slower motions in inelastic scattering experiments. Moreover, a photon carries no magnetic dipole moment whereas neutrons do, making neutron scattering also very useful for probing magnetic structures. The large energy of X-rays also causes difficulties for very high doses (from high flux sources). If the energy dissipation is slower than the impact rate, X-rays are able to provoke chemical changes as a consequence of free radical production, etc. However, this is only the case at high brilliance sources, such as synchrotrons, although there are ways to avoid or minimize these effects. For laboratory sources this is not an issue.

Despite the much higher energy, X-rays penetrate the material much less than neutrons due to their strong interactions with electrons. On the other hand, neutrons are only weakly scattering and, combined with the relatively low flux available at reactor sources (typically of the order of $\approx 10^8$ neutrons/(cm^2 s), this makes SANS an intensity-limited technique. Synchrotron sources, however, easily deliver $\approx 10^{12}$–10^{14} photons/s on the sample and thus improves the statistics issue dramatically. This opens up many exciting applications, as we will see later in Sect. 5.1, one of which is extremely fast time-resolved measurements.

Scattering Contrast and Scattering Intensity

In a scattering experiment, the intensity is most conveniently measured as the scattering cross-section, Σ per unit scattering volume divided by the solid angle Ω. This quantity is referred to as the macroscopic differential cross-section $d\Sigma/d\Omega(Q)$, which is measured as a function of the momentum transfer, $\mathbf{Q} = \mathbf{k_f} - \mathbf{k_i}$. Here, $\mathbf{k}$ is the wave vector with modulus $|\mathbf{k}| = k = 2\pi/\lambda$ and λ is the wavelength.

Assuming that the scattering process is completely elastic, i.e., $\lambda = \lambda_i = \lambda_f$, the modulus of $\mathbf{Q}$ can simply be cast into the following expression:

$$Q = 4\pi \frac{\sin(\theta)}{\lambda} \tag{57}$$

where 2θ is the scattering angle.

Within the assumptions usually valid for small angle scattering (Born approximation, Thomson scattering, single scattering events, etc.), the amplitude of scattering is given by:

$$A(\mathbf{Q}) = \sum_{i}^{N} b_i \cdot \exp\left(i\mathbf{Q} \cdot \mathbf{r_i}\right) \tag{58}$$

where b_i indicates the scattering length, i.e., the scattering amplitude of an atom i.

This important quantity is fundamentally different for X-rays and neutrons. For neutrons, the scattering length varies in a rather unsystematic fashion for the different elements across the periodic table, whereas the b_i values for X-rays vary monotonously with the amount of electrons,[5] Z. This can be expressed as:

$$b_i(Z) = \begin{cases} b_i & \text{neutrons : irregular function of } Z \\ Z \cdot r_0 & \text{X-rays : linear with } Z \end{cases} \tag{59}$$

where $r_0 \approx 5.29 \times 10^{-13}$ cm is the so-called Bohr radius.

As seen for X-rays, the trend is clear: the larger the atom, the more it scatters. For neutrons, however, b_i depends on the nuclear interactions and is unrelated to its overall size. As an example, bromide ($Z = 35$) has a very similar value of $b \approx 6.8$ fm, as compared with carbon ($Z = 6$), $b \approx 6.6$ fm. For neutrons, these two elements are thus equally visible, whereas for X-rays Br is more dominant by a factor of $(35/6)^2 \approx (5.8)^2 \approx 30$ ($d\Sigma/d\Omega \approx b^2$) (more values can be found, e.g., at the NIST webpage, http://www.ncnr.nist.gov/resources/n-lengths/).

Moreover, for neutrons, b strongly depends on isotope. For example, the value for hydrogen, H (1 p$^+$, 1 n) is -3.74 fm while that of deuterium, D (1 p$^+$, 2 n) is 6.67 fm. Hence, not only are the values very different, but the value for hydrogen also has a negative sign because the phase is inverted during the scattering process. This is an extremely important aspect that allows contrast variation experiments by selectively labeling specific parts of the system in question through H/D exchange. As we will see later in particular in Sections 3.1.7, 3.1.8 and 3.2.2, this gives rise to very interesting possibilities in soft matter science.

The corresponding macroscopic differential scattering cross-section, $d\Sigma/d\Omega(\mathbf{Q})$ is of the general form:

$$\frac{d\Sigma}{d\Omega}(\mathbf{Q}) = \frac{1}{V_s}\left\langle |A(\mathbf{Q})|^2 \right\rangle = \frac{1}{V_s}\sum_{i,j=1}^{N}\left\langle b_i b_j \cdot \exp\left(i\mathbf{Q} \cdot (\mathbf{r_i} - \mathbf{r_j})\right)\right\rangle \tag{60}$$

---

[5] This is not strictly correct because the scattering length varies with energy and at certain energies there is absorption (near absorption edges) for certain energies and atoms. Strictly speaking, the scattering length should be written as: $b_i(E) = b'_i + i\,b''_i(E)$, where the latter imaginary part describes the absorption term. For X-rays, this is only important for rather high energy and large atoms, e.g., Br, which has one K-shell edge at 13.47 keV.

where V_s is the scattering volume.

In case there is a distribution in the scattering lengths for neutrons, e.g., because of a natural distribution of isotopes and spin states, the mean values and their spread must be considered. In this way Eq. 60 can be rewritten as:

$$\frac{d\Sigma}{d\Omega}(\mathbf{Q}) = \frac{1}{V_s} \langle b \rangle^2 \sum_{i,j=1}^{N} \langle |\exp(i\mathbf{Q} \cdot \mathbf{r_i})|^2 \rangle + \frac{N}{V_s} (\langle b^2 \rangle - \langle b \rangle^2) \qquad (61)$$

Equation 61 consists of a $\mathbf{Q}$-dependent and a $\mathbf{Q}$-independent part. The $\mathbf{Q}$-dependent part contains all structural information because it contains the phase factor $\exp(i\mathbf{Q} \cdot \mathbf{r_i})$, which reflects the interference between pairs of scatterers. This is termed the coherent scattering. The last incoherent term contains no phase factor and is therefore not related to any interference and its cross-section is correspondingly isotropic. In a small-angle scattering experiment, where an elastic average is measured, the incoherent scattering represents an (inconvenient) constant background whereas for inelastic scattering experiments it opens up unique possibilities. We shall disregard such aspects in this contribution, where the focus lies on the coherent scattering giving direct access to the structure.

3.1.2 Scattered Intensity: Form and Structure Factors

Now considering the coherent scattering from particles (e.g., aggregates, micelles, etc.) dispersed in a solvent, the contrast relative to the solvent of scattering length, b_0, must be considered, $b\langle b \rangle \rightarrow \langle b \rangle - b_0$. Furthermore, because small-angle scattering deals with scattering arising from entities significantly larger than the size of an atom, the spatial coordinates can be regarded as continuous coordinates and it is thus useful to use the following form:

$$\frac{d\Sigma}{d\Omega}(\mathbf{Q}) = \frac{1}{V_s} (\rho_p - \rho_0)^2 \int_{V_s} \int_{V_{s'}} g(\mathbf{r}, \mathbf{r}') \exp(i\mathbf{Q} \cdot (\mathbf{r} - \mathbf{r}')) d^3\mathbf{r} \, d^3\mathbf{r}' \qquad (62)$$

where the scattering length density is defined as $\rho = \Sigma_i b_i / V_p$, V_p is the volume of the particle or solvent molecule, and $g(\mathbf{r}, \mathbf{r}')$ is the pair correlation function describing the probability for a correlation at a distance $\mathbf{r} - \mathbf{r}'$.

By decomposing the vector $\mathbf{r}$ in intra- and interparticle contributions [76], it is possible to separate the scattering contribution according to:

$$\frac{d\Sigma}{d\Omega}(\mathbf{Q}) = \frac{N_p}{V_s} (\rho_p - \rho_0)^2 \cdot V_p^2 \cdot P(\mathbf{Q}) \cdot \left(1 + \frac{\langle |A(\mathbf{Q})| \rangle^2}{\langle |A(\mathbf{Q})|^2 \rangle} (S(\mathbf{Q}) - 1)\right) \qquad (63)$$

Here, $P(\mathbf{Q})$ is the form factor, which relates to intraparticle correlations and gives information about the internal structure of a single particle. It can be defined as:

$$P(\mathbf{Q}) = \left\langle |A(\mathbf{Q})|^2 \right\rangle \tag{64}$$

and:

$$A(\mathbf{Q}) = \int_{V_p} n(\mathbf{r}) \exp(i\mathbf{Q} \cdot \mathbf{r}) \, dV_p \tag{65}$$

where $n(\mathbf{r})$ is the normalized density distribution of the particle and $\mathbf{r}$ is now the vector from the center of mass to an arbitrary point located within the object or particle.

Note that in the case of polydispersity (i.e., a distribution in size, etc.) or anisotropic particles, $\langle |A(\mathbf{Q})|^2 \rangle \neq \langle |A(\mathbf{Q})| \rangle^2$ and each quantity must be evaluated accordingly.

The structure factor $S(\mathbf{Q})$ is defined as:

$$S(\mathbf{Q}) = \frac{1}{N_p} \sum_{i=1}^{N_p} \sum_{i'=1}^{N_p} \exp(i\mathbf{Q} \cdot (\mathbf{R_i} - \mathbf{R_{i'}})) \tag{66}$$

This describes the interparticle correlations and gives access to the interaction between the entities. $\mathbf{R_i}$ is the vector to the centre of mass coordinate of particle i. The structure factor is close to unity at all Q values for dilute systems and, hence, Eq. 63 can be written as:

$$\frac{d\Sigma}{d\Omega}(\mathbf{Q}) = \frac{N_p}{V_s} (\rho_p - \rho_0)^2 \cdot V_p^2 \cdot P(\mathbf{Q}) \tag{67}$$

In this work we will mostly focus on dilute systems where interparticle interactions are negligible. A more detailed discussion concerning structure factors can be found in, e.g., [71, 75, 77].

3.1.3 Form Factors for Various Simple Geometrical Objects

In the remainder we will consider only isotropic systems, or isotropically averaged systems, and the momentum transfer vector will therefore be replaced with its absolute value, $|\mathbf{Q}| = Q$.

Eqs. 64–65 describe the theoretical scattering as a function of Q, which must be solved for each object or particle. Here, we will show some typical examples for different morphologies, the form factors for a sphere, cylinder, polymer chain, and a vesicle (hollow shell). The results for these structures are the following:

Fig. 7 The theoretical scattering form factor, $P(Q)$, from some common objects: (*1*) ideal polymer chain; (*2*) sphere; (*3*) cylinder; and (*4*) for vesicle/shell. See text for details. Note that the objects are for illustration only, and not to scale with respect to the depicted scattering curves
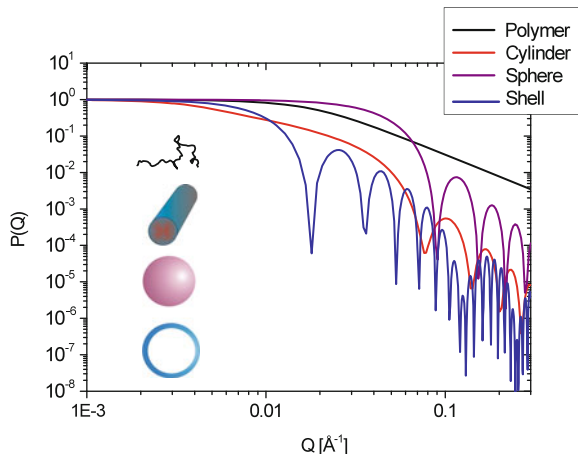
$$P(Q) = \begin{cases} \frac{2(\exp(-y)-1+y)}{y^2}, y = (QR_g)^2 & \text{Ideal Chain (Debye)} \\[2mm] (A_s(Q,R))^2, A_s(Q,R) = \frac{3(\sin(QR)-QR\cos(QR))}{(QR)^3} & \text{Sphere} \\[2mm] \left(\frac{R_2^3 A_s(Q,R_2)-R_1^3 A_s(Q,R_1)}{R_2^3-R_1^3}\right)^2 & \text{Shell/Vesicle} \\[2mm] \int_0^{\pi/2} \left(\frac{\sin(Q\cdot L\cos(\alpha)/2)}{Q\cdot L\cos(\alpha)/2}\frac{2J_1(Q\cdot R\sin(\alpha))}{Q\cdot R\sin(\alpha)}\right)^2 \sin(\alpha)d\alpha & \text{Cylinder} \end{cases}$$

(68)

where α is the angle between the cylinder axis and the scattering vector, $\mathbf{Q}$ of a cylinder with length, L.

The results are calculated and depicted in Fig. 7 for a polymer chain with radius of gyration, $R_g = 80$ Å; a sphere with radius, $R = 50$ Å; an orientationally averaged cylinder with length $L = 1{,}000$ Å and radius $R = 50$ Å; and a vesicle with outer radius $R_2 = 200$ Å and inner radius $R_1 = 50$ Å.

3.1.4 Effect of Polydispersity

In real life, many systems are not monodisperse. For example, polymers prepared by synthetic methods are statistically distributed in molecular weight. Both synthetic and naturally occurring colloidal particles are polydisperse. The same applies to self-assembled systems constituted of surfactant and block copolymers. Owing to both the intrinsic polydispersity of the components and the statistical process of self-assembly, polydispersity in terms of aggregation number and size is evident.

This can be taken into account by considering a distribution function, $f(R)$, and averaging over the theoretically calculated intensity:

Fig. 8 Illustration of the effects of polydispersity and experimental smearing: Calculated scattering function of an ideal sphere with (*a*) experimental smearing and (*b*) both experimental smearing and polydispersity
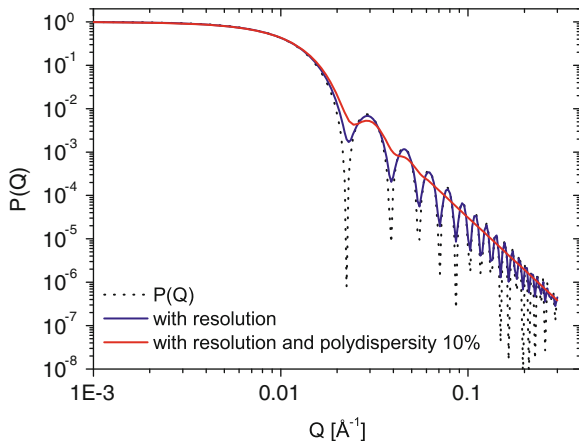
$$\frac{d\Sigma}{d\Omega}(Q) = \frac{\phi_0}{\langle V_p \rangle}(\rho_p - \rho_0)^2 \int\limits_{R} f(r) \cdot V_p(r)^2 \cdot P(Q, r)\, dr \tag{69}$$

where $\langle V_p \rangle = \int\limits_{r} f(r) \cdot V_p(r) dr$

The normalized distribution function must be chosen according to the particular physical situation. A typical choice, suitable for many physical situations, is the Gaussian distribution:

$$f(r) = \frac{1}{\sqrt{2\pi\sigma_R^2}} \exp\left(-\frac{(r - R)^2}{2\sigma_R^2}\right) \tag{70}$$

Figure 8 shows the simulated scattering from an ideal sphere, with resolution convolution and both resolution and polydispersity included.

Another distribution function such as the Schulz–Zimm distribution is asymmetric with a tail toward larger values of r:

$$f(r) = \frac{(z + 1)^{z+1} r^z}{r_0^{z+1} \Gamma(z + 1)} \exp(-(z + 1)r/r_0) \tag{71}$$

where $\Gamma(z)$ is the gamma function and z is a width parameter. The width of the distribution, σ_p, is given by: $\sigma_p = \frac{\langle R^2 \rangle - \langle R \rangle^2}{\langle R \rangle^2} = 1/(z + 1)$

The choice of distribution function is best made on the basis of theoretical expectations, e.g., for the length distribution of cylindrical micelles an asymmetric distribution such as the Schulz–Zimm or log-normal distribution function is expected to be suitable [75].

3.1.5   Effect of Experimental Resolution

In practical situations, the scattering intensity is effectively "smeared" in Q because of the intrinsic finite beam divergence, distributed (neutron) wave lengths, finite size of detector pixels and so on. These issues are more important for SANS and laboratory SAXS equipments that use rather large apertures and/or are characterized by a significant wave length spread (for SANS, $\Delta\lambda/\lambda$ is typically 10–20%). This leads to a distribution of Q at each observed scattering angle that have to be incorporated when experimental results are compared with theoretical models.

This is described by the resolution function, $R(Q, \langle Q \rangle)$ describing the distribution of Q at a given mean value: $\langle Q \rangle$. Thus, the experimentally measured scattering cross-section takes the form:

$$\frac{\mathrm{d}\Sigma}{\mathrm{d}\Omega_{\text{exp}}}(\langle Q \rangle) = \int R(Q, \langle Q \rangle) \frac{\mathrm{d}\Sigma}{\mathrm{d}\Omega_{\text{theo}}}(Q)\,\mathrm{d}Q \tag{72}$$

Following Pedersen [78], there are three main contributions that have to be incorporated when a typical diffractometer with a pin-hole geometry is used: wavelength spread, collimation effects, and the detector resolution. Using a Gaussian function for each effect, the resolution function is given by:

$$R(Q, \langle Q \rangle) = \frac{Q}{\sigma^2} \exp\left[-\frac{1}{2}\left(Q^2 + \frac{\langle Q \rangle^2}{\sigma^2} \right) \right] I_0\left(\frac{Q\langle Q \rangle}{\sigma^2} \right) \tag{73}$$

where I_0 is the modified Bessel function of the first kind and zeroth order and σ is the smearing coefficient describing the resolution of the instrument. The effects summarized above can be related independently to the dispersion coefficient, σ, using:

$$\sigma^2 = \sigma_{\text{W}}^2 + \sigma_{\text{C}}^2 + \sigma_{\text{D}}^2 \tag{74}$$

where σ_{W} is the dispersion of the wave length, σ_{C} describes the finite size of the beam due to the collimation and σ_{D} describes the detector resolution. For more details concerning the calculation of these quantities, we refer to the original work by Pedersen et al. [78]. For spallation sources, the calculation of the resolution function is a more complicated task. Here, ΔQ is, in addition to the divergence of the beam, also given by the uncertainty in the time of flight.

3.1.6   Scattering from Core–Shell Structures

For particles comprised of two or more types of materials, the scattered intensity needs to be calculated taking into account the interference between the different parts. For that it is more convenient to work in terms of scattering amplitudes defined in

Fig. 9 Scattering from a homogeneous core–shell system consisting of a core with scattering length ρ_c and a shell (ρ_{sh}) immersed in a solvent with ρ_0. Please note that all relative values are chosen arbitrarily, i.e., $\rho_c > \rho_{sh}$ is equally possible. R_c core radius, R_m micelle radius
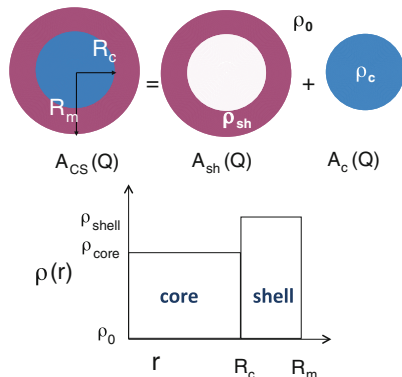
Eq. 65, correctly accounting for the volume and contrast for each part. A convenient and typical example is a sphere consisting of two layers: a core and a surrounding shell. Graphically, the scattering from such a particle can be constructed according to Fig. 9.

Compact Core–Shell Form Factor

Mathematically, the total amplitude can be written as:

$$A_{CS}(Q) = (\rho_c - \rho_0)V_c \cdot A_c(Q) + (\rho_{sh} - \rho_0)V_{sh} \cdot A_{sh}(Q) \qquad (75)$$

Here we have introduced the mean scattering length density, ρ_i of solvent ($i = 0$), core ($i = c$) and shell ($i = sh$).

$A(Q)_i$ must be calculated by integrating over the volume of core and shell respectively resulting in:

$$A_i(Q) = \begin{cases} A(Q, R_c) & \text{Core} \\ \dfrac{R_m^3 A(Q, R_m) - R_c^3 A(Q, R_c)}{R_m^3 - R_c^3} & \text{Shell} \end{cases} \qquad (76)$$

where $A(Q,R) = 3(\sin(QR) - QR\cos(QR))/(QR)^3$.

The total scattering is then given by (assuming a completely monodisperse system):

$$\frac{d\Sigma}{d\Omega_{CS}}(Q) = \frac{N}{V_s}\left\langle |A(Q)|^2 \right\rangle \qquad (77)$$

where N is the number of particles and V_s the sample volume exposed to the beam. This can also be written as: $N/V_s = \phi_0/V_{tot}$ where ϕ_0 is the total concentration and V_{tot} is the volume of the particle.

In the case of micelles, the inner core is often compact and is constituted solely by hydrophobic (solvophobic) chain segments, whereas the outer shell is constituted by a hydrophilic (solvophilic) polymer swollen by solvent. In this case, the scattering length density of the shell must be averaged over the composition, i.e., polymer and solvent content according to: $\rho_{sh} = \Phi_p \cdot \rho_p + (1 - \Phi_p) \cdot \rho_0$. Here Φ_p is the (mean) polymer concentration.

In this case, it has been realized that the scattering from the internal polymer structure within the corona must also be taken into account [44, 74, 79–81]. This scattering results from the local contrast between corona-forming polymer and the solvent, which is not included in the calculation using a centro-symmetric mean density profile. Because these correlations are short-ranged compared to the overall micellar structure, interference terms with core and shell can be assumed to be negligible. Hence, to a first approximation this can be added to the overall intensity in Eq. 77:

$$\frac{d\Sigma}{d\Omega_{CS-blob}}(Q) = \frac{d\Sigma}{d\Omega_{CS}}(Q) + \frac{d\Sigma}{d\Omega_{blob}}(Q) \qquad (78)$$

$\dfrac{d\Sigma}{d\Omega_{blob}}(Q)$ is the internal scattering from the individual polymer blobs adding up to the scattering. Inspired by correlations in semidilute polymer solutions [38, 82], Dozier et al. [83] calculated the scattering assuming the following:

$$g(r) \sim r^{1/(1-\nu)} \exp(-r/\xi) \qquad (79)$$

A Fourier transformation of $g(r)$ and subsequent normalization then yields:

$$\frac{d\Sigma}{d\Omega_{blob}}(Q) = (\rho_p - \bar{\rho}_0)^2 \frac{4\pi\beta}{Q\xi} \frac{\sin(\mu \tan^{-1}(Q\xi))}{(1 + Q^2\xi^2)^{\mu/2}} \Gamma(\mu) \qquad (80)$$

where β is a prefactor, which should be proportional to the volume of polymer inside the blob, Γ the gamma function, ξ the average blob radius, and $\mu = 1/\nu - 1$ with the Flory exponent $\nu = 0.588$ for swollen chains.

Spherical and Cylindrical Core–Shell Form Factors Including Density Gradients

In reality, most micellar systems made up from polymers are not as perfect as depicted in Fig. 9. Instead, the micelles are expected to be more "fuzzy" and may more resemble the situation depicted in Fig. 10. In this case, the segmental distribution must be considered [44, 45, 48, 74, 79, 84–86] by calculating the scattering amplitude from a realistic density profile. In addition, the intrinsic polymer scattering must be incorporated by explicitly taking into account long-range excluded volume interactions.

Fig. 10 Illustration of density distribution in real block copolymer micellar systems. The data correspond to a core with a constant density profile convoluted by Gaussian function. The density profile of the corona grafted to the core is calculated using a Fermi–Dirac function $n(r) \approx (1 + \exp[(r - R_\mathrm{m})/ (\sigma_\mathrm{m} R_\mathrm{m})])^{-1}$. The parameters (see text for details) are $R_\mathrm{c} = 30$ Å, $R_\mathrm{m} = 150$ Å, $\sigma_\mathrm{m} = 0.1$ and $\sigma_\mathrm{int} = 5$ Å
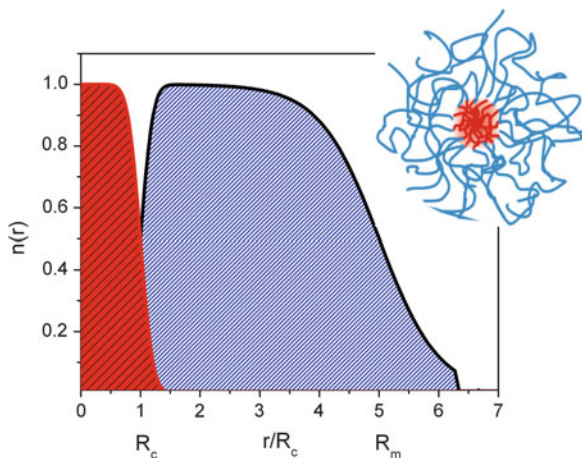
In practical situations the interface of the micellar core may not be perfectly smooth due to chemical imperfections, packing restrictions of chains, thermal fluctuations, partial swelling of core with solvent, etc. To take into account smearing due to surface roughness, the ideal constant density can be convoluted with a Gaussian distribution:

$$n_\mathrm{c}(r) \sim \int_0^\infty (1 - \Theta(r')) \frac{1}{\sqrt{2\pi\sigma_\mathrm{int}^2}} \exp\left(-(r - r' - R_\mathrm{c})^2/2\sigma_\mathrm{int}^2\right) \mathrm{d}r \qquad (81)$$

Here, $\Theta(x)$ is the Heaviside step-function, i.e., $\Theta = 0$ for $x \leq 1$ and 1 otherwise. Likewise, for the corona density distribution:

$$n_\mathrm{corona} \sim n_\mathrm{corona}^0 \int_0^\infty \Theta(r') \frac{1}{\sqrt{2\pi\sigma_\mathrm{int}^2}} \exp\left(-(r - r' - R_\mathrm{c})^2/2\sigma_\mathrm{int}^2\right) \mathrm{d}r \qquad (82)$$

where n_corona^0 is the inherent density profile of the corona, not taking into account the core–corona interface.

By virtue of the Fourier convolution theorem, this leads to a so-called Debye–Waller factor, $DW(Q)$ that modulates the scattering at high Q:

$$\mathrm{DW}(Q, \sigma_\mathrm{int}) = \exp(-Q^2\sigma_\mathrm{int}^2/2) \qquad (83)$$

The scattering amplitude for the core including a graded core–corona interface (Gaussian distribution) can thus for a spherical or cylindrical core be written as:

$$A_{\rm c}(Q) = \begin{cases} \dfrac{3(\sin(Q\cdot R_{\rm c}) - Q\cdot R_{\rm c}\cos(Q\cdot R_{\rm c}))}{(Q\cdot R_{\rm c})^3}\cdot DW(Q,\sigma_{\rm int}) & \text{Spheres} \\[2ex] \dfrac{\sin(Q\cdot L\cos(\alpha)/2)}{Q\cdot L\cos(\alpha)/2}\dfrac{2J_1(Q\cdot R_{\rm c}\sin(\alpha))}{Q\cdot R_{\rm c}\sin(\alpha)}\cdot DW(Q,\sigma_{\rm int}) & \text{Cylinders} \end{cases} \tag{84}$$

where α is the angle between the cylinder axis and the scattering vector $\mathbf{Q}$, i.e., $\mathbf{QL} = QL\cos(\alpha)$.

For the shell, the corresponding expressions can be found by performing a Fourier transformation over the density profile, $n(r)$, using the appropriate geometry:

$$A_{\rm sh}(Q) = \begin{cases} \int_{R_{\rm c}}^{\infty} 4\pi r^2 n(r)\dfrac{\sin(Qr)}{Qr}\,{\rm d}r \cdot DW(Q,\sigma) & \text{Spheres} \\[2ex] \int_{R_{\rm c}}^{\infty} 2\pi r \cdot n(r) J_0(Q\cdot r\sin(\alpha)){\rm d}r \cdot DW(Q,\sigma) & \text{Cylinders} \end{cases} \tag{85}$$

J_0 is the Bessel function of zeroth order.

The density profile can be conveniently chosen to have the following generic form [44, 45, 48, 87]:

$$n(r) = \frac{1}{C}\frac{r^{-x}}{1 + \exp((r - R_{\rm m})/\sigma_{\rm m}R_{\rm m})} \tag{86}$$

where x is a scaling exponent that for star-like micelles is predicted to be $x = 4/3$ [38], $\sigma_{\rm m}$ is the relative width of the micellar surface, and $R_{\rm m}$ is a mean (cut-off) radius of the micelle. C denotes a normalization constant obtained by integrating the density profile over the volume.

Generally, these expressions require numerical integrations. In the case of spherical symmetries, other approaches can be used such as hypergeometric [84] and spline functions [86] that reduce the problem to analytical functions. However, this might increase the number of fit parameters so extra care must be taken to ensure that the density profile is physically meaningful.

Pedersen and coworkers [74, 80, 81, 86] have modified Eq. 78 based on Monte Carlo simulation results from chains exhibiting excluded volume effects. Written in terms of a micelle constituted of a A-B block copolymer, this can be written independently of morphology (spherical, ellipsoidal, or cylindrical):

$$I(Q)_{\rm CS-acc.}^{\rm calc} = \frac{\phi}{PV_{\rm AB}}\left(\Delta\rho_{\rm c}^2 P^2\cdot V_{\rm B}^2\cdot A(Q)_{\rm c}^2 + \Delta\rho_{\rm sh}^2 P\cdot\left(P - F(0)_{\rm blob}\right)\cdot V_{\rm A}^2\cdot A(Q)_{\rm sh}^2 + \right.$$
$$\left. 2\Delta\rho_{\rm c}\cdot\Delta\rho_{\rm sh}P^2\cdot V_{\rm A}\cdot V_{\rm B}\cdot A(Q)_{\rm c}A(Q)_{\rm sh} + V_{\rm A}^2\Delta\rho_{\rm sh}^2\cdot F_{\rm blob}(Q)\right) \tag{87}$$

where $A_{\rm c}(Q)$ and $A_{\rm sh}(Q)$ are the scattering amplitudes of core and shell (corona), respectively; V_i is the molecular volume of the B- or A-block; $\Delta\rho_{\rm sh} = (\rho_{\rm A} - \rho_0)$; $\Delta\rho_{\rm c} = (\rho_{\rm B} - \rho_0)$; and $F(Q)$ is the effective scattering from the A-polymers

constituting the corona ("blob scattering"). ϕ_0 is the volume fraction of block copolymer.

As shown by Pedersen and Svaneborg, the scattering from the swollen PEO polymer chains in the corona (the blob scattering), can be written as [74, 80, 81, 86]:

$$F_{\text{blob}}(Q) = \frac{P(Q)_{\text{chain}}}{1 + \hat{v} \cdot P(Q)_{\text{chain}}} \tag{88}$$

where $P(Q)_{\text{chain}}$ is the form factor of a polymer chain, $\hat{v}$ is an effective virial type parameter that scales with the effective concentrations of corona chains [74, 86].

The form factor of a polymer chain can be conveniently approximated by the following equation suggested by Beaucage [88] for arbitrary chain statistics:

$$P(Q)_{\text{chain}} = \exp\left(-Q^2 R_{\text{g}}^2/3\right) + \left(d_{\text{f}}/R_{\text{g}}^{d_{\text{f}}}\right)\Gamma(d_{\text{f}}/2)\left(\frac{\left(\text{erf}\left(QkR_{\text{g}}/\sqrt{6}\right)^3\right)}{Q}\right)^{d_{\text{f}}} \tag{89}$$

where d_{f} is the fractal dimension and k is a numerical constant equal to 1.06. For mass fractals, $1 \leq d_{\text{f}} \leq 3$ and for polymers in a good solvent a typical value is 1.7. [88].

Alternatively, Pedersen and Schurtenberger have developed versatile expressions based on off-lattice Monte Carlo simulations that can be accurately used to describe almost any type of semiflexible polymer chain with and without excluded volume interactions [89].

3.1.7 Zero-Average Contrast in SANS

As previously mentioned, H/D substitution offers a great opportunity to perform contrast variation and thereby selectively highlight structural features in soft matter systems. Because of the abundance of hydrogen in soft matter systems and the relative easy access to deuterated materials,[6] H/D substitution can easily be applied to a large range of systems. Contrast variation SANS played a key role in verifying the scaling approaches of de Gennes and others to chain conformation in semidilute and concentrated solution [90] and in establishing a Gaussian conformation of polymers in melts [91].

For structural characterizations, zero average contrast (ZAC) conditions can be used to eliminate structure factor effects. Here, we will briefly illustrate how this works by considering a very simple case consisting of two types of monodisperse

---

[6] A large number of deuterated chemicals like solvents and monomers, particularly important in this context, are commercially available from standard chemical suppliers. In some cases, however, bottom-up organic synthesis is necessary, e.g., isoprene-d_8 or hexamethylcyclotrisoloxane-d_{18} for deuterated PI and PDMS, respectively. This requires expertise from both polymer and organic chemistry.

particles where one is proteated (H) and the other deuterated (D). As before, the total intensity assuming identical volumes can be written as:

$$I(Q) = n_z V \left(f_H \Delta \rho_H^2 A(Q)_H^2 + f_D \Delta \rho_D^2 A(Q)_D^2 + 2 \cdot f_H f_D \Delta \rho_H \Delta \rho_D A(Q)_H A(Q)_D \right) \quad (90)$$

where $\Delta \rho_i = \rho_i - \rho_0$ ($i = H/D$) is the contrast for each component with respect to the solvent ($i = 0$). $A(Q)_i$ is the scattering amplitude, which can be split into two parts: one for all atoms belonging to the same particle, $A(Q)_{i,s}$, and one for the atoms belonging to two different particles, $A(Q)_{i,d}$, such that $A(Q)_i = A(Q)_{i,s} + A(Q)_{i,d}$. By definition, $P(Q) = A(Q)_{i,s}^2$ and $S(Q) = A(Q)_{i,d}^2$. Moreover, because there is no correlation term between internal structure and the arrangement of particles, we obtain:

$$\begin{aligned} I(Q) = n_z V^2 \big(& f_H \Delta \rho_H^2 \left(P(Q)_H + S(Q)_H \right) + f_D \Delta \rho_D^2 \left(P(Q)_D + S(Q)_D \right) \\ & + 4 \cdot f_H f_D \Delta \rho_H \Delta \rho_D S(Q)_{HD} \big) \end{aligned} \quad (91)$$

Now, if the H/D content of the solvent is adjusted such that $\Delta \rho_H = -\Delta \rho_D$, i.e., the scattering length density of the solvent is exactly between those for the deuterated and proteated particle $\rho_0 = (\rho_H + \rho_D)/2$ the system is at the zero average contrast condition. Furthermore, if the particles have identical form factors and the interactions between H-type and D-type particles as well as the mutual interactions are identical [i.e., $P(Q) = P(Q)_i$ and $S(Q) = S(Q)_i$] and for a 50% mixture of H/D-particles ($f_H = f_D = 0.5$), Eq. 90 reduces to:

$$I(Q) = n_z V^2 P(Q) \quad (92)$$

and hence the form factor can be measured even in a crowded environment with interparticle interactions. This very useful trick has been widely used to probe single chain or single particle structural properties in concentrated polymer systems by SANS [82, 90, 92–94]. In the following section, we shall see how contrast variation can be used to study micellar structures.

3.1.8 SANS Contrast Variation on Block Copolymer Micelles

For block copolymer micelles, a general strategy is to selectively deuterate one block while keeping the other proteated. In this way, by varying, e.g., the H_2O/D_2O composition (or other H-and D-type solvents), the core and shell can be selectively highlighted and studied in detail. As seen in Eq. 87, if the scattering length density of the solvent matches either that of block A or block B (i.e., $\rho_0 = \rho_A$ and $\rho_0 = \rho_B$), the pure corona ($\Delta \rho_{sh} = 0$) or core ($\Delta \rho_c = 0$) scattering can be obtained separately without any interference term. Hence in this way, the different scattering contribution of a multicomponent system can be extracted. The methodology is illustrated
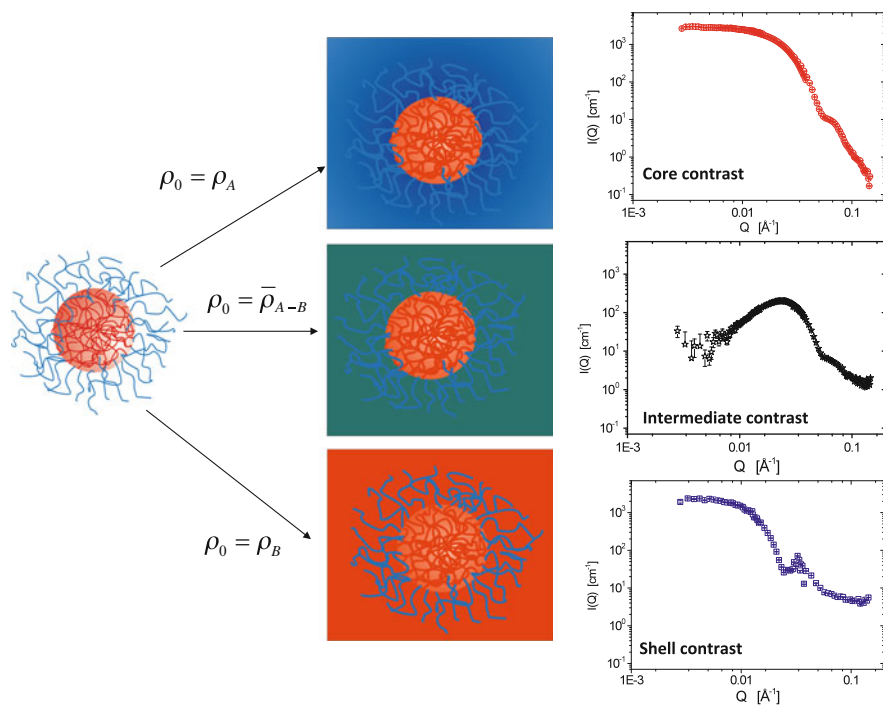
Fig. 11 Illustration of a SANS contrast variation study of block copolymer micelles (see text for details). Data to the right are reprinted with permission from [30]. Copyright (2009) American Chemical Society

more graphically in Fig. 11, where real results from a contrast variation study of proteated-polystyrene–deuterated polybutadiene (h-PS10–d-PB10) diblock copolymer micelles in heptane reproduced from [30] are also shown.

Moreover, by collecting data sets from different contrast situations and performing global fits (simultaneous fits) using a single scattering model, much more reliable and detailed structural results can be obtained. As an example, the scattered intensities from h-PS10–d-PB10 micelles in isotopic mixtures of various n-alkane solvents (selective for PB) are shown in Fig. 12. The different figures correspond to n-alkanes (C_nH_{2n+2}) with increasing length, from heptane ($n = 7$), decane ($n = 10$), dodecane ($n = 12$), and hexadecane ($n = 16$).

The different scattering patterns correspond to various isotopic solvent mixtures where the proteated PS core (h-PS) is matched: "shell" contrast; d-PB shell matched: "core" contrast and an "intermediate" contrast where the h-alkane/d-alkane mixture corresponds to a scattering length density in between that of the core and shell. Note that, in the latter case, the scattering at low angles ($Q \to 0$) almost disappears because the scattering contributions from core and shell are almost compensated by the interference term since $\Delta\rho_c = -\Delta\rho_{sh}$ and $V_A \approx V_B$ as can be rationalized from
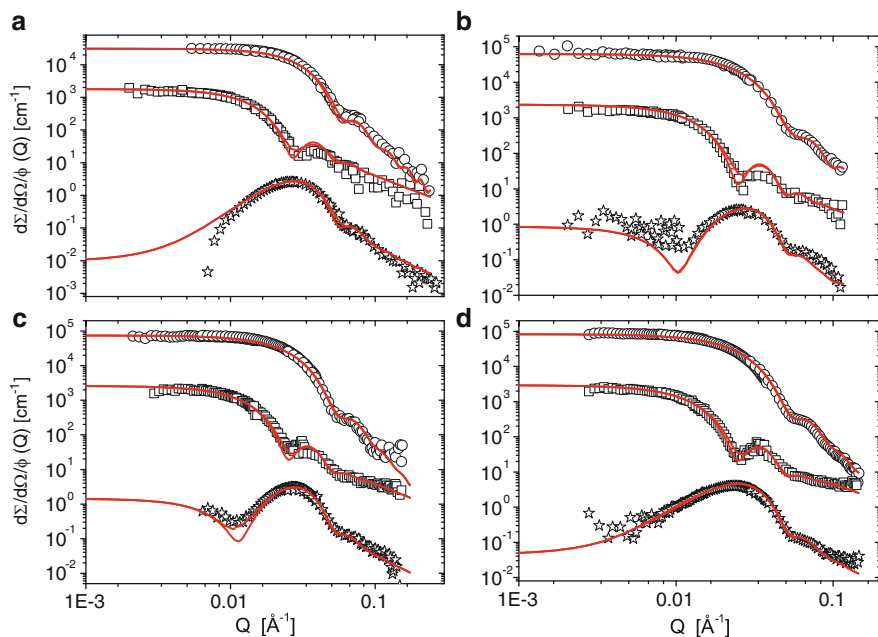
Fig. 12 Contrast variation results showing the absolute scattering cross-sections of h-PS–d-PB micelles in (**a**) heptane, (**b**) decane, (**c**) dodecane, and (**d**) hexadecane at $\phi = 0.25\%$ for different contrasts. The *solid lines* display simultaneous global fits using a core–shell model convoluted with the resolution function corresponding to the experimental settings. For better visibility, the data are shifted by a constant multiplication factor: core contrast (*circles*) 30; shell contrast (*squares*) 1; and intermediate contrast (*stars*) 0.02. Reprinted with permission from [30]. Copyright (2009) American Chemical Society

Eq. 87. At higher scattering vectors this is not the case because $A_c^2 \neq A_{sh}^2$, giving rise to scattering intensity at intermediate Q-values. The solid lines in Fig. 12 display simultaneous fits using the core–shell model above with an almost constant density profile, i.e., $x = 0$, a micellar smearing of about 10%, and $\sigma_m = 0.1$ in Eq. 86.

Thanks to the contrast variation and detailed model fitting, the internal structure could be obtained showing that the micelles are rather poorly segregated with a large quantity of solvent (approx. 30–50%) penetrating the core and a smaller compact corona. This important feature will be discussed in more detail in Sect. 4.3.

Other examples of such detailed analysis of the structure with the aid of contrast variation can be found for partially deuterated polystyrene–polyisoprene (PS-PI) diblock copolymer micelles in decane [86, 95]; "Pluronic" (PEO-PPO-PEO) micelles in water [96, 97]; PB-PEO micelles in water [85]; or PEP-PEO micelles in water [44] or in water/ DMF mixture [98].

3.2 Time-Resolved Small-Angle Scattering as a Technique for Studying Micellar Kinetics

In addition to being a powerful tool for investigating the structural details of nanostructures, small-angle scattering methods are very useful techniques for following structural changes over time, i.e., to follow phase transitions, morphological transitions, etc. [13–15, 17, 18]. In addition to studying non-equilibrium kinetics associated with structural changes and transformations over time, the sensitivity of neutrons towards H/D, contrast variation, and SANS offers a study of subtle transport/diffusive processes and kinetics under equilibrium conditions [18, 19], i.e., kinetics can be probed without perturbing the system away from equilibrium.

Modern neutron instrumentation is an extensive subject that could cover a whole book alone. Here we will just review some basic concepts related to the more practical aspects and relevant principles related to studies of soft matter systems in general and micellar systems in particular. In this section, we briefly review recent modern methods used for time-resolved SAS studies.

3.2.1 Rapid Mixing Techniques: Stopped-Flow Methods

A versatile and classical method for studying kinetic reactions and other kinetic phenomena on short time scales is the use of a stopped-flow apparatus (SFA) for fast reproducible mixing and then to apply, e.g., spectroscopic methods for detection. In this technique, the reactants are rapidly mixed in a mixing chamber, usually under full turbulent flow that ensures fast homogenization on length scales down to nanometers [99]. Provided that short, synchronized acquisitions can be made, X-ray or neutron scattering can be used to probe kinetic transitions and other processes directly by measuring the temporal evolution of the intensity of the (mixed) sample.

The importance of a stopped-flow apparatus is to control the mixing of several solutions in a short time, achieve precise synchronization between the mixing process and the acquisition to ensure reproducibility of the experiment, and obtain a well-defined kinetic time [18, 99]. For fast measurements, it is important to use both fast mixing and short acquisition times while maintaining a reasonable statistics. This is more easily achieved with synchrotron sources, where the combination of small mixing volumes and high brilliance of the beam easily allow kinetic times of the order of a few milliseconds. However, with the more optimized neutron instrumentation and, in particular, with the advent of more powerful neutron sources such as spallation sources, there are a growing number of time-resolved SANS experiments investigating kinetic processes on a typical time scale of about 100 ms and upwards [18]. With more powerful spallation sources such as the planned European Spallation Source (ESS) in Lund, Sweden, time-resolved SANS measurements are expected to approach that of TR-SAXS at current synchrotron sources.
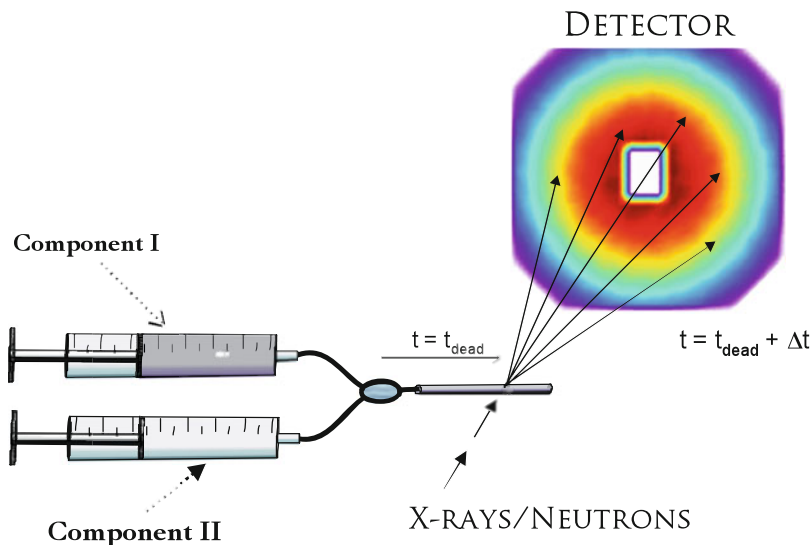
Fig. 13 Typical set-up of a small-angle scattering instrument coupled with stopped-flow apparatus. By synchronizing the mixing and transport of the solution to the observation chamber and the X-ray/neutron scattering acquisition, rapid processes occurring on a time scale down to a few milliseconds can be resolved

A crude scheme of a typical set-up for SAS combined with a stopped-flow apparatus is shown in Fig. 13. The idea is rather straightforward; the solutions are brought into contact by injecting the contents of two separate reservoirs into a "mixing chamber" that assures fast turbulent flow and homogeneous mixing. The solutions are thereafter transported to the observation cell (cuvette/capillary) through a stationary lamellar (non-turbulent/low Reynold number) flow. Although the homogenization time t_h, i.e., the time needed to completely mix the two liquids, itself is fast, there is a certain time lag associated with achieving lamellar flow, transport, and filling of the sample volume of the cuvette/capillary ($t_{dead} = V_{dead}/\mu$) where μ is the flow rate and V_{dead} is the volume that needs to be filled).

A typical measurement sequence is illustrated in Fig. 14. The reservoirs are continuously mixed by injection into the mixing chamber. Afterwards, the mixed solution is transported into the scattering volume. This transport time corresponds to t_{dead}. The flow of freshly mixed solution is maintained during a time t_{mix}, after which the flow is stopped by a hard-stop blocking the stream (hence the name "stopped-flow apparatus"). By varying the time for which the exposure/acquisition starts, defined by t_{delay}, and the duration t_{acq}, one may vary the kinetic times probed. Hence, placing an acquisition pulse within the duration of the mixing time would imply probing a fixed kinetic time $t = t_{dead}$ as fresh solution is continuously brought into the observation chamber. Placing the pulse outside the mixing duration, the kinetic time varies with
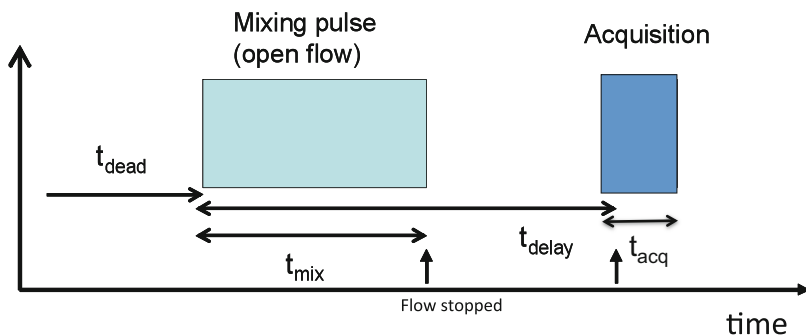
Fig. 14 Time sequence of a time-resolved small-angle scattering experiment. Using a stopped-flow apparatus, the data acquisition time, t_{acq}, can be synchronized with the mixing pulse time length, t_{mix}, giving access to fast kinetics. By varying the delay time, t_{delay}, high resolution stroboscopic measurements can be performed provided that the kinetics is reproducible. See text for details

the delay time t_{delay}. Hence, by synchronizing the SFA with the SAS instrument and varying the delay time, the kinetics can be probed stroboscopically by repeating several experiment with different time lags by varying t_{delay}, and thereby cover different initial kinetic times. The sequence of which subsequent kinetic time is probed is usually set by the detector of the instrument and the shutter. Here there is a difference between synchrotron X-rays and neutrons; whereas SAXS requires a shutter in order to avoid beam radiation damage, this is not required in SANS because such effects are absent. However, since many X-ray instruments use CCD-type detectors that require complete read-out and writing of data from each frame, the minimum lag time between frames is not set by the opening time of the shutter but rather by the readout time, which is typically between 100 and 300 ms. This is obviously only important for fast kinetics and limits the temporal resolution. However, provided that the kinetics is reproducible, this can be overcome by stroboscopic schemes whereby the kinetic is repeated with different lag times with respect to the acquisition, and can easily improve the resolution down to a few milliseconds. For SANS gas/scintillator detectors, the kinetic data can be stored in the different channels (typically 1,024 channels) and the minimal time is essentially set by the frame overlap in the wave packet and depends on the chopper speed (typically a few milliseconds for 1 m and an order of magnitude larger for 20 m).

Expressed mathematically, the first measured kinetic time in a stroboscopic experiment can be written as:

$$t_0 = \begin{cases} t_{dead}; & t_{mix} > t_{delay} \\ t_{dead} + (t_{delay} - t_{mix}); & t_{mix} \leq t_{delay} \end{cases} \tag{93}$$

The kinetic times at subsequent measurement frames numbered i are:

$$t_i = t_0 + \sum t_{i-1} + t_{acq}/2 \tag{94}$$

Often the delay time (X-rays), or the acquisition time (neutrons), is set to follow a geometrical progression to avoid oversampling and improve statistics at longer times (acquisition time). In the case, $t_{\text{delay/acq}}(i) = (t_{\text{delay/acq}}) \cdot f^i$ where f is a factor typically between 1.01 and 1.3 such that progressively slower processes can be followed. With this simple geometrical series, the kinetic time, Eq. 94, can conveniently be evaluated as: $t_i = t_{\text{dead}} + t_{\text{acq}}/2 + t_{\text{acq}} \frac{1-f^i}{1-f}$ and $t_i = t_{\text{dead}} + (i-1) \cdot t_{\text{acq}} + t_{\text{acq}}/2 + t_{\text{delay}} \frac{1-f^i}{1-f}$ for SANS and SAXS, respectively.

3.2.2 Contrast Variation and Time-Resolved SANS as a Method for Studying Exchange Kinetics

Time-resolved SAXS can be applied to the study of many types of kinetic processes. However, it must generally involve a transition from one state to another because the scattering signal only varies with changes in size, shape, etc. [14, 15]; in other words, the method is generally limited to non-equilibrium kinetics. Neutrons, however, may detect kinetics that do not necessarily alter the overall thermodynamic equilibrium state. This is essential for studying equilibrium processes such as chain exchange kinetics. Such kinetics can be studied by applying a H/D substitution scheme based on mixing H-type and D-type micelles made from block copolymers of identical volume and composition. By mixing these micelles in a solvent having an average scattering length density between the two, the contrast will decrease upon exchanging the chains between the micelles; hence, the molecular exchange kinetics is probed. The idea is schematically illustrated in Fig. 15.

This kinetic zero average contrast (KZAC) experiment [100–102] is an extension to the static zero average contrast (ZAC) described in Sect. 3.1.7. ZAC is used to effectively remove the structure factor such that interparticle correlations are eliminated and the single entities are visible, whereas in KZAC the trick is used to render mixing processes; hence, diffusion and transport become observable without perturbing the system in any substantial way.

In Fig. 16, experimental results of the time-dependent intensity after mixing proteated and deuterated PS-PB micelles in DMF under KZAC conditions [101] are shown. As can be seen the intensity decreases with time, directly showing that the micelles mix and kinetic processes are active. By analyzing the evolution of the scattered intensity and appropriate modeling, the mechanism and pathways can be determined from these experiments. In the following section, the technicalities will be described in more detail.

Model-Independent Evaluation of TR-SANS Kinetic Data

Mathematically, we might express this more precisely in the following way. The observed SANS intensity is determined by $I(t) \approx (\rho_{\text{m}} - \rho_0)^2$ where ρ_{m} is the effective scattering length density of the micelle given by the volume fraction of
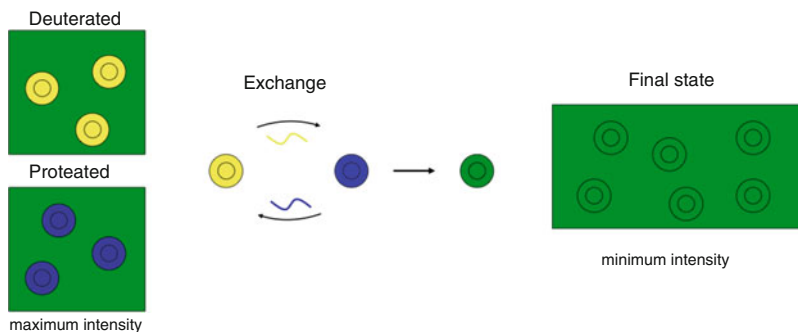
Fig. 15 Principle behind the KZAC experiment designed to measure chain exchange kinetics. Two populations of micelles, deuterated (*yellow*) and proteated (*blue*) are mixed at $t = 0$ in a solvent that matches the average color, *green* (about 50:50 deuterated/proteated solvent molecules). Upon molecular exchange of amphiphiles, the average contrast of the micelles decreases and thus the intensity in the TR-SANS experiment
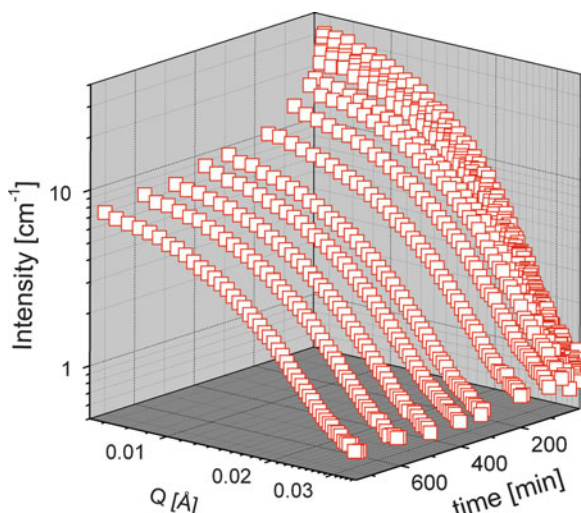

Fig. 16 Experimental curves showing a realization of the KZAC/TR-SANS technique applied to PS-PB block copolymers dissolved in DMF, which is a selective solvent for PS. At time zero, fully deuterated d-PS–d-PB micelles are mixed with fully proteated h-PS–h-PB micelles in a isotopic h-DMF/d-DMF solvent mixture exactly matching the average scattering length density. As the block copolymer chains exchange, an overall decrease in the intensity is observed while the form factor and hence the structure remains constant

proteated and deuterated chains, f and $1 - f$ respectively: $\rho_m = f\rho_h + (1 - f)\rho_d$ where ρ_h and ρ_d are the scattering length densities of the proteated and deuterated (in this section referred to as h- and d-) chains. Because in ZAC conditions we have $\rho_0 = (\rho_h + \rho_d)/2$, we see that the square root of $I(t)$ is linearly proportional to

the excess fraction of the h- or d-chains, i.e., $\sqrt{I(t)} \sim \Delta\rho(t) \sim (f(t) - 1/2)\rho_h + (1/2 - f(t))\rho_d = (f(t) - 1/2)(\rho_h - \rho_d)$. In this way, the analysis of the data is straightforward in comparison to other methods. Hence, using this method the information on the exchange kinetics is unambiguously given by the relaxation function, $R(t)$:

$$R(t) = \left(\frac{I(t) - I_\infty}{I(t=0) - I_\infty} \right)^{1/2} \tag{95}$$

where $I(t) = \int I(Q,t)\mathrm{d}Q$ is the integral intensity at a given time and I_∞ denotes the intensity of the fully mixed sample at the final stage of the kinetic process (obtainable by randomly premixing the two block copolymers with $\phi_{hh} = \phi_{dd} = 0.5$. $I(0)$ is the arithmetic average of the two reservoirs (hh and dd samples) measured separately. The latter has to be measured at dilute concentrations, where no structure factor effects are present since $S(Q)$ vanishes under KZAC conditions.

$R(t)$ is the relevant function to be analyzed for extraction of the kinetics. However, in micellar systems where the micelles are not fully proteated/deuterated or there is residual contrast between core and shell, nonlinear interference scattering contributions are present. In order to take this into account, a more accurate description of the time-dependent scattering intensity is necessary. A scattering model, where the time-dependent hyrogen/deuterium composition of the core and shell of the micelles is built into a kinetic core–shell model, is described next.

Full Model Fitting Approach

The scattering function describing the time-dependent scattering intensity of micelles in a KZAC experiment involves a time-dependent core–shell model where the contrast is a function of the fraction of chains exchanged, f_{exc}. Here, we shall limit the discussion to cylindrical and spherical structures using simple A-B diblock copolymers as an example. Inclusion of other structures such as vesicles could be slightly more complicated because the microscopic composition might be potentially different in the inner and outer shells.

In the simple case of cylinders and spheres one can write:

$$I(Q,t)^i = \frac{\phi}{PV_{\mathrm{A-B}}} \Big(\Delta\rho_{\mathrm{c}}^i(t)^2 P^2 \cdot V_{\mathrm{B}}^2 \cdot A(Q)_{\mathrm{c}}^2 + \Delta\rho_{\mathrm{sh}}^i(t)^2 P \cdot (P - F(0)_{\mathrm{blob}}) \cdot V_{\mathrm{A}}^2 \cdot A(Q)_{\mathrm{sh}}^2 + \\ 2\Delta\rho_{\mathrm{c}}^i(t) \cdot \Delta\rho_{\mathrm{sh}}^i(t) P^2 \cdot V_{\mathrm{A}} \cdot V_{\mathrm{B}} \cdot A(Q)_{\mathrm{c}} A(Q)_{\mathrm{sh}} + V_{\mathrm{A}}^2 \Delta\rho_{\mathrm{sh}}^i(t)^2 \cdot F_{\mathrm{blob}}(Q) \Big) \tag{96}$$

where i denotes either proteated ($i = \mathrm{h}$) or deuterated ($i = \mathrm{d}$) species. $A(Q)_i$ is the scattering amplitude of core (c) and shell (sh), given in Eqs. 84 and 85, respectively.

The time dependence enters via the change of contrast of core and corona, $\Delta\rho_{\mathrm{c}}^i(t)$, $\Delta\rho_{\mathrm{sh}}^i(t)$ as a consequence of chain exchange between the differently labeled micelles.

Even though, after mixing and during the course of reaching a randomized mixture of h- and d-chains at equilibrium, a strict distinction between the originally proteated and deuterated micelles is lost, one can still write the contrast in terms of a surplus of either h- or d-chains $f(t)$ in the original micelles. We will use the convention $f(t = 0) = 1$. Because the excess contrast is defined under ZAC conditions ($\rho_0 \approx (\rho_{hh} + \rho_{dd})/2$), $I(Q,t)^i$ must be symmetric around $f(t) \approx 0.5$, at least for low Q. For the situation where the micelles are completely randomized, $f(t) \approx 0.5$.

The contrast for the h- and d-cores made out of the h-B and d-B blocks, at time t is then given by:

$$\Delta\rho_c^i(t) = \begin{cases} \rho_{h-B} \cdot f(t) + \rho_{d-B} \cdot (1 - f(t)) - \rho_0 & \text{h-type micelle} \\ \rho_{h-B} \cdot (1 - f(t)) + \rho_{d-B} \cdot f(t) - \rho_0 & \text{d-type micelle} \end{cases} \quad (97)$$

and likewise for the corona:

$$\Delta\rho_{sh}^i(t) = \begin{cases} \rho_{h-A} \cdot f(t) + \rho_{d-PEO} \cdot (1 - f(t)) - \rho_0 & \text{h-type micelle} \\ \rho_{h-A} \cdot (1 - f(t)) + \rho_{d-PEO} \cdot f(t) - \rho_0 & \text{d-type micelle} \end{cases} \quad (98)$$

where the excess function is restricted to the range $0.5 \leq f(t) \leq 1$, assuming that the proteated and deuterated micelles are very similar and $V_h^{\text{mic}} \approx V_d^{\text{mic}}$.

The complete time-dependent scattered intensity can be calculated by taking the average of the two "types" of micelles in the following way:

$$I(Q,t) = \frac{1}{2}\left(I(Q,t)^h + I(Q,t)^d\right) + B \quad (99)$$

where $I(Q,t)^{h,d}$ is calculated according to Eq. 96 and B is a constant (time-independent) background reflecting the incoherent scattering of the sample.

As an example, Fig. 17 shows results [103] where the model is applied to describe the time-resolved SANS intensity in a KZAC experiment on n-alkane-PEO (C_{24}-PEO5k) micelles where only the PEO part was labeled (C_{24}-dPEO5k/ C_{24}-hPEO5k), i.e., the core-forming n-alkane block was proteated for both polymers and thus a net contrast between core and corona is always present during the course of the kinetic mixing process. As seen, both absolute values and the shape of the data are very well described at all times. At longer times, a shallow minimum at larger Q values evolves as a consequence of residual contrast between core and corona. This is also naturally described by the model. The results of this investigation are described in more detail in Sect. 4.4.

In analogy to the determination of $R(t)$ in Eq. 95, we can calculate $f_{\text{exc}}(t)$ for a better comparison of the kinetic data obtained by the two methods:

$$f_{\text{exc}}(t) = \frac{f(t) - f_\infty}{f(0) - f_\infty} \quad (100)$$
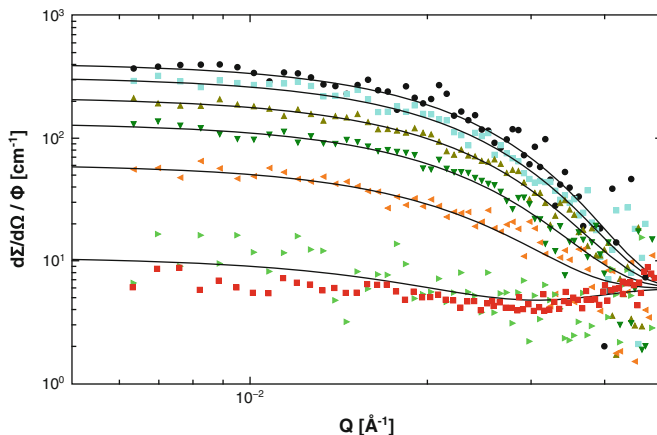
Fig. 17 Time-resolved SANS data showing the exchange process in *n*-alkyl-PEO micelles in water. *Solid lines* display fits of the core–shell model with *f(t)* as free parameter. Time evolution from *top* to *bottom*: $t = 0.05, 5.6, 14.7, 25.2, 42.4$, and 95.0 s. [103] Reproduced by permission of The Royal Society of Chemistry

As shown in two recent studies [103, 104], both $f_{exc}(t)$ and $R(t)$ give essentially the same kinetic information and results. It should be mentioned, however, that the methodology described here only applies to rather low Q. At smaller scales, excess scattering is expected during the course of mixing as there might be local domains of either h- or d-type chains.

A similar approach could be used to describe hybridization kinetics after mixing two different micelles or for processes involving non-equilibrium relaxation experiments. However, in this case the time dependence of the structural parameters [$P(t)$, $R_m(t)$, etc.] as well as micellar composition must be taken into account.

Rate Constant From a Two-Component Labeling Experiment

Independently of the evaluation method, a KZAC TR-SANS experiment allows the kinetics to be evaluated through the decay of either $R(t)$ or $f_{exc}(t)$. The unimer exchange rate constant in simple labeling experiment will now be discussed.

A kinetic model for unimer exchange mechanism has been presented by Thilo [105] as well as by Cantú et al. [106]. According to Thilo [105], the following kinetic scheme can be used. Here, we use the terminology of proteated (H) and deuterated (D) chains or surfactants because in the present review the focus is on scattering experiments.

Starting from reservoir I where the micelles only contain proteated chains (H) and reservoir II with only deuterated chains (D), we define the initial conditions as $f_I = 1$ and $f_{II} = 0$ where the subscripts denote micelle I ($i = $ I) or micelle

II ($i =$ II), i.e., $f_I = N_H^I / (N_H^I + N_D^I)$ and $f_{II} = N_H^{II} / (N_H^{II} + N_D^{II})$ where N_H and N_D are the number of chains of type H or D inside the respective micelles. Considering proteated and deuterated unimers (number denoted by U_H and U_D, respectively) undergoing insertion/expulsion between the micelles, the rate equations can be written:

$$\frac{dN_H^I}{dt} = k_+^H U_H \left(N_H^I + N_D^I\right) - k_- N_H^I \tag{101}$$

$$\frac{dN_D^I}{dt} = k_+^D U_D \left(N_H^I + N_D^I\right) - k_- N_D^I \tag{102}$$

$$\frac{dN_H^{II}}{dt} = k_+^H U_H \left(N_H^{II} + N_D^{II}\right) - k_- N_H^{II} \tag{103}$$

$$\frac{dN_D^{II}}{dt} = k_+^H U_D \left(N_H^{II} + N_D^{II}\right) - k_- N_H^{II} \tag{104}$$

From mass-conservation we have:

$$\frac{dN_H^I}{dt} + \frac{N_H^{II}}{dt} = 0 \tag{105}$$

$$\frac{dN_D^I}{dt} + \frac{N_D^{II}}{dt} = 0 \tag{106}$$

It is useful to introduce the relative fraction of H-chains, r:

$$r = \frac{N_H^I + N_H^{II}}{N_H^I + N_H^{II} + N_D^I + N_D^{II}} \tag{107}$$

From Eqs. 101–107:

$$\frac{k_+^H}{k_-^H} = \frac{r}{U_H} \tag{108}$$

$$\frac{k_+^D}{k_-^D} = \frac{1 - r}{U_D} \tag{109}$$

The time derivative of f_I and f_{II} are then obtained by direct derivation and yields:

$$\frac{df_I}{dt} = \frac{1}{N_H^I + N_D^I} \cdot \left[(1 - f_I)\frac{dN_H^I}{dt} - f_1 \frac{dN_D^I}{dt}\right] \tag{110}$$

$$\frac{df_{II}}{dt} = \frac{1}{N_H^{II} + N_D^{II}} \cdot \left[(1 - f_{II}) \frac{dN_H^{II}}{dt} - f_1 \frac{dN_D^{II}}{dt} \right] \tag{111}$$

Using Eqs. 101–109 and inserting into Eqs. 110 and 111 gives two second-order differential equations that can easily be solved using the above-mentioned boundary conditions:

$$f_I(t) = \frac{(1 - r)k_-^H \exp(-\lambda t) + rk_-^D}{(1 - r)\left(k_-^H - k_-^D\right) \exp(-\lambda t) + k_-^D} \tag{112}$$

and:

$$f_{II}(t) = \frac{1 - \exp(-\lambda t)}{1/r - \left(1 - k_-^D/k_-^H\right) \exp(-\lambda t)} \tag{113}$$

where $\lambda = rk_-^D + (1 - r)k_-^H$. In this work, all measurements have been performed by carefully balanced samples, i.e., $N_H \approx N_D$ consequently, since the fraction of free unimers is very small in these systems [31]: $r = N_H/(N_H + N_D) \approx 1/2$. Moreover, assuming that the labeled block copolymers are similar, $k_-^D = k_-^H = k_-$, Eqs. 112 and 113 can be cast to simple forms:

$$f_I(t) = \frac{1}{2}\left(\exp(k_- t) + 1\right) \tag{114}$$

$$f_{II}(t) = \frac{1}{2}\left(1 - \exp(k_- t)\right) \tag{115}$$

Hence, we see that for a simple unimer expulsion/insertion mechanism, the following expression holds:

$$\sqrt{I(t)} \sim (f_I(t) - 1/2)\rho_h + (1/2 - f_{II}(t))\rho_d \sim \exp(-k_- t) \tag{116}$$

In other words, $R(t)$ and f_{exc} would, in the case where the mechanism of unimer exchange is dominant, give rise to a simple exponential decay.

4 Equilibrium Kinetics in Block Copolymer Micelles

Experimental work on the equilibrium kinetics in block copolymer micelles is very rare in comparison with structural investigations. This is most likely due to the challenging problems in accessing the chain exchange by suitable experimental techniques or systems. Early experiments include studies using size-exclusion

chromatography [107–112] and ultracentrifugation [113, 114] as investigative tools. Since both techniques involve strong flow fields, the experiments yield information under quasi-static conditions rather than true equilibrium kinetics. Therefore, these works will not be further reviewed here. Kinetic studies have additionally been performed using ultrasonic absorption techniques [115–117] but after careful analysis it was concluded that the ultrasonic relaxation observed in micellar solution cannot be associated with the Aniansson and Wall mechanism of single chain exchange [117]. More relevant in the context of this chapter are relaxation experiments under quasi-equilibrium conditions, i.e., after small perturbations from equilibrium such as small temperature-jump (T-jump) experiments with light scattering detection in triblock copolymer micelles of the Pluronics type, PEO-PPO-PEO. Regarding this work, we will devote a small section (Sect. 4.1) to a brief summary of the main results. Other techniques like fluorescence quenching or nonradiative energy transfer [118–122] and transmission electron microscopy [123–125] have been used to assess micellar kinetics. However, strong perturbations or the incorporation of bulky labels are necessary to be able to monitor kinetic processes, which are often accompanied by reorganization of micellar structures. In any case these classical works have already been discussed extensively before in, e.g., the review of Zana [16]. Therefore, we will mainly restrict this section to the more recent results obtained by the H/D contrast variation/TR-SANS technique because this method was shown to access the chain exchange dynamics under true equilibrium conditions. By the combination of proper spatial and temporal resolution and by using suitable block copolymer/solvent systems, these experiments have given new insights into the mechanisms of chain exchange and allowed a profound discussion of the relaxation behavior within the framework of the existing theories.

This section on equilibrium kinetics is organized as follows: We will first focus on the T-jump experiments with light scattering detection on Pluronics polymers (Sect. 4.1). Thereafter, a chronological review of kinetic experiments on PEP-PEO block copolymers in aqueous solution is presented, including a summary of the morphological properties of this system (Sect. 4.2). A special focus is given on the tuning of kinetics by variation of mainly the interfacial tension. The main outcome of these experiments was the observation of an unexpected logarithmic time decay. This is discussed in more detail (Sect. 4.2.4). Further, we will review experiments obtained on block copolymers in organic solvents and discuss the dramatic effect of polydispersity on the kinetics, which finally allows an explanation of the log-time dependence (Sect. 4.3). Subsequently, a summary of kinetic experiments on n-alkyl-PEO block copolymers with monodisperse core blocks will be given, supporting the polydispersity effect by directly demonstrating the enormous influence of the n-alkyl chain length and the observed single exponential decay (Sect. 4.4). Finally, two special sections are devoted to the exchange kinetics at higher concentrations in ordered diblock copolymer micelles (Sect. 4.5) and to the influence of the morphology by comparing kinetics in spherical and cylindrical micelles (Sect. 4.6).
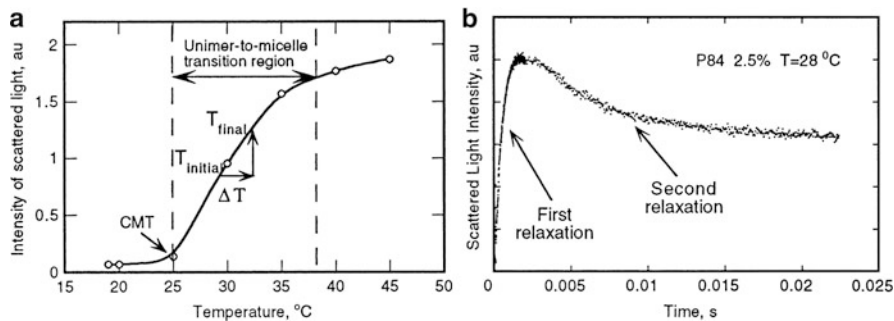
Fig. 18 Scattered light intensity (**a**) as a function of temperature in aqueous solution of PEP-PPO-PEO block copolymers, including the location of a typical temperature-jump; (**b**) as a function of time at the target temperature. Reprinted with permission from [127]. Copyright (1997) American Chemical Society

4.1 Quasi-equilibrium Kinetics of PEO-PPO-PEO in Temperature-Jump Experiments

The kinetics of poly(ethylene oxide)–poly(propylene oxide)–poly(ethylene oxide) (PEO-PPO-PEO) triblock copolymers have been intensively studied by T-jump experiments with light scattering detection [115, 126–130]. PEO-PPO-PEO triblock copolymers form micelles in aqueous solution, with PPO as the core forming hydrophobic block. Above the critical micelle concentration (cmc) and critical micelle temperature there exists a transition region of $\Delta T \approx 10$–$15°C$ where single chains disappear in favor of micellar aggregates. The temperature jumps of typically 1–2°C are performed in the transition region, leading to a change in the degree of aggregation and, consequently, to a variation in the scattered intensity. Fig. 18a shows the temperature dependent intensity of scattered light including the range and location of a typical jump experiment. Fig. 18b displays the response after the T-jump as a function of time, revealing two relaxation processes: a fast process that is accompanied by an increase in scattered light appearing on time scales in the micro- to millisecond range; and a second slow process with a negative scattering amplitude, i.e., a decrease in the light intensity with time, in the millisecond range. The fast process was assigned to the insertion of block copolymer chains into preexisting micelles, leading to aggregates, which are thermodynamically unstable. The second slow process was associated with formation–breakup processes to rearrange the micellar size distribution corresponding to thermodynamic equilibrium [115, 127]. The existence of two characteristic times is in agreement with the Aniansson and Wall picture [54–56] derived for low molecular weight surfactants. However, as the second slow process depends on concentration, fusion and fission as competing mechanisms for chain exchange need to be considered, as already proposed by Kahlweit et al. [52, 57]. Later, the T-jump experiments were extended by Kositza et al. [128, 129] to higher temperatures close to the cloud point. At the cloud point, the solvent quality becomes bad enough such that a

macrophase separation into a block-copolymer-rich phase and a water-rich phase takes place. These experiments revealed the appearance of a third process with a positive amplitude. This was assigned to intermicellar interactions, indicating the onset of the macrophase separation. We note that in these cases PPO was the major compound in the triblock copolymer. The increasing hydrophobicity at higher temperatures may thus lead to the observed clustering and macrophase separation in water. In a subsequent paper by Waton et al. [130], it was argued that the second and third relaxation processes are identical and are both due to the formation and breakup of micellar entities at the point where the sign of the amplitude changes from negative to positive by increasing the temperature. This was shown to be a consequence of the relative size of the micelles after the fast initial growth and at equilibrium. If micelles are larger after the first process than at the end of the slow process, the scattered light decreases and vice versa. Because this changes with temperature, the change in the sign of the amplitude becomes obvious.

The above discussed experiments were performed under quasi-equilibrium conditions inherently showing a rather complex relaxation behavior that is governed by processes from equilibrium and non-equilibrium kinetics. Additionally, in light of the discussion above, the presence of an apparent third mode is controversial. With respect to the understanding of equilibrium kinetics in general, the outcome of these experiments is limited as it does not provide deep insight into the exchange mechanism and the dependence of system-specific parameters like the interfacial tension, core chain length, and polydispersity. A more thorough understanding was only possible after the advent of the TR-SANS technique, as will be shown in the subsequent sections.

4.2 PEP-PEO Block Copolymers in Aqueous Solution

The study of the structure and kinetics of hydrocarbon-PEO amphiphilic diblock copolymers in selective solvents has received increased attention within the last 25 years. For example, polystyrene-*block*-poly(ethylene oxide) (PS-PEO) was intensively investigated in the 1990s [3, 131–136]. More recently, the micellar properties of block copolymers containing either polydienes like 1,4-polyisoprene (PI); 1,2- or 1,4-polybutadiene (PB); or their saturated analogues poly(ethylene-*alt*-propylene) (PEP) and poly(ethylethylene) (PEE) as the hydrocarbon block have attracted the attention of many research groups because of their potential technical and biomedical applications. The micellar properties of PE-PEO block copolymers, with PE the saturation product of 1,4-PB, have only rarely been investigated [137, 138]. In particular, equilibrium kinetics have to the best of our knowledge not been studied so far most likely due to complications arising from unwanted coupling between crystallization of PE and chain exchange dynamics at moderate temperatures. The chemical design of amphiphilic block copolymers resembles that of the well-known low molecular weight oligo(ethylene oxide)-monoalkyl ether $[C_n(EO)_m]$ surfactants, with subscript n being the number of carbon atoms of the hydrophobic n-alkyl-moiety

and m of the hydrophilic EO units. Accordingly, amphiphilic block copolymers can form micelles in aqueous media as well as in nonpolar solvents.

In this part of the review we will focus on kinetics in aqueous dispersions because water-based systems have been more commonly investigated. Among the amphiphilic block copolymers mentioned above, PEP-PEO takes a prominent position because it possesses four main features that turn it into an ideal model system for studying fundamental aspects of block copolymer micellization: (1) The synthesis of narrowly distributed PEP-PEO with predefined molecular weight and composition is easily feasible by well-established living anionic polymerization techniques [139–141]. Importantly, as a prerequisite for TR-SANS studies, PEP-PEO can be synthesized fully deuterated. (2) Compared to polydienes, the aliphatic PEP block is chemically and thermally stable, which facilitates sample handling and preparation. The addition of stabilizing agents such as antioxidants is not necessary. (3) PEO is highly water-soluble and electrostatically neutral. (4) PEP is an amorphous material with a low T_g of $-56°$C. Specific influences from glassy or crystallized micellar cores need not be considered. (5) PEP is highly incompatibility with water, as reflected by a large value for the interfacial tension, γ, of about 46 mN/m [45]. This high value of γ is the important physical quantity determining the aggregation behavior of PEP-PEO block copolymers in aqueous solutions. Moreover, the tuning of micellar structure and kinetics by varying γ through the addition of less incompatible co-solvents, e.g., DMF or ethanol becomes very effective. As the static properties are an important prerequisite for discussing exchange kinetics, the PEP-PEO micellar structure was characterized as a function of molecular weight, block composition, and solvent quality. A brief summary of the main structural features of these investigations is given in the beginning of Sect. 4.2.1.

The main part is then devoted to the equilibrium exchange kinetics of selected PEP-PEO micellar systems. We report on TR-SANS measurements in pure water that, independently of block copolymer molecular weight, composition, and temperature, revealed frozen micelles. This review further concerns the effect of tuning the kinetics by addition of co-solvents, i.e., reduction of γ. The relaxation behavior of some selected systems revealing chain exchange dynamics that can be resolved by TR-SANS will be presented, followed by a discussion of the main observation, namely, the unexpected appearance of a pseudo-logarithmic time decay of the relaxation function.

4.2.1 Morphological Behavior of PEP-PEO Block Copolymers in Aqueous Solution

The static structure of PEP-PEO block copolymer micelles in aqueous solution have been studied by small angle scattering techniques, primarily SANS [44, 45, 87, 104, 139, 142], and in one case by a combination of SAXS and static light scattering (SLS) [143]. In water, PEP-PEO block copolymers self-assemble into a variety of micellar structures depending on molecular weight and composition. A thorough structural characterization of micelles formed by a symmetric PEP5-PEO5 diblock

copolymer (numbers denote approximate molecular weight in kg/mol) was done by SANS using contrast variation and model fitting [87]. Fit results simultaneously obtained on four different contrasts revealed a spherical shape of the micelles, consisting of a compact solvent-free micellar core and a highly swollen PEO corona. It was found that the micelles have unusually large aggregation numbers of $P = 2,430$ and rather large dimensions. It was shown from thermodynamic calculations based on a mean-field model of Nagarajan and Ganesh [28] that this is a consequence of the large interfacial tension between PEP and water.

In a series of experiments, aqueous dispersions of symmetric PEP-PEO block copolymers were studied over a wide range of molecular weights, always keeping the ratio between the volumes of the blocks constant [142]. The scattering behavior of the solutions showed that a morphological transition takes place upon lowering the molecular weight. The high molecular weight materials all formed spherical, almost monodisperse, micelles with large aggregation numbers. At low molecular weights, however, cylindrical micelles were observed. An interesting intermediate case is represented by the PEP2-PEO2 system. Here spherical micelles were found at higher concentrations while cylinders occurred at larger dilutions.

The effect of a growing soluble block on the morphology of the micelles was investigated by varying the molecular weight of the PEO from about 5 to 120 kg/mol while keeping the PEP block constant at 5 kg/mol for all polymers [44]. Thus, a systematic study of the aggregation number and the corona shape became possible over a large range of compositional asymmetry ($1:1 \rightarrow 1:24$). Partial labeling of the block copolymers allowed highlighting corona structures individually by matching out core contributions using D_2O/H_2O mixtures. Data analysis using a spherical core–shell model with variable density profile indicated a crossover from a practically homogeneous corona profile for more symmetric diblocks to a star-like profile at larger asymmetries. Notably was the observation that PEP-PEO block copolymers aggregate into micelles even in a large compositional asymmetry, realizing thereby micelles with a star-like profile. It was concluded from free energy considerations that this is only possible because of the high interfacial energy as the main contribution.

In contrast to the study of Willner et al. [44], a cylinder-to-sphere transition was observed by Jensen et al. [143, 144] upon increasing the PEO block molecular weight in a similar molecular weight range. By SAXS and SLS it was found that PEP5-PEO5, PEP5-PEO10, and PEP5-PEO20 form cylindrical micelles whereas PEP5-PEO40 micelles are spherical. However, no explanation was given for the different molecular weight dependence of the morphology found in this work as compared to the work by Willner et al. [44].

The effect of interfacial tension γ on the micellar structure of a highly asymmetric PEP1-PEO20 block copolymer was examined using binary solvent mixtures of water and DMF as selective solvents [45, 145]. DMF and water are both good solvents for PEO and non-solvents for PEP, but exhibit a large difference in γ with respect to the insoluble core block. The micellar characteristics were obtained by SANS and subsequent fitting with a spherical core–shell form factor. Scattering curves together with model fits for selected water/DMF mixtures are depicted in Fig. 19a. As anticipated from the large asymmetry in block composition, the
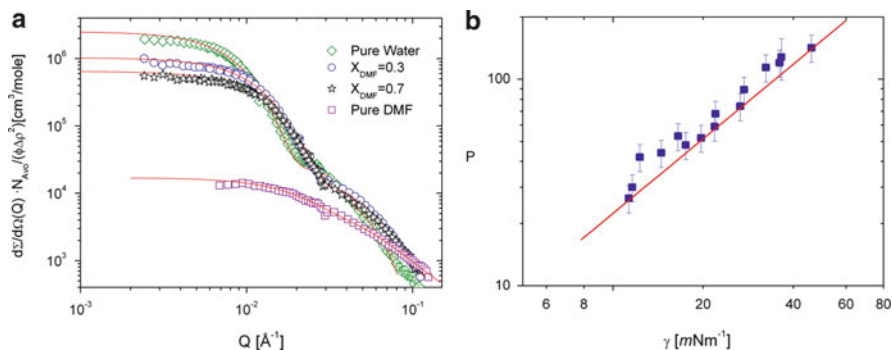
Fig. 19 (**a**) Normalized SANS curves in different D_2O/DMF-d_7 compositions at a polymer volume fraction of 0.25%. *Solid lines* represent fits with a spherical core shell model. Data in pure DMF-d_7 were fitted with a Beaucage form factor. (**b**) Aggregation number P plotted versus interfacial tension, γ. The *solid line* depicts the power-law dependence, $P \approx \gamma^{6/5}$, as predicted by Halperin for star-like micelles [40]. Reprinted with permission from [45]. Copyright (2004) American Chemical Society

scattering curves could be perfectly described using a hyperbolic density profile for the shell, $n(r) \approx r^{-4/3}$, indicative for star-like structures. The aggregation number of these micelles decreases from $P = 120$ in pure water to non-aggregated block copolymer chains in pure DMF. Corresponding interfacial tensions were measured by pendant drop tensiometry using a PEP homopolymer with similar molecular weight characteristics. In pure water, γ assumes a value of 46 mN/m, which decreases to 8.6 mN/m in pure DMF. A correlation of γ with P is shown Fig. 19b. The solid line indicates a power-law dependence of $P \approx \gamma^{6/5}$, revealing an excellent agreement of the data with the scaling prediction of Halperin [40] for star-like micelles.

The structural properties of micelles constituted of PEP1-PEO1 block copolymers were studied in DMF/water solvent mixtures [104]. Starting from cylindrical micelles in pure water, the addition of DMF (lowering of γ) leads to a morphological transition into spherical micelles at about 50% DMF mole fraction. By applying a detailed thermodynamic model, it was shown that both the dependence of the structural parameters with the interfacial tension as well as the morphological transition itself can be quantitatively understood. Interestingly, the cylinder–to–sphere transition, which is irreversible, can be also induced upon heating. This feature allowed the direct comparison of exchange kinetics in both morphologies without changing any other parameter of the system. Details of the kinetics will be discussed later in Section 4.6. Jensen et al. [143, 144] have used ethanol as co-solvent. Similar to the study of Lund et al. [48], they observed transitions from cylindrical to spherical micelles and from larger to smaller spherical micelles with increasing ethanol content.

A summary of the morphological behavior of PEP-PEO micelles is illustrated in Fig. 20a–d.
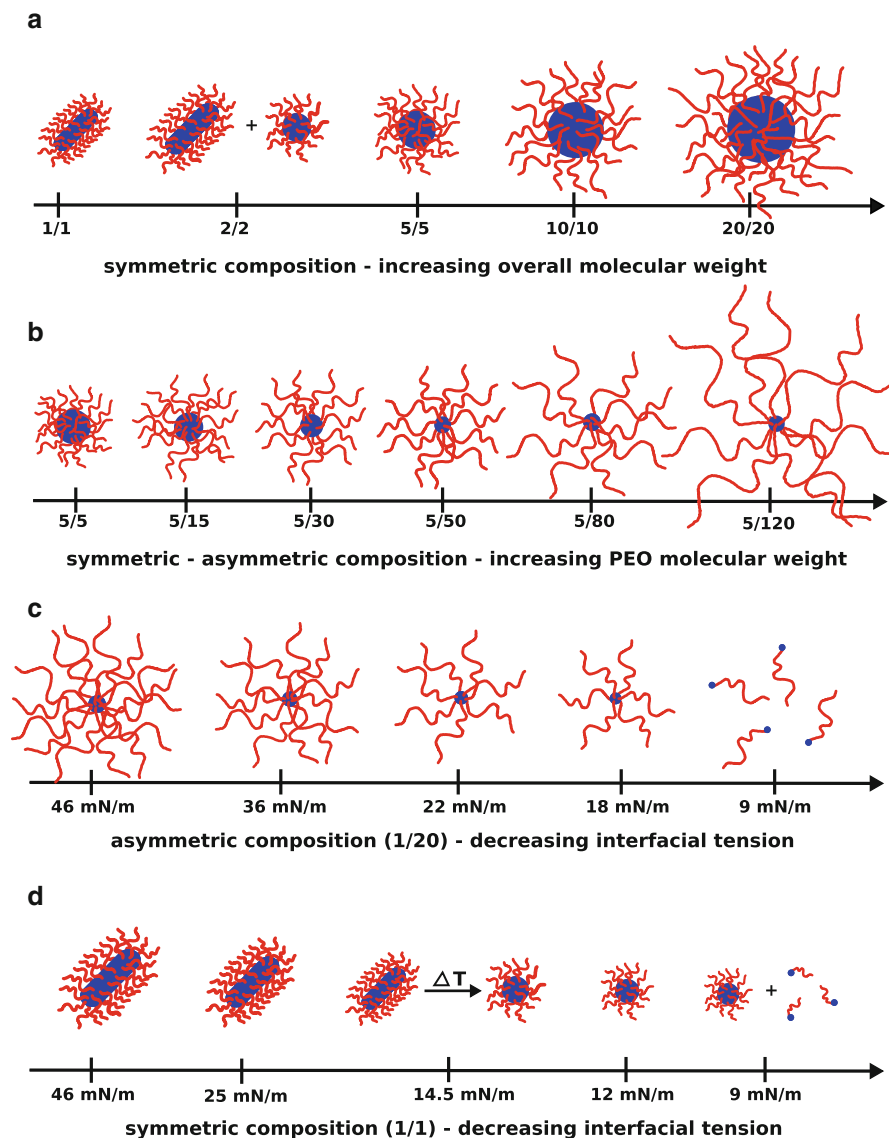
Fig. 20 Illustration of morphological behavior of PEP-PEO micelles in aqueous solution: Transition from (**a**) cylindrical to compact spherical micelles with increasing overall molecular weight at equal composition; (**b**) compact spherical micelles to star-like micelles with increasing PEO and constant PEP molecular weight; (**c**) star-like micelles to non-aggregated chains with decreasing γ by addition of DMF as co-solvent for PEP1-PEO20 block copolymers; (**d**) cylindrical to spherical micelles to coexisting spherical micelles/non-aggregated chains by adding DMF for a PEP1-PEO1 polymer

4.2.2   Equilibrium Kinetics in Pure Water: Frozen Micelles

Time-resolved SANS experiments using the H/D contrast scheme (KZAC) described
in Sect. 3.1.7 were first carried out on a PEP5-PEO15 block copolymer in water for
the determination of the unimer exchange kinetics [100]. However, there was no
decrease in intensity observable even at high temperatures and long time scales,
leading to the conclusion that the micelles are kinetically frozen due to the high
interfacial tension between PEP and water. The kinetics of star-like micelles formed
by a PEP1-PEO20 block copolymer with large compositional asymmetry and a short
core-forming PEP block was investigated by Lund et al. [101, 102]. Analogous to the
PEP5-PEO15 system, the TR-SANS experiment does not reveal any exchange of
polymers over an extended period of time and increased temperature. This becomes
obvious from Fig. 21 where SANS curves from the corresponding kinetic experiment
are shown. Before mixing, typical form factors of star-like micelles were obtained.
For better visibility, the arithmetic mean of the almost identical individual scattering
curves of the labeled micelles are shown. This curve has a shallow maximum at low
Q as a characteristic feature of a structure factor at 1% polymer volume fraction.
After mixing the two differently labeled micellar solutions, the maximum disappears
as a natural consequence of the ZAC condition. Details of the scattering behavior
under ZAC are described in more detail in Sect. 3.2.2. However, the main result of
this experiment is the fact that the intensity after mixing stays constant over an
extended period of time, even at elevated temperatures. From this observation it was
concluded that micelles are effectively frozen since due to chain exchange the
intensity was expected to approach the intensity of the blend sample, depicted as
black squares in Fig. 21. The blend sample consists of a random mixture of
h-PEP1–h-PEO20 and d-PEP1–d-PEO20, providing the smallest contrast identical
to the contrast of the final state of the kinetics after infinitely long time. A similar
observation was made by Won, Davis, and Bates [146], who attempted to observe
mixing kinetics or component exchange kinetics of PB-PEO micelles in water. Their
experiment relied on differences in the SANS profiles of two block copolymers
forming spherical or cylindrical micelles. Within a time period of 8 days, the
scattering profile of a post-mixed specimen did not approach the profile of a premixed
sample but rather resembled a superposition of the two micellar reservoirs. The
structure of the premixed sample was expected to be the final structure in the case
where chain exchange would lead to a reorganization of the micellar morphology. As
this was not observed the authors concluded that the structure of the micelles that
were initially formed upon dissolution were completely locked-in due to the effect of
strong amphiphilicity. In a subsequent study, Jain and Bates [6] examined binary
blends of PB-PEO block copolymers of different molecular weight and composition
forming either spheres, cylinders, or bilayers using cryo-transmission electron
microscopy (cryo-TEM). In agreement with the reorganization study by SANS, the
cryo-TEM showed no perceptible chain exchange between aggregates over a long
period of time, resulting in a non-ergodic state where equilibrium is never reached.
The failure to globally equilibrate is already evident at molecular weights as small as
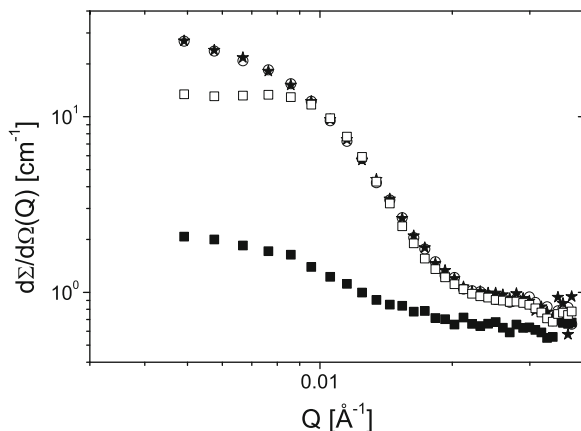
Fig. 21 SANS curves for the determination of chain exchange kinetics for h-PEP1–h-PEO20 and d-PEP1–d-PEO20 micelles in H_2O/D_2O at $\phi = 1\%$: *Open squares*, arithmetic mean of individual scattering curves before mixing; *open circles,* after mixing at $t = 0$; *filled stars*, after 24 h at 70°C; *filled squares*, final state obtained from a blend sample. Reprinted with permission from [102]. Copyright (2006) American Chemical Society

1–2 kg/mol of the core polymer. Hence, from the kinetic studies of both PEP-PEO and PB-PEO systems, it can be generally concluded that chain exchange dynamics in aggregates built from strong amphiphilic block copolymers, i.e., characterized with large interfacial tensions, is very likely to be frozen even at low molecular weights and elevated temperatures.

4.2.3 Tuning of Chain Exchange

As discussed above, chain exchange in micelles built from block copolymers with strong amphiphilicity, e.g., PEP-PEO or PB-PEO, is practically nonexistent. Consequently, such systems can be considered as effectively kinetically frozen. Therefore, in order to study such processes it is of great importance to adjust the rate of chain exchange such that it can be resolved within the time window of a typical scattering experiment. For instance, in a TR-SANS experiment using a stopped-flow apparatus for rapid mixing, the smallest achievable time resolution is about 50 ms. The longest accessible time is generally limited by the allocated beam time at neutron research facilities, which is typically 2–3 days. In order to identify effective tuning parameters we will briefly recall the Halperin and Alexander scaling approach outlined in Sect. 2.2.5. Within this theory, the exchange rate follows a single exponential behavior: $R(t) = \exp(-k_\_t)$ with $k_\_ = (1/\tau_0)\, f(N_A, N_B) \exp(-E_a/k_B T)$ the expulsion rate constant. τ_0 denotes a characteristic diffusion time, k_B the Boltzmann constant, and T the absolute temperature. The activation energy, $E_a \sim \gamma \cdot l^2 \cdot N_B^{2/3}$ depends primarily on the degree of polymerization of core-forming B-block and the interfacial tension, γ, between selective solvent and block B.

We point out that the rate thus depends double exponentially on the interfacial tension, the temperature, and the degree of polymerization of the core block. Hence, these parameters are very effective for tuning the speed of chain exchange. The expression for the expulsion rate constant further contains a pre-exponential factor $f(N_A, N_B)$, which is determined by the micellar structure, i.e., crew-cut or star-like. Tuning by N_A will therefore be less effective because the rate depends only single-exponentially. Importantly, one should be aware that changing one or more of these parameters will also affect the underlying structure of the micelle. Therefore, a study of exchange kinetics requires a complementary structural characterization for each set of parameters.

Several strategies have been used to control the kinetics in polymeric micelles, including variation of temperature, change of the hydrophobic block size, and adjustment of the interfacial tension between core block and solvent [62, 63, 100–103, 114, 119, 120, 146–152]. We will review and discuss the effect of tuning on the kinetics by variation of γ because this parameter has been primarily used to control and to modify the exchange dynamics in micellar aggregates.

The interfacial tension can be effectively varied by modifying the incompatibility between core block and selective solvent. In general, for block copolymers with strong amphiphilicity in water, γ is very large such that even for short chains the micelles are kinetically frozen on experimental time scales. This applies especially for amphiphilic block copolymers with polybutadiene (PB), polyisoprene (PI), polystyrene (PS), poly(ethylene-*alt*-propylene) (PEP), or poly(butylene oxide) (PBO) as the hydrophobic block, having interfacial tensions against water typically larger than 30 mN/m. Several strategies have been employed to reduce γ in order to overcome the high barriers for chain exchange. One approach is the addition of small surfactant molecules. In the work of Jacquin et al. [151], the melting of kinetically frozen poly(butyl acrylate)-*block*-poly(acrylic acid) (PBA-PAA) micelles was investigated. They observed structural transitions from polymeric cylindrical micelles to spherical micelles as well as from large spherical to small spherical micelles upon addition of surfactant. Pendant drop tensiometry on PBA homopolymer in water and in surfactant solution revealed a drop in the interfacial tension from 20 mN/m to 5–8 mN/m. The low value of γ was explained by the incorporation of surfactant molecules into the interface, leading to the transition from frozen polymeric micelles to equilibrated surfactant/block copolymer mixed micelles.

Lejeune et al. [153] employed a chemical approach to lowering of interfacial tension in poly(n-butyl acrylate)-(polyacrylic acid) (PnBA-PAA). PnBA-PAA forms kinetically frozen micelles in water that are not able to reorganize over a month. By statistical incorporation of hydrophilic acrylic acid (AA) units into the hydrophobic PnBA block, P(nBA$_{50\%}$-*stat*-AA$_{50\%}$)-PAA, they could moderate the hydrophobicity of the core block such that unimer exchange was promoted and thermodynamic equilibrium was reached at shorter times.

A more straightforward and facile way to tune the kinetics via reduction of the core–corona interfacial tension is by the addition of co-solvents. In the case of PEP-PEO micelles, the use of DMF/water mixtures as selective solvent for PEO
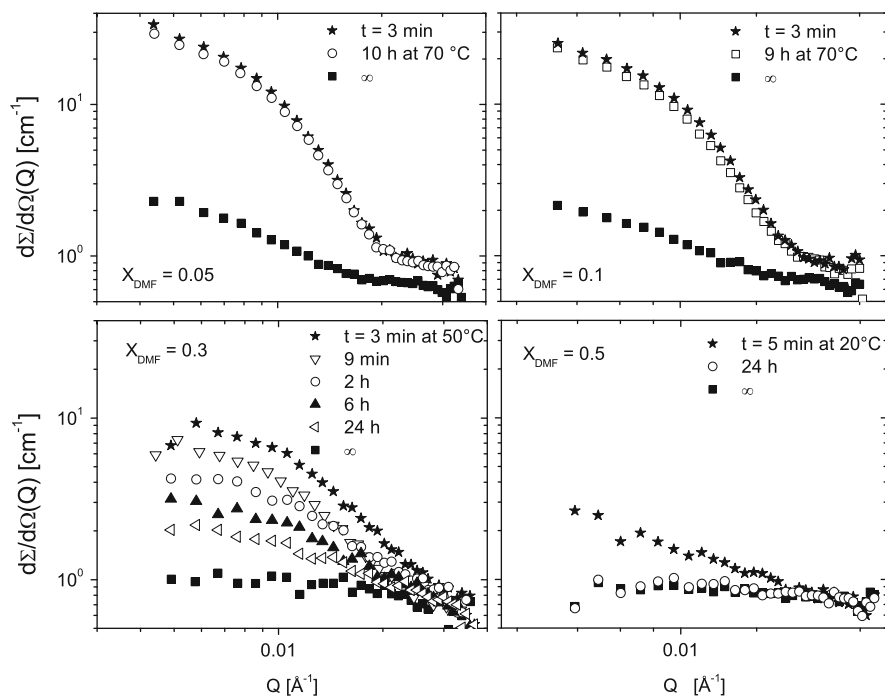
Fig. 22 Effect of the addition of DMF as co-solvent on the speed of chain exchange in aqueous PEP1-PEO20 micelles. Reprinted with permission from [102]. Copyright (2006) American Chemical Society

allows the adjustment of the rate of chain exchange from effectively frozen to accessible time scales of minutes or hours. The kinetics of a PEP5-PEO15 block copolymer was studied using pure DMF as selective solvent [100]. Although at room temperature the kinetics was still too slow, chain exchange became progressively faster at elevated temperatures between 65°C and 80°C. The influence of DMF on the kinetics of PEP1-PEO20 star-like micelles was studied by Lund et al. [102]. Figure 22 compares the time evolution of scattered intensity after mixing deuterated and proteated micelles at different DMF mole fractions in the water/DMF selective solvent mixture. At 5 and 10% DMF the intensity is only insignificantly reduced at 70°C after 9 and 10 h, respectively, revealing only slow kinetics. Upon increasing the DMF content to 30%, the scattered neutron intensity continuously decreases within a moderate time frame indicative of faster kinetics. At 50% DMF, $d\Sigma/d\Omega(Q)$ drops very fast and approaches the final state already after several minutes. For this solvent composition, the exchange dynamics was already too fast to be resolved by the TR-SANS technique. Finally, it turned out that the addition of 25 and 30% DMF, corresponding to a reduction in γ to 21.8 mN/m and 19.8 mN/m, respectively, moderates chain exchange such that the kinetic process could be conveniently followed. We note that mixing of the two micellar solutions was done by hand with a delay time of 1–2 min. A stopped-flow apparatus for rapid mixing in combination

with repetitive real-time data acquisition was not available at neutron research facilities at that time. Application of the stopped-flow mixing technique would most likely also allow resolving kinetics at 50% DMF by TR-SANS.

4.2.4 Equilibrium Kinetics in Water/DMF Mixtures: Logarithmic Relaxation

The relaxation functions, $R(t)$, of the TR-SANS experiments were quantitatively determined as described in Sect. 3.2.2. For the PEP5-PEO15 block copolymer micelles, $R(t)$ could be acceptably fitted by a sum of two exponentials. This was interpreted by the existence of two well-separated processes in time in strict conflict to the single exponential expected from the Halperin and Alexander [60] model. The activation energies of 29 KJ/mol for the slow and 12.2 KJ/mol for the fast process were deduced from Arrhenius plots. By estimation of the activation energy following the concepts of the scaling theory [60], the fast process was assigned to the unimer release. There was, however, no explanation for the existence of the second slow process. Different scenarios for the occurrence of two relaxation processes were discussed, including unimer diffusion between micelles, an isotope effect for the surface tension, the existence of two different species, and aggregation that supports fast exchange and slow rearrangement of the micelles. However, none of them could offer an explanation with a clear physical picture. Thus, the origin of the second slow process remained an open question. Double exponential time decays were also reported from TR-fluorescence measurements on various systems with characteristic rate constants well separated in time [118–120, 122]. This apparent bimodal distribution was either assigned to the presence of bulky labels [118, 122] or to competing chain transfer by micellar collision [120]. It should be pointed out that processes running in parallel, e.g., unimer exchange via micellar collision, just add to a single faster rate that still yields single exponential mixing: $R(t) \approx \exp(-(k_1 + k_2)t)$ and, consequently, cannot a priori be identified by the applied labeling techniques.

In continuation of the kinetic study of PEP5-PEO15 micelles, the relaxation functions of PEP1-PEO20 star-like micelles in water/DMF mixtures with 25 and 30% DMF were determined. Similarly to the PEP5-PEO15/DMF system, slow and heterogeneous kinetics were observed in this case but, in contrast, trial fits using a sum of two exponentials did not produce any satisfactory results. Therefore, it was more reasonable to assume a distribution of relaxation rates to describe the kinetics in PEP1-PEO20/water/DMF systems. Furthermore, as there was no explanation for the existence of two processes and no exclusive fits were performed, it was concluded that in the previous works the double exponential was more an approximation of a continuous distribution of relaxation rates. As a first obvious reason, a chain length distribution (polydispersity) of the core-forming polymer was taken into account since the rate constants exponentially depend on the activation energy, E_a, which in the Halperin and Alexander model is given by $E_a \sim N_B^{2/3} \cdot \gamma \cdot l^2$.

The PEP block was synthesized by living anionic polymerization with a rather small polydispersity (weight average molecular weight/number average molecular weight), $M_w/M_n = 1.06$. Accordingly, the effect of a distribution of chain length on the relaxation rates was taken into account by:

$$R(t) = \int_1^\infty f(N_B, \sigma) \exp(-k_-(N_B)t) \, dN_B \tag{117}$$

where:

$$f(N_B, \sigma) = \frac{(\langle N_B \rangle - 1)^{N_B - 1} \exp(-(\langle N_B \rangle - 1))}{\Gamma(N_B)} \tag{118}$$

denotes the Poisson distribution, with $\Gamma(N_B)$ being the gamma function and k_- the expulsion rate constant. Polymers prepared by living anionic polymerization exhibit a Poisson-type chain length distribution where the width is directly given by the mean value of $\langle N_B \rangle$ by $\sigma = 1 + 1\sqrt{N_B}$. Nevertheless, the agreement with the data was still very poor and, hence, it was concluded that polydispersity alone is not sufficient to explain the broad relaxation pattern. It should, however, be noted that the prefactor α in the expression for the activation barrier [37] was neglected and simply set to 1. Further, in order to describe the data, a Gaussian distribution of activation energies has been used. This more general approach takes into account all factors that independently contribute to the relaxation. Although excellent fits could be obtained, the fitted mean activation energy, the attempt time, and the distribution all assumed unphysical values such that the Gaussian distribution was considered to be inapplicable for a reasonable explanation of the relaxation behavior. Similarly, a stretched exponential, $R(t) = \exp(-kt)^\beta$ has been applied, again with unsatisfactory fits because the parameters were not well defined and β assumes very low values ($\beta \approx 0.1$–0.2) that reflect a very broad distribution. A more close inspection of the relaxation data finally revealed an extremely broad and heterogeneous logarithmical decay over several decades in time $R(t) \approx -\log(t)$ that was independent of concentration and temperature. This is represented in Fig. 23, where $R(t)$ displays an almost straight line on a logarithmic time scale. The logarithmic relaxation a priori implies that no mean rate constant exists. At that point, the appearance of the logarithmic relaxation was interpreted as a consequence of uncharacterized hierarchical processes [154]. A more straightforward explanation for the existence of the broad relaxation was presented by Choi et al. [63], based on the polydispersity model already introduced earlier [101, 102] (Eq. 117). By taking into account prefactors and the temperature dependence of the diffusion coefficient previously ignored, it was argued that the observed hypersensitivity to core chain length was responsible for the logarithmic relaxation. This will be discussed in detail in the subsequent section.

Fig. 23 Ln-log
representation of the
relaxation function $R(t)$
of PEP1-PEO20 star-like
micelles in water/DMF
mixtures with 25% DMF
at different temperatures.
Dashed lines depict fits with
a logarithmic time decay.
Reprinted with permission
from [101]. Copyright (2006)
by the American Physical
Society
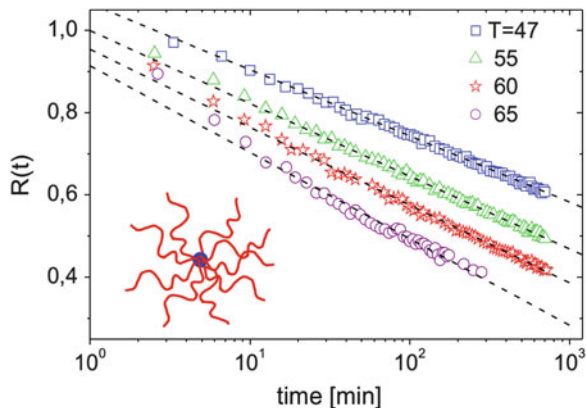
## 4.3 Block Copolymer Micelles in Organic Solvents

In this section, we will focus on the kinetics of micelles built from diblock copolymers
in organic solvents. Typical systems are polystyrene–polybutadiene (PS-PB),
polystyrene–polyisoprene (PS-PI), or polystyrene–poly(ethylene-*alt*-propylene)
(PS-PEP) block copolymers in hydrocarbon solvents like alkanes. Alkanes are poor
solvents for PS and good solvents for the polydienes and PEP, respectively, such that
in all cases PS forms the micellar core. A common feature of these systems is the fact
that the thermodynamic interactions are significantly weaker than in water-based
micelles, reflected by small χ parameters or correspondingly by low interfacial
tensions. Accordingly, such systems are only weakly segregated, which may lead to
micellar cores considerably swollen by the solvent. This has been observed, e.g., by
SANS on PS-PI micelles in *n*-decane [74] and PS-PB micelles [30] in a series of
n-alkanes (C_nH_{2n+2}, where $n = 7,10,12,14,$ or 16) by using contrast variation and
detailed model fitting. For the PS-PI micelles in *n*-decane, the core was swollen with
15–25% solvent, depending on molecular weight. For micelles formed by a symmet-
ric PS-PB block copolymer, the solvent fraction was even higher (35–55%) but
decreased with increasing number of carbon atoms of the *n*-alkane solvent. The
opposite trend was observed for the aggregation number, which increases with
n although the interfacial tension stays constant or even slightly decreases from
5.7 mN/m for *n*-heptane to 4.8 mN/m for *n*-hexadecane. This unexpected behavior
can be understood by applying a modified mean-field model that properly takes into
account solvent entropy effects [30]. The chain exchange kinetics of the PS-PB
system was studied in the different *n*-alkanes by TR-SANS [150, 155]. The study
revealed that the exchange dynamics depend strongly on the choice of solvent. For
instance, in *n*-decane exchange is very fast and outside the time window accessible by
TR-SANS. This was still the case after lowering the temperature to 10°C. If the
carbon length of the solvent is increased, the exchange dynamics decrease and is
slowest for *n*-hexadecane where the time scale is optimal for TR-SANS
measurements. It should be noted that the activation barrier, E_a, for unimer release

does not significantly change with the solvent size because γ stays almost constant. Therefore, in order to explain the effect of solvent chain length, it was considered that PS in the bulk state has a glass transition temperature (T_g) of 105°C but when swollen with n-alkanes, T_g is significantly reduced. The swelling ability and solvent quality, however, depend drastically on the number of carbons, n, of the n-alkyl solvent, which in turn also changes T_g. For example, for a bulk PS containing 18 vol% n-heptane, the glass transition is reduced from 105°C to -11°C whereas with 15 vol% n-octane T_g is only lowered to 40°C [156]. Quintana et al. [157, 158] have studied the micellization behavior of PS-PEP polymers in n-alkanes. They reported that the dependence of micellar properties on the temperature is decreased for longer n-alkanes. This was explained by a higher T_g of the PS core that is swollen to a lesser extent as n increases. This trend was further confirmed by structural studies of PS-PEP micelles in squalane by Choi et al. [159]. Squalane is a natural hydrocarbon with the molecular formula $C_{30}H_{62}$. Dynamic light scattering and SAXS experiments showed that below 100°C micellar cores are practically unswollen. Clear penetration of solvent into the PS core was observed only above 100°C close to the bulk T_g of PS. Nevertheless, the glass transition of PS-rich domains of PS-PI polymers in squalane was found to be considerably reduced as measured by Lai et al. [160]. They found that, depending on the PS weight fraction in solution, T_g is reduced to 70°C. Based on these findings it is reasonable to assume that the measured decrease in the exchange dynamics of PS-PB polymers in n-alkanes is directly related to the increase in T_g of the PS core.

In order to be independent of any feature related to the glass transition, the kinetics of PS-PB micelles formed in DMF were additionally studied by Lund et al. [101]. DMF is selective for PS such that the micelles consist of a melt-like PB core with a T_g of -95°C and a swollen PS corona. Structural studies by SANS have shown that the PB core is solvent-free and the corona has a compact structure with a constant polymer density distribution [155]. Hence, in DMF these micelles are inverted analogues to those in n-alkanes but with unswollen cores. Exchange kinetics could be conveniently measured by TR-SANS in a time range of 10 h until an almost statistical distribution of proteated and deuterated block copolymers across the micelles was reached. A thorough evaluation of the relaxation kinetics of the symmetric PS-PB block copolymer micelles in n-hexadecane and in DMF shows in agreement with the exchange kinetics in PEP-PEO micelles in water/DMF, i.e., a logarithmic time dependence indicating an extremely broad distribution of relaxation rates (Figs. 23 and 24).

Because this observation was obtained independently from three structurally different types of micelles, it was concluded that the broad relaxation is an inherent property of block copolymer micelles. Consistent with these findings is the almost linear dependence of $R(t)$ on a log-time scale of PS-PEP micelles in squalane presented by Choi et al. [63]. They used TR-SANS to study two pairs of PS-PEP micelles, d-PS–h-PEP-1/h-PS–h-PEP-1 and d-PS–h-PEP-2/h-PS–h-PEP-2 with different PS degrees of polymerization: pair 1, $N_{PS} \approx 255$ and pair 2, $N_{PS} \approx 412$. Each specimen was measured at three different temperatures. Individual master curves for $R(t)$ were obtained by time–temperature superposition principles. A comparison of $R(t)$ of the two PS-PEP samples was done at a reference temperature of 125°C and

Fig. 24 Logarithmic chain exchange kinetics of PS-PB block copolymer micelles (*top*) in DMF at 20°C (*stars*) and of inverted micelles (*bottom*) with swollen PS cores in *n*-hexadecane at 20°C (*circles*) and 30°C (*triangles*). *Lines* depict fits with a logarithmic time decay. Reprinted with permission from [101]. Copyright (2006) by the American Physical Society
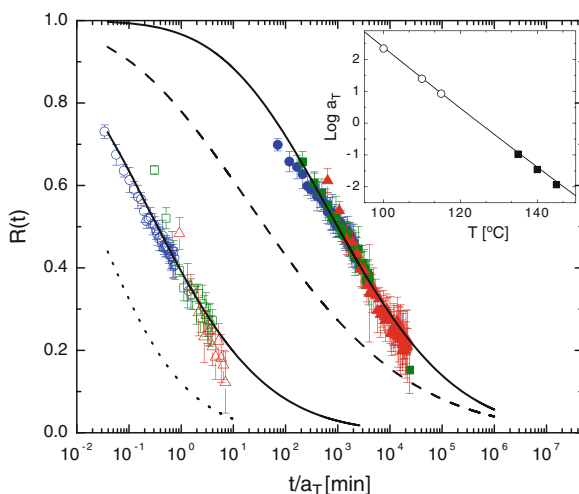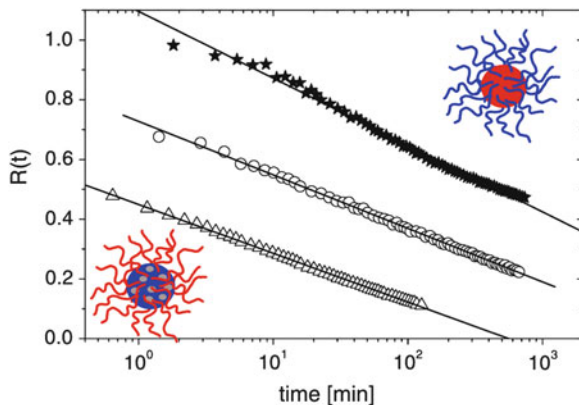
Fig. 25 Comparison of the master curves in dilute solution of PS-PEP-1 (*open symbols*: *blue* $T = 100°C$; *green* $T = 110°C$; *red* $T = 115°C$); and PS-PEP-2 (*filled symbols*: *blue* $T = 135°C$; *green* $T = 140°C$; *red* $T = 145°C$) in squalane at $T_{ref} = 125°C$. The shift factors a_T used for generating the master curves are shown in the *inset*. *Solid lines* are fits of the theoretical model of Choi et al. [63, 152]. The dashed and dotted lines represent calculations with varying $\alpha\chi$ in order to demonstrate the high sensitivity of the fit to this parameter. Reprinted with permission from [63]. Copyright (2010) by the American Physical Society

demonstrated an extremely strong dependence on N_{PS} by approximately four orders of magnitude in time (Fig. 25).

In order to describe the data, Choi, Lodge, and Bates [63] based their model on theories of diffusion in block copolymer melts [161]. In their approach, the activation energy is written as:

$$E_a = \alpha\chi \cdot N_B \tag{119}$$

where α again is a free prefactor and χ the Flory–Huggins interaction parameter, χN denotes enthalpically unfavorable contacts between solvent and hydrophobic block segments. We note that the scaling is equivalent to that presented for E_a in Eq. 37 with $\beta = 1$.

Setting the time scale for the escape rate constant, Choi and colleagues used the longest Rouse time to replace the pre-exponential factor in Eq. 37[7]:

$$\tau_0 = \tau_R = \xi N_B^2 l_B^2 / (6\pi^2 k_B T) \tag{120}$$

with ξ being the monomeric friction for PS. The use of Rouse relaxation was justified by the fact that the short PS blocks are only weakly entangled. Motivated by the observed dramatic dependence on N_{PS} the authors anticipated that the distribution of core chain length must play an important role in the exchange dynamics. Hence, they modified the kinetics by using a Schulz–Zimm distribution for the core chain length:

$$f(N_B, \zeta) = \frac{\zeta^{\zeta+1}}{\Gamma(\zeta + 1)} \cdot \frac{N^{\zeta-1}}{\langle N_B \rangle^\zeta} \cdot \exp(-\zeta \cdot N_B / \langle N_B \rangle) \tag{121}$$

Here $\zeta = 1/(N_w/N_n - 1)$, where N_w/N_n defines the polydispersity of the PS polymer. We note that the Schulz–Zimm distribution is a two parameter function where the width and the mean value can be adjusted independently. The use of the one-parameter Poisson distribution requires that the polymerization process occurs under ideal conditions, which in practical situations is not always guaranteed. By fitting with the above-described model, Choi et al. obtained an excellent agreement with the kinetic data using $\alpha\chi$ and N_w/N_n as free parameters. Optimal fitting was obtained for narrow polydispersities in close agreement with values received from standard polymer characterization. Variation of this fit parameter results in significant changes in the structure of $R(t)$, while on the other hand small changes in $\alpha\chi$ lead to a strong shift of $R(t)$ along the time axis, as demonstrated by the dashed and dotted lines in Fig. 25. By using two block copolymers with different core block molecular weights, the authors could finally uncover the hypersensitivity of chain length on the kinetics that, consequently, leads to the pronounced effect of polydispersity. In light of these results, Lund and coworkers [62] re-evaluated their data by considering the prefactor α as a free parameter. Moreover, to account for the temperature dependence, an attempt time $\tau = \tau_0 \cdot \xi(T) / \left(\xi(47) \cdot \left(\frac{N}{\langle N \rangle} \right)^{2/25} \right)$, with $\langle N \rangle$ being the mean number of repeat units, that scales with the friction coefficient $\xi(T)$ of PEP for a homopolymer melt was considered. Thus, a perfect reproduction of the logarithmic time decay was possible. However, a fit of β revealed $\beta = 2/3$, indicating a fully

---

[7] In the original work by Halperin and Alexander (c.f. Eq. 33), τ is a function of N_B and N_A, i.e., $\tau = \tau_0 \cdot g(N_A, N_B)$, also taking into account the diffusion of the chain within the corona. Here, this is replaced by the Rouse time.

collapsed insoluble block during the expulsion process. The parameter $\alpha(36\pi)$ was fitted to be approximately equal to 3.3 instead of 4.8, as expected for spherical globules. This disagreement was thought to be due to deviations from the spherical conformation or to interfacial effects resulting from modifications of the surface energy by the other block. The best value for τ_0 was fitted to 2.4×10^{-7} s, which is comparable to a typical elemental time expected for polymer dynamics. In summary, the work of Choi et al. and, subsequently, the novel interpretation of the data of Lund et al. strongly corroborate that the pseudo-logarithmic time decay in the equilibrium kinetics is a consequence of core block polydispersity, which can be rationalized by a double exponential dependence of the exchange rate on chain length. In principle, both experiments essentially confirm the validity of the theory of Halperin and Alexander. However, there remain several contradictions concerning the exact mechanism, in particular the adopted chain conformation during the activated step of the exchange process. This still needs to be delineated in future experiments. These details of the mechanism can be more conveniently studied using a monodisperse system. Such a system will be discussed in the next section.

4.4 n-*Alkyl-PEO Polymeric Micelles*

The chain exchange kinetics of n-alkyl-PEO (C_nH_{2n-1}, where $n = 18$, 24, or 30) polymeric micelles in water was studied by Zinn et al. [103]. Structurally, the n-alkyl-PEO polymers can be considered as hybrids between amphiphilic block polymers (e.g., PEP-PEO or PEE-PEO) and nonionic $C_n(EO)_m$ surfactants. With respect to the exchange kinetics, these materials were taken as model system because the polydisperse hydrocarbon block is replaced by a relatively short but truly monodisperse ($M_w/M_n = 1$)) aliphatic chain. Accordingly, if the above considerations were true, the relaxation kinetics was expected to follow a single exponential decay. Moreover, variation of n should directly reflect the dependence on chain length and thus the effect of polydispersity on the time decay of $R(t)$. In fact, the kinetic measurements reveal a strong dependence on the alkyl chain length, as depicted in Fig. 26, where the neutron detector count rates are plotted versus time after mixing the two differently labeled (H/D) micellar species at room temperature (22°C). The figure shows that within five orders of magnitude in time up to 1,000 s, the count rate of the $C_{30}H_{61}$-PE05 micelles (squares in Fig. 26) stays constant revealing no chain exchange. For the $C_{18}H_{37}$-PEO5 micelles (triangles Fig. 26) on the other hand, full equilibration (depicted by the solid line in Fig. 26) was already obtained after a few milliseconds. Apparently, the relaxation process is too fast to be resolved by TR-SANS. Only for the $C_{24}H_{49}$-PEO5 system (circles Fig. 26) could the full process of chain exchange be measured, indicated by the continuous decay of the count rate from initial to final state in a time frame of 100 s. Figure 27 shows the corresponding relaxation function on a logarithmic time scale. The linear decay in this representation perfectly revealed the theoretically expected single exponential decay: $R(t) = \exp(-t/\tau_0)$ with a characteristic time $\tau_0 = 44$ s. It should be mentioned that evaluation of the data using either the model-dependent, f_{exc}, or model-independent method, $R(t)$, (for details see Sect. 3.2.2)

Fig. 26 Detector count rates as a function of time after mixing oppositely labeled *n*-alkyl-PEO5 polymeric micelles: *squares n = 30; dots n = 24; triangles n = 18; solid line* final state. [103]. Reproduced by permission of The Royal Society of Chemistry
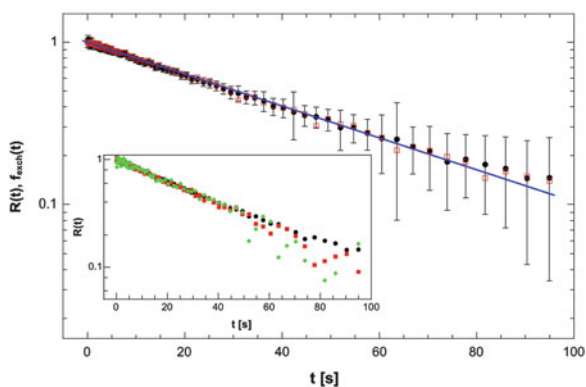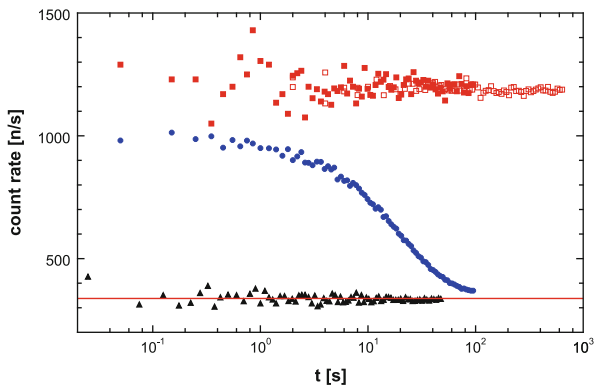
Fig. 27 Relaxation function $R(t)$ (*filled circles*) and $f_{exch}(t)$ (*open squares*) of $C_{24}H_{49}PEO5$ in a log-ln plot at room temperature. The *line* represents the single exponential fit for $R(t)$. *Inset*: Concentration dependence of $R(t)$ at 0.25% (*diamonds*), 0.5% (*squares*), and 1% (*circles*) polymer volume fraction. [103]. Reproduced by permission of The Royal Society of Chemistry

gave the same results, most likely due to the chosen small Q-range, where form factor differences of the two differently labeled polymers do not play a role. The inset of Fig. 27 shows relaxation curves measured at different polymer volume fractions of $\phi = 0.25\%$, 0.5%, and 1%. By normalization with ϕ, all curves fall on top of each other indicating single unimer exchange as the dominating mechanism. Fusion and fission as competing processes for chain exchange would lead to accelerated kinetics because the probability of micellar collisions is increased with concentration. A single exponential decay was also observed by dissipative particle dynamics simulation but, in addition to single unimer exchange, contributions from small aggregate fragmentation/merging and unequal size fusion/fission were found as additional kinetic mechanisms; however, all exhibit very similar relaxation times [162].

The observed strong dependence of the exchange rate on the *n*-alkyl chain length together with the single exponential relaxation found for the $C_{24}H_{49}$-PEO5 system supports the assumption of Choi et al. [63] that core block polydispersity leads to the
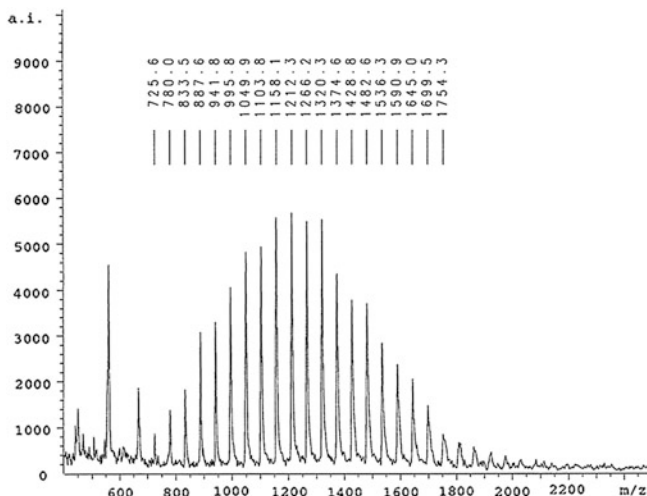
Fig. 28 MALDI-TOF measurement of a 1,4-PB with $M_n = 1.305$ kg/mol and $M_w/M_n = 1.05$

pseudo-logarithmic relaxation in polymeric micelles. This applies also for polymers with small polydispersities (M_w/M_n smaller than 1.1), usually obtained by living polymerization techniques. The actual distribution of chain length is demonstrated in Fig. 28, which shows the result of a MALDI-TOF measurement of a polybutadiene with $M_n = 1.305$ kg/mol and $M_w/M_n = 1.05$, similar to the molecular weight characteristics of PEP1 used as hydrophobic block in the kinetic study of the PEP1-PEO20 water/DMF system. In the MALDI spectrum, the individual chains with different mass constituting the PB polymer are resolved. If one considers that each of these chains has its own activation energy, the measured broad relaxation pattern becomes obvious. It further leads to the conclusion that many block copolymer micellar systems can only partially equilibrate since long chains with high activation energies will not exchange on finite time scales. Therefore, the strict distinction between dynamic polymeric micelles versus frozen nanoparticles, as recently suggested by Nicolai et al. [163], cannot be made a priori. This presumes on the one hand that the exchange rate is either very fast, such that even the long chains will equilibrate, or on the other hand is very slow so that short chains are also frozen on experimental time scale. However, in order to be certain, a kinetic study for each individual block copolymer solvent system is required.

4.5 Chain Exchange in Soft Solids: Effect of Concentration

Kinetic experiments reviewed so far were all made in dilute solution at less than 2% polymer volume fraction. In this concentration range the measured relaxation curves were found to be independent of concentration, revealing single unimer

exchange as the dominant mechanism for chain exchange in agreement with the theoretical picture of Halperin and Alexander. Exchange due to other mechanisms, e.g., fusion/fission or fragmentation/defragmentation, if at all existent can play only a minor role because they would show a clear concentration dependence.

Recently, Choi et al. [152] measured the molecular exchange in ordered diblock copolymer micelles, employing the same PS-PEP micelles in squalane as already studied before in dilute solution by TR-SANS. At 15% polymer volume fraction, the spherical micelles are packed on body centered cubic (bcc) lattices. Individual micellar solution with 15 vol% of h-PS-PEP or d-PS-PEP were annealed far above T_g, resulting in soft solids after cooling to room temperature. Blending of the soft solids on a nanoscale level with a complete statistical arrangement of micelles was achieved by a special cup-rotor mixer device [94]. The efficiency of this technique was demonstrated by a combination of SANS and SAXS measurements. While the SAXS data confirmed the bcc structure of the mixture, the SANS data showed the single micellar form factor since intraparticle contributions were canceled out due to the applied ZAC. Notable was the observation that in comparison to dilute solution, individual micelles had increased aggregation numbers and core radii. This was attributed to the system's tendency to avoid energetically unfavorable corona overlap by reducing the number density of micelles, as discussed in the mean-field model of Grason [164]. The kinetic studies were carried out at different temperatures above the glass transition of PS in an isotopic mixtures of squalane ($T_g \approx 70°C$). In order to account for the temperature dependence, individual master curves were derived by the principle of time–temperature superposition. A comparison of the master curves at dilute solution and at 15% polymer volume fraction are shown in Fig. 29 at a reference temperature $T_{ref} = 110°C$ for PS-PEP-1 and $T_{ref} = 145°C$ for PS-PEP-2. We note that time-temperature superposition for the higher concentrations does not work as well as for the dilute solutions. The data do not exactly superimpose by using the shift factors, a_T, shown in the inset of Fig. 29. Nevertheless, the obtained curves show the typical logarithmic time decay consistent with the finding at dilute solution. The relaxation curves obtained for the soft solids are, however, shifted to longer times by more than one order of magnitude. Because of the logarithmic form of $R(t)$, the molecular exchange kinetics could be described by the same theoretical model as already used for the dilute solutions (see Eqs. 119, 120, and 121). Reasonable fits were obtained by increasing the activation barrier through an increase in the parameter $\alpha\chi$ and by slightly adjusting the polydispersity of the core block.

The authors postulated several reasons for the slowing down of the exchange rate at higher concentrations. These include weaker mobility arising from a higher glass transition of the core polymer. A higher T_g was assumed because the tendency of solvent to penetrate the core is reduced at higher block copolymer concentration. However, this effect was considered to be too small to account for the dramatic change observed for the chain exchange dynamics. It was also suggested that increased core chain stretching arising from increased micellar sizes in the bcc state could lead to altered Rouse dynamics. It was, however, estimated that core block stretching cannot be so significant in the low entanglement regime to reasonably explain the slowdown of the kinetics. As the most probable explanation,
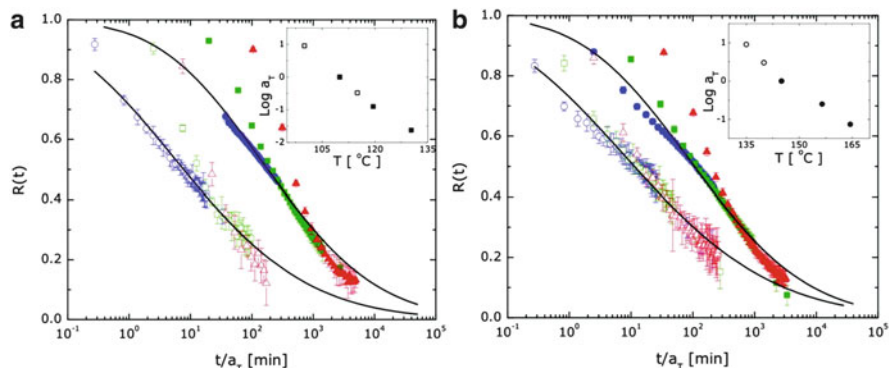
Fig. 29 Comparison of the relaxation curves at dilute solution (*open symbols*, already shown in Fig. 25) and of soft solids at 15% polymer volume fraction (*filled symbols*) in squalane for (**a**) PS-PEP-1 at $T_{ref} = 110°C$ [originally measured at 110°C (*filled circles*), 119.5°C (*filled squares*) and 130.3°C (*filled triangles*); and (**b**) PS-PEP-2 for $T_{ref} = 145°C$ [originally measured at 144.5°C (*filled squares*), 156.5°C (*filled circles*), and 165.5°C (*filled triangles*)]. The shift factors a_T used for generating master curves are shown in the *inset*. *Solid lines* are fits of the theoretical model of Choi et al. [63, 152]. Reprinted with permission from [152]. Copyright (2011) American Chemical Society

the authors proposed that the deceleration in chain exchange might arise from considerable corona overlap of neighboring micelles at higher concentration. Crowding of corona polymer should generate an additional contribution to the activation barrier because a single polymer would be more easily soluble in dilute solution than in semidilute solution.

Based on this experimental observation, Halperin extended the original scaling model to higher concentrations by introducing an additional penalty term that takes into account an increase in the osmotic pressure due to coronal screening. This was outlined in Sect. 2.2.7. Halperin further suggested that for a systematic investigation, coronal screening can also be obtained by the addition of soluble corona homopolymer while keeping a dilute solution of micelles. This would facilitate the interpretation because other possible mechanisms like fusion and fission, which are expected from computer simulation and theory, occur at higher concentrations and need not to be discussed.

4.6 Cylinders Versus Spheres: Effect of Morphology

The influence of micellar morphology on the exchange kinetics in diblock copolymer micelles has been investigated by Lund et al. [104]. The studied system was a short chain PEP1-PEO1 copolymer with symmetric block composition in water/DMF mixtures as selective solvents for PEO. The morphological behavior of this system has already been described. The main features are illustrated in Fig. 20d.

It can be seen that cylinders are formed in water and in water/DMF mixtures with low DMF fractions, i.e., high interfacial tensions, whereas spherical micelles occur above ~50 mol % DMF at low interfacial tensions. TR-SANS experiments were performed at different DMF/water compositions for both cylindrical and spherical geometries at 41%, 47%, 60%, and 75% DMF mole fraction. As already observed for PEP1-PEO20 micelles [102], chain exchange became increasingly faster with growing DMF content due to lower interfacial tensions (see Fig. 22). In order to access the initial part of the relaxation, a stopped-flow apparatus for rapid mixing was used. Technical details of the stopped flow method are given in Sect. 3.2.1. However, with 75% DMF in the selective solvent mixture, chain exchange was already too fast to be resolved even with the stopped-flow fast mixing technique. The relaxation curves obtained for the other solvent compositions showed an extended decay over several orders of magnitude in time, which for intermediate and long time scales was again quasi-logarithmic. Accordingly, the data were analyzed using Eq. 117 by taking into account the polydispersity of the PEP block by a Schulz–Zimm distribution (Eq. 121). In accord with the model of Choi, Bates, and Lodge [63], the longest Rouse time was used as pre-exponential factor as defined in Eq. 120. Independent of the morphology, good fits were only obtained by taking $\beta = 1$ implying a stretched conformation of the insoluble block during the expulsion process (see Sect. 2.2.6.).

The parameter α assumed values that were about a factor of three smaller than expected from the geometrical estimate. Parallel to the transition from cylinders to spheres, α slightly decreases. However, this does not clearly reflect any influence of the morphology because the fits are very sensitive to α and other influences (e.g., arising from experimental uncertainties) cannot be fully excluded. Therefore, in order to delineate any factors arising from the different morphologies, Lund et al. have exploited the fact that at 50% DMF fraction the transition can be also induced by heating. Dissolution of the polymer at room temperature leads first to stable cylindrical micelles, which transform into spherical entities after annealing for several hours at 70°C. Importantly, the transition is irreversible, meaning that the spherical shape is preserved at low temperatures. The exchange kinetics was then measured in both morphologies on the same specimen by TR-SANS under exactly the same conditions. The authors found that the kinetics in spherical morphology is slightly but unambiguously faster than for cylinders, as shown in Fig. 30. With respect to the fit parameters, the faster kinetics is reflected by a slightly smaller α while $\beta = 1$ was kept constant. This was found to be in accordance with the slightly more pronounced decrease in α for varying DMF composition. The value of $\beta = 1$ was in contrast to $\beta = 2/3$ found for PEP1-PEO20 star-like micelles in which the PEP1 chain assumes a completely segregated spherical bud. It was argued that a stretched conformation facilitates passage through the more dense corona of the spherical and cylindrical crew-cut type micelles obtained from PEP1-PEO1 block copolymers. An interpretation of the small differences in α is, however, difficult. It was speculated that this has its origin in small variances in the local coronal structure, which may be different for the cylindrical and spherical morphologies.

Fig. 30 Comparison of
exchange kinetics in spherical
and cylindrical morphology
of PEP1-PEO1 block
copolymers in water/DMF
mixture before and after the
thermally induced transition.
Solid lines represent model
fits as described in the text.
Reprinted with permission
from [48]. Copyright (2011)
American Chemical Society
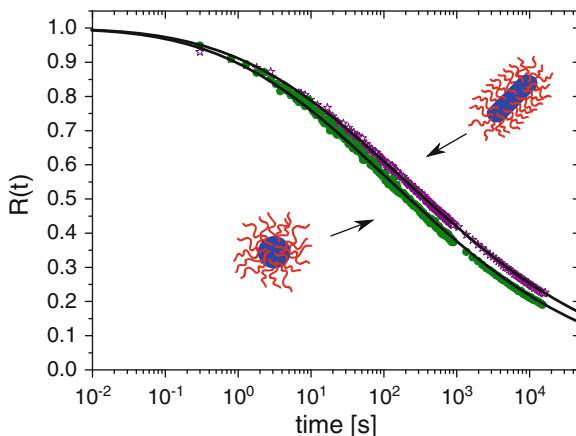
4.7 Summary

In general, the experimental results obtained by the TR-SANS technique strongly
indicate that the component exchange kinetics of all the micellar systems investigated
occurs solely via the Aniansson and Wall mechanism, i.e., the insertion/expulsion of
only single chains at a given time even for elevated concentrations. The involved
activation energy for chain expulsion scales with the core block degree of polymeri-
zation and the interfacial tension: $E_A \sim \alpha\gamma N_B^\beta$, thus determining the relaxation rate
double exponentially. The observed strong dependence on the core block degree of
polymerization finally allowed explanation of the logarithmic time decay by the finite
polydispersity of the insoluble block, even for chains with a narrow chain length
distribution. Thus, from theoretical and experimental points of view one can conclude
that the equilibrium kinetics in block copolymer micelles in dilute solution is
essentially understood. Solely the value of the exponent β and of the numerical
prefactor α remain unclear. For $\beta = 2/3$, the activation energy is determined by the
interfacial tension arising from surface contacts between the fully collapsed insoluble
block and the solvent in the corona of the micelle. For $\beta = 1$, the expelled insoluble
block is still swollen with solvent and E_a is determined by monomer–solvent contacts
via the Flory–Huggins interaction parameter, χN. A visualization of the two discussed
possibilities for chain expulsion is shown in Fig. 31.

Deviations of the parameter α from the theoretical value may be due to small
variations in local structural properties of the "activated complex" during the expul-
sion process. Here, factors like screening of solvent/core polymer contacts by the
corona block and ill-defined core–corona interfaces might come into play. However,
discrepancies could also arise from small uncertainties in the determination of
polymer characteristics. However, these discrepancies are obviously system-specific
and depend on selective solvent, type of block polymer, temperature, and degree of
polymerization and are thus of minor relevance for the general understanding of
equilibrium kinetics. From the experimental point of view, a more systematic study
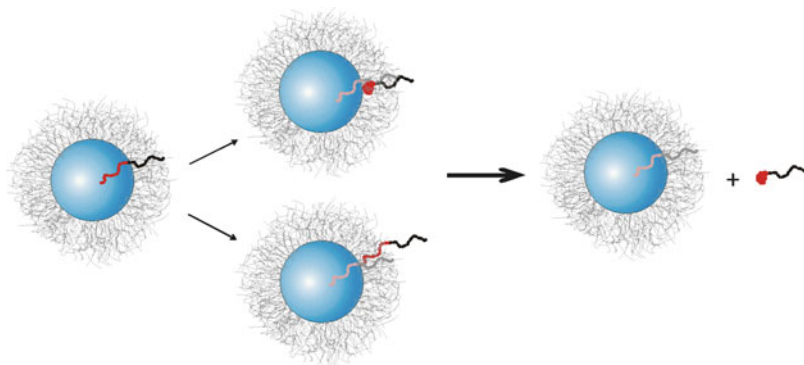
Fig. 31 Scheme for two possible scenarios for chain expulsion determining the activation energy: core chain forms a bud in the corona (*top*) or adopts a linear conformation (*bottom*) leading to an exponent $\beta = 2/3$ or 1, respectively. Reprinted with permission from [104]. Copyright (2011) American Chemical Society

of the concentration dependence is desirable in order to scrutinize in more detail the slowing down of chain exchange observed in ordered diblock copolymer micelles. Moreover, the diffusion process through the corona should be investigated. Thus, variation of the corona chain length needs still to be explored although this might only be a minor factor and perhaps mostly relevant for star-like micelles. Motivation for such a study can be found in recent computer simulation results [162], where a quicker exchange rate was found by increasing the corona block length, which is in conflict with the slower rate predicted by theory. The double exponential dependence of γ and N could effectively be used to tailor micellar properties for applications such as the production of frozen nanoparticles, for tuning rheological properties of transient networks built from telechelic polymers, or the control of release from micellar cores for biomedical purposes.

5 Non-equilibrium Kinetics in Block Copolymer Micelles

5.1 Formation and Micellization Kinetics

Non-equilibrium kinetic processes typically involve monitoring a change in micellar structure or morphology over time, or following the formation of micelles from a molecular solution (unimers), i.e., micellization kinetics. Thus, in contrast to equilibrium processes a perturbation is required. Typically this is achieved by abruptly altering the thermodynamic conditions, which can be achieved either via extensive parameters like temperature and pressure, or by changing intensive parameters such as salt concentration or pH.

Classically, studies of micellization kinetics involve monitoring the time-resolved response of micelles using either fluorescence spectroscopy or light scattering methods. SAX/SANS techniques have not been used very extensively so far but are becoming increasingly popular because the technical feasibility has increased significantly over the last few years due to more advanced instrumentation and more powerful sources. The main limitation of light scattering and fluorescence spectroscopy methods is the lack of relevant structural resolution. Consequently, the structural evolution of micellar systems, whose typical sizes are of the order of 1–50 nm, cannot be followed during the course of the kinetic process. An exception is large particles of the order of several hundreds of nanometers, which thus enter into the window of light scattering. Consequently, most studies discuss relaxation times, which cannot be straightforwardly related to specific kinetic processes.

As mentioned in the Introduction, there is some unclear terminology related to kinetics of micelles: often the terms "micelle dynamics" or "micelle kinetics" are used interchangeably for equilibrium kinetics (exchange kinetics), relaxation kinetics (micelle–micelle relaxation kinetics) and micellization kinetics (unimer–micelle transition). We will focus on results related to micellization kinetics of block copolymers starting from unimers, although in some cases we will also mention results more related to re-equilibration kinetics. The term "dynamics" will be associated with molecular level diffusion, rotations or elemental rotations/vibration, etc. and will be left out of this review.

5.1.1 Temperature-Jump Experiments

As in experiments related to equilibrium or near-equilibrium kinetics, micellar growth can be induced using larger amplitude T-jumps, thereby perturbing the system from a unimer to micellar state. This requires temperature-sensitive polymers that undergo micellization upon heating or cooling. A particularly well-studied block copolymer system is poly(ethylene oxide)–poly(propylene-oxide)–poly(ethylene oxide) (PEO-PPO-PEO; Pluronics) triblock copolymer in aqueous dispersions. PPO exhibits a LCST and is generally not water soluble at ambient temperature. PEO-PPO-PEO undergoes a unimer–micelle transition in a range of approximately 10–35°C, depending on molecular weight, composition, and concentration [165]. The transition temperature is referred to as the critical micellization temperature (cmt), which is equivalent to the cmc at constant temperature.

The first applications of the T-jump method to study kinetics related to micelles is due to Kreschek et al. [166] and Eyring and coworkers [167, 168] in the late 1960s to early 1970s. The rate of dissociation of various ionic surfactants was measured by suddenly increasing the temperature using electrical resistance heating and capacitor discharge following the change in time using scattered light. While the experiments showed qualitatively that the kinetics occurred on a typical millisecond timescale, not much more information could be obtained due to a lack of angular resolution. Block copolymer systems are generally more robust towards environmental changes than surfactants. Consequently, polymer systems where at

least one block is thermosensitive are used and micellization is induced by crossing the cmt via a sudden temperature jump or quench. A disadvantage is, however, that systems are usually in the proximity of the microphase boundary and thus typically not well segregated, complicating comparisons with theories that often assume strong segregation.

Honda et al. [169, 170] employed a thermosensitive poly(α-methylstyrene)–poly (vinyl phenethyl alcohol) (PαMS-PVPA) block copolymer system with two molecular weights that micellize in benzyl alcohol below 24°C and 50°C, respectively. In the experiments, the system was completely dissolved into unimers at 60°C and subsequently abruptly quenched to various temperatures in the micellar region of the phase diagram using a pre-thermostated sample and measuring cells. Subsequently, the system was monitored in real time using simultaneously time-resolved static and dynamic light scattering. By investigating two molecular weights and various temperatures, a thorough and systematic investigation of the system was made. Interestingly, the micellization process was found to be very slow and occurred on a time scale of hours. For the lowest molecular weight (8.1 kg/mol), a single exponential growth was found whereas for the higher molecular weight block copolymer (12.5 kg/mol) the kinetics was slower and could be fitted with a double exponential decay. This behavior was interpreted in terms of nucleation and growth type kinetics and a clear distinction was made with respect to the Aniansson and Wall-type kinetics that predicts a double exponential behavior close to equilibrium. By comparing the information obtained from both dynamic and static light scattering, it was observed that the radius of gyration and the hydrodynamic radius increase more rapidly in the beginning compared to the molecular mass. The polydispersity, obtained using a cumulant expansion, appeared to decrease towards the end of the micellization process. The micellization process was therefore pictured as having a rapid initial process that bears some similarity to a nucleation and growth process and is characterized by an increase in the number of micelles. The time constant of the first process was observed to decrease with increasing concentration. This process is followed by a slower reorganization process, independent of concentration, reflecting an equilibration mechanism where the number of micelles decreases but the micelles increase in overall size.

Small Temperature-Jump Studies of Pluronics

Hecht and Hoffman [126] investigated the kinetics of Pluronics micelles using a capacitor discharge in the micellar solution containing electrolytes to increase the conductivity and amplify the temperature jumps. Using this method, T-jumps ranging from 0.05 to 2.4 K were obtained. The micellization was followed using light scattering at a fixed angle of 90°. T-jumps were performed both below and above cmt at different concentrations without any clear distinction between the nature of the kinetic process. In other words premicellization, micellization and micelle–micelle equilibration kinetics were investigated, leaving a theoretical comparison difficult. This study thus indicates the existence of "pre-critical" micelles. Interestingly, the

Fig. 32 Time-dependent
fluorescence intensity of a
hydrophilic fluorescent probe
(ANS) in a Pluronics aqueous
solution under different laser
powers. *Solid lines* display
fits of a single exponential
growth law. Reprinted with
permission from [171].
Copyright (2007) American
Chemical Society
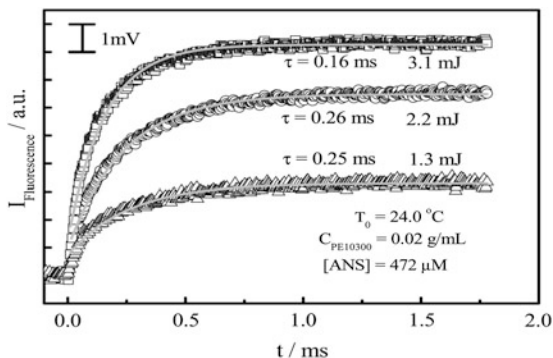
time evolution of the scattered signal was found to be close to exponential in all cases. Typical time constants ranged from 1 s to a few milliseconds; however, no clear physical interpretation of the results was presented.

Later studies of Pluronics have similarly been performed without a clear distinction between micellization kinetics and micelle–micelle relaxation kinetics [115, 127–129]. Contrary to the study of Hecht and Hoffmann, these studies reveal the presence of two [115, 127] or three time constants [128, 129]. The first two were interpreted in terms of the Aniansson and Wall theory and attributed to unimer absorption and unimer exchange-mediated reorganization kinetics. The third relaxation time constant was proposed by Kositza et al. [128, 129] on the basis of a infrared laser-induced T-jump and attributed to "clustering of micelles into larger aggregates" and was observed with increasing amplitude close to the cloud point of the sample, i.e., a micellar fusion mechanism related to a macrophase separation. In one of the works by Kositza et al. [128], the effect of impurities, inherently present in industrial grade Pluronic samples, was investigated by fractionation and purification. The results showed that although the first (fast) process was not appreciatively affected by impurities, the second and third processes were slowed down, suggesting that these processes are dependent on the structural composition. It was also found that addition of hydrophobic compounds led to much larger clusters, especially around the cmt.

In the experiments of Goldmints et al. [127] and Kositza et al.[128, 129] mentioned above, an iodine-based laser heating was used, which provides a faster heating as compared to a traditional resistance-based heating apparatus ("Joule heating"). Using Joule heating, a certain thermal inertia may be important and cause a time-lag as opposed to the instantaneous perturbation often assumed in theories. Consequently, if the heating time is slow, the process may be regarded as a gradual thermal equilibration process rather than a deep non-equilibrium quench, which would lead to a nucleation-like process. Using an intense laser operating in the infrared region, Ye el al. [171] obtained a much faster heating (typical time of 10 ns) and a tunable T-jump by fine-tuning the laser output power. However, because of thermal loss, the temperature relaxed back to its initial value after only about 100 ms. The fluorescence intensities of a dilute Pluronics solution containing a hydrophilic fluorophore after several ultrafast heating runs with different laser power are displayed in Fig. 32.

Interestingly, the study showed that both the fluorescence and light scattering signals exhibited a similar single exponential growth law, with a relaxation time of about 0.1–1 ms after a temperature jump $\Delta T \approx 1$ K close to the cmt. A single time constant was interpreted in terms of the unimer insertion rate constant, k_+, and discussed within the Aniansson and Wall theory (c.f. Sect. 2.2.5). The absence of a slower relaxation process could be related to a restricted total time interval of only 100 ms.

Other Temperature-Jump Studies

The temperature jumps achieved by lasers and capacitor discharge Joule heating are usually very small; of the order of some few degrees Kelvin, limiting the techniques to marginally segregated systems close to cmt. In addition, the temperature will typically follow a pulse-like time dependence and will decay to the initial temperature after a relative short time (typically 100 ms [171]) due to energy dissipation. An alternative method can overcome this problem by using a stopped-flow apparatus with a rapid mixing temperature jump system (mT-Jump from BioLogic Scientific Instruments, France). This set-up achieves temperature changes by mixing two solutions of different initial temperatures T_1 and T_2. The final temperature of the mixture (T_3) is calculated from the initial temperatures and the mixing ratio of the two solutions and can be kept stable over a long period after mixing. In this way, the initial solution can be quenched rapidly through fast mixing to a different temperature with relatively large temperature jumps, ΔT.

Liu and coworkers employed this method to study the micellization kinetics of a double hydrophilic diblock poly(N-isopropylacrylamide)–poly(2-diethylamino ethyl methacrylate) (PNIPAM-PDEA) in aqueous solution [172]. The results obtained after a temperature jump from 20°C (unimers) to different final temperatures are shown in Fig. 33.

As seen in Fig. 33, the micellization occurs increasingly rapidly with the amplitude for moderate ΔT, reflecting deeper quench and thus increasingly unstable unimers. For the largest ΔT, the intensity is smaller and the terminal relaxation is actually slower than for the lower temperatures. This might indicate that the micelles are trapped in smaller aggregates and the terminal kinetics is slower at higher temperatures where the segregation between the core PNIPAM block and the solvent is larger. Interestingly, at intermediate ΔT the size of the initial micelles are larger than the terminal ones. The resulting intensity curves (reflecting both a change in aggregation number and number of micelles as well as distribution) could be tentatively fitted to a double exponential growth model. The fit results show that the fast relaxation time (τ_1) decreased with the micellar concentration while the second, slower relaxation time, τ_2, was found to be virtually independent of the concentration, in line with the observations by Honda et al. [169]. The results were discussed in terms of a dominating unimer exchange mechanism.
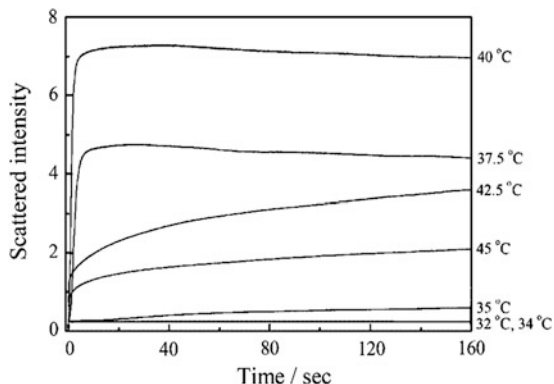
Fig. 33 Time evolution of the scattered intensity upon different temperature jumps of the poly (*N*-isopropylacrylamide)–poly(2-diethylamino ethyl methacrylate) (PNIPAM-PDEA) block copolymers undergoing micellization in water. The temperatures shown indicate the final temperature after a jump from 20°C. Reprinted with permission from [172]. Copyright (2007) WILEY-VCH Verlag GmbH & Co. KGaA, Weinheim

5.1.2 Stopped-Flow Experiments

As seen from the results from the T-jump experiments described above, there is a tendency in the literature to analyze the data in terms of two relaxation constants, even for highly non-equilibrium processes such as micellization kinetics. This is not obvious because micelle formation kinetics involves a distribution of many types of intermediate aggregates and will not necessarily behave in the way Aniansson and Wall predicted for small perturbations away from equilibrium ("linear regime"). Perhaps a more convenient way of inducing micellization is by adding a component that selectively precipitates one of the blocks. Fast kinetic measurements in the order of microseconds can be achieved with modern instruments by using a stopped-flow apparatus for rapid mixing, as described in Sect. 3.2.1. Because micellization is induced very rapidly, this technique is in principle very suitable for comparing experimental data with theory.

The earliest measurements using stopped-flow and light scattering to study kinetics of block copolymer micelles were done by Bednar et al. [173]. In their work, both the micellization kinetics and dissociation kinetics of two commercial block copolymers ("Kraton") were studied: an A-B poly(styrene-*b*-ethylene/propylene) (SEP) diblock and an A-B-A poly(styrene-*b*-ethylene/butylene-*b*-styrene) (SEBS) triblock copolymer. The polymers were molecularly dissolved in mixtures of 1,4-dioxane and heptane that were poor solvents for either EP/EB or S blocks. Micelle formation with EP or EB as core block was then studied by rapidly adding additional pure 1,4 dioxane to the solution. Dissociation of the micelles could be observed by adding heptane to the mixture. Although heptane is a good solvent for the EP or EB blocks it is a marginally bad solvent for PS and thus dissolution of the system is only possible in a solvent mixture and the micelles are likely to have partially swollen

cores. The kinetics was observed using a light scattering instrument at a fixed angle $\theta = 90°$, thus limiting the experimental outcome to a net scattered intensity without structural resolution in terms of the radius of gyration, R_g, or similar quantities. For micelle formation, the data were best fitted with a sum of two simple exponential decay functions. The individual relaxation time constants, τ_1 and τ_2, were not given but an "average" value was defined by $\tau = a_1\tau_1 + a_2\tau_2$ where a_1 and $a_2 = 1 - a_1$ are the normalized amplitudes. The mean relaxation time was found to be about 40 and 70 ms for the diblock and triblock copolymer micelles, respectively. For the decomposition kinetics, the process was observed to be too fast for the diblock copolymer (< 1 ms) whereas for the triblock copolymer micelle a mean relaxation time of about 140 ms was found. Although a theoretical analysis was not performed, the authors speculate that the finding of two relaxation times probably reflects a continuous spectrum of relaxation times.

In a study by Kositza el al. [129] on Pluronic micelles, the kinetics was investigated using both the laser temperature jump and a stopped-flow method. The results after adding salt to a solution originally below cmt showed that micellization could be induced. The associated intensity was characterized by a double or single relaxation time constant depending on concentration. Despite the fact that the initial conditions were completely different, the stopped-flow results seem to indicate a terminal relaxation time similar to the T-jump experiments (τ_2) for certain temperatures. No quantitative correspondence was found for the fast process. A similar dependence, where τ_2 decreased with concentration, was observed and interpreted as a redistribution process by which the micelles might undergo fusion or fission.

Johnson and Prud'homme [174] investigated the micellization kinetics indirectly by applying an analytical confined impinging (CIJ) mixer to induce micelles and studied the effect of the mixing speed on particle size (a process coined "flash nanoprecipitation"). By using poly(butyl acrylate)–poly(acrylic acid) (PBA-PAA) diblock copolymers, the system could be molecularly dissolved in methanol. By adding water, which is selective towards the PPA block, micelles can be induced. Once formed, the micelles were expected to be kinetically frozen, i.e., further ripening of the micelles was inhibited by the high interfacial tension and the aggregates could be regarded as stable particles. By applying various mixing times, τ_{mix}, the supersaturation as well as the so-called Darmköhler number were varied. The latter is defined here as $Da \equiv$ mixing time/micellization time, τ_{mix}/τ_{mic}. The dependence of Da on concentration and mixing time is given in Fig. 34.

As can be seen from Fig. 34, below certain mixing times of between 20 and 60 ms, depending on concentration, the micellar dimensions were independent of both mixing time and concentration. At the breakpoints, the characteristic time was taken as the micellization time, hence $Da \equiv 1$. For $Da > 1$, the measured radii were found to be a function of concentration [generally $R = R(\text{conc})$], as well as to depend on τ_{mix}. The latter regime is characterized by large inhomogeneities in the solvent mixture that homogenize at time scales longer than the time it takes to form the particles, i.e., the system can fuse and exchange unimers for a long time, leading to larger particles. It is also likely that the particles in this regime would be much

Fig. 34 Hydrodynamic
diameter of the particles
formed in a CIJ mixer
induced by a selective solvent
to a stream of soluble
copolymer. The mixing time
and aggregation time are
equivalent at the breakpoint,
where $Da \equiv 1$. [174].
Copyright (2003) by the
American Physical Society
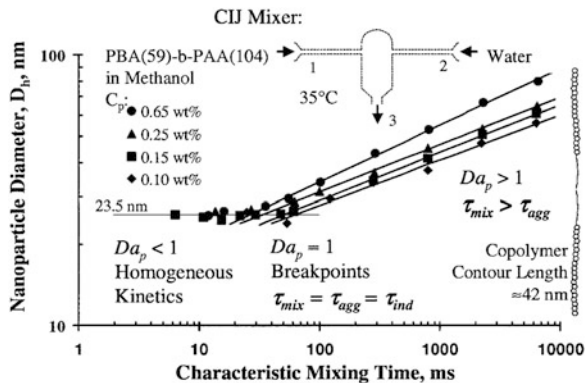
less defined and more polydisperse. The characteristic micellization times deduced
from the breakpoints were found to increase with decreasing concentration. From
this fact it was speculated that the micellization process follows a two-step mecha-
nism, characterized by a nucleation event almost independent of concentration,
followed by a concentration-dependent fusion/fission event. It should be mentioned,
however, that a nucleation process followed by unimer exchange should also
depend on concentration (see Sects. 2.3.2 and 2.3.3). Thus, a definitive conclusion
cannot be reached from these data alone without measuring the actual time
evolution.

In a series of publications, Liu and coworkers employed a sophisticated experi-
mental design using a stopped-flow apparatus combined with both light scattering
and fluorescence techniques to study a range of block copolymer systems ranging
from responsive A-B diblock [8, 175–177], A-B-C triblock [47, 178], and miktoarm
star block copolymers [179]. We will briefly go through results related to diblock
copolymers. In a study from 2007, Zhang et al. [176] investigated a pH-responsive
double-hydrophilic poly(2-diethylamino ethyl methacrylate)–poly(dimethylamino
ethyl methacrylate) block copolymer system end-labeled with a pyrene group,
allowing fluorescence spectroscopy to be used in parallel with light scattering.
The time dependence after pH-jumps qualitatively indicated that the growth curve
of the fluorescence intensity displays a more "stretched behavior", i.e., the process
is characterized by the existence of several, or perhaps a distribution, of rate
constants. The fits performed showed that although the time evolution of the
scattered light displayed a double exponential behavior, the fluorescence intensity,
characterizing the association of pyrene groups into excimers, demanded three
rather than two discrete relaxation constants for reasonable fits. The initial incre-
ment of the intensity was assigned to the formation of oligomeric aggregates that
cannot be detected with light scattering. Although the second process observed with
fluorescence spectroscopy showed a similar time scale as the initial process in light
scattering, the slow process (τ_3) was much slower than that observed with light
scattering. All time constants were found to decrease with increasing concentration.

Chain Length Dependence

In a study by Zhang et al. [177], the effect of hydrophobic chain length on the micellization kinetics was investigated in a series of poly(ethylene oxide)–poly (2-diethylamino) ethyl methacrylate) (PEO-PDEA) block copolymers with varying PDEA molecular weight. Again, the time dependence of the scattered light was approximated by a growth function consisting of a sum of two exponentials. Interestingly, the time constant of the second, slow process slightly decreases with increasing hydrophobic block length. This was accompanied by a tendency for increasing concentration dependence as well as a decreasing apparent activation energy with chain length. These rather unexpected results were interpreted as an increasing dominance of fusion and fission processes because of an increasing suppression of pathways involving unimer exchange (increasing hydrophobicity). The activation energy, E_a, varied from about 8 to 3 kJ/mol, which seems rather low for a fusion process. However, the measurements were performed on time scales from some milliseconds to seconds and it is not clear whether the terminal relaxation reflects the final equilibration to the true equilibrium state. As the final relaxation may be exceedingly slow, it might be that the measured τ_2 only reflects an apparent value.

"Schizophrenic" Block Copolymer Micelle Systems

In a series of studies [8, 175], so-called schizophrenic systems were investigated. These are diblock copolymers that may undergo micellization with either one block or the other to form the micellar core, depending on pH and/or salt concentration. In one study, for micelles formed by poly(4-vinylbenzoic acid)–poly(N-morpholino ethyl methacrylate) (PVBA-PMEMA), the results show that the micellization process induced by a pH-jump exhibited a fast initial growth and a slow terminal growth, where the latter could not be described by a simple relaxation constant. Consequently, only the initial part of the data was fitted to a two-exponential growth function. With this description, the initial process was found to accelerate upon increasing the concentration whereas the second process remained roughly constant. Salt-induced micellization, however, led to a τ_1 that was roughly independent of concentration while τ_2 decreased. Interestingly, the micellar dissolution kinetics induced by dilution or an inverse pH-jump led to a very fast decay that could be described with a single exponential. Also, the remicellization kinetics ("inversion kinetics"), whereby the systems are transformed from micelles with one core-forming block to the other, was investigated. The associated kinetics exhibited in some cases an initial decay followed by a slower growth characterizing the re-equilibration of the micelles.

In a work on a double stimuli-responsive PNIPAM-PDEA block copolymer, micellization was triggered by either precipitating the PDEA upon a pH-jump or by performing a T-jump to selectively precipitate the PNIPAM block. The kinetics upon T-jumps has already been discussed above and was found to be represented by two relaxation constants: τ_1 was found to decrease with concentration while τ_2 was

essentially independent of concentration. However, for the pH-induced micellization process, both τ_1 and τ_2 were found to decrease with concentration. This difference was attributed to electrostatic charges present in the corona during the thermally induced micelization process, leading to a prevention of corona overlap and hence a decreased probability of micellar fusion. Moreover, activation energies for both processes were found to be very similar (about 35 and 38 kJ/mol, respectively) and the time scales differed by a factor of about five. This was taken as an indication of a predominant fusion/fission mechanism in both processes, although in this case these time constants might reflect a continuum.

Influence of Salt Addition

Liu and coworkers investigated a series of A-B-C triblock copolymers, where the C-block is selectively precipitated upon a pH-jump to alkaline conditions [47]. The results showed very similar results as for the A-B diblock copolymers and was again analyzed in terms of two relaxation constants, the first decreasing with concentration and the second being concentration independent. Again, two very similar apparent activation energies were found, where E_a for the second, slower process was even smaller than for the faster process. This indicates a larger entropic barrier for the second process, leading to $\tau_2 > \tau_1$. In a second paper [178], the effect of addition of salt was studied. It was found that upon addition of salt, a gradual increase in the concentration dependence of the second process was found. The obtained results for τ_2 as a function of concentration are given for different added salt amounts in Fig. 35. The results were interpreted as a signature of an increased occurrence of fusion/fission due to screening of electrostatic interactions between corona blocks. Interestingly, the micellization rate was faster at lower salt contents, indicating that, although the fusion might occur in addition to unimer exchange, the terminal process is slower, possibly due to higher interfacial energies and more stable micelles. The latter may occur because addition of electrolytes is well known to induce larger interfacial tensions between hydrocarbons and aqueous solutions [180].

Ge et al. [179] investigated the formation kinetics of vesicles by pH-jumps in a system consisting of a zwitterionic diblock copolymer, poly(2-(methacryloyloxy) ethyl phosphorylcholine)–poly(2-(diisopropylamino)ethyl methacrylate) (PMPC-PDPA) using a combination of stopped-flow and light scattering. The kinetics of pH-induced formation was shown to be tentatively described by three distinct relaxation processes for the early stages of vesicle self-assembly (0–40 s). The kinetics of vesicle formation in the later stage (for times longer than some minutes) was investigated using dynamic light scattering. It was found that both the hydrodynamic radius and the polydispersity decrease approximately exponentially with a single characteristic relaxation time. The observed multiple time constants were interpreted in terms of theoretical considerations, where the unimer-to-vesicle transition is proposed to proceed via a series of four steps: spherical micelles to cylindrical micelles to lamellae platelets that are finally wrapped-up into vesicles [10, 181, 182]. Such a
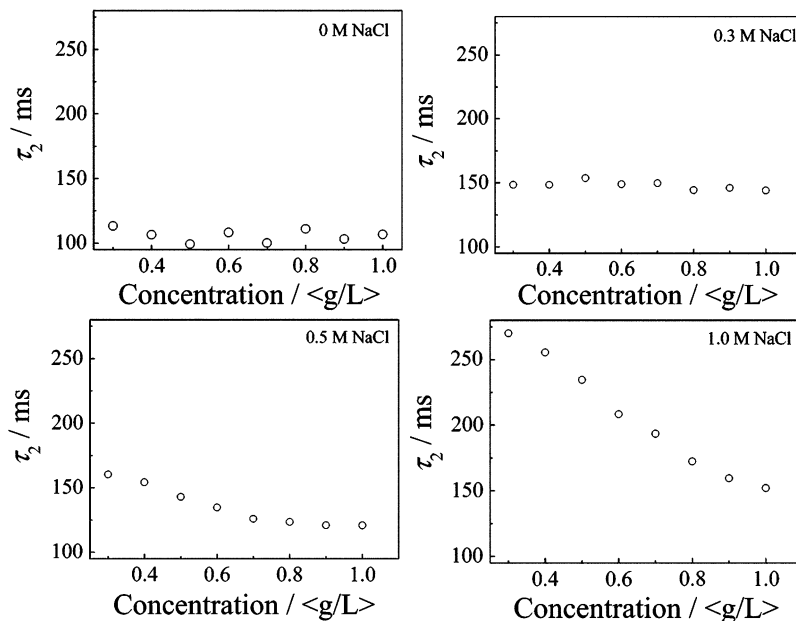
Fig. 35 Concentration of the slow terminal relaxation constants observed for the micellization kinetics of pH-sensitive A-B-C triblock copolymers with different amount of added salts. Reprinted with permission from [178]. Copyright (2007) American Chemical Society

pathway could be more rigorously verified using time-resolved SAXS or SANS whereby the intermediate nanostructures can be observed directly. An example using this technique is given in the next section.

5.1.3 Time-Resolved SAXS with Millisecond Resolution

Most of the works mentioned so far have used light scattering or fluorescence spectroscopy to follow the kinetics, hence the experiments provide little or no structural resolution. In a recent work by Lund et al. [183], synchrotron SAXS was coupled with a stopped-flow apparatus in order to study micellization kinetics with a millisecond time resolution and nanometer structural resolution. In this study, an amphiphilic model system consisting of a well-defined PEP1-PEO20 block copolymer in DMF/water mixtures was used. As previously mentioned, both DMF and water are bad solvents towards PEP but good solvents for PEO. The PEP1-PEO20 system is very useful for studying micellization because in pure DMF only single chains (unimers) are present, but the block copolymers aggregate into well-segregated micelles as soon as some water is added. Hence, micellization can be induced by rapidly mixing a solution of PEP1-PEO20 in DMF with water in a

stopped-flow apparatus. Typical time-resolved scattering curves were obtained using a high-brilliance synchrotron SAXS instrument (ID02, at the European Synchrotron Radiation Facility, ESRF) and show the increase in scattered intensity associated with the formation of micelles (see Fig. 36a). The scattering could be described with a core–shell micellar scattering model (c.f. Sect. 3.1.6), thereby allowing the extraction of detailed parameters of the internal structure of the micelles at all times.

Fig. 36b shows the aggregation number, P_{mean}, plotted against the corresponding thickness of the micellar corona, $R_{corona} = R_m - R_c$ for three concentrations in a double logarithmic representation. The data agree well with the prediction [38, 40]: $R_{corona} \sim P_{mean}^{1/5}$ expected for star-like micelles. The results thus show that the micelles grow like well-defined star-like micellar entities. No regime where the size grows faster than the molecular weight, which was observed on a less segregated system by Honda et al. [169], were observed in this case. This probably reflects the fact that the initial time range of the micellization in this is too fast to be captured ($t < 2$–3 ms). Also, for star-like micelles only a few chains are necessary to achieve a star-like structure [38].

The time dependence of the aggregation number, P_{mean}, deduced from the core–shell model fits (Sect. 3.1.6) for three concentrations, is given in Fig. 37.

The observed growth behavior shown in Fig. 37 could be approximately fitted using a phenomenological model in the form of a stretched exponential $P_{mean} \approx 1 - \exp[-(kt)^{\beta}]$. This yields in all cases an exponent β of about 0.2. A trial fit to a sum of two exponentials did not give satisfactory fits, in contrast to other results [169, 171, 176]. The broad relaxation suggests an intrinsically broadly distributed kinetic growth process that cannot be described with a finite number (typically 1–3) of relaxation times An approximate two-exponential behavior is expected for micelle relaxation kinetics after a sudden external disturbance, but only very close to equilibrium [55, 60] that is not the case for micellization kinetics observed deep in the micelle region. The data at the shortest times suggest the existence of a fast initial aggregation ($t < \approx 5$ ms) that cannot be entirely resolved experimentally. This process seems to become exhausted at intermediate times leading to a "shoulder" of P_{mean} that changes with concentration. The terminal relaxation towards a common equilibrium then appears to slow down with time, the overall rate increasing with concentration.

The concentration dependence of the terminal relaxation has been observed earlier in light scattering experiments and sometimes qualitatively attributed to fusion/fission processes [176]. In [183], however, the relaxation curves could be described using the nucleation and growth model highlighted in Sect. 2.3.3 where growth was only allowed to occur unitarily through unimer exchange kinetics. The corresponding size distribution extracted from the fits are displayed in Fig. 38.

The size distribution of micelles gives a very detailed view of the micellization process. Extracted parameters such as the unimer concentration and the Gaussian width are correlated with the mean aggregation number, giving a complete view of the process in Fig. 38b. The results reveal the following scenario: First, the initial free unimers are consumed rapidly in a nucleation-like event that leads to the formation of

Fig. 36 (**a**) Scattered intensity at different kinetic times during the micellization of a 0.25 vol% PEP1-PEO20 block copolymer in a 90 mol% DMF/water solution. *Solid lines* display fit results using the scattering model functions (see text for details). (**b**) Scaling of the thickness of the corona, R_{corona}, with the aggregation number of the micelles, P_{mean}, both deduced from the core–shell fits for the 0.125% (*stars*), 0.25% (*squares*), and 0.5% (*triangles*) solutions, in double logarithmical representation. The linear fits (*solid lines*) almost perfectly reproduce the theoretically expected scaling law for star-like micelles: $R_{corona} \sim P_{mean}^{1/5}$ [183]. Copyright (2009) by the American Physical Society
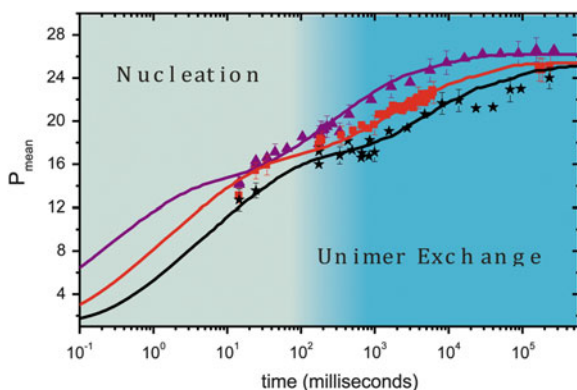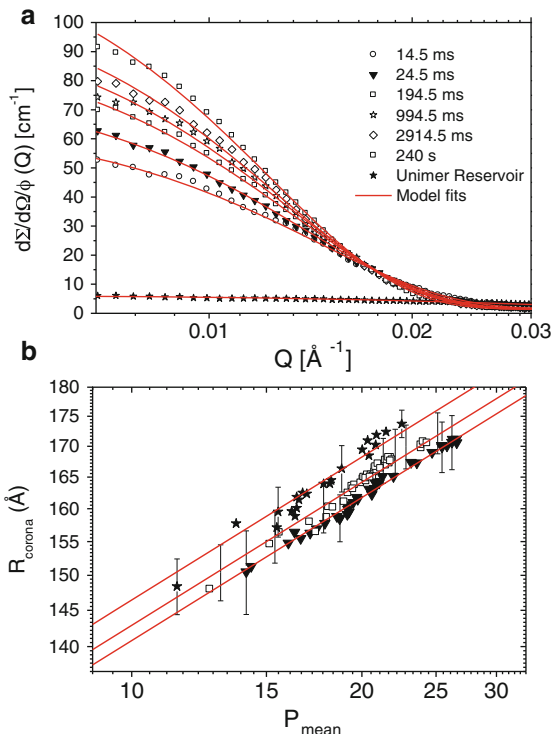
Fig. 37 Experimentally determined growth behavior and comparison with a unified nucleation and growth model. Time dependence of the aggregation number, P_{mean}, extracted from the fits for all three total volume fractions on a logarithmical time scale: 0.125% (*stars*), 0.25% (*squares*), and 0.5% (*triangles*). *Solid lines* represent a fit using the nucleation model described in the text. Typical *error bars* are shown [183]. Copyright (2009) by the American Physical Society
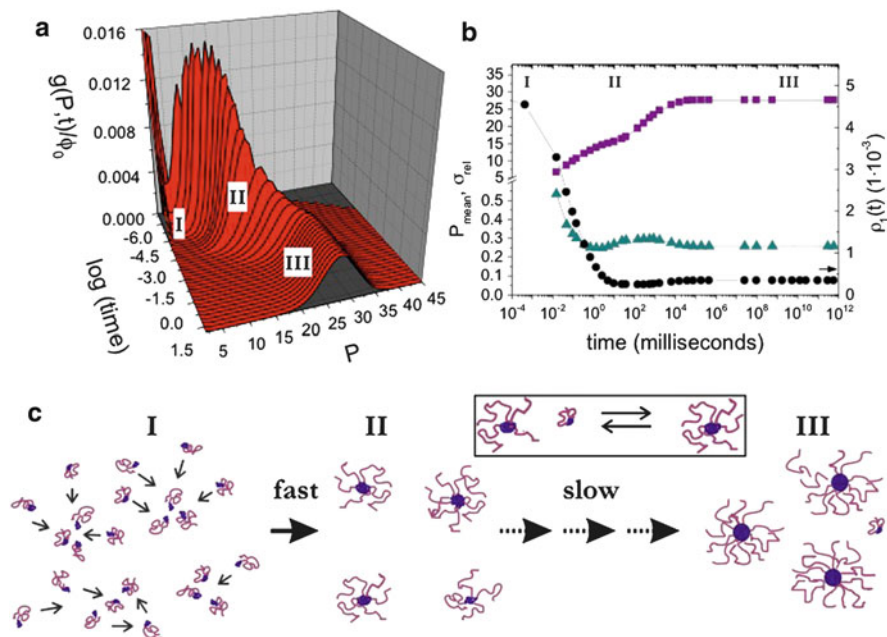
Fig. 38 Nucleation and growth view of the micellization process. (**a**) The time evolution of the distribution of the micellar ensemble in terms of the aggregation number, P_{mean}, corresponding to the fit results of the 0.5% micellar system. (**b**) Time evolution of the unimer concentration (*circles*) compared to the associated increase in P_{mean} (*squares*). Also shown is the relative Gaussian width of the micellar distribution $\sigma_{rel} = \sigma/P_{mean}$ (*triangles*). (**c**) Illustration of the micellization process showing the fast nucleation event, which essentially consumes all the unimers (region I), followed by a region where the micellar growth slows down and is temporarily nearly frozen due to the lack of available unimers (region II). The terminal slow growth towards the final equilibrium is governed by the amount of free unimer and thus effectively limited by the unimer expulsion/insertion process between the metastable micelles (region III). [183]. Copyright (2009) by the American Physical Society

metastable micelles (region I in Fig. 38c). In analogy with Ostwald ripening for macrophase separation, the microphase separated micelles can only grow further if other micelles dissolve. However, an important distinction here is that while in Ostwald ripening the system in principle grows to macroscopical scales, the micelles are limited to the equilibrium size set by the thermodynamics of the micelle itself. In this model, this "coarsening mechanism" occurs through unimer exchange (region II in Fig. 38c). This continues until the micelles achieve their equilibrium size (region III in Fig. 38c). These results show that nucleation and growth including only unimer exchange kinetics is sufficient to describe the kinetics. This does not necessarily exclude the presence of other mechanisms such as fusion and fission but, in the sense of a physical minimum model, unimer exchange is sufficient to describe all data. In order to further advance understanding, systematic TR-SAS studies in which molecular parameters such as molecular weight, composition, etc. are varied

would be very helpful. Complementary, more theoretical modeling is necessary in order to fully understand the mechanisms and kinetic pathways. Here computer simulations are particularly useful. A summary of existing works on this topic will be covered in the next section.

5.1.4 Computer Simulations

The central questions occupying theoreticians and experimentalists are the mechanism and kinetic pathways of self-assembly. To answer these questions, computer simulations are particularly useful because the coordinates of each molecule can be traced individually and pathways can be observed directly. The challenge for computer simulations is to access the relatively long time scales needed to observe micellization kinetics, which can only be done using coarse-grained models, relatively few particles, and/or by excessively long computation times.

An early simulation work was presented by Mattice and coworkers [184] in which A-B diblock copolymers consisting of 5–45 monomers for each block were studied. The simulations were performed in cubic simulation cells with 44^3–88^3 lattice sites. The total concentration of the polymers were found to be in the range of 0.5–6%. Results obtained after starting from typically a few hundred chains revealed a rapid initial step that essentially consumed all single unimers, followed by a very slow coarsening process that was not fully equilibrated within the simulation time. In the work, no direct detailed analysis or evaluation of the kinetic pathway was performed. Nevertheless it was observed that upon increasing the interaction strength between the hydrophobic block and the solvent or increasing the insoluble block length, smaller trapped metastable micelles were detected. These micelles were found to essentially "freeze" the self-assembly process, at least on the time scale of the simulations.

Using full atomistic force field-based molecular dynamics simulations, Marrink et al. [185] simulated the micellization process of 54 dodecylphosphocholine (DPC) surfactant molecules in water on short time scales from some picoseconds to some tenths of nanoseconds. The results showed that the process is diffusion limited but that the surfactant aggregation still occurred on time scales much faster than expected from theoretical calculations. It was speculated that long-range interactions could enhance the aggregation rate. However, upon varying the interaction potential, it was concluded that this did not influence the results. Instead, water-mediated long-range hydrophobic interactions were suggested as a possible alternative explanation for the observed behavior. Interestingly, the simulation runs revealed that the micelles aggregate into larger cylindrical micelles at higher DPC concentration, whereas smaller spherical micelles are formed at lower concentrations. The difference was attributed to finite size effects and a small number of particles.

In a work by Chen et al. [186], Brownian dynamics was used to simulate the formation of micelles constituted of PS-PEO in water, with the particular aim of investigating the processes involved in "flash nanoprecipitation". The effective (coarse-grained) potential was carefully mapped to experimentally determined

quantities of the system in order to obtain as realistic simulations as possible. In that way, the authors were able to reproduce the structural and thermodynamic properties of the system. Still, instead of changing the interaction parameters associated with the abrupt change in solvent composition experienced by the diblock copolymer under the experimental conditions, micellization was induced by quenching the temperature. Thus, the quenching time, corresponding to the mixing time in experiments, is controlled by the cooling rate. The results showed that the block copolymers aggregated into micelles with similar sizes and dimensions as observed experimentally. However, the time scale (a few milliseconds) was found to be considerably faster than that experimentally determined, which ranged from 20 to 60 ms. Also, although previous experiments showed that the micellar size decreases with increasing mixing time until the break (20–60 ms), the simulations showed the opposite trend; the micellar size increases with mixing time until a breakpoint that occurs at lower times than in experiments. This discrepancy was attributed to the different time scales probed in simulations ($t \leq 5$ ms) and that in the experiments the system was allowed to grow further through fusion/fission, although the mechanisms were not analyzed in detail in this work.

The mechanism and pathways of self-assembly were investigated in great detail in a work by Li and Dormidontova [162], who analyzed a system consisting of oligomeric block copolymers, A_2-B_3 and A_4-B_x (the numbers indicate the numbers of beads, $x = 4$, 6, or 8) using dissipative particle dynamics. This simulation technique combines molecular dynamics and Brownian dynamics-type simulations, giving the advantage of accessing relatively large temporal and spatial time scales. The growth curve associated with the weight and number average molecular weights of the aggregates (M_w and M_n respectively), was found to be significantly different. Here M_n was found to stabilize to an equilibrium size more rapidly than M_w, indicating that the number of micelles assumes a constant value earlier but the micelles are increasingly polydisperse in size with time. By tagging different micelles as a function of time, it was found that the aggregation numbers exhibited discrete jumps with amplitudes much larger than 1, indicating fusion events during the course of the reaction. It was also found that unimer exchange was primarily important in the first part of the micellization process (nucleation event); at later stages processes involving fusion/fission of micelles were more dominating. The latter was manifested in a bimodal character of the distribution function of M_w where two peaks were clearly visible at intermediate stages during the micellization process. Increasing oligomer concentrations were found to speed up the whole micellization process, which was attributed to increased probabilities of micellar collision and fragmentation. The distribution function in terms of the aggregation number is plotted as a function of time in Fig. 39.

In order to understand the interactions controlling the mechanisms behind self-assembly, the interaction energy between the hydrophobic core chains and the solvents as well as the corona chain length were also varied. The results show that the effect of incrementing the hydrophobic energy is threefold: First, the initial nucleation-like event appears to be essentially unaffected; second, the time window of micellization expands, i.e., the time for completion increases; and third, the

Fig. 39 Time evolution of the aggregation number distribution for A_2B_3 oligomers undergoing micellization. Note the bimodal character of the distribution function at intermediate time stages. Reprinted with permission from [162]. Copyright (2010) American Chemical Society
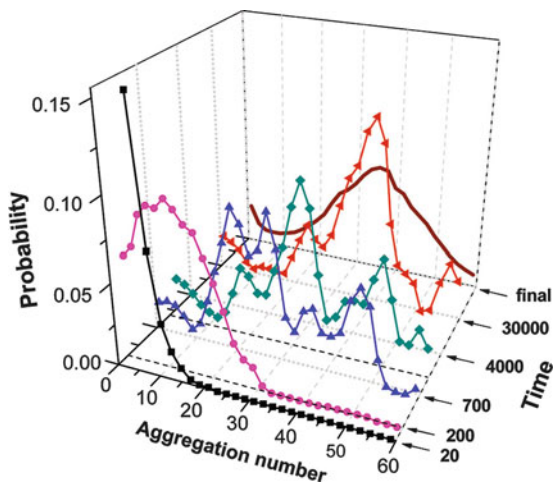
importance of unimer exchange increases during the final stage of micellization. Also, fusion/fission events appear to be virtually unaffected upon an increase in the interaction energy although events involving small aggregates were found to be less likely to occur. The effect of increasing corona length was, perhaps surprisingly, found not to affect the relative contributions from the different mechanisms; instead, the overall rate of events decreased. It should be mentioned that the range of molecular weights studied by Li and Dormidontova corresponds to oligomers and that there might be a significant difference for polymers. This is still to be studied and compared to experimental results, providing a significant challenge for future studies.

5.2 Morphological Transition Kinetics

Most of the works related to the kinetics of morphological transitions have been performed in systems of regular (low molecular weight) surfactant micelles. Examples include micelle-to-vesicle transitions [187–189] studied by TR-SANS coupled with stopped-flow or with time resolved small-angle static and dynamic light scattering [190, 191]. Such morphological transitions have also been observed using TR-SAXS in other systems [192–194], where the processes can be resolved on time scales of only a few milliseconds. Since morphological transition kinetics of surfactant micelles have been extensively reviewed elsewhere [14, 15, 189, 195], this will not be covered in more detail here because we are mainly dealing with block copolymer systems in this review.

For block copolymer systems, most studies are related to ordering kinetics and morphological transition in melts or concentrated solutions. Examples include disorder-to-order [196], lamella-to-cylinder [197], cylinder-to-sphere [198], and

cylinder-to-gyroid [199] transition kinetics. Because we are dealing here with micellar solutions, these examples fall out of the scope of this review.

It has been widely reported that amphiphilic diblock copolymers can self-assemble into various nanoscale morphologies such as spheres, cylinders, and vesicles [46, 200]. The type of morphology that is obtained in a certain block copolymer solvent system was found to depend on the hydrophilic fraction of the block copolymer [201, 202], the overall molecular weight [142], solvent quality [48, 203], and temperature [204, 205]. Also, the polymer concentration was found to affect the morphology and the size of the aggregates [203]. The transitions between different morphologies of strong amphiphilic block copolymer aggregates in water are generally irreversible. In particular, vesicles are non-equilibrium structures in a trapped metastable state analogous to frozen spherical micelles [46]. The kinetics of the morphological transitions can be accelerated by the use of co-solvents with higher compatibility to the insoluble block or by variation of temperature such that the transitions are reversible [203–205]. Hence, it was argued that the speed of single chain exchange also determines the reversibility of the transition process. However, in a recent work by Lund et al. [48], it was shown that the transition from cylinders to spheres is very fast whereas the reverse process will not take place on finite time scales, although the single unimer exchange was measured to be very fast in the transition region. We note that both morphologies are thermodynamically stable within their range of existence, as was explicitly shown from model calculations taking into account the variation of structural parameters with the interfacial tension [48]. The irreversibility of the cylinder-to-sphere transition is thus due to a kinetic hindrance, which generally implies that for morphological transitions mechanisms other than pure chain exchange are active.

Unfortunately, kinetic studies of morphological transitions in block copolymer micellar systems are very rare. Most important in this context is the work of Eisenberg and colleagues, who explored the kinetics and mechanisms of various transitions of polystyrene$_{310}$-b-poly(acrylic acid)$_{52}$ (PS$_{310}$-b-PAA$_{52}$) block copolymer in water/1,4-dioxane mixtures. A morphological phase diagram of the ternary system, PS$_{310}$-b-PAA$_{52}$/water/1,4-dioxane was elaborated by Shen and Eisenberg [203] employing freeze-drying transmission electron microscopy (TEM), turbidity measurements, and static and dynamic light scattering. Starting from molecularly dissolved block copolymer chains in 1,4-dioxane they found upon addition of water the following sequence of morphologies: spheres, coexisting spheres and rods, rods, coexisting rods and vesicles, and vesicles at all polymer concentrations. It was found that in this system the appearance of the morphologies is reversible. The formation of the coexisting mixtures of morphologies is thermodynamically controlled, as concluded from the fact that they are identically formed independent of the pathway. Burke and Eisenberg [206] studied the kinetics and mechanisms involved in the sphere-to-rod and rod-to-sphere transitions of this system by TEM and turbidity measurements. The transition was induced by adding small amounts of water close to the morphological boundary for the forward transition and 1,4-dioxane for the reverse transition. Analysis by double exponential equations revealed two relaxation steps in both directions. The observed time scales in

forward and backward directions were found to be comparable to each other. In the forward direction, the evaluation of TEM micrographs showed the formation of an irregular pearl necklace structure by adhesive collision of spheres, which reorganize in a second slow step into smooth rods. The inverse transition starts with the formation of bulbs at the end of the rods, which in the rate-determining second step are released from the ends of the cylindrical body. The kinetics of both transitions was found to depend on the initial solvent composition, the magnitude of the solvent jump, and the initial polymer concentration. Systematic studies have shown that the kinetics are mostly affected by the initial conditions, i.e., location in the morphological phase diagram.

Using the same techniques as described above, Chen et al. [207] studied the rod-to-vesicle transition by adding water to the ternary system, PS_{310}-b-PAA_{52}/water/1,4-dioxane in the corresponding region of the phase diagram. Similar to the observation in the sphere-to-rod transition, the kinetics were governed by two consecutive steps. The first step involves the flattening of short rods to circular lamellae followed by the second step, which is the closing of the vesicles. The rates of the shape transformation crucially depend on the initial water content. The studies revealed that the larger the initial water content, the slower the relaxation times. This was also the case for increasing polymer concentration, while the size of the jump did not change the relaxation times significantly.

The corresponding vesicle-to-rod transition was investigated by Burke and Eisenberg [208]. The transition, monitored by turbidity measurements, could be described by a single relaxation step. The TEM micrographs revealed that the reorganization to rods proceeds through a sequence of intermediate structures: first the deformation of a vesicle to a "bowtie" shape structure was seen, which afterwards develops into dumbbells. Elongation of the long axis finally leads to the formation of thin rods. It was argued that the driving force is the increase in the curvature energy due to the change in the bilayer thickness. The instability is then relaxed by the transformation to thinner rods which, apparently, is the energetically favorable morphology for the final solvent composition. In summary, the work by Eisenberg and colleagues impressively demonstrates that the transition between different morphologies proceeds via different pathways, including the formation of different irregular intermediate structures. Thus this work reveals that, besides single chain exchange, other mechanisms are important for a shape transformation. However, reorganization of structures will not take place whenever unimer exchange is not existent, i.e., aggregates are in a frozen metastable state. We note that, except for the studies of Eisenberg and colleagues, there is a lack of systematic studies on the kinetics and mechanisms of morphological transitions. Time resolved small angle scattering on suitable block copolymer/solvent systems may help to obtain a clear picture of the general mechanisms governing morphological transitions in block copolymer micelles.

6 Concluding Remarks and Future Challenges

In this review, we have provided a selective overview of theoretical and experimental studies on kinetic processes in block copolymer micellar systems. We have demonstrated the strengths of time-resolved small-angle scattering techniques by highlighting recent examples from the literature. Most of the available literature in this field is either related to equilibrium exchange kinetics or micellization kinetics.

Although limited in number, the examples given illustrate impressively the potential and strength of these techniques. Primarily, as a common feature of both methods, TR-SAXS and TR-SANS provide a structural resolution of the kinetic processes of self-assembled systems on the nanometer scale. Individually, the strengths of TR-SAXS for studying kinetic processes is the high flux available at synchrotron sources, which allows experimenters to resolve fast kinetic processes such as block copolymer micellization in the millisecond range on small sample volumes. The advantage of TR-SANS on the other hand is the ability to exploit H/D contrast variation, which makes this technique unique for studying fundamental aspects of equilibrium kinetics like the influence of temperature, interfacial tension, and chain length. Even fine details like the chain conformation during the expulsion process or contributions from "hidden" processes like diffusion or fusion/fission are accessible.

Time-resolved techniques show promise for the future as improved technical capabilities and more powerful neutron and X-ray sources emerge. For neutrons, particularly promising is the planned construction of the powerful European Spallation Source (ESS), which will allow time resolutions approaching submilliseconds as well as the use of smaller and more dilute samples. Although the flux at synchrotron sources will still be significant larger, H/D contrast variation provides enhanced contrast over X-rays as well as a playground for performing studies of equilibrium kinetics in soft matter systems that cannot easily be achieved by other techniques. Additionally, neutrons may provide a significant advantage because beam radiation damage, which is a concern in particular for synchrotron studies of aqueous systems, is not an issue with SANS.

Increased flux and more powerful sources will also be particularly useful for the study of biological or biohybrid materials, which often are only available in small quantities. This demands a significant quality in terms of both flux and background as biomaterials often are characterized by weak signals and/or low contrast. Combining time-resolved wide-angle and small-angle scattering techniques can be expected to be particularly useful to bridge mesoscopic and microscopic scales, providing full structural information and information on correlations between local and global motions. This places an additional demand for low background and accurate background subtraction that constitutes a significant challenge to instrumentation development in terms of stability and optimization.

Despite its rather short history, TR-SAS techniques have helped to resolve many aspects of kinetic processes in micellar systems, in particularly the equilibrium kinetics. However, many challenges remain for the future. For block copolymer micelles, these include studies of morphological transitions, drug encapsulation and

release, etc. For the kinetics of biological systems, such as membranes and assemblies involving secondary and tertiary structures of proteins, TR-SAS is still to be exploited on a wider scale. In a notable example, the KZAC/TR-SANS technique was used to study and understand the equilibrium exchange kinetics in phospholipid vesicle structures [209, 210], showing the existence of both intermicellar exchange processes and "flip-flop" motions. In the future, studies are likely to be related to conformational changes, diffusion, and structural transitions that can be investigated in great detail using the combined structural and temporal resolution of TR-SAS techniques. Other applications likely to come are investigations of kinetics in drug delivery carrier systems, where stability as well as diffusion processes can be investigated.

For surfactant micelles, studies on the micellization kinetics and equilibrium kinetics are still to come although, for the latter, results from a hybrid system consisting of a short *n*-alkyl head group and a polymer tail were presented in Sect. 4.4. Studies of such systems constitute significant challenges for the instrumentation as the time scale of these systems approaches ranges of a few milliseconds and even submilliseconds. With improved and increased availability of neutron and X-ray sources, the next decade is likely to see a significant increase in the application and continued success of time-resolved scattering techniques in soft matter, material, and biological sciences.

References

1. Israelachvili JN (1985) Intramolecular and surface forces- with applications to colloidal and biological systems. Academic, London
2. Hamley IW (1998) The physics of block copolymers. Oxford University Press, New York
3. Yu K, Zhang L, Eisenberg A (1996) Langmuir 12(25):5980
4. Zhang L, Eisenberg A (1999) Macromolecules 32(7):2239
5. Jain S, Bates F (2003) Science 300(5618):460
6. Jain S, Bates FS (2004) Macromolecules 37:1511
7. Cui H, Chen Z, Zhong S, Wooley KL, Pochan DJ (2007) Science 317(5838):647
8. Wang X, Guerin G, Wang H, Wang Y, Manners I, Winnik MA (2007) Science 317(5838):644
9. Hayward RC, Pochan DJ (2010) Macromolecules 43(8):3577
10. He X, Schmid F (2008) Phys Rev Lett 100(1):137802
11. Cabral H, Matsumoto Y, Mizuno K, Chen Q, Murakami M, Kimura M, Terada Y, Kano MR, Miyazono K, Uesaka M, Nishiyama N, Kataoka K (2011) Nat Nanotechnol 6(12):815
12. Patist A, Oh S, Leung R (2001) Colloids Surf A Physicochem Eng Asp 176:3
13. Bras W, Ryan AJ (1997) Adv Colloid Interface Sci 75(1):1
14. Gradzielski M (2003) Curr Opin Colloid Interface Sci 8:337
15. Gradzielski M, Grillo I, Narayanan T (2004) Prog Colloid Polym Sci 129:32

16. Zana R (ed) (2005) Dynamics of Surfactant Self-assemblies Micelles, Microemulsions, Vesicles, and Lyotropic Phases. Surfactant science series, vol 125. Taylor and Francis, London
17. Narayanan T (2009) Curr Opin Colloid Interface Sci 14(6):409
18. Grillo I (2009) Curr Opin Colloid Interface Sci 14(6):402
19. Lund R (2010) Stud Kinet Neutrons 161:213
20. Hill TL (1964) Thermodynamics of small systems. Benjamin, New York
21. Hall DG, Pethica BA (1967) In: Schick MJ (ed) Nonionic surfactants. Arnold, London, ch. 16
22. Tanford C (1972) J Phys Chem 76(21):3020
23. Tanford C (1974) Proc Natl Acad Sci USA 71(5):1811
24. Tanford C (1974) J Phys Chem 78(24):2469
25. Flory PJ (1953) Principles of polymer chemistry. Cornell University Press, Ithaca
26. Leibler L, Orland H, Wheeler JC (1983) J Chem Phys 39(7):3550
27. Hong K (1983) Macromolecules 14:727
28. Nagarajan R, Ganesh K (1989) J Chem Phys 90(1):5843
29. Balsara N, Tirrell M, Lodge TP (1991) Macromolecules 24(8):1975
30. Lund R, Willner L, Lindner P, Richter D (2009) Macromolecules 42(7):2686
31. Nagarajan R (1991) Langmuir 7:2934
32. Landau LD, Lifshitz EM (1976) Statistical physics. Nauka, Moscow
33. Kadanoff L (2000) Statistical physics: statics, dynamics and renormalization. World Scientific Publishing, London
34. de Gennes PG (1979) Scaling concepts in polymer physics. Cornell University Press, Ithaca
35. des Cloizeaux J, Jannink G (1990) Polymers in solution: their modelling and structure. Claradon, Oxford
36. De Gennes PG (1976) Journal de Physique 37(12):1445
37. Alexander S (1977) Journal de Physique 38(8):977
38. Daoud M, Cotton JP (1982) Journal de Physique 43(3):531
39. Semenov A (1985) Zhurnal Eksperimentalnoi I Teoreticheskoi Fiziki 88(4):1242
40. Halperin A (1987) Macromolecules 20(11):2943
41. Halperin A, Tirrell M, Lodge TP (1992) Adv Polym Sci 100:31
42. Izzo D, Marques CM (1993) Macromolecules 26:7189
43. de Gennes P (1980) Macromolecules 13(5):1069
44. Willner L, Poppe A, Allgaier J, Monkenbusch M, Lindner P, Richter D (2000) Europhys Lett 51(6):628
45. Lund R, Willner L, Stellbrink J, Radulescu A, Richter D (2004) Macromolecules 37:9984
46. Förster S, Borchert K (2005) Polymer Vesicles. Encyclopedia of Polymer Science and Technology, pp. 1–52
47. Zhulina EB, Adam M, LaRue I, Sheiko SS, Rubinstein M (2005) Macromolecules 38(12):5330
48. Lund R, Pipich V, Willner L, Radulescu A, Colmenero J, Richter D (2011) Soft Matter 7(4):1491
49. Haliloglu T, Bahar I, Erman B, Mattice WL (1996) Macromolecules 29(13):4764
50. Muller N (1972) J Phys Chem 76(21):3017
51. Lang J, Zana R, Bauer R, Hoffmann H, Ulbricht W (1975) J Phys Chem 79(3):276
52. Lessner E, Teubner M, Kahlweit M (1981) J Phys Chem 85:1529
53. Lessner E, Teubner M, Kahlweit M (1981) J Phys Chem 85:3167
54. Aniansson E, Wall S, Almgren M (1976) J Phys Chem 80(9):905
55. Aniansson E (1974) J Phys Chem 78(10):1024
56. Aniansson E (1975) J Phys Chem 79(8):857
57. Kahlweit M (1982) J Colloid Interface Sci 90:92
58. Lang J, Zana R (1987) In: Zana R (ed) Surfactant solutions. New methods of investigation. Marcel Dekker, New York
59. Atkins PW (1988) Physikalische Chemie. VCH Verlagsgesellschaft GmbH, Weinheim

60. Halperin A, Alexander S (1989) Macromolecules 22:2403
61. Kramers H (1940) Physica 7:284
62. Lund R, Willner L, Stellbrink J, Lindner P, Richter D (2010) Phys Rev Lett 104:049902
63. Choi SH, Lodge TP, Bates FS (2010) Phys Rev Lett 104:047802
64. Halperin A (2011) Macromolecules 44(13):5072
65. Dormidontova EE (1999) Macromolecules 32(22):7630
66. Doi M, Edwards SF (1986) The theory of polymer dynamics. Oxford University Press, Oxford
67. Hadgiivanova R, Diamant H, Andelman D (2011) J Phys Chem B 115(22):7268
68. Nyrkova IA, Semenov AN (2005) Macromol Theory Simul 14(9):569
69. Shchekin AK, Grinin AP, Kuni FM, Rusanov AI (2005) Nucleation in micellization processes. In: Schmelzer JWP (ed) Nucleation theory and applications. Wiley-VCH, Weinheim
70. Onsager L (1931) Phys Rev 37:405
71. Lindner P, Zemb T (eds) (2002) Neutrons, X-ray and light scattering methods applied to soft condensed matter. Elsevier, Amsterdam
72. Guinier A, Fournet G (1955) Small angle scattering of X-rays. Wiley, London
73. Feigin L, Svergun D (1987) Structure analysis by small-angle X-ray and neutron scattering. Plenum, New York
74. Pedersen JS, Svaneborg C (2002) Curr Opin Colloid Interface Sci 7:148
75. Pedersen JS (2008) Small-Angle Scattering from Surfactants and Block Copolymer Micelles. In: Borsali R, Pecora R (eds) Soft-Matter Characterization. Springer, Berlin 1:191–234
76. Sheu E (1992) Phys Rev A 45(4):2428
77. Pedersen JS (1997) Adv Colloid Interface Sci 70:171
78. Pedersen JS, Posselt D, Mortensen K (1990) J Appl Cryst 23:321
79. Richter D, Schneiders D, Monkenbusch M, Willner L, Fetters LJ, Huang JS, Lin M, Mortensen K, Farago B (1997) Macromolecules 30:1053
80. Svaneborg C, Pedersen JS (2001) Phys Rev E 64(1):010802
81. Svaneborg C, Pedersen JS (2002) Macromolecules 35(3):1028
82. Daoud M, Cotton JP, Farnoux B, Jannink G, Sarma G, Benoit H, Duplessix C, Picot C, De Gennes PG (1975) Macromolecules 8:804
83. Dozier WD, Huang JS, Fetters LJ (1991) Macromolecules 24:2810
84. Förster S, Burger C (1998) Macromolecules 31:879
85. Won YY, Davis HT, Bates FS, Agamalian M, Wignall GD (2000) J Phys Chem B 104(30):7134
86. Pedersen JS, Svaneborg C, Almdal K, Hamley IW, Young RN (2003) Macromolecules 36(2):416
87. Poppe A, Willner L, Allgaier J, Stellbrink J, Richter D (1997) Macromolecules 30:7462
88. Beaucage G (1996) J Appl Cryst 29:134
89. Pedersen JS, Schurtenberger P (1996) Macromolecules 29:7602
90. Cotton J (1996) Adv Colloid Interface Sci 69:1
91. Wignall G, Hendricks R, Koehler W, Lin J et al. (1981) Polymer 22:886
92. Willner L, Jucknischke O, Richter D, Roovers J, Zhou LL, Toporowski PM, Fetters LJ, Huang JS, Lin MY, Hadjichristidis N (1994) Macromolecules 27:3821
93. Benmouna M, Hammouda B (1997) Prog Polym Sci 22(1):49
94. Choi SH, Lee S, Soto HE, Lodge TP, Bates FS (2011) J Am Chem Soc 133(6):1722
95. Pedersen JS, Hamley IW, Ryu CY, Lodge TP (2000) Macromolecules 33(2):542
96. Yang L, Alexandridis P, Steytler DC, Kositza MJ, Holzwarth JF (2000) Langmuir 16(23):8555
97. Goldmints I, Yu G, Booth C, Smith KA, Hatton TA (1999) Langmuir 15(5):1651
98. Laurati M, Stellbrink J, Lund R, Willner L, Zaccarelli E, Richter D (2007) Phys Rev E 76:041503
99. Panine P, Finet S, Weiss TM, Narayanan T (2006) Adv Colloid Interface Sci 127(1):9
100. Willner L, Poppe A, Allgaier J, Monkenbusch M, Richter D (2001) Europhys Lett 55(5):667

101. Lund R, Willner L, Stellbrink J, Lindner P, Richter D (2006) Phys Rev Lett 96:068302
102. Lund R, Willner L, Richter D, Dormidontova EE (2006) Macromolecules 39(13):4566
103. Zinn T, Willner L, Lund R, Pipich V, Richter D (2012) Soft Matter 8(3):623
104. Lund R, Willner L, Pipich V, Grillo I, Lindner P, Colmenero J, Richter D (2011) Macromolecules 44(15):6145
105. Thilo L (1977) Biochim Biophys Acta 469(3):326
106. Cantú L, Corti M, Salina P (1991) J Phys Chem 95(15):5981
107. Price C, Stubbersfield R, Elkafrawy S, Kendall K (1989) Br Polym J 21(5):391
108. Booth C, Naylor TD, Price C, Rajab NS, Stubbersfield RB (1978) J Chem Soc, Faraday Trans 1 74:2352
109. Malmsten M, Lindman B (1992) Macromolecules 25(20):5440
110. ŠpaČek P, Kubin M (1985) J Appl Polym Sci 30(1):143
111. ŠpaČek P (1986) J Appl Polym Sci 32(3):4281
112. Holmqvist P, Nilsson S, Tiberg F (1997) Colloid Polym Sci 275(5):467
113. Procházka K, Glöckner G, Hoff M, Tuzar Z (1984) Die Makromolekulare Chemie 185(6):1187
114. Tian MM, Qin AW, Ramireddy C, Webber SE, Munk P, Tuzar Z, Procházka K (1993) Langmuir 9(7):1741
115. Michels B, Waton G, Zana R (1997) Langmuir 13(12):3111
116. Waton G, Michels B, Zana R (1999) J Colloid Interface Sci 212(2):593
117. Thurn T, Couderc-Azouani S, Bloor DM, Holzwarth JF, Wyn-Jones E (2003) Langmuir 19(10):4363
118. Procházka K, Bednář B, Mukhtar E, Svoboda P, Trněná J, Almgren M (1991) J Phys Chem 95(11):4563
119. Procházka K, Kiserow D, Ramireddy C, Tuzar Z, Munk P, Webber S (1992) Macromolecules 25(1):454
120. Wang Y, Kausch C, Chun M, Quirk RP, Mattice WL (1995) Macromolecules 28(4):904
121. Smith C, Liu G (1996) Macromolecules 29(6):2060
122. Underhill R, Ding J, Birss V, Liu G (1997) Macromolecules 30(26):8298
123. Zhang L, Shen H, Eisenberg A (1997) Macromolecules 30(4):1001
124. Esselink FJ, Dormidontova EE, Hadziioannou G (1998) Macromolecules 31(9):2925
125. Esselink FJ, Dormidontova EE, Hadziioannou G (1998) Macromolecules 31(15):4873
126. Hecht E, Hoffmann H (1995) Colloids Surf A Physicochem Eng Asp 96:181
127. Goldmints I, Holzwarth JF, Smith KA, Hatton TA (1997) Langmuir 13:6130
128. Kositza MJ, Bohne C, Alexandridis P, Hatton TA, Holzwarth JF (1999) Langmuir 15(2):322
129. Kositza MJ, Bohne C, Alexandridis P, Hatton TA, Holzwarth JF (1999) Macromolecules 32(17):5539
130. Waton G, Michels B, Zana R (2001) Macromolecules 34(4):907
131. Xu R, Winnik MA, Hallett F, Riess G, Croucher M (1991) Macromolecules 24(1):87
132. Wilhelm M, Zhao C, Wang Y, Xu R, Winnik MA, Mura J, Riess G, Croucher M (1991) Macromolecules 24(5):1033
133. Xu R, Winnik MA, Riess G, Chu B, Croucher M (1992) Macromolecules 25(2):644
134. Calderara F, Hruska Z, Hurtrez G, Lerch J, Nugay T, Riess G (1994) Macromolecules 27(5):1210
135. Hickl P, Ballauff M, Jada A (1996) Macromolecules 29(11):4006
136. Jada A, Hurtrez G, Siffert B, Riess G (1996) Macromol Chem Phys 197(11):3697
137. Yin L, Hillmyer MA (2011) Macromolecules 44(8):3021
138. Li T, Wang WJ, Liu R, Liang WH, Zhao GF, Li Z, Wu Q, Zhu FM (2009) Macromolecules 42(11):3804
139. Allgaier J, Poppe A, Willner L, Richter D (1997) Macromolecules 30:1582
140. Hillmyer M, Bates F (1996) Macromolecules 29(22):6994
141. Förster S, Krämer E (1999) Macromolecules 32(8):2783

142. Kaya H, Willner L, Allgaier J, Stellbrink J, Richter D (2002) Appl Phys A Mater Sci Process 74:s499
143. Jensen G, Shi Q, Hernansanz M, Oliveira C, Deen G, Almdal K, Pedersen JS (2011) J Appl Cryst 44: 473–482
144. Jensen GV, Shi Q, Deen GR, Almdal K, Pedersen JS (2012) Macromolecules 45(1):430
145. Lund R, Willner L, Stellbrink J, Radulescu A, Richter D (2004) Physica B: Condens Matter 350(1–3):E909
146. Won YY, Davis HT, Bates FS (2003) Macromolecules 36:953
147. van Stam J, Creutz S, De Schryver FC, Jérôme R (2000) Macromolecules 33(17):6388
148. Bronstein LM, Chernyshov DM, Vorontsov E, Timofeeva GI, Dubrovina LV, Valetsky PM, Kazakov S, Khokhlov AR (2001) J Phys Chem B 105(38):9077
149. Nordskog A, Fütterer T, von Berlepsch H, Böttcher C, Heinemann A, Schlaad H, Hellweg T (2004) Phys Chem Chem Phys 6(12):3123
150. Lund R, Willner L, Richter D, Iatrou H, Hadjichristidis N, Lindner P (2007) J Appl Crystallogr 140:S327
151. Jacquin M, Muller P, Cottet H, Crooks R, Théodoly O (2007) Langmuir 23(20):9939
152. Choi SH, Bates FS, Lodge TP (2011) Macromolecules 44(9):3594
153. Lejeune E, Drechsler M, Jestin J, Müller AHE, Chassenieux C, Colombani O (2010) Macromolecules 43(6):2667
154. Palmer RG, Stein DL, Abrahams E, Anderson PW (1984) Phys Rev Lett 53(10):958
155. Lund R (2004) Chain exchange kinetics and structure of polymeric micelles – a comprehensive study of three model systems. Ph.D. thesis, Mathematisch-Naturwissenschaftliche Fakultät der Westfälischen Wilhelms-Universität Münster, Germany
156. Kambour R, Gruner C, Romagosa E (1973) J Polym Sci B Polym Phys 11(10):1879
157. Quintana J, Villacampa M, Munos M, Andrio A, Katime I (1992) Macromolecules 25(12):3125
158. Quintana J, Villacampa M, Andrio A, Munos M, Katime I (2001) Macromolecules 25(12):3129
159. Choi SH, Bates FS, Lodge TP (2009) J Phys Chem B 113(42):13840
160. Lai C, Russel WB, Register RA (2002) Macromolecules 35(3):841
161. Fredrickson GH, Bates FS (1996) Annu Rev Mater Res 26:501
162. Li Z, Dormidontova EE (2010) Macromolecules 43(7):3521
163. Nicolai T, Colombani O, Chassenieux C (2010) Soft Matter 6(14):3111
164. Grason GM (2007) J Chem Phys 126(11):114904
165. Mortensen K (1996) J Phys Condens Matter 8:A103
166. Kresheck GC, Hamori E, Davenpor G, Scheraga HA (1966) J Am Chem Soc 88(2):246
167. Bennion B, Eyring E (1970) J Colloid Interface Sci 32(2):286
168. Lang J, Eyring E (1972) J Polym Sci Part a-2-Polym Phys 10(1):89
169. Honda C, Hasegawa Y, Hirunuma R, Nose T (1994) Macromolecules 27:7660
170. Honda C, Abe Y, Nose T (1996) Macromolecules 29(21):6778
171. Ye X, Lu Y, Liu S, Zhang G, Wu C (2007) Langmuir 23:10366
172. Zhang Y, Wu T, Liu S (2007) Macromol Chem Phys 208(23):2492
173. Bednář B, Edwards K, Almgren M, Tormod S, Tuzar Z (1988) Makromolekulare Chemie-Rapid Communications 9(12):785
174. Johnson B, Prud'homme RK (2003) Phys Rev Lett 91:118302
175. Wang D, Yin J, Zhu Z, Ge Z, Liu H, Armes SP, Liu S (2006) Macromolecules 39(21):7378
176. Zhang J, Li Y, Armes SP, Liu S (2007) J Phys Chem B 111(42):12111
177. Zhang J, Xu J, Liu S (2008) J Phys Chem B 112(36):11284
178. Zhu Z, Xu J, Zhou Y, Jiang X, Armes S (2007) Macromolecules 40:6393
179. Ge Z, Cai Y, Yin J, Zhu Z, Rao J, Liu S (2007) Langmuir 23(3):1114
180. Sweeney J, Scriven L, Davis H (1987) J Chem Phys 87(10):6120
181. Noguchi H, Takasu M (2001) Phys Rev E 64:041913
182. Sevink GJA, Zvelindovsky AV (2005) Macromolecules 38(17):7502

183. Lund R, Willner L, Monkenbusch M, Panine P, Narayanan T, Colmenero J, Richter D (2009) Phys Rev Lett 102:188301
184. Wang Y, Mattice WL, Napper D (1993) Langmuir 9(1):66
185. Marrink SJ, Tieleman DP, Mark AE (2000) J Phys Chem B 104(51):12165
186. Chen T, Hynninen AP, Prud'homme RK, Kevrekidis IG, Panagiotopoulos AZ (2008) J Phys Chem B 112(51):16357
187. Egelhaaf SU, Schurtenberger P (1999) Phys Rev Lett 82(13):2804
188. Egelhaaf SU, Olsson U, Schurtenberger P (2000) Physica B Condens Matter 276–278:326
189. Bressel K, Muthig M, Prévost S, Grillo I, Gradzielski M (2010) Colloid Polym Sci 288(8):827
190. Leng J, Egelhaaf SU, Cates M (2002) Europhys Lett 59(2):311
191. Leng J, Egelhaaf SU, Cates M (2003) Biophys J 85(3):1624
192. Schmölzer S, Gräbner D, Gradzielski M, Narayanan T (2002) Phys Rev Lett 88(25):258301
193. Weiss T, Narayanan T, Wolf C, Gradzielski M, Panine P, Finet S, Helsby W (2005) Phys Rev Lett 94(3):1
194. Gummel J, Sztucki M, Narayanan T, Gradzielski M (2011) Soft Matter 7(12):5731
195. Egelhaaf SU (1998) Curr Opin Colloid Interface Sci 3(6):608
196. Nie H, Bansil R, Ludwig K, Steinhart M, Konak C, Bang J (2003) Macromolecules 36(21):8097
197. Jeong U, Lee HH, Yang H, Kim JK, Okamoto S, Aida S, Sakurai S (2003) Macromolecules 36(5):1685
198. Krishnamoorti R, Modi MA, Tse MF, Wang HC (2000) Macromolecules 33(10):3810
199. Wang CY, Lodge TP (2002) Macromolecules 35(18):6997
200. Mai Y, Eisenberg A (2012) Chem Soc Rev 41(18):5969-5985
201. Antonietti M, Förster S (2003) Adv Mater 15(16):1323
202. Won YY, Brannan AK, Davis HT, Bates FS (2002) J Phys Chem B 106(13):3354
203. Shen H, Eisenberg A (1999) J Phys Chem B 103(44):9473
204. Wang L, Yu X, Yang S, Zheng JX, Van Horn RM, Zhang WB, Xu J, Cheng SZD (2012) Macromolecules 45(8):3634
205. Bhargava P, Tu Y, Zheng JX, Xiong H, Quirk RP, Cheng SZD (2007) J Am Chem Soc 129(5):1113
206. Burke SE, Eisenberg A (2001) Langmuir 17(21):6705
207. Chen L, Shen H, Eisenberg A (1999) J Phys Chem B 103(44):9488
208. Burke S, Eisenberg A (2001) Polymer 42(21):9111
209. Nakano M, Fukuda M, Kudo T, Endo H, Handa T (2007) Phys Rev Lett 98:238101
210. Nakano M, Fukuda M, Kudo T, Matsuzaki N, Azuma T, Sekine K, Endo H, Handa T (2009) J Phys Chem B 113(19):6745

Ordering of Polypeptides in Liquid Crystals, Gels and Micelles

Chunhua Cai, Jiaping Lin, Zeliang Zhuang, and Wenjie Zhu

Abstract Ordered structures assembled from polypeptides have attracted a great deal of attention over the past few decades. Both α-helix and β-sheet conformations of polypeptides support the formation of ordered structures during the assembly process. For polypeptides with α-helix conformation, the ordered structures are formed mainly by side-by-side packing of α-helix rods. For polypeptides with β-sheet conformation, ordering of the chains can be achieved by parallel or antiparallel packing. The ordering characteristic of polypeptide chains gives rise to fascinating assembly behaviors of polypeptide homopolymers and copolymers in solution. Usually, a decrease in polymer concentration is accompanied by the assembly of polypeptides into liquid crystals (LCs), gels, and micelles. This review describes the ordering structures of polypeptides in these assemblies. In LC structures, polypeptide homopolymer chains are packed in a highly ordered fashion with smectic, nematic, and cholesteric phases. Both polypeptide homopolymers and copolymers support the formation of gels in solution. The dislocated side-by-side packing of polypeptide helices is the basic ordering characteristic of the polypeptides in gels. Compared with the α-helix conformation, gels formed from polypeptides with β-sheet conformation show higher stability. In dilute solutions, amphiphilic polypeptide copolymers can self-assemble into micelles that include cylinders, vesicles, and complex hierarchical structures. The ordering nature of the polypeptide chains can be observed in the assemblies. The close relationship with proteins makes polypeptides and their assembly structures ideal models for protein research and promising candidates in biorelated applications.

Keywords Gels · Liquid crystals · Micelles · Ordered structure · Polypeptide · Self-assembly

C. Cai, J. Lin (✉), Z. Zhuang, and W. Zhu
Shanghai Key Laboratory of Advanced Polymeric Materials, Key Laboratory for Ultrafine Materials of Ministry of Education, School of Materials Science and Engineering, East China University of Science and Technology, Shanghai 200237, China
e-mail: jlin@ecust.edu.cn

Contents

Abbreviations

AFM	Atomic force microscopy
B	Biphasic region
BD	Brownian dynamics
$CDCl_3$	Deuterated chloroform
$CHCl_3$	Chloroform
DCA	Dichloroacetic acid
DL-PA	Poly(DL-alanine)
DHP	Dendron-helical polypeptide
DMF	N,N'-dimethylformamide
DP	Degree of polymerization
DPD	Dissipative particle dynamics
EDC	Dichloroethane
I	Isotropic phase
LC	Liquid crystal
L-PA	Poly(L-alanine)
LSCM	Confocal laser scanning microscopy
NCA	N-Carboxyanhydride
PArg	Poly(L-arginine)
PBLG	Poly(γ-benzyl L-glutamate)
PClBLA	Poly(β-p-chlorobenzyl L-aspartate)
PDI	Polydispersity index
PDMS	Poly(dimethylsiloxane)
PEG	Poly(ethylene glycol)
PEO	Poly(ethylene oxide)
PFS	Poly(ferrocenylsilane)
PHEG	Poly[N^5-(2-hydroxyethyl) L-glutamine]

PIAA	Poly(isocyano-L-alanine-L-alanine)
PIAH	Poly(isocyano-L-alanine-L-histidine)
PLeu	Poly(L-leucine)
PLGA	Poly(L-glutamic acid)
PLL	Poly(L-lysine)
PMLG	Poly(γ-methyl L-glutamate)
PNIPAm	Poly(N-isopropylacrylamide)
POM	Polarizing optical micrograph
PPLA	Poly(β-phenethyl L-aspartate)
PZLys	Poly(ε-carbobenzoxy L-lysine)
S	Periodicity of cholesteric LC
SAXD	Small-angle X-ray diffraction
SAXS	Small-angle X-ray scattering
SEM	Scanning electron microscopy
SFM	Scanning force microscopy
TCE	Trichloroethylene
TEM	Transmission electron microscopy
TFA	Trifluoroacetic acid
THF	Tetrahydrofuran

1 Introduction

Over the past few decades, increasing attention has been paid to synthetic polypeptide materials, including their syntheses, properties, and applications [1–14]. Polypeptides are derived from amino acids and their derivates. The continuing interest in polypeptides is mainly stimulated by their close relationship with proteins. Polypeptides can be used as a model system for protein research. Learning from natural proteins, polypeptides with diverse structures and functionalities have been widely synthesized and studied. The biorelated applications of the polypeptides and their assemblies are active topics of current research.

Polypeptides can be synthesized through biological and chemical methods [15]. In biological strategies, pure polypeptides with exact molecular weights and identical monomer sequences can be obtained [16–18]. Chemical techniques can be applied to prepare polypeptides with high molecular weights and are also advantageous for preparing polypeptide–polymer conjugates [19–25]. The most applied chemical method for polypeptide synthesis is the N-carboxyanhydride (NCA) route, which was first proposed by Leuchs about 100 years ago [26]. The synthesis of high molecular weight polypeptides and diverse polypeptide–polymer conjugates makes the research on polypeptides an active topic.

One of the unique properties of polypeptides is that they can adopt various conformations such as intramolecularly H-bonded α-helix, intermolecularly H-bonded extended β-sheet, and flexible random coil [5, 27]. For high molecular weight polypeptides, the α-helix conformation is a predominate structure.

Polypeptides with low molecular weights usually adopt the β-sheet conformation. When polypeptides are dissolved in denaturant solvents, the random coil conformation can be observed [28, 29].

The ordered structures assembled from polypeptide homopolymers and copolymers in both bulk and solution have attracted a great deal of attention over the past few decades and could continue to be an active theme in the future [30–38]. In solution, both the α-helix and β-sheet conformations of polypeptides facilitate the formation of ordered structures in liquid crystals (LCs), gels, and micelles during the assembly process. Usually, LC structures are assembled from polypeptide homopolymers in concentrated solutions [39–41]. In solutions with moderate concentrations, gels are usually formed by both polypeptide homopolymers and copolymers [42–44]. In dilute solutions, polypeptide copolymers are able to self-assemble into diverse micelle structures with a solvophilic shell, while the solvophobic polypeptide chains are packed in an ordered manner in the micelle core [45–47].

The ordering of polypeptide chains, typically for α-helix conformation, is similar in the structures of LCs, gels, and micelles. In LCs, polypeptide homopolymers are usually packed in a side-by-side manner to form a highly ordered arrangement in the form of nematic and cholesteric phases [39, 40]. For polypeptide homopolymers with identical chain length (polydispersity index, PDI = 1.0) or polydisperse polypeptides end-capped with a bulky group, a smectic LC phase can be observed [48, 49]. In homopolymer gel structures, larger dislocation of side-by-side packing of polypeptide helices is essential to form fiber-like structures as well as physical crosslinkers [42, 50–52]. For block copolymer gels, because of the existence of flexible chains, a smectic-like packing manner of polypeptide helices is adopted, in which the long axis of polypeptide helices is perpendicular to the long axis of gel fiber, and the flexible chains are spread out into the surroundings [44, 48, 53, 54]. Polypeptide-based copolymer micelles self-assembled in dilute solutions can preserve the ordered packing of polypeptides in the aggregates of cylinders, vesicles, and complex hierarchical structures. The ordering nature within the domain endows the polypeptide micelles with unique properties compared with conventional coil–coil type copolymer micelles, e.g., high stability and diverse morphologies [55–59]. For the polypeptides with β-sheet conformation, ordered structures can be achieved by parallel or antiparallel packing of polypeptide chains, which can be found in polypeptide gels and micelles [36, 54, 60]. When the α-helix or β-sheet conformation transforms to a random coil conformation, the ordering feature of polypeptides in these structures is destroyed and a subsequent variation in structure and morphology can be observed [61–63].

The research on polypeptides and their assembly behaviors is important and beneficial for several areas. First, polypeptides can be used as a model polymer with various chain rigidities. Polypeptides can adopt conformations of α-helix, β-sheet and random coil, which can transform into each other under controlled conditions. The α-helix to random coil transition in solutions is especially interesting. Thus, polypeptides can serve as an ideal model for investigating the influence of polymer rigidity on the assembly behavior of polymers. Second, the synthetic polypeptides

can be regarded as a simple model for proteins. Both α-helix and β-sheet conformations are basic secondary structures of proteins. The studies on ordered structures of the polypeptides, especially in hierarchical structures, can contribute to the prediction of the tertiary structures of proteins. Third, due to their biocompatibility and biodegradability, polypeptides and their assemblies are promising candidates as biorelated materials for use in, for example, drug delivery and tissue engineering scaffolds. Overall, the research on polypeptides and their ordered structures can enrich our knowledge of polymer science and also provide useful information for preparing advanced materials for medical and biotechnological applications.

In this review, we summarize the features of polypeptide ordered structures in LCs, gels and micelles and outline recent advances in this field. The article is divided into four main parts. The first part reviews the ordering of polypeptide homopolymers in LC structures. Polypeptides with rigid α-helix conformation can form LCs in concentrated organic solutions. Common aspects of the LC structures are briefly described. Recent advances, such as the conformation-induced cholesteric LC chirality transitions, the discovery of smectic phase, and the reentrant isotropic transitions, are the main content of the section. In the second part, ordering of polypeptide chains in gels is discussed. The structure of homopolymer gels is compared with homopolymer LCs and studies on copolymer gels are featured in detail. Samples formed in both organic and aqueous solutions are referred to. The ordering of polypeptides in self-assembled micelles in dilute solution is summarized in the third section. The ordering structures can be found in self-assemblies of cylinders and vesicles. The ordered packing tendency makes polypeptide copolymers an important candidate for producing hierarchical aggregates. Lastly, conclusions and outlook are presented.

2 LC Structures of Polypeptide Homopolymers

Polypeptides adopt α-helix conformation when they are dissolved in organic solvents such as N,N'-dimethylformamide (DMF), $CHCl_3$, and benzene. When the concentration is relatively high, LC structures are usually formed by the side-by-side ordered packing of rigid polypeptide chains. The ordering characteristics of polypeptides was first observed from the LC structure [39, 49, 64–72]. The formation of polypeptide LCs requires two crucial characteristics, rigidity of the polymer chain and ordering of the rod chains. Thus, only the α-helix polypeptide supports the LC structures. The helix-to-coil transition of polypeptide chains can destroy the LC ordering. In this section, typical LC structures and the arrangement of polypeptide chains in the LCs are discussed.

Fig. 1 Classification of polypeptide LCs: (**a**) smectic, (**b**) nematic, and (**c**) cholesteric phases. *S* indicates the periodicity of cholesteric LC
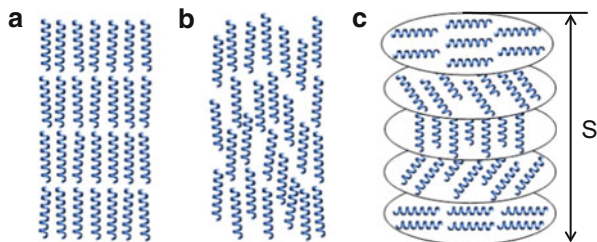
2.1 Typical LC Structures

LCs of polypeptide homopolymers were first described in the 1950s by Elliott and Ambrose, who observed a birefringent solution phase of poly(γ-benzyl L-glutamate)/chloroform (PBLG/CHCl$_3$) mixtures [71]. As shown in Fig. 1, polypeptides are able to form classical LCs with smectic, nematic and cholesteric phases. Smectic LC (Fig. 1a) shows the highest degree of order among the three phases, and is mainly found for polypeptides with identical degrees of polymerization (DPs). In the smectic phase, polypeptide chains are positionally ordered along one direction, forming well-defined layers that can slide over one another. In the nematic phase (Fig. 1b), polypeptide chains have no positional order and self-align to have long-range directional order with their long axes roughly parallel. Aligned nematics have the optical properties of uniaxial crystals, which makes them useful in LC displays. The most common polypeptide LC structure is the cholesteric phase (Fig. 1c). This phase exhibits a twisting of the molecules perpendicular to the director, with the molecular axis parallel to the director. The polypeptide molecules rotate by a small constant angle from one layer to the next. The cholesteric LCs show a unique property in that they reflect circularly polarized light when it enters along the helical axis and elliptically polarized light if it comes in obliquely. When the rotated angle of neighboring layers is zero, the cholesteric LC structure transforms to nematic phase. Therefore, in some cases, the cholesteric LC structure is classified as a chiral nematic phase.

2.2 Nematic and Cholesteric LC Structures

The most prominent characteristic of cholesteric LC is a set of equally spaced parallel lines (bright and dark lines) somewhat reminiscent of a fingerprint when observed by polarizing optical micrograph (POM). The distance between the alternating bright and dark lines is called the periodicity *S*, which is equal to half the pitch of the torsion of cholesteric LC. Such experimental results are explained by a helicoidal structure, as shown in Fig. 1c.

The periodicity *S* of polypeptide LCs is found to be dependent on the temperature, polymer concentration, solvent nature, molecular weight, etc. [40, 73–75].
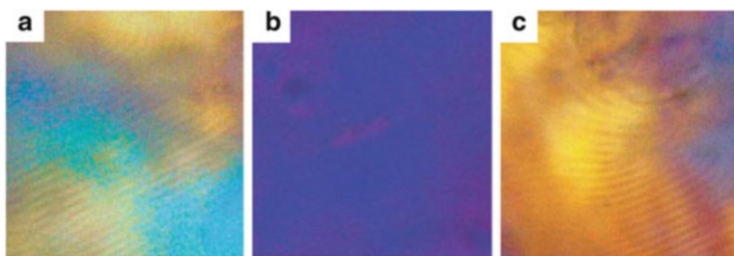
Fig. 2 POM observations of a concentrated PClBLA solution (25 wt%) in TCE. The birefringent cholesteric texture changes its sign from (**a**) left (90°C) to (**c**) right (102°C) with increasing temperature. (**b**) The cholesteric pitch diverges in the transition region (97°C). The screw sense of the polypeptide backbone transforms from right to left, accordingly. Reprinted with permission from [76]. Copyright 2005 Wiley-VCH

For example, for the system of PBLG/m-cresol LCs, in the temperature range of 30–60°C, right-handed cholesteric LCs are observed and the periodicity S increases with increasing temperature [74]. At 60°C, the cholesteric character disappears and nematic LCs are formed. Above this temperature, left-handed cholesteric structures appear and the periodicity S decreases with increasing temperature. Regarding the dependence on the nature of the solvent, results from the PBLG LCs formed in dioxane-dichloroethane mixed solvent showed that the chirality of the LC transformed from right-handed to left-handed with increasing volume fraction of dichloroethane [75]. For such phenomenon, the dielectric constant of the solvents is believed to be one of the important influencing factors. Usually, a solvent with lower dielectric constant supports a right-handed cholesteric structure.

In addition, the chirality of polypeptide backbones was found to have a remarkable influence on the handedness of LC structures. For example, Abe et al. investigated the LC structure of poly(β-*p*-chlorobenzyl L-aspartate)/trichloroethylene (PClBLA/TCE) systems [76]. They found that the chirality of the LCs is opposite to the screw sense of the polypeptide backbone. At room temperature, PClBLA takes the right-handed α-helical conformation, while the chirality of the LC is left-handed. Discrete conformation change of the polypeptide from right-handed to left-handed α-helical takes place between 80 and 100°C. Accordingly, the LC structures change from left-handed to right-handed, separated by the nematic phase. Figure 2 shows the POM images of LC structures that changed from left cholesteric (90°C) to nematic (97°C) and then to right cholesteric (102°C) with increasing temperature.

In another work on poly(β-phenethyl L-aspartate)/trichloroethylene/dichloroacetic acid (PPLA/TCE/DCA) systems, they found a more complex LC phenomenon [77]. With increasing the solution temperature, the screw sense of the polypeptide backbone changed from left-handed to right-handed and then to left-handed (L–R–L). The primary reason responsible for such a helix–helix transition resides in a small free-energy difference in the conformational states of the flanking side chain of the opposite handedness [78]. Simultaneously with the helix–helix transition,
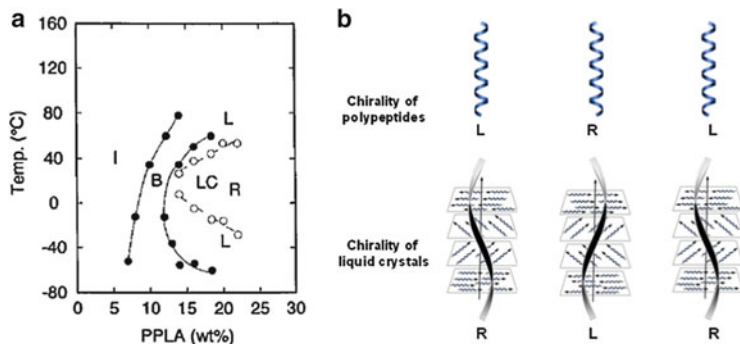
Fig. 3 (**a**) Phase diagrams for a ternary solution of PPLA in TFA/CHCl$_3$ (3/97 w/w). *Solid lines* indicate phase boundaries between liquid crystalline (*LC*) and isotropic (*I*) states and *dashed lines* those between right- and left-handed α-helical states; *B* biphasic region. (**b**) PPLA conformation-induced the transition of LC handedness. Reprinted with permission from [77]. Copyright 1997 Wiley-VCH

the handedness of LCs gradually changes from right to left and then to right (R–L–R). Thus, the temperature dependence of the LC structures can be divided into three characteristic regions: I ($T < 25°$C), II ($25°$C $< T < 89°$C) and III ($T > 89°$C), each of which is separated by the nematic phase. The cholesteric sense inversion at the boundary between regions I and II, as well as between II and III, is triggered by the reversal of the screw sense of the α-helical backbone. When DCA is eliminated from the system, the transitions shown in the lower part of Fig. 3a tend to be suppressed and a result similar to that presented in Fig. 2 from PClBLA/TCE solution can be obtained.

2.3 Smectic LCs

Smectic ordering is common in low molecular weight LC compounds and has also been observed for rodlike tobacco mosaic virus in colloidal solutions [49, 64]. However, the smectic LC phase in solution is rarely observed for polypeptide homopolymers due to the polydisperse nature of chemically synthetic polypeptide. Tirrell's group reported for the first time the formation of smectic LC structures from monodisperse polypeptides derived from PBLG (DP = 76, counter length 114 Å), which was synthesized via recombinant DNA technology [49]. The LCs of modified PBLG were obtained in mixtures of CHCl$_3$ (97%, v/v) and trifluoroacetic acid (TFA; 3%, v/v). The addition of TFA inhibits aggregation of PBLG in concentrated solutions while the low concentration does not destroy the rigidity of polymer chains. Figure 4a shows a POM image of a ~35 wt% solution of PBLG in CHCl$_3$/TFA. The solution is iridescent with a fan-like texture suggestive of smectic order. The solution-cast films maintained their LC order after solvent
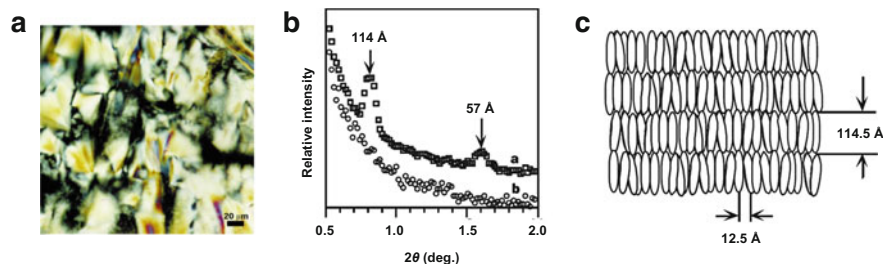
Fig. 4 (**a**) POM image of PBLG in CHCl$_3$/TFA. (**b**) Densitometer scans of the SAXD patterns of films prepared from solutions of monodisperse PBLG (*curve a*) and polydisperse PBLG (*curve b*). (**c**) Smectic structure of PBLG, showing the origin of the 12.5 Å and 114.5 Å reflections. Reprinted from [49], by permission from Macmillan Publishers Ltd: Nature, copyright (1997)

evaporation. The densitometer scan of the SAXD pattern of the film (Fig. 4b, curve a) shows a well-defined maximum at a spacing of 114.5 $\pm$ 1.4 Å, as well as the corresponding second-order reflection at 57.0 $\pm$ 0.3 Å. The coincidence of the helix length and the observed layer spacing strongly suggests smectic-like ordering in the cast solid film. In contrast, a solid film of polydisperse PBLG with comparable molecular weight (DP $\approx$ 98, PDI = 1.2) yields no small-angle reflections in a similar diffraction experiment (Fig. 4b, curve b). Shown in Fig. 4c is the illustration for the smectic LC structures. As can be seen, the helical rods arrange in layers of thickness 114.5 Å, and the distance between two PBLG rods is 12.5 Å, which corresponds to the diameter of PBLG rods.

The polydispersity of polymer is the main reason for the lack of a smectic LC phase of chemically synthetic polypeptides. However, when a compact and bulky group is capped on polypeptide ends, the situation can be rather different. During self-assembly in concentrated solutions, such modified polypeptides can self-assemble into a smectic LC phase [48, 79]. For example, Winnik et al. found that dendron-helical PBLG (DHP; Fig. 5a) copolymers can form smectic phases in CHCl$_3$ [48]. The dendritic block prevents the DHP copolymers from aligning into a nematic phase. As shown in Fig. 5b, the concentrated solution (>40 wt%) of the DHP copolymers in THF shows a birefringent texture under the POM observation. SAXS experiments on the dried solid from the concentrated THF solution show two diffraction peaks at 7.2 and 3.3 nm, which suggests that the DHP exhibits smectic-like order in concentrated solution. The proposed two-dimensional layer structure of DHP that results from an antiparallel stacking of DHP is presented in the inset of Fig. 5b. The result suggests that smectic ordering of the DHP copolymers in solution is feasible with a dendritic molecule as a non-random coil block, even though the PBLG block is polydisperse in chain length. However, it should be noted that due to the polydispersity of PBLG blocks and the flexible nature of the peripheral alkyl chains of the dendron block, the LC phase of DHP is not well ordered and thus it is proper to call the LC structure a "smectic-like" phase.

The success in constructing highly ordered smectic phase in solution by using modified polydisperse polypeptide homopolymers rather than monodisperse
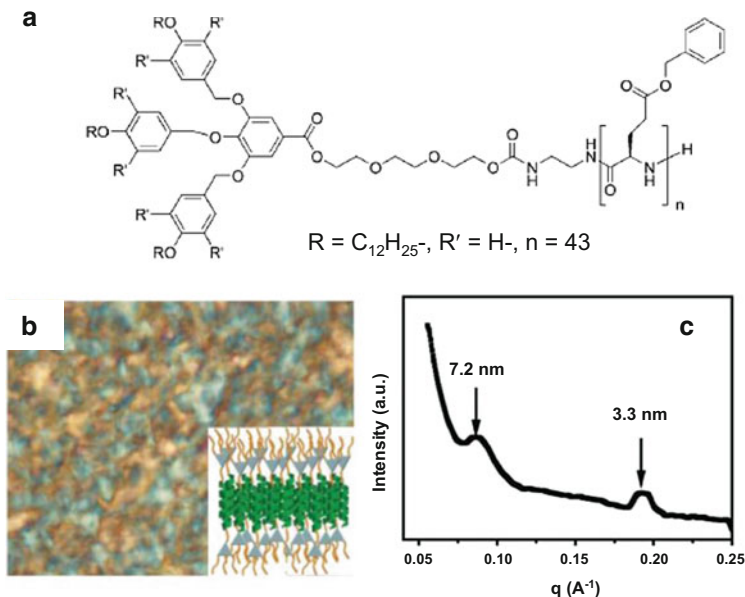
Fig. 5 (**a**) Molecular structure of dendron-helical polypeptide (DHP) copolymers. (**b**) Optical birefringent texture of THF solution of DHP (40 wt%) and proposed layered structures of LC state (*inset*). (**c**) SAXS profile of dried solid of THF solution. Reproduced from [48] with permission of The Royal Society of Chemistry

samples is significantly valuable for the preparation of well-defined supramolecular structures. From smectic PBLG LCs, highly ordered ultrathin PBLG films with controlled layer spacing and thickness can be prepared. When the rods are oriented perpendicular to the substrate, they can be used as nonlinear optical and piezoelectric materials [49, 64]. When the rods in the films are organized parallel to the substrate, the mono- or multilayer films are useful in creating patterned arrays for use in sensor technology. In addition, the LCs can be further functionalized through functionalizing the tethered bulky groups or polymer chains. The findings on the smectic LC structure from modified polydisperse PBLG thus not only promote understanding of the fundamental physics of rodlike polymers, but also have substantial impact for the application of rodlike polymers in a variety of technologies.

2.4 Reentrant Isotropic Transition of Polypeptide LCs

Polymer chains with fully rigid conformation are rare in nature. Usually, the nematogenic chain molecules are able to adopt a variety of conformations, some more extended and rodlike than others. Occurrence of liquid crystallite in such
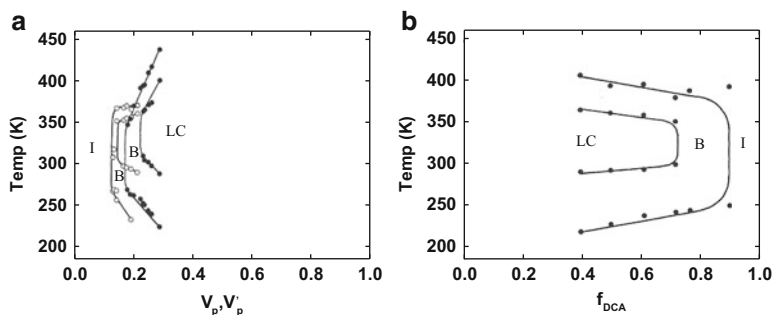
Fig. 6 (**a**) Phase diagram for PBLG/DCA/EDC ternary system. *Open circles* indicate the values obtained for PBLG ($M_v = 130,000$) dissolved in DCA/EDC (85.3/14.7 w/w). *Solid circles* are those for PBLG ($M_v = 62,000$) dissolved in DCA/EDC (80/20 w/w). (**b**) Phase boundary curves of PBLG/DCA/EDC solutions as functions of acid composition at a given polymer volume fraction of 0.25, where f_{DCA} (mole fraction) = DCA/(DCA + EDC). *I* Isotropic phase, *B* biphasic region, *LC* liquid crystalline phase. Reprinted with permission from [80]. Copyright 1997 Elsevier

systems must invariably be accompanied by selective reorganization favoring more extended chain conformations. The intramolecular conformational change can, therefore, be coupled with the isotropic–anisotropic transition and be accelerated by the intermolecular order. Such an effect is termed "conformational ordering" and pertains to semi-rigid chains in general.

An example of conformational ordering is the reentrant isotropic phase transition in polypeptide LCs. In the presence of a denaturant acid, the polypeptide molecules tend to adopt a random coil state by lowering the temperature [80–82]. An anisotropic–isotropic transition(reentrant transition) occurs at low temperature because the coil chain is unable to support the LC ordering. Shown in Fig. 6a is a typical phase diagram of a PBLG/DCA/dichloroethane (PBLG/DCA/EDC) system in which PBLG samples have relative molecular weights (M_r) of 130,000 and 62,000 [80]. Two anisotropic–isotropic transitions occur at high and low temperatures, with the latter a result of the intramolecular conformation transformation from helix to coil. An acid-induced LC to isotropic transition was also observed. The result is replotted in Fig. 6b. With increasing acid content, the LC phase tends to be destabilized along both the high- and low-temperature boundaries. In the range of high acid concentrations, no LC phase could be observed at any temperature due to the coiled molecular conformations being unable to sustain the anisotropic ordering. The helix structures tend to remain more stable in the LC state than in the isotropic phase due to the conformational ordering effect exerted by the environment.

Regarding the theoretical considerations for the possibilities of a reentrant isotropic phase in the polypeptide LC, Lin et al. proposed a theory based on the Flory–Matheson lattice model in which the free energy change for the helix–coil transition has been incorporated into the lattice scheme [80]. Some assumptions were also adopted. First, the molecular conformation in the isotropic phase was considered to be temperature-dependent and follow a modified Zimm–Bragg notion
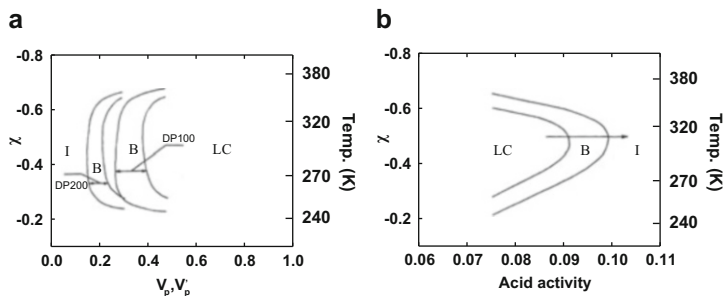
Fig. 7 (**a**) Phase diagrams calculated for DP = 100 and 200. (**b**) Plot of solvent–polymer interaction parameter (χ) values and phase transition temperatures versus acid activity at a given polymer volume fraction of 0.45. *I* Isotropic phase, *B* biphasic region, *LC* liquid crystalline phase. Reprinted with permission from [80]. Copyright 1997 Elsevier

for the helix–coil transition, in which the acid effect has been taken into account. Second, the solvent–polymer interaction parameter (χ) was considered to be negative in the whole temperature range and was regarded as an inverse measure of temperature.

Figure 7a shows a typical calculated phase diagram for polypeptides in denaturant solvents. Two samples of DP = 100 and DP = 200 are considered. Taking the curve for DP = 100 as an example, on the left-hand side of the diagram (low polymer volume fraction, v_p) all solutions are isotropic. Within the intermediate χ value or temperature range, a single anisotropic phase forms when the polymer concentration becomes higher. The transition from the isotropic to the anisotropic phase is bridged by a biphasic chimney-like region. As the temperature goes down, or equivalently χ turns positive, v_p and v_p' tend to be higher, and eventually no anisotropic phase can be formed. In other words, with a decrease in temperature, an anisotropic-to-isotropic reentrant transition caused by the intramolecular helix–coil transformation is predicted. In this reentrant isotropic region, the rigid helix anisotropic phase is in equilibrium with an isotropic solution comprising flexible chain molecules. At higher temperatures, a gradual blending of the chimney region towards a higher concentration region is demonstrated. Such a blending is related to the enhanced chain flexibility in the isotropic phase caused by the thermal energy at elevated temperatures, as normally observed in real polymer systems. These results reproduced well the experimental observations shown in Fig. 6a.

The effect of acid activity on the reentrant isotropic phase was also examined. Figure 7b shows the theoretical results for both high- and low-temperature anisotropic–isotropic transition temperatures as functions of acid activity at a given polymer concentration. As can be seen, with increasing acid content, the LC phase tends to be destabilized along both the high- and low-temperature boundaries and lower temperature reentrant isotropic transition tends to take place at higher temperatures. In the range of high acid concentration, no LC phase could be detected at any temperature due to the coiled molecular conformations being unable to sustain the anisotropic ordering. These predictions are also in line with the experiments shown in Fig. 6b.
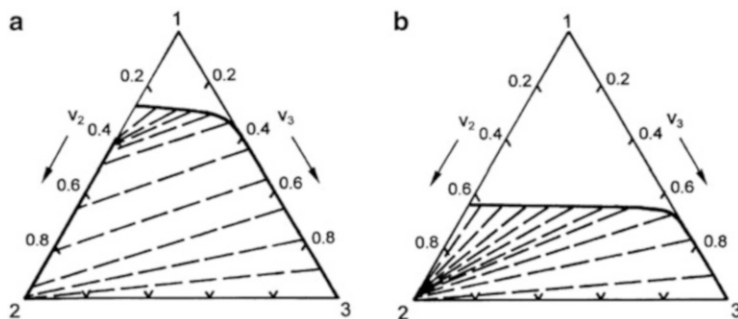
Fig. 8 Phase diagrams calculated for the ternary systems at (**a**) 300 K and (**b**) 245 K; v_2 and v_3 are the volume fraction of polypeptide and coil polymer, respectively. Reprinted with permission from [83]. Copyright 2003 American Chemical Society

Lin et al. further extended the theoretical considerations from binary systems to ternary systems involving polypeptide chain and a randomly coiled polymer [83]. Two polymers are predicted to be miscible in isotropic phase. However, the flexible chains are severely excluded from conjugated anisotropic phases (see Fig. 8a). If denaturing component is present in the ternary system, the polypeptide can undergo helix–coil transition as the temperature decreases. Such a reduction in the backbone rigidity should enlarge the miscible isotropic phase, as shown in Fig. 8b. A further decrease in temperature could result in entire elimination of the anisotropic phase (reentrant isotropic phase) due to the random coil polypeptide structure being unable to support the anisotropic ordering. On the other hand, increasing temperature results in diminishing of the anisotropic–isotropic biphasic area. At higher temperatures, the polypeptide chains become flexible. As a result, the LC phase diminishes because of the flexible chains being unable to support the anisotropic ordering.

The lattice model, as put forth by Flory [84, 85], has been proved successful in the treatments of the liquid crystallinity in polymeric systems, despite its artificiality. In our series of work, the lattice model has been extended to the treatment of biopolypeptide systems. The relationship between the polypeptide ordering nature and the LC phase structure is well established. Recently, by taking advantage of the lattice model, we formulated a lattice theory of polypeptide-based diblock copolymer in solution [86]. The polypeptide-based diblock copolymer exhibits lyotropic phases with lamellar, cylindrical, and spherical structures when the copolymer concentration is above a critical value. The tendency of the rodlike block (polypeptide block) to form orientational order plays an important role in the formation of lyotropic phases. This theory is applicable for examining the ordering nature of polypeptide blocks in polypeptide block copolymer solutions. More work on polypeptide ordering and microstructure based on the Flory lattice model is expected.

3   Ordering of Polypeptides in Gel Structures

Gels are soft materials comprising a liquid-like phase and a solid network, the latter preventing the bulk flow of the liquids. They have potential in diverse applications for tissue engineering, nanoscale electronics, etc. Polymer gels are usually formed in a moderately concentrated solution, in which physical or chemical crosslinks are necessary. Both polypeptide homopolymers and copolymers can assemble into gel structures. Similar to that in LCs, the ordering of polypeptide chains takes important responsibility for the gelation behavior. In addition to the α-helix conformation, the β-sheet conformation also supports the formation of polypeptide gels. In this section, the ordering of polypeptides in gel structures is discussed. The content is organized into three subsections. The first section describes the organic gels formed by polypeptide homopolymers, the second polypeptide block copolymer gels in organic solvents, and the third hydrogels formed by polypeptide block copolymers in aqueous solutions.

3.1   Polypeptide Homopolymer Gels in Organic Solvents

Polypeptide homopolymers (typically PBLG) with rigid α-helix conformation can form LC structures at a high concentration and temperature. When the solution is cooled, a transparent, mechanically self-supporting gel is always observed [42, 87–91]. The gel formation was found to be concentration and temperature dependent and completely reversible. It is well known that the physical or chemical crosslinks are necessary for polymer gels. Flexible polymers can easily form crosslinking domains with crystalline or semicrystalline structures. However, for rigid polypeptide chains, it is less clear how the rodlike polypeptides participate extensively in intermolecular crosslinks.

There are various approaches to explain this effect but a common aspect is that rigid polypeptide chains aggregate into nanofibers and the interfiber crosslinking results in the formation of networks. Figure 9a shows a TEM photograph of the PBLG gels from DMF (concentration 1 wt%) [42]. Random networks were observed to be formed by branching and rejoining of different strands. The strands are of diameters ranging from tens to hundreds nanometers and are composed of bundles of aligned rods (rod diameter ~2 nm, corresponding to the diameter of PBLG helix). The benzene ring interaction or stack, as well as the dislocated side-by-side packing tendency of PBLG rods, is responsible for the formation of such strands. Figure 9b shows a scheme for the polypeptide gel structure. As can be seen, physical crosslinks are formed by the branching and rejoining of different sheaf-like aggregates, which stabilize the gel structures in solution.

Usually, gels are physically crosslinked and the ordered structures cannot be preserved under heating or other treatments because of the breakage of the physical crosslinks. However, when the gels are chemically crosslinked, the shape and inner
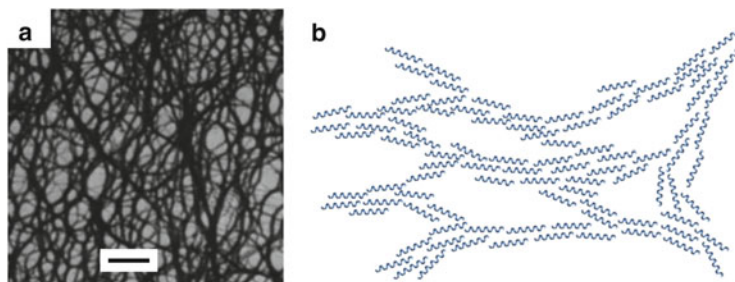
Fig. 9 (**a**) TEM photograph of a PBLG-DMF gel (dry state, scale bar = 1 μm). (**b**) Model of networks formed by aggregation of rigid polymers. Reprinted by permission from Macmillan Publishers Ltd: Nature, [42], copyright (1981)

structure of the gels can be recovered by reversing the solution conditions. An example is crosslinked "LC gel." The LC polypeptide gels are usually prepared by crosslinking the LC polypeptides (typically using diamines) and subsequently lowering the solution temperature [92–94]. Very recently, Inomata et al. reported a preparation of uniaxially oriented PBLG LC gels by crosslinking the lyotropic LC PBLG through pentaethylenehexamine in a magnetic field. Meanwhile, the PBLG was converted to PHEG by side chain aminolysis [94]. The obtained PHEG gel retains the LC structure when immersed in ethylene glycol, which is an α-helix-supporting solvent. By the addition of water into the immersion solvent, conformational transition of PHEG from α-helix to random coil occurs and the optical anisotropy of the gel disappears. With this helix-to-coil transition of PHEG, the gel is swollen in the direction perpendicular to the orientational axis of PHEG and is shrunk in the parallel direction. Such a reverse gel shape transition from cylindrical to isotropic with the change of the solvent from helix-supporting ethylene glycol to coil-supporting water is shown in Fig. 10. The original cylindrical shape in the LC state changes to the more isotropic shape as a result of the helix-to-coil transition of PHEG. Because the gel is crosslinked, not only the position but also the orientational order of the rodlike polypeptide chains is fixed. This anisotropic feature characteristic of polypeptide gels may be useful in shape-memory applications, in contrast to conventional stimuli-sensitive polymer gels that are in the disordered isotropic state.

3.2 Ordering of Polypeptides in Copolymer Organogels

Polypeptide copolymers can assemble into gels in organic solvent through ordered packing of polypeptide blocks with conformations of both α-helix and β-sheet [44, 48, 53, 54, 95–100]. For copolymers with α-helix polypeptides, the side-by-side packing of the polypeptide rods in a smectic fashion has been commonly observed. For the copolymers with β-sheet polypeptides, the strong intermolecular

Fig. 10 Illustration of the helix-to-coil transition, anisotropic-to-isotropic transition, and shape change of the uniaxial PHEG gel. Reprinted with permission from [94]. Copyright 2012 American Chemical Society

Gel formed by α-helices   **Gel formed by random coils**
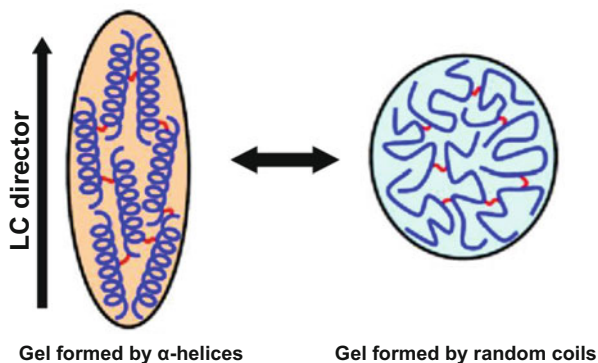
attractions are responsible for the formation of stable gels. Due to the good solubility of polypeptide in diverse solvents, organogels can be easily prepared at the proper concentration and temperature. In the following section, we discuss the formation of organic gels from polypeptide block copolymers with both α-helix and β-sheet conformations.

3.2.1 Organic Gels from Polypeptide Copolymer with α-Helix Conformation

Polypeptides with α-helix conformation prefer to take ordered packing in solutions and thus induce the formation of LCs and gels. Similar to LC structures formed by bulky group-capped polypeptide homopolymers, as described in the Sect. 2.3, the smectic-like rather than nematic ordering of polypeptide rods is preferred for polypeptide block copolymers. In the polypeptide copolymer gels, the long axis of the polypeptide rods is usually perpendicular to the long axis of gel fiber. Winnik et al. reported, for the first time, thermoreversible gelation of polypeptide block copolymers in organic solvent [44]. In their work, poly(ferrocenylsilane)-b-PBLG (PFS-b-PBLG) block copolymers (Fig. 11a) were first dissolved in hot toluene. Upon cooling to ambient temperature, optically transparent gels were formed (Fig. 11b). Fibrous nanoribbons can be observed in the AFM image shown in Fig. 11c. For these gels, the strong dipolar interactions between the PBLG helices are proposed to stabilize the stacked structure, where the PFS blocks protrude outside of the ribbon into the toluene-rich environment, thereby preventing aggregation of the nanoribbons. The gel structure is illustrated in Fig. 11d. As can be seen, PBLG rods assembled in one-dimensional antiparallel stacking of the building blocks in a monolayer fashion, and the flexible PFS blocks extended off the fibers.

In a recent work, Mezzenga et al. synthesized PBLG-b-PDMS-b-PBLG triblock copolymers with DP of PBLG blocks from 24 to 120. For these block copolymers, the conformation of the PBLG blocks is mainly α-helix. Thermoreversible gels were prepared in toluene [63]. The gel structure is illustrated in Fig. 12a and shows that PBLG rods are confined within the core of the nanofibrils, whereas the soluble
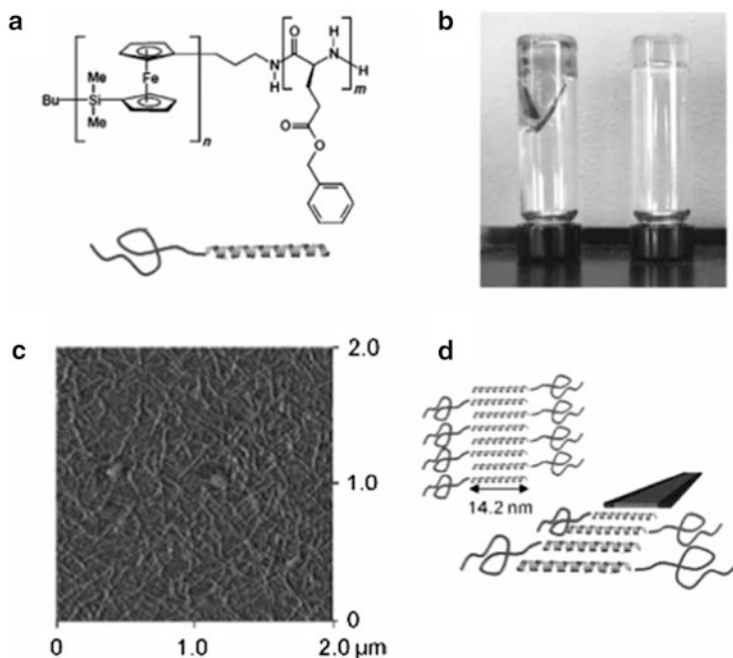
Fig. 11 (**a**) Structure of PFS-*b*-PBLG block copolymer. (**b**) Optical photograph of inverted vials containing a toluene-swollen gel. (**c**) AFM image of PFS-*b*-PBLG gel. (**d**) Scheme of the nanoribbon formed in the network structure of the gel. Reprinted with permission from [44]. Copyright 2005 Wiley-VCH

PDMS coils remain exposed to the toluene. They found that the thickness of the nanofibrils changes little with the DP of PBLG blocks. As shown in Fig. 12b, for the sample with the shortest PBLG block (DP = 24), PBLG rods assembled into a bilayer morphology with 7 nm thickness. Increasing the DP to 43, a monolayer morphology with 6–8 nm thickness is observed (Fig. 12c). Interestingly, for the sample with the longest PBLG block (DP = 120), PBLG rods are packed with a folded manner to produce 9-nm thick fibrils (Fig. 12d).

3.2.2 Organic Gels from Polypeptide Copolymer with β-Sheet Conformation

Strong interchain attractions between polypeptides with β-sheet conformation enable polypeptide chains to pack in an orderly manner, which facilities the formation of gels. Furthermore, these polypeptide gels are more stable because the interchain attractions between β-sheets are much stronger than those between helix–helix pairs. Schlaad and coworkers have investigated the effects of the secondary structure of polypeptides on the gelation of polypeptide-based organo-gelators in THF [36]. Three poly(ethylene oxide)-*b*-poly(ε-carbobenzoxy L-lysine)
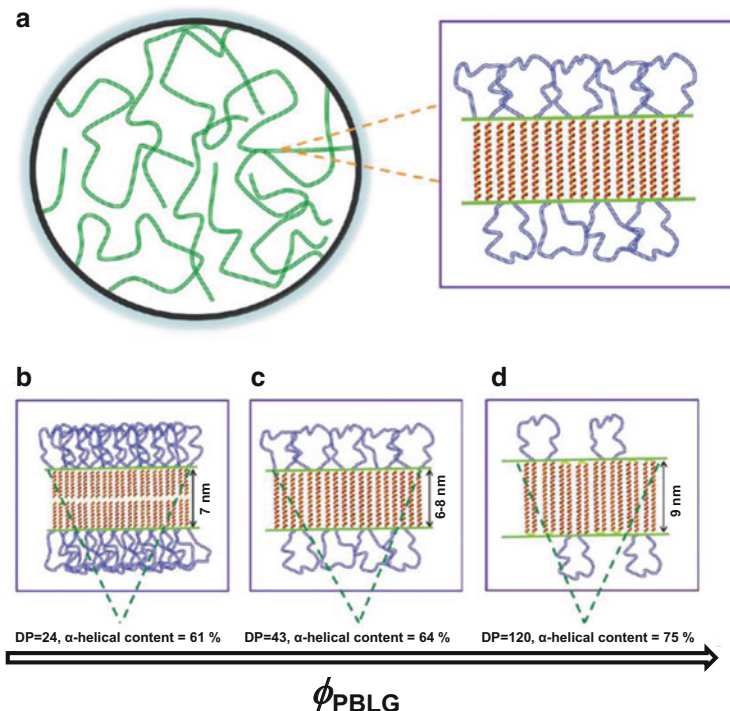
Fig. 12 (**a**) Self-assembly of the PBLG rods during the nanofibril formation for the PBLG-*b*-PDMS-*b*-PBLG triblock copolymers. (**b–d**) Changes in thickness due to the increase in the degree of polymerization of the PBLG block: (**b**) DP = 24, a head-to-head bilayer morphology of the α-helical rods; (**c**) DP = 43, a monolayer morphology; and (**d**) DP = 120, a head-to-head packing of folded α-helical rods. Reprinted with permission from [63]. Copyright 2012 American Chemical Society

(PEO-*b*-PZLys) block copolymers (samples 1, 2 and 3) with various polypeptide conformations were synthesized. All the polypeptide blocks consisted of 18 ZLys peptide segments with D and L configurations of predefined stereosequences. In sample 1, D and L configuration peptide units are randomly polymerized (L_{10}-*co*-D_8) and the polypeptide conformation is random coil. In sample 2, D and L configuration peptide units link in a manner similar to that of a triblock copolymer ($L_7D_4L_7$) and the polypeptide conformation is β-sheet. In sample 3, all the peptide segments are in the L configuration (L_{18}) and thus the polypeptide adopts α-helix conformation. From the time-dependent evolution of the dynamic viscosity of THF solutions of the samples (shown in Fig. 13a), it was found that the tendency for gelation in THF increases in the order of the polypeptide conformation of random coil < α-helix < β-sheet. For example, at the concentration of 20 g/L, samples 1 and 3 are liquids and sample 2 is a gel (Fig. 13b). From the set of SFM images shown in Fig. 13c–e, one can see that sample 1 formed spherical micelles (Fig. 13c) whereas
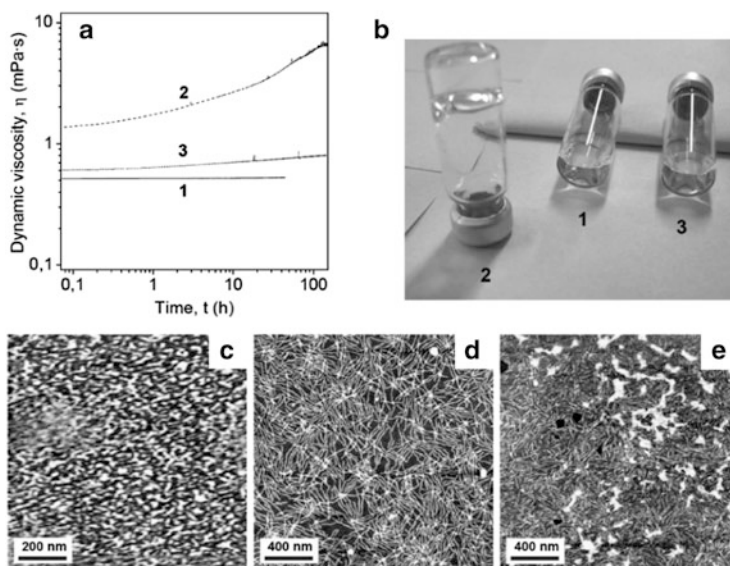
Fig. 13 (**a**) Time-dependent evolution of the dynamic viscosity of THF solutions of samples *1–3* (5 g/L) at room temperature. (**b**) Photographs of samples at 20 g/L in THF. (**c–e**) SFM height images of samples *1* (**c**), *2* (**d**), and *3* (**e**) at 20 g/L in THF. Reprinted with permission from [36]. Copyright 2011 American Chemical Society

nanofibrils formed for sample 2 and 3 (Fig. 13d, e). Evidently, the fibrils of the gelled sample 2 are considerably longer than those of the nongelled sample 3.

Organogels could potentially be used in fields of template synthesis and functional materials [101–104]. Stable organogels with controlled structure and functionality are thus highly desired to meet practical applications. The high stability of the polypeptide gels due to the ordered packing tendency of the polypeptide chains is a significant advantage. Meanwhile, polypeptide blocks are easily functionalized, which makes them promising candidates for preparation of organogels with diverse functions. Moreover, the variability of the chirality of the polypeptide backbone should bring additional opportunity to fabricate smart organogels. However, there are few works so far on the preparation of functional organogels with controlled structures. Further investigations are needed on the dependence of structure and functionality of organogels on polypeptide building blocks as well as on preparation strategies.

3.3 Hydrogels Formed by Polypeptide Block Copolymers

In recent years, hydrogels have obtained increasing attention because they have promising applications in biorelated areas, e.g., drug delivery, tissue engineering, etc. [2, 105–116]. Because hydrophobic polypeptide chains cannot be dissolved in

Fig. 14 (**a**) Conformational changes of PEG-*b*-L-PA in water as a function of polymer concentration. *Thick straight brown lines, thick flexible brown lines*, and *thin flexible blue lines* denote the β-sheet structure, random coil structure and flexible PEG, respectively. (**b**) Temperature-induced sol-to-gel transition of PEG-*b*-L-PA. As the temperature increases, PEG (*thin flexible blue lines*) is partially dehydrated (*thick flexible yellow lines*). Reproduced from [117] with permission of The Royal Society of Chemistry
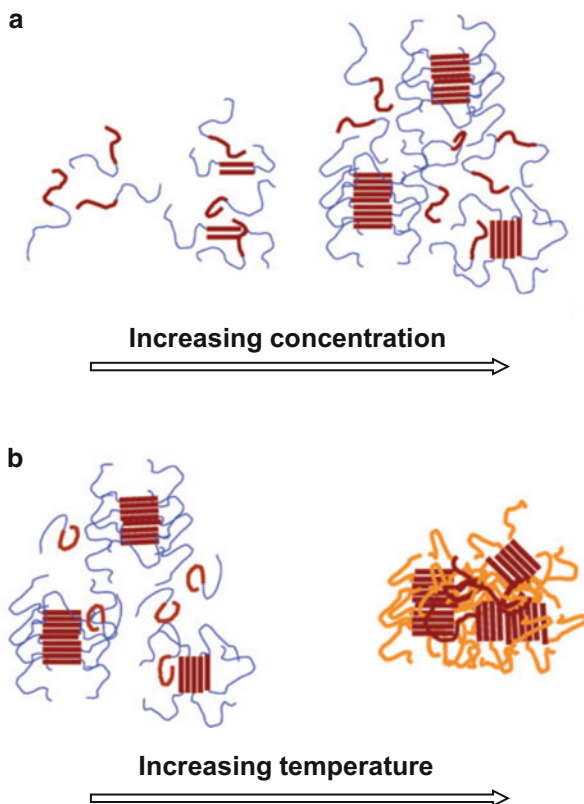
water, it is difficult for the copolymers bearing high molecular weight hydrophobic polypeptide blocks to form hydrogels. On the other hand, hydrophilic polypeptides usually adopt a random coil conformation, which does not support the formation of gel containing ordered structures. As a result, polypeptide hydrogels are usually formed by copolymers consisting of low molecular weight polypeptides. This section discusses the formation of polypeptide copolymer hydrogels based on both β-sheet and α-helix polypeptide blocks.

3.3.1 Hydrogels Based on β-Sheet Polypeptide Copolymers

Jeong et al. studied the gelation behavior of poly(ethylene glycol)-*b*-poly(L-alanine) (PEG-*b*-L-PA) block copolymers in water [117, 118]. They suggested that the β-sheet structure of L-PA plays a critical role in developing a fibrous nanostructure as well as in the sol-to-gel transition of the copolymer solutions (Fig. 14). The conformation of L-PA in water is random coil at low concentrations. As the concentration increases, block copolymers start to aggregate and the conformation
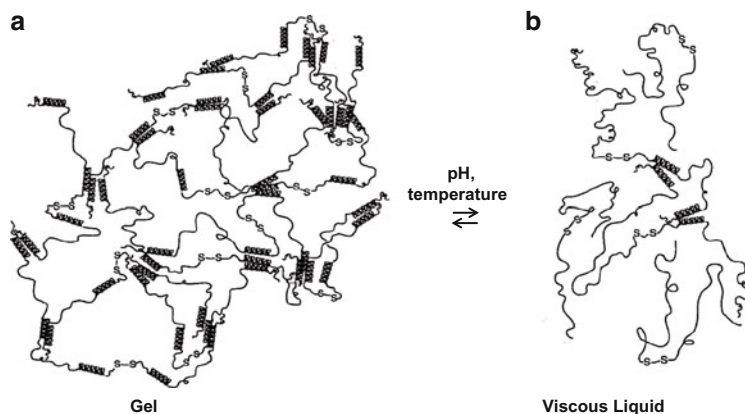
Fig. 15 Proposed physical gelation of monodisperse triblock artificial protein: (**a**) gel; (**b**) viscous liquid. From [119]. Reprinted with permission from AAAS

of L-PA transforms to β-sheet. Further increase of the polymer concentration results in nanofibrous rod formation through the packing of the β-sheet in a one-dimensional manner. Such a nanostructural growth can be stabilized by the hydrophilic PEG blocks (Fig. 14a). As the temperature increases, the PEG blocks are partially dehydrated and the sol-to-gel transition occurs by the further aggregation of preassembled PEG-*b*-L-PA aggregates at high concentrations of polymer (Fig. 14b). As a controlled experiment, they also studied the gelation behavior of PEG-*b*-DL-PA block copolymers in the same conditions. Poly(DL-alanine) (DL-PA) always takes random coil conformation. With increasing polymer concentration, the PEG-DL-PA cannot form specific nanostructures. Therefore, PEG-*b*-DL-PA shows a sol-to-gel transition at much higher concentrations and temperatures.

3.3.2 Hydrogels Based on α-Helix Polypeptide Copolymers

There are a few reports focused on hydrogels from block copolymers consisting of α-helix polypeptide segments. Tirrell et al. investigated the gelation of a multidomain ("triblock") artificial protein in which the interchain binding and solvent retention functions were engineered independently [119]. The authors describe a polypeptide consisting of 230 amino acids, 84 of which make up the helix repeat and 90 of which make up the alanylglycine-rich repeat. The helical motifs can form coiled-coil aggregates in near-neutral aqueous solutions, which trigger the formation of a three-dimensional polymer network, with the polyelectrolyte segments retaining solvent and preventing precipitation of the chains (Fig. 15a). Dissociation of the coiled-coil aggregates through increasing the pH or temperature causes dissolution of the gel (Fig. 15b). These hydrogels have potential

Fig. 16 (**a**) Representation of a block copolypeptide chain and (**b**) proposed packing of block copolypeptides into twisted fibrillar tapes. Polylysine chains were omitted from the fibril drawing for clarity. Reproduced from [105] with permission of The Royal Society of Chemistry
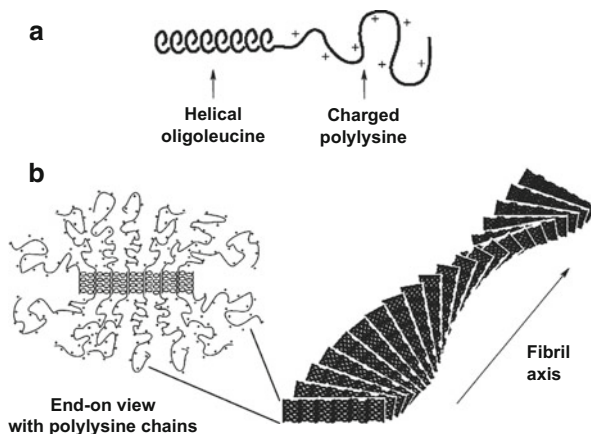
in bioengineering applications that require the encapsulation or controlled release of molecular and cellular species.

Studying the gelation behavior of poly(L-lysine)-b-poly(L-leucine) (PLL-b-PLeu) diblock copolypeptide, Deming et al. found that the self-assembly process of block copolymers is responsible for gelation and that the gel-forming ability increases with the length of water-soluble PLL chains [105, 107, 108]. The copolymer and gel structure models are presented in Fig. 16a, b. The longer PLL polyelectrolyte segments increase interchain repulsions so that the packing of PLeu hydrophobic helices, which appear to prefer to form flat two-dimensional sheets, must distort to minimize the overall energy of the system. The best way to do this, while maintaining favorable helix packing, is to twist the sheets into fibrillar tapes, where the tape width is determined by the degree of twist. In this model, the helices are still able to pack perpendicular to the fibril axis, but with a slight twist between planes of parallel packed helices.

From these examples, we conclude that both the α-helix and β-sheet conformations support the gelation of polypeptide homopolymers and copolymers. For homo-polypeptide organogels, the building polymers usually have large relative molecular weights (usually in the scale of 10^4–10^6), thus the strength of the gels can be quite good. However, for block copolymer gels, most polymers have low relative molecular weights (typically from hundreds to thousands), thus the mechanical property is poor, which inhibits their application. Improving the mechanical properties of polypeptide gels is one of the main tasks. Due to the strong intermolecular attractions, the polypeptide copolymers with β-sheet conformation have better gelation ability and strength. Thus, preparing copolymers with multiblocks of β-sheet polypeptide could be an efficient way to improve the gel strength. In addition, partially modifying high molecular weight polypeptide with hydrophilic segments, for example grafting hydrophilic side chains onto a hydrophobic polypeptide backbone, is also a promising approach for preparing stable hydrogels. However, related works are limited, especially for hydrogels. Studies of this topic are expected.

4 Ordering of Polypeptide Chains in Micelles

In dilute solutions, block copolymers can self-assemble into micelles with a core–shell structure, which have great potential applications in drug delivery systems, coatings, cosmetics, and nanoreactors [120–127]. In selective solvents, block copolymers consisting of solvophobic polypeptide segments, such as PBLG and PZLys, can self-assemble into diverse structures through ordering of polypeptide chains with the α-helix conformation. The helical polypeptide–solvophilic polymer conjugates are typical rod–coil copolymers. As compared with intensively investigated coil–coil block copolymers, the self-assembly behavior of rod–coil block copolymers is far from well studied. Polypeptide-based rod–coil block copolymers can be used as model copolymers for investigating the effect of ordered packing of the rods on the self-assembly behavior of block copolymers. Besides the α-helix conformation, ordered packing of β-sheet polypeptides is also observed in micelles. Graft copolymers are another important category of copolymers capable of forming aggregates. This section describes the ordering of polypeptide chains of block and graft copolymers as well as copolymer mixtures in assembly structures of cylindrical micelles, vesicles, and other complex structures.

4.1 Cylindrical Micelles Self-Assembled from Polypeptide Copolymers

The fiber-like structure of polypeptide block copolymers is essential in organogels that are formed by the side-by-side packing of polypeptide rods. Similarly, such side-by-side packing of polypeptide rods can also be found in cylindrical micelles self-assembled from polypeptide block copolymers. In both the fiber-like gels and cylindrical micelles, polypeptide rods assemble into ordered structures, while the flexible chains are spread out into the surroundings to stabilize the structures.

In a recent work, Lin et al. reported the self-assembly behavior of PBLG-*b*-PEG block copolymer in CHCl$_3$/ethanol/TFA mixed solution. In solution, the micelles are formed with PEG as the shell and PBLG as the core [61]. In the absence of TFA, PBLG adopts a rigid α-helix conformation and the block copolymers self-assemble into cylindrical micelles (Fig. 17a). With the introduction of TFA into the solution, the conformation of PBLG transforms from α-helix to random coil and the aggregate morphology transforms to spherical micelles (Fig. 17b). Concomitantly with the changes in morphology, the micelle size tends to become smaller. Further understanding of such a micelle morphology transition induced by polypeptide conformation variation is assisted by a Brownian dynamics (BD) simulation. Based on the experimental and simulation results, a well-founded mechanism regarding the effect of PBLG conformation on the self-assembly behavior was proposed. As shown in Fig. 17c, polypeptide blocks within the cores are interdigitated and favor ordered parallel packing, with their long axis aligning in an orientation vector.
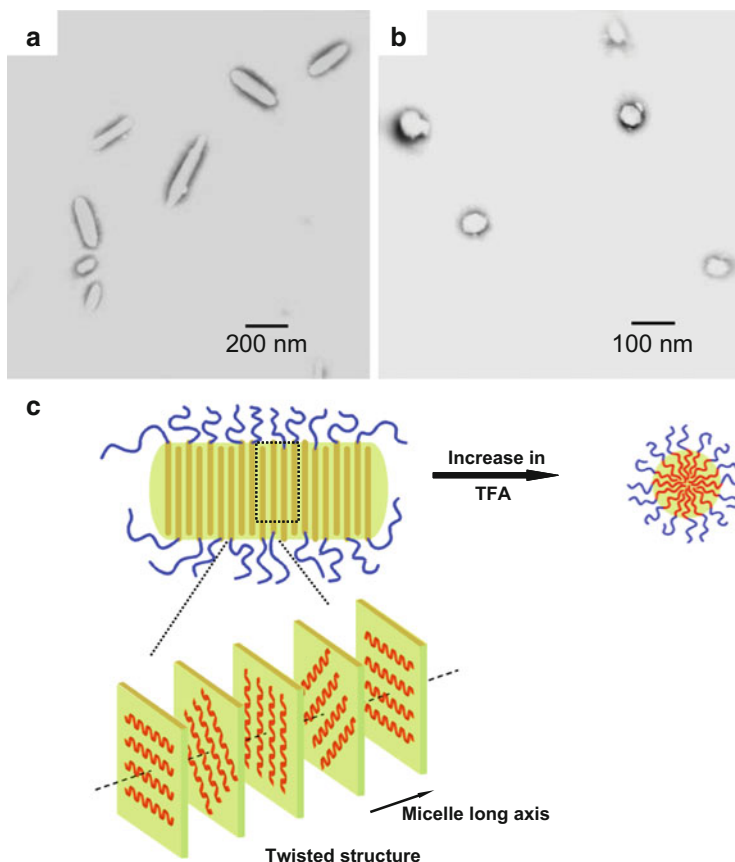
Fig. 17 TEM photographs of PBLG-*b*-PEG micelles formed in (**a**) CHCl$_3$/ethanol solution and (**b**) CHCl$_3$/ethanol/TFA solution. (**c**) Scheme for the aggregate morphology transition from cylinder to sphere as the polypeptide conformation changes from helix to coil. Reprinted with permission from [61]. Copyright 2008 American Chemical Society

The vector could gradually change along the long-center-axis of the micelle in a cholesteric LC manner. Such a packing of the PBLG blocks in the core satisfies the natural tendency toward twisted packing of helical rods and can also maximize the effective volume for the PEG blocks in the micelle shells. The PEG segments relax and laterally form the corona of the micelle to maximize their conformation entropy. When the denaturant acid TFA is added, polypeptide chains become random coils and the regular packing of PBLG blocks in the core is destroyed. As a result, spherical micelles with coiled polypeptide blocks randomly packing inside the cores are formed.

The above example shows that a conformation transition from α-helix to random coil can destroy the ordered packing of polypeptide chains in micelle core, which simultaneously induces a cylinder-to-sphere morphology transition. A similar
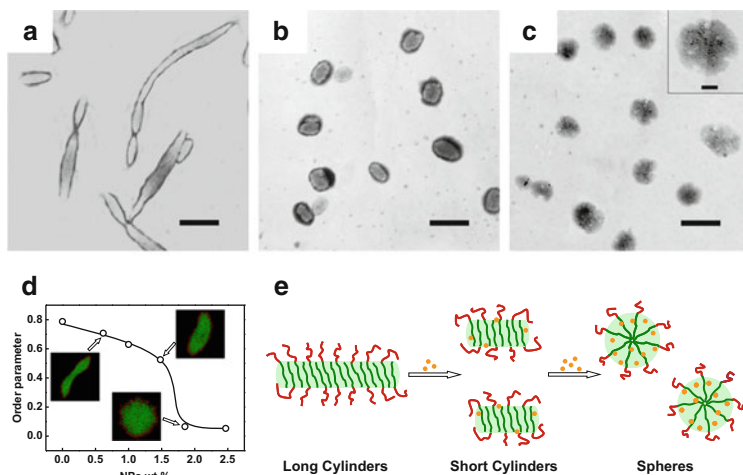
Fig. 18 TEM images of PBLG-*b*-PEG/AuNP hybrid micelles with various AuNP content: (**a**) 0, (**b**) 1, and (**c**) 3 wt%. The *inset* in (**c**) shows a magnified image of hybrid micelles. (**d**) Simulation prediction for the order parameter of rod blocks as a function of the concentration of nanoparticles. The *insets* show the corresponding structures of hybrid micelles. The nanoparticles are not shown for clarity. (**e**) Proposed self-assembly behaviors of PBLG-*b*-PEG/ AuNP mixtures. Reprinted with permission from [128]. Copyright 2012 American Chemical Society

micelle morphology transition from cylinder to sphere for the same PBLG-*b*-PEG block copolymers is achieved by adding a small portion of gold nanoparticles (AuNPs), as reported in a recent work by Cai et al. [128]. The main reason for the aggregate morphology transition is the breakage of ordered packing of PBLG rods in the cylindrical micelle core by the added nanoparticles. As shown in Fig. 18a, pure block copolymers form cylindrical micelles in solution of CHCl$_3$/ethanol (v/v = 4/6). When the AuNPs is introduced, as shown in Fig. 18b, short cylinders are produced. These short cylinders have the same diameter as the long cylinders, which indicates that the short cylinders could be fragments of the long cylinders. Further increasing the AuNP content to 2–10 wt% leads to the formation of spherical micelles (Fig. 18c, AuNPs 3 wt%). From the TEM image shown in the inset of Fig. 18c, it can be observed that AuNPs exist in the micelle core. The authors also performed a dissipative particle dynamics (DPD) simulation study on this system. As shown in Fig. 18d, the simulation results from a model system of rod–coil copolymer/nanoparticles reproduced the experimental findings well. In addition, the simulations reveal that with the incorporation of NPs into the micelle core, the ordered packing of rod block in the micelle core is gradually destroyed. The order parameter of the rod block gradually decreases from about 0.8 for cylinders to nearly zero for spherical micelles. Fig. 18e schematically presents the self-assembly behaviors of PBLG-*b*-PEG/AuNPs mixtures. It can be clearly seen that when the weight fraction of NPs is lower, the ordered arrangement of PBLG rods in the micelle core is partially destroyed and short cylinders are
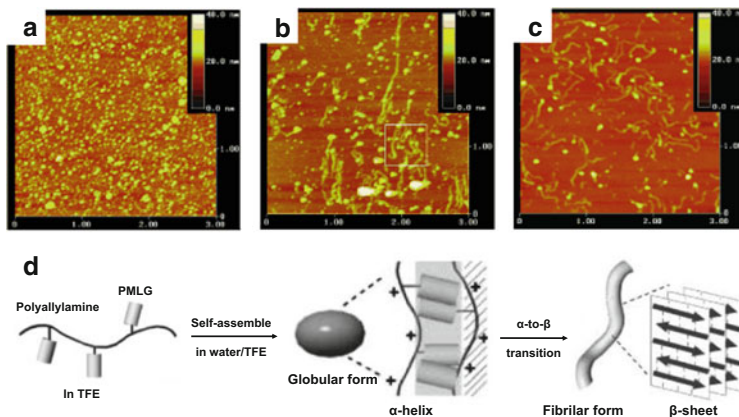
Fig. 19 AFM images showing the time dependent changes in morphology of polyallylamine-*g*-PMLG in water/TFE (8:2 v/v) solution: (**a**) 0 h, (**b**) 5 h, and (**c**) 48 h. (**d**) Morphology and conformation of the graft copolymer. Reprinted with permission from [130]. Copyright 2003 Wiley-VCH

produced. When the weight fraction of NPs increases, the sustaining filling of the nanoparticles destroys the global ordering of the PBLG rods and spherical micelles are formed.

Cylindrical micelles were also observed for graft copolymers with solvophobic polypeptide side chains [129, 130]. For example, Higuchi et al. found that in water/2,2,2-trifluoroethanol (TFE) mixture solution (pH < 8), polyallylamine-*g*-PMLG graft copolymers can first assemble into small globules, and then transform into long fibrils [130]. The aggregate morphology was observed by AFM. As shown in Fig. 19a, when the graft polymer is dispersed in water/TFE mixture solution, globular aggregates are first formed by the strong hydrophobic interaction between PMLG chains. In this stage, PMLG grafts take mainly α-helical form. After incubation for 5 h, fibrils together with globular aggregates are observed (Fig. 19b). After further incubation for 48 h, the major structures were found to be amyloid-like fibrils (Fig. 19c). Such a morphology transition from globules to fibrils is accompanied by a change in the conformation of PMLG from α-helix to β-sheet. The PMLG β-sheets are antiparallel and form fibril structures. Figure 19d schematically illustrates the morphology and PMLG conformation transition of graft copolymer in solutions.

Lin et al. reported that PBLG-*g*-PEG graft copolymers with a rigid polypeptide backbone can self-assemble into spindles and cylindrical micelles in which the PBLG backbones take side-by-side ordered packing with their long axes aligned in a nematic manner, while spread out hydrophilic PEG chains stabilize the aggregates [62, 131]. For a PBLG-*g*-PEG/CHCl$_3$/ethanol solution system, when TFA is introduced the rigid α-helix conformation of the PBLG backbone transforms to a random coil conformation. The flexible polypeptide chains tend to randomly pack in the aggregate core. As a result, spindles transform to large spheres [62].
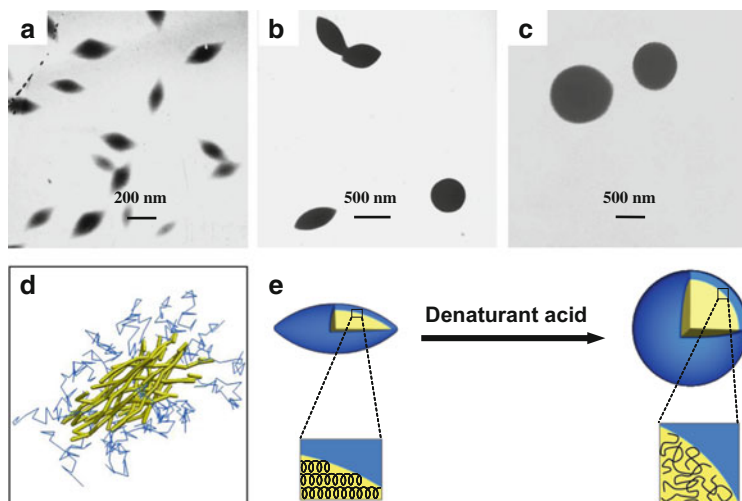
Fig. 20 TEM images of PBLG-*g*-PEG aggregates formed in CHCl₃/ethanol/TFA solutions with various TFA mole fractions: (**a**) 0, (**b**) 0.012, and (**c**) 0.016. (**d**) Simulation results of aggregates obtained from rod–coil graft copolymer at rigid conformation fractions of 87.5%. (**e**) Model proposed for the PBLG-*g*-PEG aggregates formed under various conditions. Reprinted with permission from [62]. Copyright 2008 Elsevier

Figure 20a–c shows the TEM images of the PBLG-*g*-PEG graft copolymer aggregates. With no TFA, small spindles are observed (Fig. 20a). At a lower TFA content, the intramolecular H-bonding of PBLG is partially destroyed and thus the PBLG backbone becomes a semi-rigid chain and the PBLG-*g*-PEG graft copolymers self-assemble into a mixture of spindles and spheres (Fig. 20b). With further increase in the TFA content, PBLG becomes random coil and larger spheres are formed by the graft copolymers (Fig. 20c).

Lin and coworkers also carried out a DPD simulation on model graft copolymers with various rigid fractions of the backbone. Figure 20d shows a typical result for the spindle self-assembled from the graft copolymers with a semi-rigid backbone (rigid conformation fraction of backbone is 87.5%). This result captures the essential feature of the structure observed in experiments (Fig. 20b). Some information that is difficult to be gained through experiments can be obtained. For example, an orientational order parameter of the polypeptide backbones of about 0.7 is obtained. Figure 20e illustrates a model proposed for the morphology transition of PBLG-*g*-PEG aggregation as a function of polypeptide backbone conformation.

Combining the experimental and simulation work is an effective strategy for studying complex polymer self-assembly and understanding the mechanism behind the phenomena. On one hand, simulations can not only reproduce the experimental observations, but also provide additional information that is difficult to be obtained from experiments, such as chain orderings and distributions. On the other hand, the validity of the simulation should be tested by comparing the simulation results with experimental observations. If the simulation can only give similar results to those observed experimentally, it tells us no more than that the building model is rational.

Fig. 21 TEM images of
PNIPAm$_{90}$-b-PZLys$_{71}$:
(**a**) giant vesicles prepared
with DMF as initial solvent
and (**b**) compact vesicles
prepared with THF as initial
solvent. (**c**) Proposed self-
assembly behaviors.
Reprinted with permission
from [37]. Copyright 2008
American Chemical Society
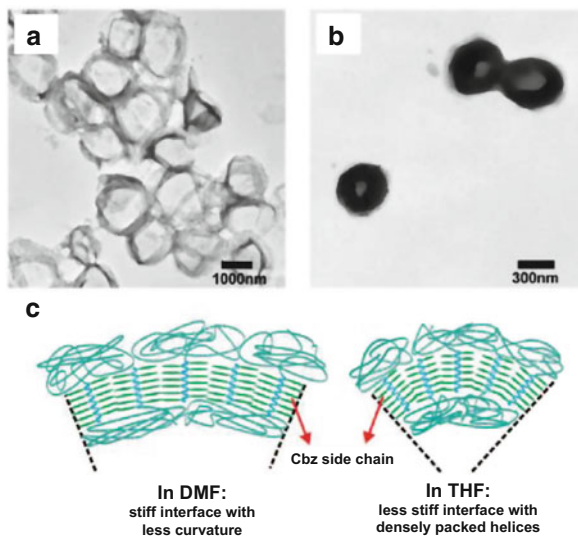
In addition to capturing the feature of experimental results, the computer
simulations should serve as a tool to give information beyond the experimental
observations.

In the above experiments, the simulation results supply missing information like
the packing of rigid PBLG and therefore are of significance. However, some aspects
of the models were coarse-grained, such as the polydispersity of the polymers and
the chiral characteristic of the PBLG. These facts may play an important role in
determining the self-assembly behaviors of the present systems, for example, if the
chirality of PBLG is incorporated into the model, morphologies with chiral nature
would be simulated. This would be an interesting topic for further simulation of the
polypeptide systems.

4.2 Vesicles Self-Assembled from Polypeptide Copolymers

Amphiphilic copolymers can self-assemble into vesicles. Polypeptide vesicles have
attracted considerable attention due to their large loading capacity and similarity to
living cells [10, 132, 133]. The ordered packing of polypeptide chains has also been
observed in polypeptide vesicles in which hydrophobic polypeptide chains form the
vesicle wall [37, 134–136]. For example, Chang et al. studied the self-assembly
behavior of PNIPAm-b-PZLys rod–coil block copolymers [37]. They found that by
varying the polymer composition and the helicogenic common solvents, these
amphiphilic block copolymers were able to form universal aggregate morphologies
of spherical micelles, wormlike micelles, and vesicles. For example, PNIPAm$_{91}$-b-
PZLys$_{71}$ self-assembles into vesicles in water with THF or DMF as initial solvent
(Fig. 21a, b). Furthermore, the size of vesicles from DMF/water system is much

Fig. 22 (**a**) Proposed self-assembly of $PArg_{60}$-*b*-$PLeu_{20}$ vesicles. (**b**) LSCM image of the vesicles. (**c**) LSCM image of the vesicles containing Texas-Red-labeled dextran. Scale bar = 5 μm. Reprinted by permission from Macmillan Publishers Ltd: Nature Materials, [137], copyright (2007)
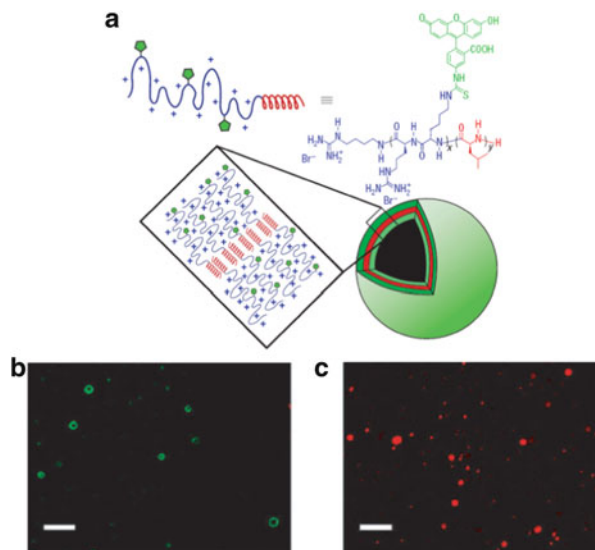
larger than that from THF/water system. As illustrated in Fig. 21c, polypeptide chains in the vesicle wall take the side-by-side packing mode. Because the dipole moment of DMF is larger than that of THF, when DMF is the initial solvent, the side chain of PZLys possesses a greater dimension, which induces a looser packing of PZLys chains. As a result, the size of the vesicles prepared with DMF as initial solvent is much larger than those prepared with THF.

Deming's group reported a series of work on the polypeptide vesicles formed by copolypeptide amphiphiles of PLL_{60}-*b*-$PLeu_{20}$, $PLGA_{60}$-*b*-$PLeu_{20}$, and $PArg_{60}$-*b*-$PLeu_{20}$ in aqueous solution [46, 137]. For these block copolymers, PLeu is hydrophobic, whereas PLL, PLGA, and PArg are hydrophilic. Vesicle formation is due to a combination of the α-helical hydrophobic segments that favor formation of flat membranes and the highly charged hydrophilic segments that impart solubility and fluidity to these membranes. Typical results from $PArg_{60}$-*b*-$PLeu_{20}$ block copolymers are presented in Fig. 22. Figure 22a shows the proposed vesicle structure from $PArg_{60}$-*b*-$PLeu_{20}$ block polymers. As shown in Fig. 22b, micrometer-sized vesicles in aqueous solution are observed from LSCM. These vesicles are able to entrap water-soluble species, such as dextran. As shown in Fig. 22c, the loading of Texas-Red-labeled dextran in vesicles can be observed.

Up to now, few studies have focused on the formation of vesicles from polypeptide-based graft copolymers. In a recent work, Cai et al. studied the self-assembly behavior of PBLG-*g*-PEG graft copolymers [138]. The degree of grafting of short PEG ($M_n = 750$) is low (0.28 mol%). With THF as the initial solvent, the graft copolymers self-assemble into vesicles, as shown in Fig. 23a. The three-dimesional SEM image in the inset of Fig. 23a confirms the vesicular structure. It is the first report of the formation of polymeric vesicles from graft copolymers with a rigid polypeptide backbone. When DMF, a better solvent for PBLG than THF, is
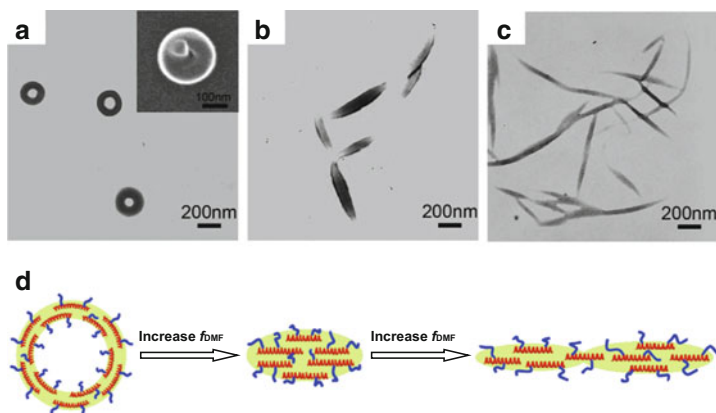
Fig. 23 TEM images of PBLG-*g*-PEG graft copolymer aggregates as a function of initial common solvents: (**a**) THF; (**b**) THF/DMF at 1/1 v/v; (**c**) DMF. (**d**) Aggregation as a function of the initial solvent composition. The *inset* in (**a**) is a magnified SEM image of the vesicle. Reprinted with permission from [138]. Copyright 2010 American Chemical Society

introduced into the initial solvent, the aggregate morphology transforms to spindles and connected spindles (see Fig. 23b–c). For the vesicles, PBLG backbones should align in ordered packing and bend in the wall of the vesicle. Because of the imperfect nature of the PBLG helices, such a bended state of the PBLG chains can be achieved without raising the system energy markedly. In addition, such a packing mode prevents the exposing of the PBLG chain to water. While in the spindles and connected spindles, PBLG chains are believed to take a dislocated side-by-side packing manner. Figure 23d is a schematic illustration of the aggregation as a function of the initial solvent composition. Polypeptide graft copolymers have obvious advantages in adjusting the self-assembly behavior by changing the side-chain properties, such as grafting density, chain length, environmental sensitivity, etc. Thus these polypeptide-based vesicles may be potential candidates for drug carriers and the like.

In a subsequent work, Cai et al. investigated the effect of PBLG-*b*-PEG block copolymer on the self-assembly of the PBLG-*g*-PEG graft copolymers [139]. They found that the cooperative self-assembly of mixtures containing vesicle-forming PBLG-*g*-PEG graft copolymers and vesicle- or micelle-forming PBLG-*b*-PEG block copolymers always produces cylindrical micelles (Fig. 24). For the hybrid cylinders, block copolymers are found to mainly locate at the ends of the aggregates, which prevents the fusion of cylinders to vesicles in the assembly process. Thus, the cylindrical structure is preserved by removing organic solvent. These results are not only beneficial to understanding the formation of vesicles from polypeptide-based graft copolymers, but also enrich our knowledge of the self-assembly of multicomponent systems.
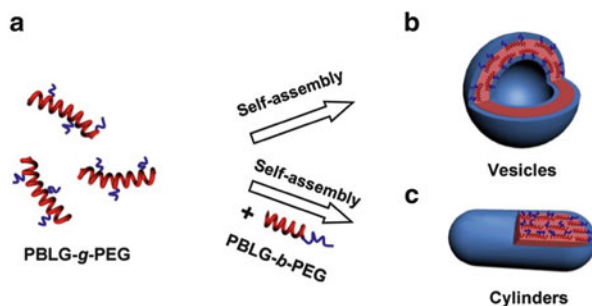
Fig. 24 Self-assembly of polypeptide-based block and graft copolymer mixtures. Reprinted with permission from [139]. Copyright 2012 American Chemical Society

4.3 Complex Structures Self-Assembled from Polypeptide Copolymers

In addition to the cylindrical micelles and vesicles, the ordering of polypeptide chains also contributes to the formation of complex structures with hierarchical feature [140–142]. For example, Nolte et al. found that the polypeptide-based block copolymers of polystyrene with poly(isocyano-L-alanine-L-alanine) and poly (isocyano-L-alanine-L-histidine), PS_{40}-b-$PIAA_{10}$ (Fig. 25a) and PS_{40}-b-$PIAH_{15}$ (Fig. 25b), are able to self-assemble into super-helical structures in a sodium acetate buffer of pH 5.6 (0.2 mM) [140]. Structures with two length-scales are involved in such super-helices: fiber-like whole structures and screws of the super-helices. As shown in Fig. 25c–e, the super-helices have an opposite chirality to that of the constituent polypeptide segments of building block copolymers. Since the polypeptide chains take rigid α-helix conformation and the chirality of the formed super-helices is related to the handedness of the building polypeptides, it can be deduced that the ordering of polypeptide rods is an important factor in determining the formation of these hierarchical structures.

As reported by Cai et al., virus-like right-handed super-helical fibers and rings can be self-assembled from a binary system consisting of rod–coil PBLG-b-PEG block copolymers and PBLG rigid homopolymers [141]. The hierarchical structures are formed with PBLG bundles as the core wrapped by PBLG-b-PEG block copolymers. They revealed that the high molecular weight of PBLG homopolymer is crucial for the construction of the super-helical structures. For the mixture system containing low molecular weight PBLG homopolymers ($PBLG_{40000}$), spheres are observed (Fig. 26a). With increasing molecular weight of the PBLG homopolymers ($PBLG_{110000}$), super-helical rods start to appear (Fig. 26b). With further increase in the molecular weight of homo-PBLG ($PBLG_{520000}$), long super-helical fibers and rings with uniform diameter of 140 nm and screw-pitch of 80 nm are obtained (Fig. 26c). The detailed surface profile of the super-helices was examined using AFM analysis. As shown in
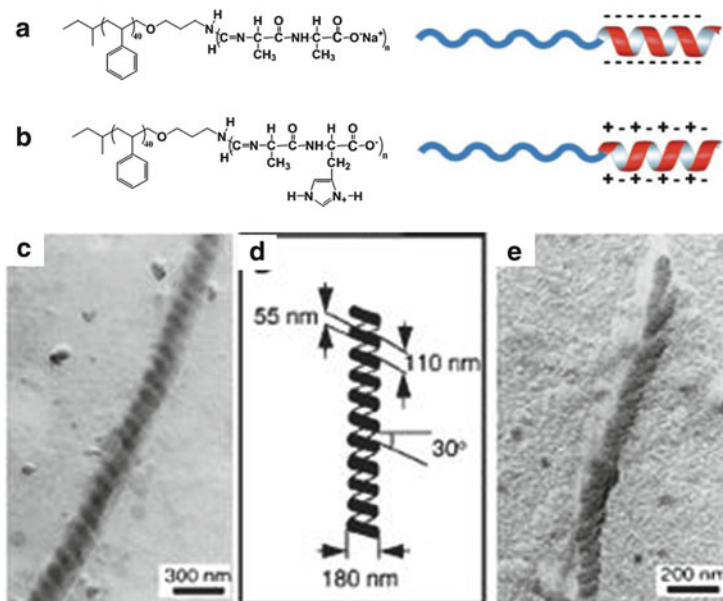
Fig. 25 Polymer structures of (**a**) PS$_{40}$-*b*-PIAA$_{10}$, right-handed polypeptide backbone and (**b**) PS$_{40}$-*b*-PIAH$_{15}$, left handed polypeptide backbone. (**c**) Left-handed super-helix from PS$_{40}$-*b*-PIAA$_{10}$. (**d**) Representation of the helix in (**c**). (**e**) Right-handed super-helical aggregate formed by PS$_{40}$-*b*-PIAH$_{15}$. From [140]. Reprinted with permission from AAAS

Fig. 26d, the width and screw pitch of the assemblies are similar to those observed in SEM images. The orientation of the height contour indicates that these super-helices have a right-handed sense. Many possible interactions, including hydrophobic, dipolar π–π interactions, and ordered packing tendency of α-helical polypeptide segments, are believed to be responsible for the formation of super-helical structures.

Usually, hierarchical structure-forming systems contain complex interactions, thus it is a daunting task to understand exactly how the observed structures were formed. Computer simulation is a useful tool for investigating multicomponent self-assembly systems and elucidating the supramolecular structures. Cai et al. also carried out a BD simulation on a model rod–coil block copolymer/rigid homopolymer binary system. From the simulation results, it was found that the homopolymers and block copolymers formed ordered structures with different scales. The polypeptide homopolymers packed side-by-side to form bundles; the block copolymers were helically wrapped on the homopolymer bundles; and the packing mode of block PBLG rods exhibited characteristics of the cholesteric LC structure. In such a structure, there exist two levels of polypeptide chain ordering. The interplay of these two level orderings has an important role in determining the final structures.
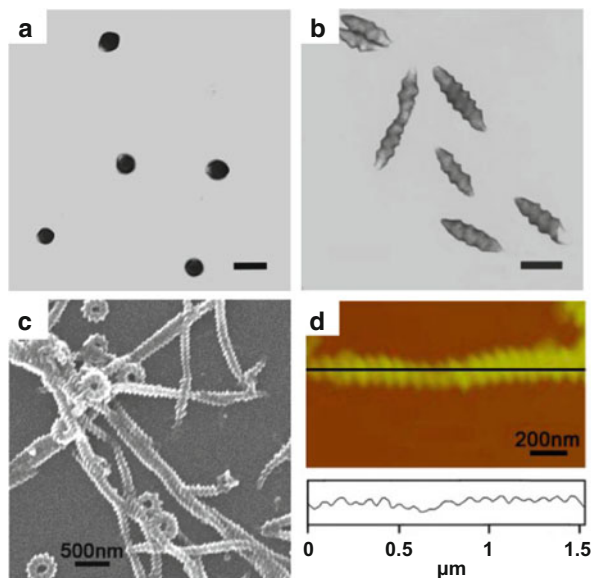
Fig. 26 (**a**) TEM image of spheres self-assembled from PBLG-*b*-PEG/PBLG$_{40000}$. (**b**) TEM image of super-helical rods self-assembled from PBLG-*b*-PEG/PBLG$_{110000}$. (**c**) SEM image of super-helical fibers and rings self-assembled from PBLG-*b*-PEG/PBLG$_{520000}$. (**d**) AFM images length profile of super-helical fibers self-assembled from PBLG-*b*-PEG/PBLG$_{520000}$. Reproduced from [141] with permission of The Royal Society of Chemistry

In this work, Cai et al. presented a simple strategy for preparation of polypeptide hierarchical super-helical structures by self-assembly of block copolymer and homopolymer mixtures. The helices have a PBLG bundle covered by PBLG-*b*-PEG chains, which is reminiscent of the structure of tobacco mosaic virus (RNA in the core, covered with a protein shell). This progress is promising for the construction of complicated biological analogs such as a model virus and subsequent investigation of its physiological behavior, e.g., cell penetration of the virus. Therefore, understanding the self-assembly of the mixture system is important and may become a focus of future research [121].

5 Concluding Remarks and Outlook

Polypeptides can take rigid form with an intramolecularly H-bonded α-helix conformation, which enables polypeptide homopolymers and copolymers to assemble into ordered structures by the orderly packing of polypeptide segments in both concentrated and dilute solutions. In addition, the intermolecularly H-bonded β-sheet conformation facilitates the formation of ordered structures, especially gels in solution. Ordered packing of polypeptide segments makes polypeptide

homopolymers and copolymers assemble into distinct structures. Great efforts have been made to construct polypeptide-based assemblies with ordered domains formed by polypeptide chains.

LCs were the earliest studied structures, in which polypeptide homopolymer rods pack in an ordered manner to form smectic, nematic, and cholesteric phases. The smectic LCs are mainly formed by polypeptide homopolymers with identical polymer length. The cholesteric phase can be prepared by synthetic polypeptides with polydisperse chain length. The nematic phase can be regarded as a special example of the cholesteric phase with an infinite cholesteric pitch. The cholesteric pitch and chirality in the polypeptide LCs are dependent on many factors, such as temperature, polymer concentration, solvent nature, and polypeptide conformation. Deep understanding of such phenomena is necessary for preparation of ordered polypeptide assembles with delicate structures. The addition of denaturing solvent to polypeptide solution can lead to an anisotropic–isotropic reentrant transition at low temperatures where the intramolecular helix–coil transformation occurs. However, the helical structure is more stable in LC phase than in dilute solution due to the conformational ordering effect.

Gels have attracted considerable attention for a long time. In polypeptide homopolymer gels, polypeptides assemble into fiber structures with dislocated side-by-side packing of rods. Thus, they possess a similar structure to LC structures; however, the order parameter is relatively lower. For polypeptide block copolymers, gels are formed with packing of polypeptide chains, while the other flexible chains are spread out into the surrounding to stabilize the gels in solution. Both the α-helix and β-sheet conformation of polypeptides support the formation of gels through inter- and intramolecular attractions. The gels formed from β-sheet polypeptides are found to have higher strength than those formed by α-helix polypeptides. However, most of the gels, especially the hydrogels, are still not strong enough for practical applications. Modified hydrophilic polypeptides are promising for the preparation of strong hydrogels. It is fundamentally important to construct gels with controlled structures and morphologies for diverse applications in the fields of template synthesis, functional materials, and tissue engineering scaffolds.

The ordered packing of polypeptides can be also found in copolymer micelles self-assembled in dilute solutions. The ordering tendency of polypeptide segments is favorable for the formation of cylindrical micelles, large vesicles, and hierarchical structures. The formed structures show higher stabilities due to the ordering within domains in the assemblies. Introducing a second component, including polymers and nanoparticles, is an effective way to adjust the self-assembly behavior of parent block and graft copolymers. The conformation transition of the polypeptide chains is also an important factor affecting the assembly behavior of polypeptide copolymers. The study of hierarchical structures of polypeptides is an especially attractive and promising topic because polypeptides are the fundamental building blocks for fabricating hierarchical structures in living organisms. Such hierarchical structures usually show chirality. Further work eliciting the relationship between handedness of the polypeptides and the chirality of the formed hierarchical

structures is highly desired. In addition, development in such fields will open a door to the preparation of advanced functional biomaterials, which is eagerly demanded in medicaland biorelated areas.

It is evident that the bioapplication of polypeptide assemblies is one of the most promising and important directions for research. Based on the ordering packing of polypeptide segments with α-helix and β-sheet conformations, novel superstructures in the forms of LCs, gels, and micelles have been sucessfully created. Although started about 60 years ago in the late 1940s, the ordering of polypeptides in the fabrication of diverse structures is still at a early stage. The assembly mechanisms behind the phenomena for LCs, gels, and micelles have not been well understood. The combination of experiments with computer simulations is a promising strategy for unveiling the fundamental principles of polypeptide assembly behavior. The application potential of the polypeptide assemblies has also not been well evaluated. More research is needed to implement the applications of polypeptide assemblies, which will further push the advance of polypeptide assembly research. Moreover, since polypeptides resemble proteins in structure, mimicking proteins is a charming aspect of polypeptide research, which could be helpful for investigating complex protein systems.

References

1. Deming TJ (1997) Polypeptide materials: new synthetic methods and applications. Adv Mater 9:299–311
2. Mart RJ, Osborne RD, Stevens URV (2006) Peptide-based stimuli-responsive biomaterials. Soft Matter 2:822–835
3. Osada K, Kataoka K (2006) Drug and gene delivery based on supramolecular assembly of PEG-polypeptide hybrid block copolymers. Adv Polym Sci 202:113–153
4. Schlaad H (2006) Solution properties of polypeptide-based copolymers. Adv Polym Sci 202:53–73
5. Carlsen A, Lecommandoux S (2009) Self-assembly of polypeptide-based block copolymer amphiphiles. Curr Opin Colloid Interface Sci 14:329–339
6. Deming TJ (2007) Synthetic polypeptides for biomedical applications. Prog Polym Sci 32:858–875
7. Banwell EF, Abelardo ES, Adams DJ, Birchall MA, Corrigan A (2009) Rational design and application of responsive α-helical peptide hydrogels. Nat Mater 8:596–600
8. He C, Zhuang X, Tang Z, Tian H, Chen X (2012) Stimuli-sensitive synthetic polypeptide-based materials for drug and gene delivery. Adv Healthc Mater 1:48–78
9. Lowik DWPM, Leunissen EHP, van den Heuvel M, Hansen MB, van Hest JCM (2010) Stimulus responsive peptide based materials. Chem Soc Rev 39:3394–3412
10. Choe U-J, Sun VZ, Tan JKY, Kamei DT (2012) Self-assembly polypeptide and polypeptide hybrid vesicles: from synthesis to application. Top Curr Chem 310:117–134

11. Chow D, Nunalee ML, Lim DW, Simnick AJ, Chilkoti A (2008) Peptide-based biopolymers in biomedicine and biotechnology. Mater Sci Eng R Rep 62:125–155

12. Lim Y-b, Lee E, Lee M (2007) Cell-penetrating-peptide-coated nanoribbons for intracellular nanocarriers. Angew Chem Int Ed 46:3475–3478

13. Kopecek J, Yang J (2012) Smart self-assembled hybrid hydrogel biomaterials. Angew Chem Int Ed 51:7396–7417

14. Higashihara T, Ueda M (2011) Block copolymers containing rod segments. In: Hadjichristidis N, Hirao A, Tezuka Y, Du Prez F (eds) Complex macromolecular architectures: synthesis, characterization, and self-assembly. Wiley, Hoboken, pp 395–429

15. Klok H-A (2002) Protein-inspired materials: synthetic concepts and potential applications. Angew Chem Int Ed 41:1509–1513

16. Zhang G, Fournier MJ, Mason TL, Tirrell DA (1992) Biological synthesis of monodisperse derivatives of poly(α, L-glutamic acid): model rodlike polymers. Macromolecules 25:3601–3603

17. Rabotyagova OS, Cebe P, Kaplan DL (2011) Protein-based block copolymers. Biomacromolecules 12:269–289

18. Kiick KL (2002) Genetic methods of polymer synthesis. In: Mark HF (ed) Encyclopedia of polymer science and technology. Wiley, Hoboken, pp 515–522

19. Merrifield RB (1963) Solid phase peptide synthesis. I. The synthesis of a tetrapeptide. J Am Chem Soc 85:2149–2154

20. Aliferis T, Iatrou H, Hadjichristidis N (2004) Living polypeptides. Biomacromolecules 5:1653–1656

21. Hadjichristidis N, Iatrou H, Pitsikalis M, Sakellariou G (2009) Synthesis of well-defined polypeptide-based materials via the ring-opening polymerization of alpha-amino acid N-carboxyanhydrides. Chem Rev 109:5528–5578

22. Kricheldorf HR (2006) Polypeptides and 100 years of chemistry of α-amino acid N-carboxyanhydrides. Angew Chem Int Ed 45:5752–5784

23. Kricheldorf HR (1987) α-aminoacid-N-carboxy-anhydrides and related heterocycles: syntheses, properties, peptide synthesis, polymerization. Springer, Berlin

24. Penczek S, Kricheldorf HR (1990) Models of biopolymers by ring opening polymerization. CRC, Boca Raton

25. Duran H, Ogura K, Nakao K, Vianna SDB, Usui H (2009) High-vacuum vapor deposition and in situ monitoring of N-carboxy anhydride benzyl glutamate polymerization. Langmuir 25:10711–10718

26. Leuchs H, Geiger W (1908) The anhydrides of alpha-amino-N-carboxylic and alpha-amino acids. Ber Dtsch Chem Ges 41:1721–1726

27. Voet D, Voet JG (eds) (1995) Biochemistry, Solutions Manual. Wiley, Hoboken

28. Zimm BH, Bragg JK (1959) Theory of the phase transition between helix and random coil in polypeptide chains. J Chem Phys 31:526–535

29. Teramoto A, Fujita H (1975) Conformation-dependent properties of synthetic polypeptides in the helix-coil transition region. Adv Polym Sci 18:65–149

30. Parras P, Castelletto V, Hamley IW, Klok H-A (2005) Nanostructure formation in poly (γ-benzyl-L-glutamate)-poly(ethylene glycol)-poly(γ-benzyl-L-glutamate) triblock copolymers in the solid state. Soft Matter 1:284–291

31. Hadjichristidis N, Iatrou H, Pitsikalis M, Pispas S, Avgeropoulos A (2005) Linear and non-linear triblock terpolymers: synthesis, self-assembly in selective solvents and in bulk. Prog Polym Sci 30:725–782

32. Klok H-A, Lecommandoux S (2006) Solid-state structure, organization and properties of peptide-synthetic hybrid block copolymers. Adv Polym Sci 202:75–111

33. Sanchez-Ferrer A, Mezzenga R (2010) Secondary structure-induced micro- and macrophase separation in rod-coil polypeptide diblock, triblock, and star-block copolymers. Macromolecules 43:1093–1100

34. Babin J, Taton D, Brinkmann M, Lecommandoux S (2008) Synthesis and self-assembly in bulk of linear and mikto-arm star block copolymers based on polystyrene and poly(glutamic acid). Macromolecules 41:1384–1392
35. Kopecek J, Yang J (2009) Peptide-directed self-assembly of hydrogels. Acta Biomater 5:805–816
36. Hermes F, Otte K, Brandt J, Grawert M, Borner HG, Schlaad H (2011) Polypeptide-based organogelators: effects of secondary structure. Macromolecules 44:7489–7492
37. Huang C-J, Chang F-C (2008) Polypeptide diblock copolymers: syntheses and properties of poly(N-isopropylacrylamide)-b-polylysine. Macromolecules 41:7041–7052
38. Gebhardt KE, Ahn S, Venkatachalam G, Savin DA (2008) Role of secondary structure changes on the morphology of polypeptide-based block copolymer vesicles. J Colloid Interface Sci 317:70–76
39. Robinson C (1956) Liquid-crystalline structures in solutions of a polypeptide. Trans Faraday Soc 52:571–592
40. Uematsu I, Uematsu Y (1984) Polypeptide liquid crystals. Adv Polym Sci 59:37–73
41. Flory PJ, Leonard WJ (1965) Thermodynamic properties of solutions of helical polypeptides. J Am Chem Soc 87:2102–2108
42. Tohyama K, Miller WG (1981) Network structure in gels of rod-like polypeptides. Nature 289:813–814
43. Cohen Y (1996) The microfibrillar network in gels of poly(γ-benzyl-L-glutamate) in benzyl alcohol. J Polym Sci, Part B: Polym Phys 34:57–64
44. Kim KT, Park C, Vandermeulen GWM, Rider DA, Kim C, Winnik MA, Manners I (2005) Gelation of helical polypeptide-random coil diblock copolymers by a nanoribbon mechanism. Angew Chem Int Ed 44:7964–7968
45. Rodriguez-Hernandez J, Lecommandoux S (2005) Reversible inside-out micellization of pH-responsive and water-soluble vesicles based on polypeptide diblock copolymers. J Am Chem Soc 127:2026–2027
46. Holowka EP, Pochan DJ, Deming TJ (2005) Charged polypeptide vesicles with controllable diameter. J Am Chem Soc 127:12423–12428
47. Bellomo EG, Wyrsta MD, Pakstis L, Pochan DJ, Deming TJ (2004) Stimuli-responsive polypeptide vesicles by conformation-specific assembly. Nat Mater 3:244–248
48. Kim KT, Park C, Kim C, Winnik MA, Manners I (2006) Self-assembly of dendron-helical polypeptide copolymers: organogels and lyotropic liquid crystals. Chem Commun 1372–1374
49. Yu SM, Conticello VP, Zhang G, Kayser C, Fournier MJ, Mason TL, Tirrell DA (1997) Smectic ordering in solutions and films of a rod-like polymer owing to monodispersity of chain length. Nature 389:167–170
50. Schmidtke S, Russo P, Nakamatsu J, Buyuktanir E, Turfan B, Temyanko E, Negulescu I (2000) Thermoreversible gelation of isotropic and liquid crystalline solutions of a "sticky" rodlike polymer. Macromolecules 33:4427–4432
51. Ginzburg B, Siromyatnikova T, Frenkel S (1985) Gelation in the poly(γ-benzyl-L-glutamate)-dimethylformamide system. Polym Bull (Berl) 13:139–144
52. Russo PS, Magestro P, Miller WG (1987) Gelation of poly(γ-benzyl-α,L-glutamate). In: Russo PS (ed) Reversible polymeric gels and related systems. ACS symposium series, vol 350. American Chemical Society, Washington, DC, pp 152–180
53. Kuo S-W, Lee H-F, Huang W-J, Jeong K-U, Chang F-C (2009) Solid state and solution self-assembly of helical polypeptides tethered to polyhedral oligomeric silsesquioxanes. Macromolecules 42:1619–1626
54. Kim EH, Joo MK, Bahk KH, Park MH, Chi B, Lee YM, Jeong B (2009) Reverse thermal gelation of PAF-PLX-PAF block copolymer aqueous solution. Biomacromolecules 10:2476–2481
55. Li T, Lin J, Chen T, Zhang S (2006) Polymeric micelles formed by polypeptide graft copolymer and its mixtures with polypeptide block copolymer. Polymer 47:4485–4489

56. Cai C, Zhang L, Lin J, Wang L (2008) Self-assembly behavior of pH- and thermosensitive amphiphilic triblock copolymers in solution: experimental studies and self-consistent field theory simulations. J Phys Chem B 112:12666–12673

57. Ueda M, Makino A, Imai T, Sugiyama J, Kimura S (2011) Transformation of peptide nanotubes into a vesicle via fusion driven by stereo-complex formation. Chem Commun 47:3204–3206

58. Cai C, Wang L, Lin J (2011) Self-assembly of polypeptide-based copolymers into diverse aggregates. Chem Commun 47:11189–11203

59. Kim MS, Dayananda K, Choi EY, Park HJ, Kim JS, Lee DS (2009) Synthesis and characterization of poly(L-glutamic acid)-block-poly(L-phenylalanine). Polymer 50:2252–2257

60. Schenck HL, Gellman SH (1998) Use of a designed triple-stranded antiparallel β-sheet to probe β-sheet cooperativity in aqueous solution. J Am Chem Soc 120:4869–4870

61. Ding W, Lin S, Lin J, Zhang L (2008) Effect of chain conformational change on micelle structures: experimental studies and molecular dynamics simulations. J Phys Chem B 112:776–783

62. Lin J, Zhu G, Zhu X, Lin S, Nose T, Ding W (2008) Aggregate structure change induced by intramolecular helix-coil transition. Polymer 49:1132–1136

63. Kotharangannagari VK, Sanchez-Ferrer A, Ruokolainen J, Mezzenga R (2012) Thermoreversible gel–sol behavior of rod-coil-rod peptide-based triblock copolymers. Macromolecules 45:1982–1990

64. Yu SM, Soto CM, Tirrell DA (2000) Nanometer-scale smectic ordering of genetically engineered rodlike polymers: synthesis and characterization of monodisperse derivatives of poly(γ-benzyl α, L-glutamate). J Am Chem Soc 122:6552–6559

65. Sasaki S, Tokuma K, Uematsu I (1983) Phase behavior of poly(γ-benzyl L-glutamate) solutions in benzyl alcohol. Polym Bull (Berl) 10:539–546

66. Watanabe J, Takashina Y (1991) Columnar liquid crystals in polypeptides. 1. A columnar hexagonal liquid crystal observed in poly(γ-octadecyl L-glutamate). Macromolecules 24:3423–3426

67. Robinson C, Ward JC (1957) Liquid-crystalline structures in polypeptides. Nature 180:1183–1184

68. Robinson C (1961) Liquid-crystalline structures in polypeptide solutions. Tetrahedron 13:219–234

69. Robinson C, Ward JC, Beevers RB (1958) Liquid crystalline structure in polypeptide solutions. Part 2. Discuss Faraday Soc 25:29–42

70. Samulski ET, Tobolsky AV (1967) Solid "liquid crystal" films of poly-γ-benzyl-L-glutamate. Nature 216:997

71. Elliott A, Ambrose EJ (1950) Evidence of chain folding in polypeptides and proteins. Discuss Faraday Soc 9:246–251

72. Marx A, Thiele C (2009) Orientational properties of poly-γ-benzyl-L-glutamate: influence of molecular weight and solvent on order parameters of the solute. Chem Eur J 15:254–260

73. Watanabe J, Nagase T (1988) Thermotropic polypeptides. 5. Temperature dependence of cholesteric pitches exhibiting a cholesteric sense inversion. Macromolecules 21:171–175

74. Toriumi H, Kusumi Y, Uematsu I, Uematsu Y (1979) Thermally induced inversion of the cholesteric sense in lyotropic polypeptide liquid crystals. Polym J 11:863–869

75. Toriumi H, Minakuchi S, Uematsu Y, Uematsu I (1980) Helical twisting power of poly (γ-benzyl-L-glutamate) liquid crystals in mixed solvents. Polym J 12:431–437

76. Abe A, Hiraga K, Imada Y, Hiejima T, Furuya H (2005) Screw-sense inversion characteristic of α-helical poly(β-p-chlorobenzyl L-aspartate) and comparison with other related polyaspartates. Peptide Sci 80:249–257

77. Abe A, Furuya H, Okamoto S (1997) Spatial configurations, transformation, and reorganization of mesophase structures of polyaspartates-a highly intelligent molecular system. Peptide Sci 43:405–412

78. Abe A, Imada Y, Furuya H (2010) Mechanism of the screw-sense reversal of tightly hydrogen-bonded α-helical network triggered by the side-chain conformation. Polymer 51:6234–6239
79. Junnila S, Houbenov N, Hanski S, Iatrou H, Hirao A, Hadjichristidis N, Ikkala O (2010) Hierarchical smectic self-assembly of an ABC miktoarm star terpolymer with a helical polypeptide arm. Macromolecules 43:9071–9076
80. Lin J (1997) Re-entrant isotropic transition of polypeptide liquid crystal. Polymer 38:4837–4841
81. Lin J (1998) Reentrant isotropic transition of polypeptide liquid crystal: effect of steric and orientation–dependent interactions. Polymer 39:5495–5500
82. Lin J, Abe A, Furuya H, Okamoto S (1996) Liquid crystal formation coupled with the coil-helix transition in the ternary system poly(γ-benzyl L-glutamate)/dichloroacetic acid/dichloroethane. Macromolecules 29:2584–2589
83. Lin J, Lin S, Liu P, Hiejima T, Furuya H, Abe A (2003) Phase behavior of ternary systems involving a conformationally variable chain and a randomly coiled polymer. Macromolecules 36:6267–6272
84. Flory PJ (1984) Molecular theory of liquid crystals. Adv Polym Sci 59:1–36
85. Abe A, Ballauff M (1991) The Flory lattice model. In: Ciferri A (ed) Liquid crystallinity in polymers: principles and fundamental properties. Wiley-VCH, Weinheim, Chap. 4
86. Lin J, Lin S, Zhang L, Nose T (2009) Microphase separation of rod-coil diblock copolymer in solution. J Chem Phys 130:094907
87. Watanabe J, Imai K, Uematsu I (1978) Light scattering studies of poly(γ-benzyl L-glutamate) solutions and films. Polym Bull 1:67–72
88. Tadmor R, Khalfin RL, Cohen Y (2002) Reversible gelation in isotropic solutions of the helical polypeptide poly(γ-benzyl-L-glutamate): kinetics and formation mechanism of the fibrillar network. Langmuir 18:7146–7150
89. Tipton DL, Russo PS (1996) Thermoreversible gelation of a rodlike polymer. Macromolecules 29:7402–7411
90. Oikawa H, Nakanishi H (2001) Dynamics of probe particles during sol–gel transition of PBLG-DMF solution and the resulting gel structure. J Chem Phys 115:3785–3791
91. Niehoff A, Mantion A, McAloney R, Huber A (2013) Elucidation of the structure of poly(γ-benzyl-L-glutamate) nanofibers and gel networks in a helicogenic solvent. Colloid Polym Sci 291:1353–1363
92. Kishi R, Sisido M, Tazuke S (1990) Liquid-crystalline polymer gels. 1. Cross-linking of poly(γ-benzyl L-glutamate) in the cholesteric liquid-crystalline state. Macromolecules 23:3779–3784
93. Kishi R, Sisido M, Tazuke S (1990) Liquid-crystalline polymer gels. 2. Anisotropic swelling of poly(γ-benzyl L-glutamate) gel crosslinked under a magnetic field. Macromolecules 23:3868–3870
94. Inomata K, Iguchi Y, Mizutani K, Sugimoto H, Nakanishi E (2012) Anisotropic swelling behavior induced by helix-coil transition in liquid crystalline polypeptide gels. ACS Macro Lett 1:807–810
95. Gibson MI, Cameron NR (2008) Organogelation of sheet-helix diblock copolypeptides. Angew Chem Int Ed 47:5160–5162
96. Choi YY, Jeong Y, Joo MK, Jeong B (2009) Reverse thermal organogelation of poly(ethylene glycol)-polypeptide diblock copolymers in chloroform. Macromol Biosci 9:869–874
97. Naik SS, Savin DA (2009) Poly(Z-lysine)-based organogels: effect of interfacial frustration on gel strength. Macromolecules 42:7114–7121
98. Sun J, Chen X, Guo J, Shi Q, Xie Z, Jing X (2009) Synthesis and self-assembly of a novel Y-shaped copolymer with a helical polypeptide arm. Polymer 50:455–461
99. You Y, Chen Y, Hua C, Dong C (2010) Synthesis and thermoreversible gelation of dendron-like polypeptide/linear poly(ε-caprolactone)/dendron-like polypeptide triblock copolymers. J Polym Sci A Polym Chem 48:709–718

100. Borner HG, Smarsly BM, Hentschel J, Rank A, Schubert R, Geng Y, Discher DE, Hellweg T, Brandt A (2008) Organization of self-assembled peptide–polymer nanofibers in solution. Macromolecules 41:1430–1437

101. van Bommel KJC, Friggeri A, Shinkai S (2003) Organic templates for the generation of inorganic materials. Angew Chem Int Ed 42:980–999

102. Sone ED, Zubarev ER, Stupp SI (2002) Semiconductor nanohelices templated by supramolecular ribbons. Angew Chem Int Ed 41:1705–1709

103. Estroff LA, Addadi L, Weiner S, Hamilton AD (2004) An organic hydrogel as a matrix for the growth of calcite crystals. Org Biomol Chem 2:137–141

104. Shumburo A, Biewer MC (2002) Stabilization of an organic photochromic material by incorporation in an organogel. Chem Mater 14:3745–3750

105. Deming TJ (2005) Polypeptide hydrogels via a unique assembly mechanism. Soft Matter 1:28–35

106. Breedveld V, Nowak AP, Sato J, Deming TJ, Pine DJ (2004) Rheology of block copolypeptide solutions: hydrogels with tunable properties. Macromolecules 37:3943–3953

107. Nowak AP, Breedveld V, Pakstis L, Ozbas B, Pine DJ, Pochan D, Deming TJ (2002) Rapidly recovering hydrogel scaffolds from self-assembling diblock copolypeptide amphiphiles. Nature 417:424–428

108. Nowak AP, Breedveld V, Pine DJ, Deming TJ (2003) Unusual salt stability in highly charged diblock co-polypeptide hydrogels. J Am Chem Soc 125:15666–15670

109. Pakstis LM, Ozbas B, Hales KD, Nowak AP, Deming TJ, Pochan D (2003) Effect of chemistry and morphology on the biofunctionality of self-assembling diblock copolypeptide hydrogels. Biomacromolecules 5:312–318

110. Oliveira ED, Hirsch SG, Spontak RJ, Gehrke SH (2003) Influence of polymer conformation on the shear modulus and morphology of polyallylamine and poly(α-L-lysine) hydrogels. Macromolecules 36:6189–6201

111. Choi BG, Park MH, Cho S-H, Joo MK, Oh HJ, Kim EH, Park K, Han DK, Jeong B (2011) Thermal gelling polyalanine–poloxamine–polyalanine aqueous solution for chondrocytes 3D culture: initial concentration effect. Soft Matter 7:456–462

112. Chen Y, Pang X, Dong C (2010) Dual stimuli-responsive supramolecular polypeptide-based hydrogel and reverse micellar hydrogel mediated by host-guest chemistry. Adv Funct Mater 20:579–586

113. Cheng Y, He C, Xiao C, Ding J, Zhuang X, Huang Y, Chen X (2012) Decisive role of hydrophobic side groups of polypeptides in thermosensitive gelation. Biomacromolecules 13:2053–2059

114. Altunbas A, Pochan D (2012) Peptide-based and polypeptide-based hydrogels for drug delivery and tissue engineering. Adv Polm Sci 310:135–167

115. Aggeli A, Nyrkova IA, Bell M, Harding R, Carrick L, McLeish TCB, Semenov AN, Boden N (2001) Hierarchical self-assembly of chiral rod-like molecules as a model for peptide β-sheet tapes, ribbons, fibrils, and fibers. Proc Natl Acad Sci USA 98:11857–11862

116. Smeenk JM, Otten MBJ, Thies J, Tirrell DA, Stunnenberg HG, van Hest JCM (2005) Controlled assembly of macromolecular β-Sheet fibrils. Angew Chem Int Ed 44:1968–1971

117. Choi YY, Joo MK, Sohn YS, Jeong B (2008) Significance of secondary structure in nanostructure formation and thermosensitivity of polypeptide block copolymers. Soft Matter 4:2383–2387

118. Choi YY, Jang JH, Park MH, Choi BG, Chi B, Jeong B (2010) Block length affects secondary structure, nanoassembly and thermosensitivity of poly(ethylene glycol)-poly(L-alanine) block copolymers. J Mater Chem 20:3416–3421

119. Petka WA, Harden JL, McGrath KP, Wirtz D, Tirrell DA (1998) Reversible hydrogels from self-assembling artificial proteins. Science 281:389–392

120. Eloi J-C, Rider DA, Cambridge G, Whittell GR, Winnik MA, Manners I (2011) Stimulus-responsive self-assembly: reversible, redox-controlled micellization of polyferrocenylsilane diblock copolymers. J Am Chem Soc 133:8903–8913

121. Ho R-M, Chiang Y-W, Lin S-C, Chen C-K (2011) Helical architectures from self-assembly of chiral polymers and block copolymers. Prog Polym Sci 36:376–453

122. Lin J, Zhu J, Chen T, Lin S, Cai C, Zhang L, Zhuang Y, Wang X-S (2009) Drug releasing behavior of hybrid micelles containing polypeptide triblock copolymer. Biomaterials 30:108–117
123. Fuks G, Mayap Talom R, Gauffre F (2011) Biohybrid block copolymers: towards functional micelles and vesicles. Chem Soc Rev 40:2475–2493
124. Qian J, Zhang M, Manners I, Winnik MA (2010) Nanofiber micelles from the self-assembly of block copolymers. Trends Biotechnol 28:84–92
125. Cauet SI, Lee NS, Lin LY, Wooley KL (2012) Individual nano-objects obtained via hierarchical assembly of polymer building blocks. In: Matyjaszewski K, Moller M (eds) Polymer science: a comprehensive reference. Elsevier, Amsterdam, pp 775–820
126. Feng C, Li Y, Yang D, Hu J, Zhang X, Huang X (2011) Well-defined graft copolymers: from controlled synthesis to multipurpose applications. Chem Soc Rev 40:1282–1295
127. Bian Q, Xiao Y, Lang M (2012) Thermoresponsive biotinylated star amphiphilic block copolymer: synthesis, self-assembly, and specific target recognition. Polymer 53:1684–1693
128. Cai C, Wang L, Lin J, Zhang X (2012) Morphology transformation of hybrid micelles self-assembled from rod-coil block copolymer and nanoparticles. Langmuir 28:4515–4524
129. Cai C, Zhu W, Chen T, Lin J, Tian X (2009) Synthesis and self-assembly behavior of amphiphilic polypeptide-based brush-coil block copolymers. J Polym Sci A Polym Chem 47:5967–5978
130. Koga T, Taguchi K, Kobuke Y, Kinoshita T, Higuchi M (2003) Structural regulation of a peptide-conjugated graft copolymer: a simple model for amyloid formation. Chem Eur J 9:1146–1156
131. Tang D, Lin J, Lin S, Zhang S, Chen T, Tian X (2004) Self-assembly of poly(γ-benzyl L-glutamate)-graft-poly(ethylene glycol) and its mixtures with poly(γ-benzyl L-glutamate) homopolymer. Macromol Rapid Commun 25:1241–1246
132. Marsden HR, Handgraaf J-W, Nudelman F, Sommerdijk NAJM, Kros A (2010) Uniting polypeptides with sequence-designed peptides: synthesis and assembly of poly (γ-benzyl L-glutamate)-b-coiled-coil peptide copolymers. J Am Chem Soc 132:2370–2377
133. Huang J, Bonduelle C, Thevenot J, Lecommandoux S, Heise A (2012) Biologically active polymersomes from amphiphilic glycopeptides. J Am Chem Soc 134:119–122
134. Checot F, Lecommandoux S, Gnanou Y, Klok HA (2002) Water-soluble stimuli-responsive vesicles from peptide-based diblock copolymers. Angew Chem Int Ed 41:1339–1343
135. Sun J, Chen X, Deng C, Yu H, Xie Z, Jing X (2007) Direct formation of giant vesicles from synthetic polypeptides. Langmuir 23:8308–8315
136. Schatz C, Louguet S, Le Meins J-F, Lecommandoux S (2009) Polysaccharide-block-polypeptide copolymer vesicles: towards synthetic viral capsids. Angew Chem Int Ed 48:2572–2575
137. Holowka EP, Sun VZ, Kamei DT, Deming TJ (2007) Polyarginine segments in block copolypeptides drive both vesicular assembly and intracellular delivery. Nat Mater 6:52–57
138. Cai C, Lin J, Chen T, Tian X (2010) Aggregation behavior of graft copolymer with rigid backbone. Langmuir 26:2791–2797
139. Zhuang Z, Zhu X, Cai C, Lin J, Wang L (2012) Self-assembly of a mixture system containing polypeptide graft and block copolymers: experimental studies and self-consistent field theory simulations. J Phys Chem B 116:10125–10134
140. Cornelissen JJLM, Fischer M, Sommerdijk NAJM, Nolte RJM (1998) Helical superstructures from charged poly(styrene)-poly(isocyanodipeptide) block copolymers. Science 280:1427–1430
141. Cai C, Lin J, Chen T, Wang X, Lin S (2009) Super-helices self-assembled from a binary system of amphiphilic polypeptide block copolymers and polypeptide homopolymers. Chem Commun 2709–2711
142. Bull SR, Palmer LC, Fry NJ, Greenfield M, Messmore B, Meade T, Stupp SI (2008) A templating approach for monodisperse self-assembled organic nanostructures. J Am Chem Soc 130:2742–2743

Synthesis, Characteristics, and Applications of Intrinsically Light-Emitting Polymer Nanostructures

Young Ki Hong, Dong Hyuk Park, Seok Ho Lee, and Jinsoo Joo

Abstract Light-emitting π-conjugated polymers and their nanostructures have been intensively studied from the viewpoints of both fundamental research and optoelectronic applications. The characteristics of light-emitting polymer nanostructures, such as light absorption and emission efficiencies, can be tuned through chemical processing and by varying their physical dimensions. In this review article, recent progress in the synthesis, characterization, modification, and applications of light-emitting polymer-based nanostructures is presented. Various synthetic methods for light-emitting polymer nanostructures are introduced, and their intrinsic optical properties at a nanoscale level are summarized. Post-synthetic treatments for modification of the characteristics related to the morphologies and doping states are discussed. Finally, potential applications of these nanostructures to barcode/quasi-superlattice nanowires, biosensors, and nano-optoelectronics are presented.

Keywords π-Conjugation · Barcode · Biosensor · Doping · Electron beam · Hybridization · Hydrothermal · Light-emitting polymer · Nanoscale optical property · Nanostructure · Optoelectronics

Contents

Y.K. Hong, D.H. Park, S.H. Lee, and J. Joo (✉)
Department of Physics, Korea University, Seoul 136-713, Korea
e-mail: jjoo@korea.ac.kr

Abbreviations

1D	One-dimensional
2D	Two-dimensional
3D	Three-dimensional
c-AFM	Conducting atomic force microscope
CCD	Charge-coupled device
CV	Cyclic voltammetry
DBSA	Dodecylbenzenesulfonic acid
E-beam	Electron-beam
HDL	Hybrid double-layered
HR	High-resolution
I–V	Current–voltage
LCM	Laser confocal microscope
LECB	Light-emitting color barcode
MEH-PPV	Poly[2-methoxy-5-(2′-ethylhexyloxy)-p-phenylenevinylene]
NP	Nanoparticle
NT	Nanotube
NW	Nanowire
P3BT	Poly(3-butylthiophene)
P3HT	Poly(3-hexylthiophene)
P3MT	Poly(3-methylthiophene)
PCBM	[6,6]-Phenyl C_{61}-butyric acid methyl ester
PEDOT	Poly(3,4-ethylenedioxythiophene)
PL	Photoluminescence
PTh	Polythiophene
SEM	Scanning electron microscope
SPR	Surface plasmon resonance
TEM	Transmission electron microscope
UV–vis	Ultraviolet–visible

1 Introduction

Light-emitting polymers with a π-conjugated structure have attracted considerable interest in the fields of both fundamental science and applied research owing to their fascinating one-dimensional (1D) characteristics and potential optoelectronic applications [1–6]. Figure 1 shows the chemical structures of a few examples of π-conjugated light-emitting polymers: polythiophene (PTh), poly(3-alkylthiophene) (P3AT), poly(3,4-ethylenedioxythiophene) (PEDOT), poly(p-phenylenevinylene) (PPV), and poly[2-methoxy-5-(2'-ethylhexyloxy)-p-phenylenevinylene] (MEH-PPV).

The π-conjugated structure of light-emitting polymers refers to the alternation of single and double covalent bonds between adjacent carbon atoms [7]. This π-conjugation leads to delocalized π-electrons along the polymeric main chains, which play an important role in the electronic and optical properties of light-emitting polymers [8]. The electronic structures of π-conjugated polymers are successfully described by the Su–Schrieffer–Heeger (SSH) Hamiltonian model [9–11]. As a consequence of the π-conjugated structure, these light-emitting polymers have a semiconducting band gap. Both theoretical and experimental studies have been conducted on chemical processes for engineering the energy band structure of π-conjugated polymers [10, 12–24]. Thus, the optical and electrical properties of π-conjugated polymers can be varied by controlling the energy band structure and by chemical doping.

With rapid developments in nanoscience and nanotechnology, various nanostructures, including nanotubes (NTs), nanowires (NWs), and nanoparticles (NPs), have been fabricated using light-emitting polymers [4–6]. The intrinsic characteristics of π-conjugated polymer nanostructures can be controlled through the physical dimensions, chemical processes, and post-synthetic treatments.

This review article introduces and summarizes the fabrication, characterization, and modification processes as well as optoelectronic applications of various light-emitting polymer nanostructures.

2 Synthetic Methods for Nanostructures

π-Conjugated light-emitting polymer nanostructures, including NTs, NWs, and NPs have been synthesized using template and template-free methods [5, 6, 25–29]. Recently, Jenekhe et al. reviewed various synthetic methods for 1D nanostructures of π-conjugated molecular systems [30]. Template-based methods are categorized into two sub-categories depending on the type of template, i.e., soft templates and hard templates. Anodic aluminum oxide (Al_2O_3), particle track-etched membrane, mesoporous silica, microchannel array, and zeolite are typically employed as hard templates. The synthesis of π-conjugated polymer NTs or NWs with hard templates involves a combination of electrochemical [25, 31–33], chemical [34–37], and organic vapor deposition [38] techniques. The formation of NTs or NWs and their physical dimensions, such as diameter and length, are determined by the
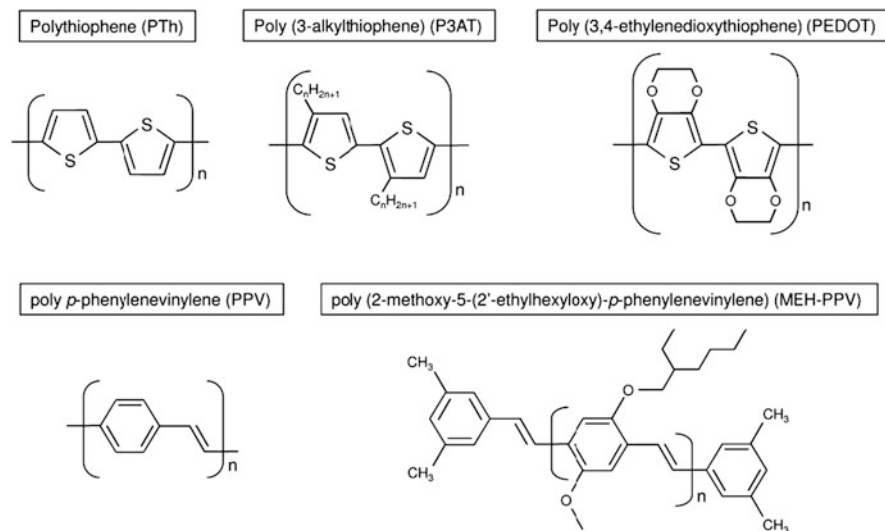
Fig. 1 Chemical structures of various light-emitting polymers with π-conjugated structure

size of the nanoporous template used. Of the template-free methods, this section presents the reprecipitation method for the synthesis of NPs and the electrospinning method for NWs.

2.1 Electrochemical Polymerization

In this section, we focus on the synthesis of light-emitting polymer NTs and NWs through electrochemical polymerization using nanoporous Al_2O_3 templates. For electrochemical synthesis of the polymer NTs and NWs, the electrolyte consists of a solution of monomers and dopants in appropriate solvents such as deionized water, *N*-methyl-2-pyrrolidinone (NMP), and acetonitrile (CH_3CN). Aniline, pyrrole, and thiophene and its derivatives such as 3-methylthiophene (3-MT), 3-butylthiophene (3-BT), 3-hexylthiophene (3-HT), and ethylenedioxythiophene (EDOT) are typical monomers. Dopants can include anionic salts such as BF_4^-, PF_6^-, and ClO_4^- as well as camphorsulfonic acid (CAS) and dodecylbenzenesulfonic acid (DBSA), which also act as surfactants that promote homogeneous dispersion of the hydrophobic monomers in deionized water. Thin metal layers, for example, gold (Au), platinum (Pt), and aluminum (Al), are thermally evaporated on one side of the nanoporous Al_2O_3 template and attached to the metal working electrode.

When a current or voltage is applied to the electrodes, the monomers are oxidized at the surface of the electrode. As a result of the initial oxidation, the monomers form radical cations that react with other monomers in the electrolyte to form oligomeric products, as shown in Fig. 2. The extended π-conjugation in the polymeric chain (i.e., polymerization) is assisted by dopant anions, and the synthesis and doping of the
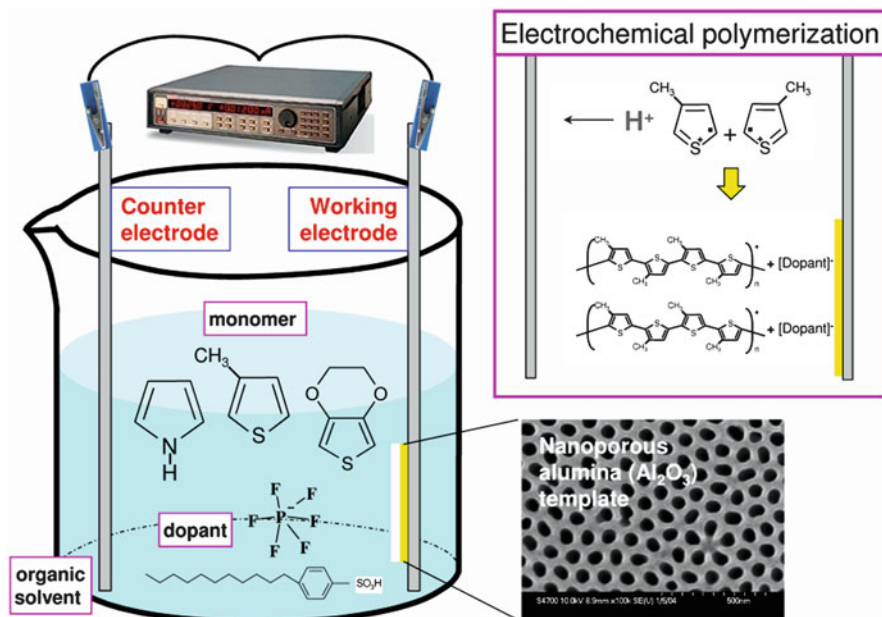
Fig. 2 Electrochemical polymerization method using alumina (Al_2O_3) nanoporous template

light-emitting polymer NTs and/or NWs are generally accomplished simultaneously [39]. After polymerization, an acid (e.g., HF or H_3PO_4), base (e.g., NaOH or KOH), or organic solvent can be used to dissolve the nanoporous template and isolate the synthesized NTs or NWs. The intrinsic optical properties of the electrochemically synthesized light-emitting polymer NTs or NWs can be controlled by the synthetic conditions such as molar ratio of monomer to dopant, applied current or voltage, synthetic temperature, and type of solvent used for the dissolution of the nanoporous template.

Figure 3 shows scanning electron microscope (SEM) and transmission electron microscope (TEM) images of various light-emitting polymer NTs or NWs synthesized through electrochemical polymerization with nanoporous Al_2O_3 templates [40–43]. The SEM image in Fig. 3a shows open ends of the P3MT NTs, and the inset shows filled ends of P3MT NWs. In the TEM image, the formation of NTs can be clearly identified; the thickness of the NT wall was estimated at 5−10 nm. In order to synthesize P3MT NTs, a current density of ~1.7 mA/cm^2 was applied for 18−20 min. For the formation of P3MT NWs, the applied current density and polymerization time were increased up to 2.0−2.5 mA/cm^2 and ~23 min, respectively [40]. Martin et al. reported that polymerization was initiated at the bottom of nanopores on the working electrode and proceeded along the inside walls of the nanoporous Al_2O_3 template [44]. The results indicated that NTs could be converted to NWs by increasing the polymerization time and applied current density.

The formation of P3BT NWs can also be controlled by adjusting the applied current density and polymerization time [41]. P3BT NWs with open ends at the top
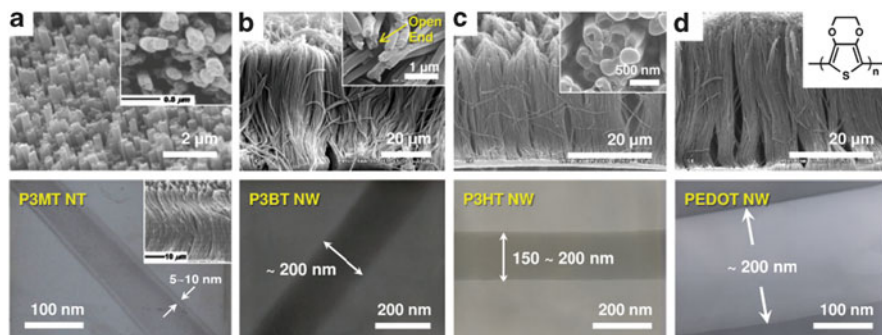
Fig. 3 SEM and TEM images of the electrochemically synthesized light-emitting polymer NTs and NWs: (**a**) P3MT NTs, (**b**) P3BT NWs, (**c**) P3HT NWs, and (**d**) PEDOT NWs. [Reproduced in part from (**a**) [40], (**b**) [41], (**c**) [42], and (**d**) [43] with permission. (**a**) Copyright 2005 American Institute of Physics. (**b**) Copyright 2008 Electrochemical Society. (**c**) Copyright 2007 American Institute of Physics. (**d**) Copyright 2008 Elsevier B.V.]

are observed in the SEM and TEM images in Fig. 3b. The length and diameter of the NWs are ~20 μm and ~200 nm, respectively. A TEM image of an isolated single P3HT NW with open ends is shown in Fig. 3c. The diameter of the single P3HT NW is 150−200 nm. Figure 3d shows the SEM and TEM images of PEDOT NWs. A uniform and continuous array of the PEDOT NWs with a length of ~30 μm was observed by SEM. From the magnified TEM image, the diameter of a single PEDOT NW can be estimated at ~200 nm.

2.2 Reprecipitation

Horn and Rieger reviewed the various synthetic methods and optical properties of organic NPs [45]. Reprecipitation is a representative method for fabricating π-conjugated polymer NPs [45–48]. As shown in Fig. 4, a polymer powder is dissolved in an amphiphilic solvent (e.g., tetrahydrofuran) and the polymer solution rapidly dropped into deionized water under vigorous stirring. During this process, polymer molecules form spherically shaped NPs through aggregation in order to minimize the interfacial energy between the polymer solution and water. The size of the NPs can be controlled by varying the concentration of the polymer solution, stirring speed, temperature of deionized water, as well as by addition of polar solvents such as acetone. A mini-emulsion method has been recently developed to synthesize homogeneously dispersed polymer NPs [45, 49, 50]. In this method, an aqueous solution of surfactant is added to a solution of the polymer in an organic solvent such as chloroform. The mixture of solutions is then emulsified through ultrasonication to afford an aqueous suspension of polymer NPs.

Figure 5a shows an SEM image of MEH-PPV NPs fabricated by reprecipitation [51]. The NPs were spherical and had diameters estimated to be in the range
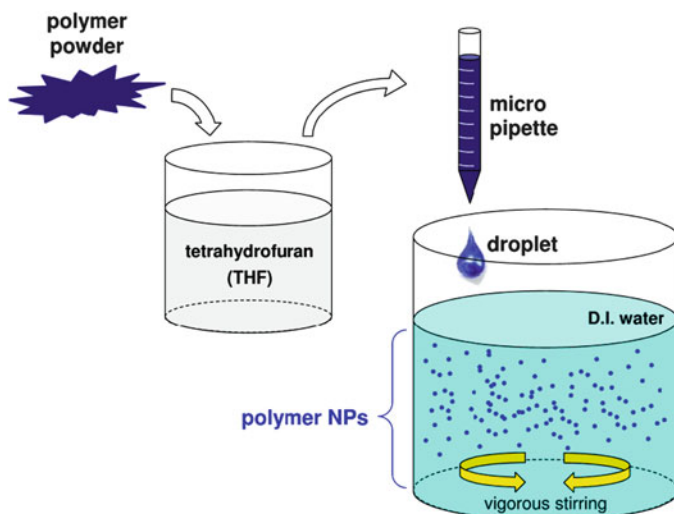
Fig. 4 Scheme showing the reprecipitation process
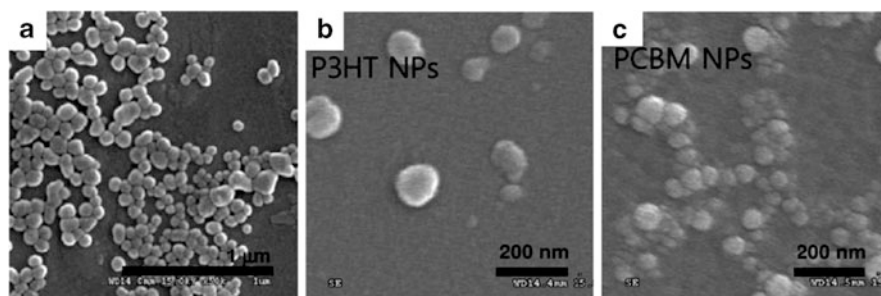
Fig. 5 SEM images of (**a**) MEH-PPV NPs, (**b**) P3HT NPs, and (**c**) PCBM NPs. [Reproduced in part from (**a**) [51] and (**b, c**) [52] with permission. (**a**) Copyright 2009 American Chemical Society. (**b**, **c**) Copyright 2012 Royal Society of Chemistry.]

40−150 nm. SEM images of P3HT and [6,6]-phenyl C_{61}^{-} butyric acid methyl ester (PCBM) NPs fabricated by the mini-emulsion method are shown in Fig. 5b and Fig. 5c, respectively [52]. The diameters of the P3HT and PCBM NPs were ~108 ($\pm$28) and 77 ($\pm$20) nm, respectively.

2.3   *Electrospinning*

Electrospinning is a simple, inexpensive, and efficient method based on application of a high electric field for fabricating relatively long and continuous NWs (i.e., nanofibers) of various organic and/or inorganic materials [53–57]. With this

Fig. 6 Modified electrospinning system with two-capillary spinneret. [Reproduced with permission from [59]. Copyright 2004 American Chemical Society]
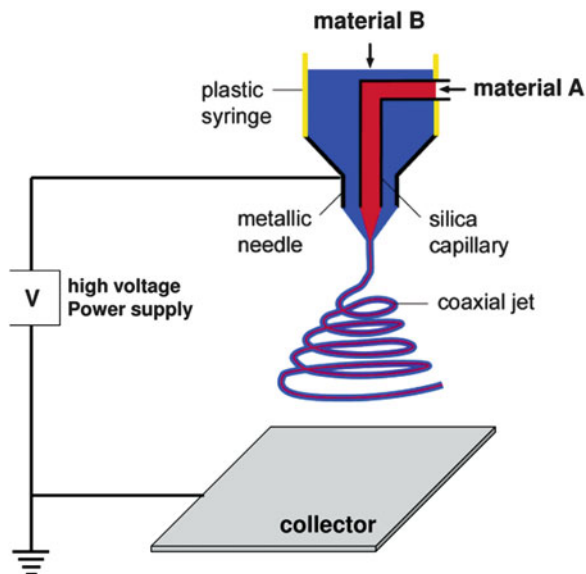
method, ultrathin fibers can be obtained from solutions and melts by the uniaxial elongation of viscoelastic jets owing to the electrostatic repulsive interaction between surface charges. Conventional electrospinning systems consist of three major components: a high-voltage power supply, a metallic needle (i.e., capillary spinneret), and a grounded collector as the counter electrode. An electric field applied between the metallic needle and collector (typically on the order of 1×10^5 V/m) causes charging on the surface of a droplet at the needle tip, which transforms into a funnel-shape known as a Taylor cone. Then, a fluidic jet is ejected that is accelerated from the needle tip owing to the electrostatic force from the oppositely charged collector plate [30, 54, 56].

The dimensions and morphology of the electrospun nanofibers are determined by the intrinsic properties of the materials (e.g., chemical structure, molecular weight, and solubility), properties of the solvent (e.g., surface tension, viscosity, conductivity, vapor pressure, polarity, and dielectric constant), and external processing parameters (e.g., electric potential and field distribution, concentration of constituent materials and any additional ions, and feed rate). Electrospinning systems have been modified to allow greater control over the process and to tailor the structure of the nanofibers. The substitution of a rotating drum for a collector plate results in uniform mats of electrospun nanofibers [58]. Figure 6 shows a modified electrospinning system with a two-capillary spinneret for different materials [59]. This system affords composite nanofibers or NTs combined with the proper elimination process of inner materials.

Laforgue et al. reported on a combination of electrospinning and vapor-phase polymerization to fabricate PEDOT nanofibers [60]. Figure 7 shows the optical microscope and SEM images of these electrospun PEDOT nanofibers. Their average diameter was 350 ($\pm$60) nm.
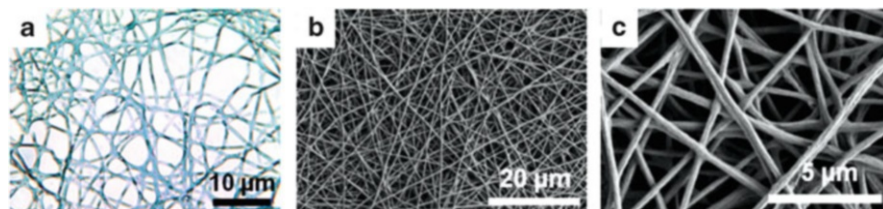
Fig. 7 (**a**) Optical microscope and (**b**, **c**) SEM images of PEDOT nanofibers at different magnifications. [Reproduced with permission from [60]. Copyright 2011 Elsevier B.V.]

3 Optical Properties of As-Prepared Nanostructures

In this section, we discuss the optical properties of the as-prepared light-emitting polymer nanostructures described in Sect. 2. The ultraviolet and visible (UV–vis) absorption and photoluminescence (PL) spectra of the polymer nanostructures dispersed in organic solvents are introduced and discussed. The nanoscale and solid-state optical properties of a single unit of the light-emitting polymer nanostructures can be investigated using high-resolution laser confocal microscope (LCM) systems built around an inverted optical microscope, coupled with luminescence color charge-coupled device (CCD) measurements. In this method, the LCM PL intensities of single units of nanostructures are measured in units of voltage or photon count. For a quantitative comparison of the nanoscale and solid-state optical properties of polymer nanostructures, the LCM PL spectra must be normalized with respect to those of pristine (i.e., as-prepared) samples. The details of the methods for the LCM and CCD experiments are reported elsewhere [41, 42, 61–65].

3.1 Electrochemically Synthesized Nanotubes and Nanowires

3.1.1 P3MT Nanotubes

Park and coworkers reported that the doping level and structural properties of electrochemically synthesized P3MT NTs could be controlled by varying the synthetic temperature [40]. Figure 8a shows a comparison of the UV–vis absorption spectra of P3MT NTs synthesized at various temperatures. For HF-treated P3MT NTs, the π–π* transition peak shifted from 2.27 to 2.33 eV for NTs synthesized at 20°C and −20°C, respectively. Furthermore, as the synthetic temperature decreased from 20°C to −20°C, the intensity of the bipolaron peaks at ~1.6 eV increased, implying a variation in the degree of doping with temperature [24]. For NaOH-treated P3MT NTs, a bipolaron peak was only observed at ~1.6 eV for the NTs synthesized at −20°C, as shown in the inset of Fig. 8a. The π–π* transition peak of the NaOH-treated P3MT NTs was observed at ~2.15 eV. The results indicate that the optical properties of P3MT NTs can be controlled by varying the synthetic
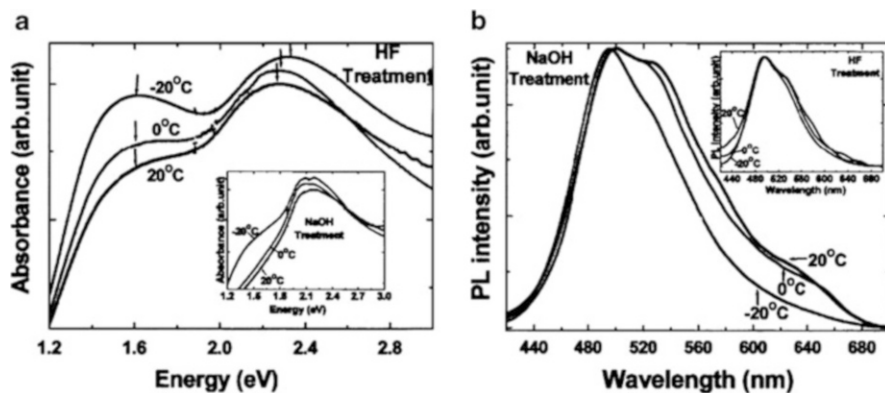
Fig. 8 (**a**) Comparison of UV–vis absorption spectra of HF-treated P3MT NTs synthesized at −20°C, 0°C, and 20°C. *Inset*: spectra of NaOH-treated P3MT NTs synthesized at −20°C, 0°C, and 20°C. (**b**) Comparison of solution PL spectra of NaOH-treated P3MT NTs. *Inset*: spectra of HF-treated P3MT NTs. [Reproduced with permission from [40]. Copyright 2005 American Institute of Physics.]

temperature as well as the template-dissolving organic solvents. It was reported that lower temperatures in electrochemical synthesis of conducting polymers lead to enhanced electrical properties owing to the better chain alignment and extended conjugation length [66].

Figure 8b shows the normalized solution PL spectra of P3MT NTs synthesized at 20°C, 0°C, and −20°C. For NaOH-treated P3MT NTs, the main PL peaks were observed at ~490 nm, together with shoulder peaks at ~530 nm attributed to the S 0–1 transition. As the synthetic temperature decreased, the shoulder peak at ~530 nm disappeared, and the main peak at ~490 nm became sharper. As shown in the inset of Fig. 8b, similar dependence on the synthetic temperature was observed for HF-treated P3MT NTs. These results might be attributed to the better chain alignment and extended conjugation for the P3MT NTs synthesized at lower temperatures, in agreement with the findings based on the UV–vis absorption spectra.

3.1.2 P3MT Nanowires

Recently, Hong et al. reported the optical properties of electrochemically synthesized P3MT NWs that were separated from nanoporous Al_2O_3 templates by treatment with HF [62]. Figure 9a shows the UV–vis absorption spectrum of P3MT NWs that were synthesized at a lower temperature and higher applied current than those shown in Fig. 8. A broad and relatively intense bipolaron absorption band was observed at ~780 nm and a relatively weak π–π^* transition peak was observed at ~390 nm, which indicates that the P3MT NWs shown in Fig. 9 were more heavily doped than those shown in Fig. 8.
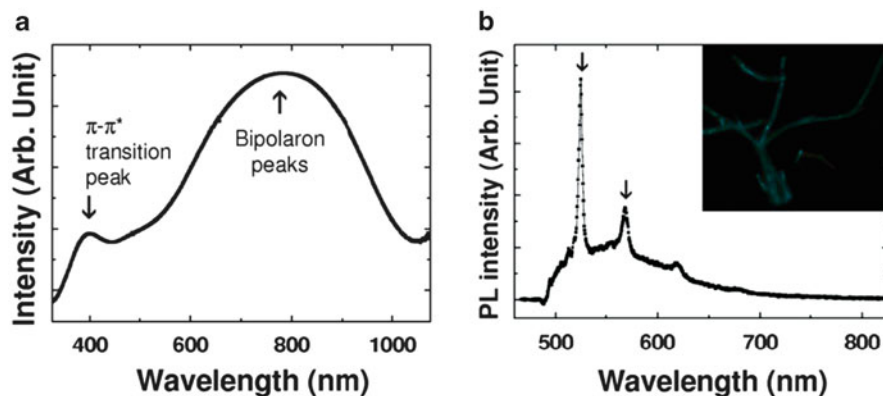
Fig. 9 (**a**) UV–vis absorption spectrum of as-prepared P3MT NWs. (**b**) LCM PL spectrum of single P3MT NW. *Inset*: color CCD image of single P3MT NW. [Reprinted with permission from [62]. Copyright 2011 Wiley-VCH.]

Figure 9b shows the LCM PL spectrum of an isolated single P3MT NW. The sharp peaks observed at 525 and 569 nm are the anti-Stokes' Raman shift of the P3MT material corresponding to 1,459 and 2,917 cm^{-1}, which were assigned to the symmetric $C_\alpha = C_\beta$ ring-stretching mode and the methyl (CH_3) symmetric stretching mode in the thiophene ring out-of-plane deformation, respectively [63, 67–69]. Excluding these Raman modes, which are commonly observed in nanoscale and solid-state PL measurements, the maximum LCM PL peak was observed at 520−530 nm. This is reflected in the green light emission seen in the color CCD image of the P3MT NWs shown in the inset of Fig. 9b.

3.1.3 P3BT Nanowires

Park et al. also reported that the doping levels of electrochemically synthesized P3BT NWs are correlated with the type of solvent (i.e., acid or base) used for dissolution of the nanoporous Al_2O_3 templates [41]. Figure 10a shows the normalized UV–vis absorption spectra of P3BT NWs. The π–π* transition peaks of the P3BT NWs treated with HF and NaOH solutions appeared at 393 and 438 nm, respectively. Thus, the π–π* transition peak of the HF-treated P3BT NWs was blue-shifted by ~45 nm compared with that of the NaOH-treated NWs [70]. A broad bipolaron peak was observed at ~816 nm for the HF-treated P3BT NWs; however, this peak almost disappeared in the spectra of the NaOH-treated NWs [71, 72]. These results stem from the light doping and dedoping of the P3BT NWs during treatment with HF and NaOH solutions, respectively.

Figure 10b shows the normalized solution PL spectra of P3BT NWs treated with HF and NaOH solutions. The main PL peaks of the HF- and NaOH-treated P3BT NWs were observed at 547 and 564 nm, respectively. The inset of Fig. 10b shows photographs of light emission from HF- and NaOH-treated P3BT NWs that were
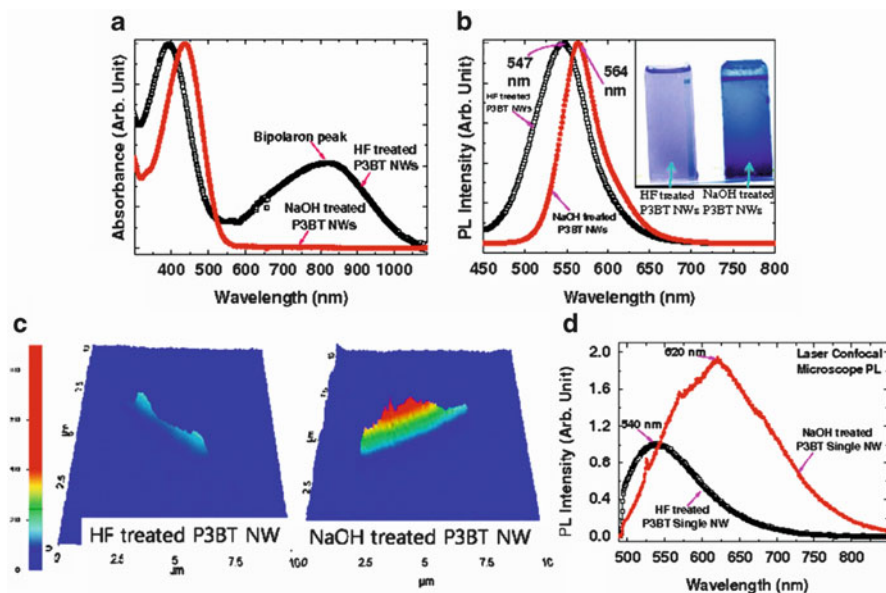
Fig. 10 (**a**) Normalized UV–vis absorption spectra of HF- and NaOH-treated P3BT NWs. (**b**) Normalized solution PL spectra of corresponding samples. *Inset*: luminescent photographs of HF- and NaOH-treated P3BT NWs. (**c**) 3D LCM PL images of isolated single NWs. Color scale bar represents LCM PL intensities in the unit of measured voltages. (**d**) Comparison of LCM PL spectra of HF- and NaOH-treated P3BT NWs. [Reprinted with permission from [41]. Copyright 2008 Electrochemical Society.]

homogeneously dispersed in chloroform (CHCl$_3$) solutions. The HF- and NaOH-treated P3BT NWs emitted green and yellow light, respectively.

Figure 10c shows three-dimensional (3D) LCM PL images of isolated single HF- and NaOH-treated P3BT NWs. The LCM PL intensities of the HF- and NaOH-treated P3BT single NWs were 20−25 and 45−55 mV, respectively. The LCM PL intensity of the NaOH-treated P3BT single NW was 1.8−2.8 times higher than that of the HF-treated NW because of the reduction in PL quenching owing to the dedoping effect. Figure 10d compares the averaged LCM PL spectra of isolated single HF- and NaOH-treated P3BT NWs for five different positions on the same NW under the same LCM experimental conditions. The maximum LCM PL peaks of the HF- and NaOH-treated P3BT single NWs were observed at ~540 nm (green–yellow light emission) and ~620 nm (orange–red light emission), respectively. The intensity of the LCM PL peak at 620 nm for the NaOH-treated P3BT NW was about two times higher than that of the HF-treated P3BT NW. The enhanced PL intensity and bright light emission in the NaOH-treated P3BT single NW are attributed to the dedoping effect.
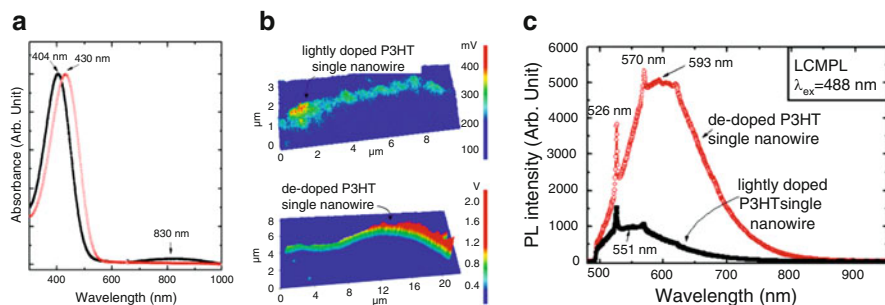
Fig. 11 (**a**) Normalized UV–vis absorption spectra of P3HT NWs. (**b**) 3D LCM PL images of isolated single NWs. Color scale bar represents the LCM PL intensities in the unit of measured voltages. (**c**) Comparison of LCM PL spectra of P3HT NWs. (Reprinted with permission from [42]. Copyright 2007 American Institute of Physics.)

3.1.4 P3HT Nanowires

The dedoping effects of NaOH treatment on electrochemically synthesized P3HT NWs were also reported by Lee and coworkers [42]. Figure 11a shows the normalized UV–vis absorption spectra of P3HT NWs. Shifting of the π–π^* transition peaks and variation of the doping-induced bipolaron peaks were also observed after treatment with HF and NaOH solutions, respectively. The broad bipolaron peak at 830 nm for the HF-treated P3HT NWs was decreased by NaOH treatment as a result of the dedoping effect [41].

Figure 11b shows the 3D LCM PL images of single lightly doped and de-doped P3HT NWs obtained after HF and NaOH treatments, respectively. The LCM PL intensities for these strand were $0.3-0.4$ and $1.2-2.3$ V, respectively. The LCM PL intensity of the de-doped P3HT single NW was three to eight times higher than that of the lightly doped NWs. Figure 11c compares the averaged LCM PL spectra of individual lightly doped and de-doped P3HT NWs. The main PL peaks for the isolated lightly doped and de-doped P3HT NWs were observed at 551 nm (green light emission) and 593 nm (yellow–green light emission), respectively. The sharp peaks in the PL spectra at 526 and 570 nm originated from the Raman modes. The integrated area of the LCM PL spectrum of the de-doped P3HT NW was approximately six times larger than that of the lightly doped P3HT NW.

Light-emitting polymer NTs and NWs synthesized through electrochemical polymerization exhibit doped states owing to dopant-assisted polymerization [39]. Analysis of the UV–vis spectra showed that the doping level of NTs and NWs can be controlled by varying the synthetic temperatures as well as the applied current or voltage, which directly influence the intrinsic optical properties of the nanostructures. In addition, the solvent used for removing the Al_2O_3 template is also an important determiner of the doping characteristics of the NTs and NWs.
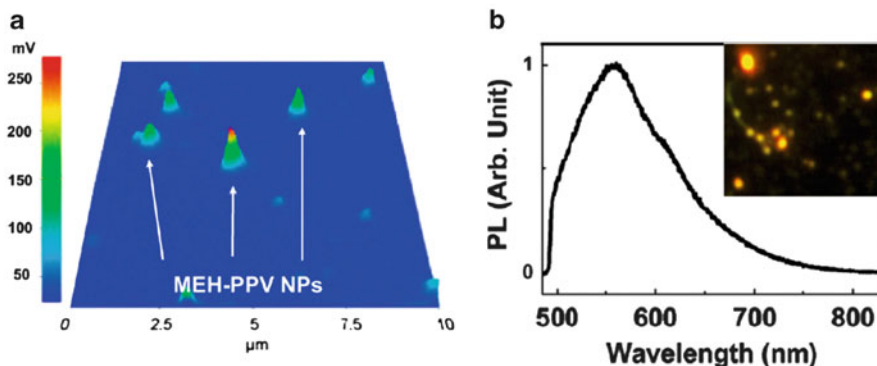
Fig. 12 (**a**) 3D LCM PL image of isolated MEH-PPV NPs. Color scale bar represents the LCM PL intensities in the unit of measured voltages. (**b**) LCM PL spectrum of MEH-PPV single NP. *Inset*: color CCD image of the NPs. (Reproduced with permission from [51]. Copyright 2009 American Chemical Society.)

3.2   Nanoparticles Prepared by Reprecipitation

3.2.1   MEH-PPV Nanoparticles

The nanoscale and solid-state optical properties of MEH-PPV NPs fabricated by reprecipitation have been reported [51]. Figure 12a shows a 3D LCM PL image of a single MEH-PPV NP. The LCM PL intensity of a single MEH-PPV NP was measured at ~267 ($\pm$17.7) mV, which is the average over 100 different NPs. Figure 12b shows the LCM PL spectrum of the MEH-PPV NP. The main PL peak was observed at ~560 nm, which corresponds to the π–π* transition peak of MEH-PPV observed at ~490 nm [51, 73, 74]. These results are reflected in the yellow–orange light emission seen in the color CCD image in the inset of Fig. 12b. In addition, the LCM PL peak of MEH-PPV NPs in the solid state (~578 nm) was blue-shifted compared with the solution PL peak [51]. This is attributed to the reduction in the conjugation length due to the steric confinement of NPs, which results in bending or kinking of the polymer backbone [73, 74], as well as to oxidation of NPs in air [75].

3.3   Electrospun Nanowires

3.3.1   Nanowires of MEH-PPV Derivatives

Di Benedetto et al. reported the optical properties of electrospun NWs of MEH-PPV and various derivatives such as poly{[2-methoxy-5-(2-ethylhexyloxy)-1,4-(1-cyanovinylenephenylene)]-*co*-[2,5-bis(*N,N*′-diphenylamino)-1,4-phenylene]},
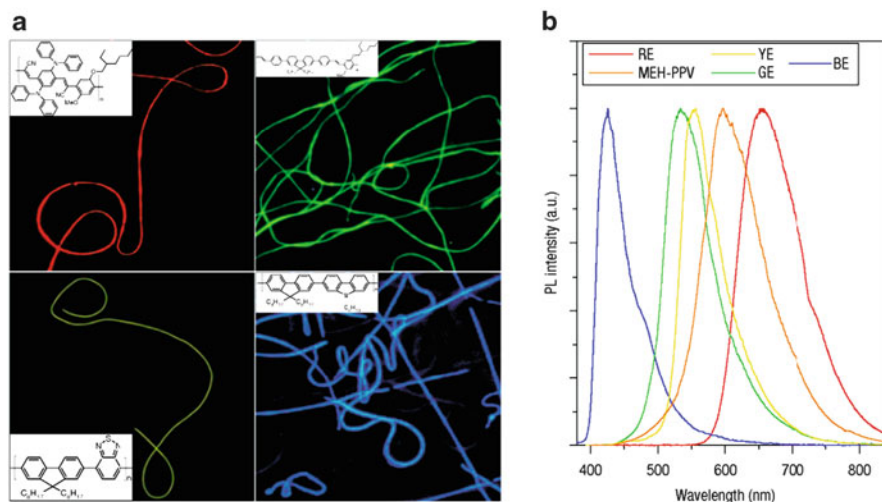
Fig. 13 (**a**) Fluorescence microscope images of electrospun light-emitting polymer NWs. *Insets*: chemical structure of each light-emitting polymer. (**b**) Normalized PL spectra of the corresponding samples. (Reproduced with permission from [76]. Copyright 2008 Nature Publishing Group.)

poly{[9,9-dioctylfluorenylene-2,7-diyl]-*co*-[1,4-diphenylenevinylene-2-methoxy-5-(2-ethylhexyloxy)-benzene]}, poly{[9,9-dioctylfluorenyl-2,7-diyl]-*co*-[1,4-benzo-(2,1′,3)-thiadiazole]}, and poly[(9,9-dioctylfluorenyl-2,7-diyl)-*alt-co*-(9-hexyl-3,6-carbazole)] [76]. These MEH-PPV derivatives are denoted as RE, GE, YE, and BE, respectively, according to the color of the light they emit. Figure 13a shows the fluorescence microscope images of the electrospun NWs of MEH-PPV derivatives. The images show well-defined colors that agree with the corresponding PL spectra shown in Fig. 13b. These results indicate that the optical properties of various light-emitting polymer NWs can be successfully controlled by the molecular design.

4   Post-synthetic Treatments for Modification of Nanostructure Characteristics

In this section, we introduce post-synthetic treatments that enable further modification of the physical properties such as the structural, electrical, and optical properties of the as-prepared light-emitting polymer nanostructures. Of the various methods of controlling the intrinsic characteristics of nanostructures, we discuss the electrochemical doping and dedoping process using cyclic voltammetry (CV) and unfocused electron (E)-beam irradiation. Hydrothermal treatment of undoped NPs is presented, which involves application of external pressure and heat to NPs. Finally, we describe hybridization with nanoscale

metals, which allows drastic variations in the optical properties by exploiting the surface plasmon resonance (SPR) coupling effect between the light-emitting polymer and the nanoscale metal.

4.1 Electrochemical Doping and Dedoping: Cyclic Voltammetry

Electrochemical reduction and oxidation (redox) using CV is widely used to control the doping characteristics of π-conjugated polymers and their nanostructures [77–80]. Doping of π-conjugated polymers induces changes in structure and electronic state owing to intercalation of dopants between the polymeric chains. These structural modifications induce variations in the π-conjugation length, polymeric chain alignment, and intra-/interchain interactions, which in turn directly influence the light absorption and emission properties.

Park et al. reported that additional doping and dedoping of the as-prepared P3MT NTs and PEDOT NWs can be accomplished through electrochemical means by controlling the applied potentials and scan rates using CV in a mixture of an ionic liquid and a CH_3CN solution without monomers [43, 65]. It is noted that 1-butyl-3-methylimidazolium hexafluorophosphate ($BMIMPF_6$) is an environmentally stable and recyclable ionic liquid that has shown negligible loss of electroactivity when used as a dopant [77].

4.1.1 P3MT Nanotubes

Figure 14a shows the normalized UV–vis absorption spectra of P3MT NTs at different doping levels. The π–π* transition peaks were observed at ~385 nm for all the P3MT NTs. Broad bipolaron peaks due to doping were observed near 750−800 nm [81]. The relative intensity ratio of the bipolaron peak to the π–π* transition peak for the doped-P3MT NTs was estimated to be 0.67, 0.52, 0.25, and 0.04, depending on the degree of additional doping or dedoping. The relative integrated area ratio of the bipolaron peak to the π–π* transition peak was 0.67, 0.54, 0.22, and 0.01, respectively. On the basis of the UV–vis absorption spectra, the various doped-P3MT NTs are denoted as doped-P3MT(0.04), doped-P3MT(0.25), doped-P3MT(0.52), and doped-P3MT(0.67) NTs, where the number in brackets represents the relative doping level. The relatively small ratios of intensity or area of the bipolaron peaks compared with those of the π–π* transition peaks imply that the P3MT NTs were lightly doped systems.

Figure 14b shows a comparison of the LCM PL spectra of a single P3MT NT with various doping levels: doped-P3MT(0.04), doped-P3MT(0.25), doped-P3MT (0.52), and doped-P3MT(0.67). The peak intensity and area of the LCM PL spectra of these single strands gradually increased up to 14 times as the doping level decreased. Two characteristic peaks in the LCM PL spectra for the P3MT materials were observed at 640 and 685 nm.
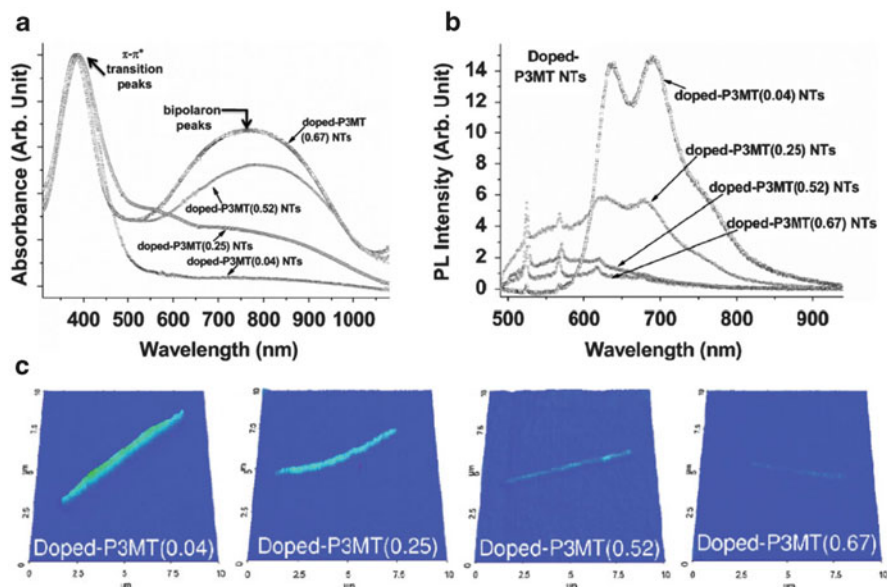
Fig. 14 (**a**) Comparison of UV–vis absorption spectra of P3MT NTs with different doping levels. (**b**) LCM PL spectra and (**c**) 3D LCM PL images of the corresponding samples. (Reproduced with permission from [65]. Copyright 2008 Wiley-VCH.)

Figure 14c shows the LCM PL images for isolated single doped-P3MT NTs with different doping levels under the same LCM experimental conditions. The color scale bar with the unit of voltage at the left-hand side of Fig. 14c represents the measured LCM PL intensity. The measured voltages of the LCM PL intensity for doped-P3MT(0.04), doped-P3MT(0.25), doped-P3MT(0.52), and doped-P3MT (0.67) single NTs were about $40-44$, $26-31$, $12-16$, and $5-8$ mV, respectively. These results indicate that the LCM PL intensity of the P3MT NTs decreased with an increase in the doping levels, which is attributed to PL quenching by the dopant or the counter-ions.

4.1.2   PEDOT Nanowires

PEDOT, one of the most popular π-conjugated polymers, has been intensively studied for developing nanoscale materials as well as for application to various nanodevices such as biosensors and electrochromic devices, and for drug delivery [82–84]. However, studies on PEDOT nanomaterials and bulk films have mainly focused on their electrical and structural properties and on the various applications of the conducting form of the material (i.e., doped PEDOT systems). The light-emitting characteristics of doped and de-doped PEDOT nanomaterials were first reported by Park et al. in 2008 [43].
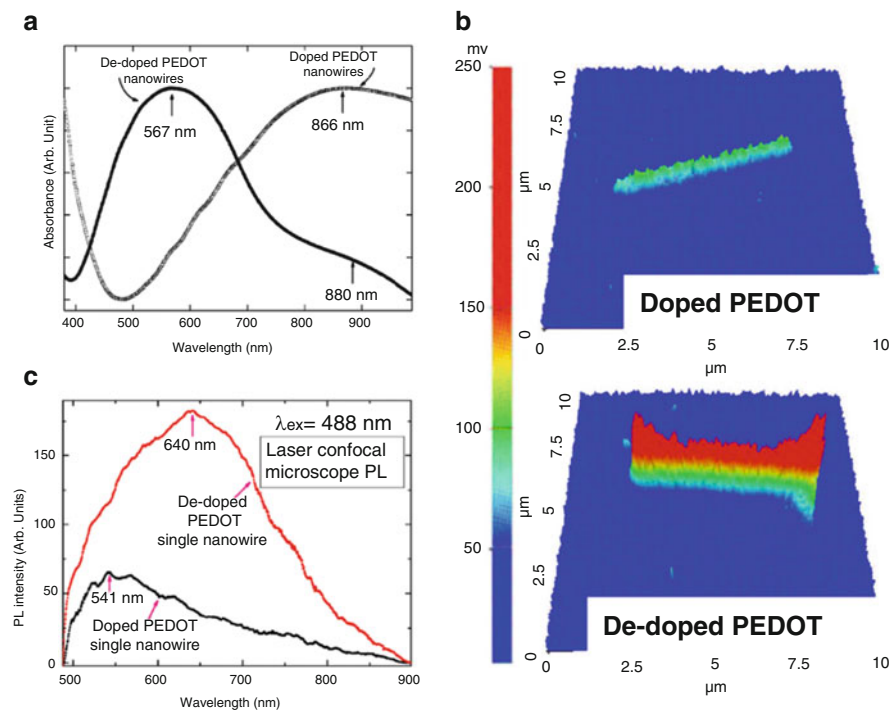
Fig. 15 (**a**) Comparison of UV–vis absorption spectra of doped and de-doped PEDOT NWs. (**b**) 3D LCM PL images and (**c**) LCM PL spectra of isolated single NWs. Color scale bar represents the LCM PL intensities in the unit of measured voltages. (Reprinted with permission from [43]. Copyright 2008 Elsevier B.V.)

Figure 15a shows the normalized UV–vis absorption spectra of electrochemi-cally doped and de-doped PEDOT NWs. A broad electrochemical reduction peak was observed at ~1.0 V. The first cycle of the cyclic voltammogram exhibited a well-defined reduction peak, showing that a stable reduction process occurs in a solution of the ionic liquid BMIMPF$_6$ [77]. For de-doped PEDOT NWs, the π–π* transition peak was observed at ~567 nm, and a weak bipolaron peak was observed at ~880 nm, as shown in Fig. 15a. For doped PEDOT NWs, a broad bipolaron band was observed at ~866 nm, and the π–π* transition peak disappeared owing to the doping effect, as shown in Fig. 15a. The π–π* transition of a pristine PEDOT sample is usually observed at ~610 nm and, for doped PEDOT systems, a long-wavelength absorption appears above 900 nm owing to the narrow band gap [85]. Compared with bulk PEDOT [85], the PEDOT NWs that were de-doped and doped by CV exhibited relatively blue-shifted π–π* transition and bipolaron peaks.

As shown in Fig. 15b, the LCM PL spectra of single doped and de-doped PEDOT NWs were compared under the same experimental conditions. The maximum LCM PL peaks for the single doped and de-doped PEDOT NWs were observed at ~541 nm (green light emission) and ~640 nm (orange–red light emission), respectively.

The LCM PL peak of the PEDOT single NW was blue-shifted after doping. The PL peaks of pristine PTh and P3HT film samples are usually observed at 610 and 640 nm (i.e., orange–red light emission), respectively [84]. The LCM PL peak intensity of the single de-doped PEDOT NW increased up to a maximum of approximately threefold as compared with that of the doped PEDOT NW, as shown in Fig. 15b.

Figure 15c shows 3D LCM PL images of isolated single doped and de-doped PEDOT NWs. The PL image of the single de-doped PEDOT NW is brighter than that of the doped PEDOT NW. The measured voltages of the PL intensity for the doped and de-doped PEDOT single NWs were $60-90$ and $180-260$ mV, respectively. The PL intensity of the de-doped PEDOT single NW was two to three times higher than that of the doped PEDOT NW because of the reduction in PL quenching through the dedoping process.

4.2 Unfocused E-Beam Treatment

Hong et al. reported the dedoping and conformational effects of unfocused E-beam treatment of NTs and NWs of light-emitting and conducting polymers [67, 86, 87]. Compared with the conventional solution-based techniques for the control of doping level, such as chemical doping [31–33] or electrochemical redox by CV [79, 80], E-beam treatment enables control of the optical properties of light-emitting polymer nanostructures in a quantitative manner through adjustment of the E-beam parameters such as dosage and/or energy. This approach has the advantages of a relatively simple procedure and reduced of contamination by solvents.

An unfocused E-beam from a linear electron accelerator was directed onto P3MT NTs along the length direction. The energy of the E-beam was fixed at 1 MeV, and the dosage of the E-beam was varied in the range from 1.6×10^{13} to 8.0×10^{16} electrons/cm^2. The treatment was performed in air at atmospheric pressure and room temperature. The heating effect produced by the E-beam was compensated for by air cooling [67]. Figure 16a shows the normalized UV–vis absorption spectra of P3MT NTs in the pristine state (i.e., before E-beam treatment) and after treatment with an unfocused E-beam of different dosages. For the pristine P3MT NTs, a broad and relatively strong bipolaron peak and relatively weak π–π* transition peak were observed at ~800 and 400 nm, respectively, which indicate highly doped states. As the dose of the E-beam irradiation was increased from 1.6×10^{13} to 8.0×10^{16} electrons/cm^2, the doping-induced bipolaron peak considerably decreased and the π–π* transition peak was shifted from 400 to ~550 nm. It is known that there exist two helical configurations for the polymeric chain in P3MT, namely, the coil-like and rod-like configurations, which correspond to the peaks at 400 and ~550 nm in the UV–vis absorption spectra, respectively [88–90]. From Fig. 16a, it is seen that rod-like configurations with π–π* transition peaks at ~550 nm were observed after E-beam treatment with a dose of 4.8×10^{16} to 8.0×10^{16} electrons/cm^2. The π–π* transition peaks of the electrochemically de-doped P3MT NTs were not very far from their original positions [65].
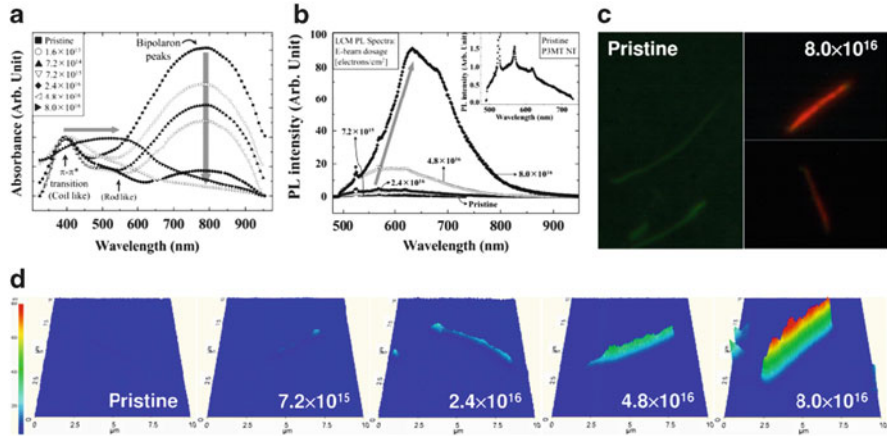
Fig. 16 Comparison of (**a**) UV–vis absorption spectra, (**b**) LCM PL spectra, and (**c**) color CCD images of single P3MT NTs in pristine state and after treatment with a 1-MeV E-beam. (**d**) 3D LCM PL images of P3MT NTs treated with an unfocused E-beam dose of 7.2×10^{15} to 8.0×10^{16} electrons/cm^2. Color scale bar represents the LCM PL intensities in the unit of measured voltages. (Reproduced with permission from [67]. Copyright 2009 Wiley-VCH.)

Figure 16b shows the LCM PL spectra for an isolated single P3MT NT in the pristine state and after treatment with an unfocused E-beam of different dosages. With increasing dosage of the E-beam, the intensity of the LCM PL spectra rapidly increased up to about 90 times that of the pristine P3MT NTs. Its peak was gradually red-shifted from about 550 nm for the pristine P3MT NT to about 620 nm after treatment with a 1-MeV E-beam dose of 8.0×10^{16} electrons/cm^2, as shown in Fig. 16b.

Figure 16c shows color CCD images of the NTs in the pristine state and after treatment with a 1-MeV E-beam dose of 8.0×10^{16} electrons/cm^2. The pristine P3MT NTs emitted green light with a relatively low brightness. After irradiation with the E-beam, the luminescence color was dramatically changed from green to red. Moreover, the luminescent intensity clearly increased.

Figure 16d shows the 3D LCM PL images under identical LCM experimental conditions for an isolated single P3MT NT in the pristine state and after E-beam irradiation with different E-beam dosages. As the dose of the 1-MeV E-beam was increased from 7.2×10^{15} to 8.0×10^{16} electrons/cm^2, the LCM PL intensity of the isolated single P3MT NTs dramatically increased. The averaged voltage of the LCM PL intensity in the pristine state was 10 (± 2.8), and after irradiation with a 1-MeV E-beam it was 22 (± 2.1), 34 (± 2.5), 127 (± 3.8), and 716 (± 4.6) mV, corresponding to doses of 7.2×10^{15}, 2.4×10^{16}, 4.8×10^{16}, and 8.0×10^{16}, respectively. These results indicate that E-beam treatment causes an increase in PL efficiency and alters the luminescence color of P3MT NTs. The significant enhancement in PL intensity might originate from the dedoping effect.

4.3   Hydrothermal Treatment

Hydrothermal processes have been used to synthesize metal oxides such as titanium oxide and zinc oxide and to modify the material properties [26, 91]. Zhou et al. reported that hydrothermal treatment converted graphene oxide to a stable graphene solution [92]. Jung et al. studied the structural transformation of organic copper phthalocyanine NWs into hollow rectangular NTs during a hydrothermal process [93]. Recently, Lee et al. reported that the structural and optical properties of P3HT NPs prepared by reprecipitation [48] can be controlled through hydrothermal treatment at different temperatures [94]. In their study, an autoclave served as the chamber for the hydrothermal process. Pristine (i.e., before hydrothermal treatment) P3HT NPs dispersed in deionized water were placed in a Teflon beaker in the chamber, which was heated in an oven to a temperature between $60°C$ and $150°C$. In this process, external pressure is applied on the P3HT NPs, roughly estimated to be 15 bar at $100°C$ [95]. Then, the chamber was allowed to cool naturally. A homogenous dispersion of NPs was obtained by sonicating the P3HT NP solution with a high-power ultrasonicator.

Figure 17a and its insets show the SEM and TEM images, respectively, of P3HT NPs in the pristine state and after hydrothermal treatment at various temperatures. The numerical labels of the hydrothermally treated (HT) samples (HT060, HT090, HT110, HT120, HT130, and HT150) indicate the temperature of treatment in degrees Celsius. The diameters of the pristine, HT060, HT110, and HT150 P3HT NPs were 77 ($\pm$11), 88 ($\pm$11), 184 ($\pm$50), and 471 ($\pm$107) nm, respectively. The shape and degree of aggregation for P3HT NPs treated at temperatures of $110°C$ and above were clearly different from those of the pristine and HT060 NPs.

Figure 17b shows the normalized UV–vis absorption spectra of the pristine and hydrothermally treated P3HT NPs. The absorption peaks were observed at 510, 550, and 610 nm for the pristine P3HT NPs, which coincide with those of spin-coated P3HT films [90, 96, 97]. The UV–vis absorption spectra changed with increasing hydrothermal temperature, as shown in Fig. 17b: the peaks shifted to longer wavelengths and their relative intensities changed. The absorption peak at ~510 nm was dominant for the pristine, HT060, and HT090 samples. However, with increasing temperature, the absorption intensity at ~550 nm gradually increased, as seen for the HT110, HT120, and HT130 samples. The peak at 610 nm, corresponding to the 0–0 transition, was the strongest for the HT150 P3HT NPs. A long-wavelength tail also progressively developed with increasing hydrothermal temperature owing to the scattering effect. These results are attributed to the interchain interactions and ring planarity in the P3HT main chains that are strengthened owing to the higher pressure applied during the hydrothermal process with increasing temperature [98–100].

Figure 17c shows the normalized LCM PL spectra for single pristine and HT P3HT NPs averaged over 20 different dry NPs. The intensity and position of the 0–1 emission peak at 692−708 nm were different for the individual NPs and varied with the hydrothermal temperature. Its dominance increased for the HT060 and HT110
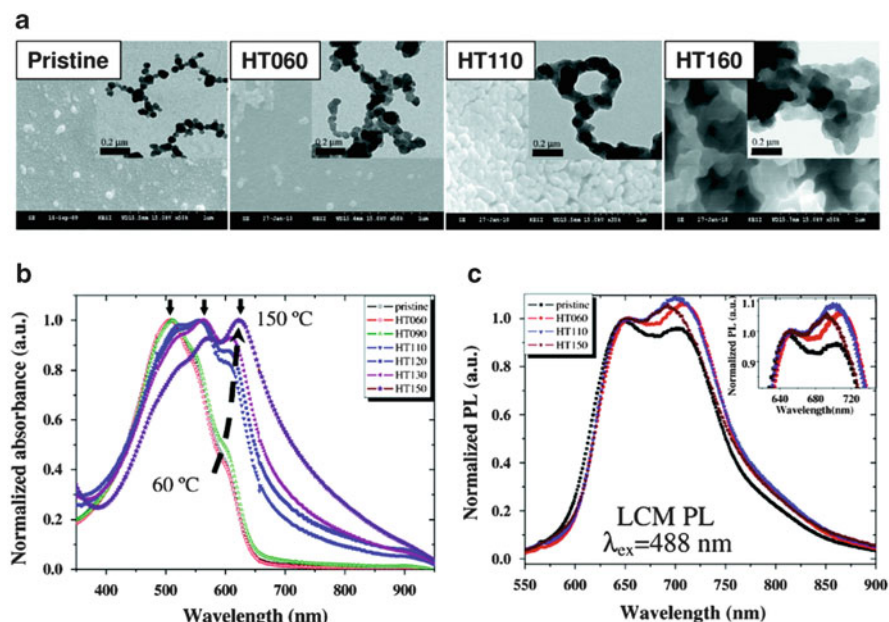
Fig. 17 (**a**) SEM images of P3HT NPs in pristine state and after hydrothermal treatment at various temperatures. *Inset*: TEM images of corresponding NPs. Comparison of (**b**) UV–vis absorption and (**c**) LCM PL spectra of P3HT NPs in pristine state and after hydrothermal treatment at various temperatures. (Reproduced with permission from [94]. Copyright 2011 Institute of Physics.)

samples, in qualitative agreement with the changes in the UV–vis absorption spectra. The 0–1 to 0–0 PL intensity ratio was maximum for the HT110 sample. The external pressure in the hydrothermal process strengthened the interchain interactions, leading to the increase in the degree of tilt of the alkyl side chains and the planarity of the thiophene rings, and a decrease in the distance of interchain π-stacking. The LCM PL spectra suggest that the interchain interactions strengthened (i.e., the interchain distance decreased) as the hydrothermal temperature was increased from 60 to 110°C; however, severe conformational changes might have occurred in the P3HT chains during hydrothermal processing at temperatures of 130°C and above, leading to the decrease in the 0–1 emission for the HT150 sample.

4.4 Hybridization with Metal Nanostructures

Hybridization between π-conjugated polymers and metals at the nanoscale level has been used for luminescence enhancement and to realize biosensing through SPR coupling [6, 64, 65, 101, 102]. The surface plasmon defines a coherent excitation of free electrons in metal nanostructures interacting with an incident electromagnetic

wave, resulting in collective in-plane oscillations [101]. When the dimensions of metal nanostructures, such as the thickness of an NT and diameter of an NP are scaled down to levels comparable to the skin depth, the incident electromagnetic energy is effectively absorbed by light-emitting polymers. Furthermore, SPR coupling in hybrid nanostructures occurs if the surface plasmon absorption energy of the metal matches the photon energy of the light-emitting polymer, which leads to drastic variations in the optical properties of the hybrid nanostructures [6, 64, 65].

4.4.1 Hybrid Double-Layered Nanowires and Nanotubes

The variation in luminescence efficiency and color of hybrid double-layered (HDL) NWs or NTs that were fabricated by coating the surface of light-emitting polymer NWs or NTs with a nanoscale film of metal was reported [103, 104]. Figure 18a–c shows the SEM and TEM images of pristine and HDL-NWs of P3BT/Ni and P3BT/Cu [103]. The formation of two clear layers was observed: the inside and outside layers of the HDL-NWs were P3BT and the metal (Ni or Cu), respectively. The TEM image of an isolated single HDL-NW shows that the total diameter of the hybrid P3BT/Cu NW and the thickness of the external Cu NT were ~200 and ~10 nm, respectively, as shown in Fig. 18b. The high-resolution (HR) TEM image shows the fine and periodic stripe patterns of the outer metal NT, which match the crystalline structure of Cu (lattice spacing $\cong$ 0.21 nm). As shown in the inset of Fig. 18c, the crystalline spots in the selected area electron diffraction (SAED) pattern of the P3BT/Cu HDL-NWs support the conclusion that the outer Cu NT has a crystalline structure in accordance with the HR-TEM results.

Figure 18d, e shows luminescent color CCD and 3D LCM PL images of an isolated single P3BT NW and HDL-NWs of P3BT/Ni and P3BT/Cu. Weak green light emission was observed for the P3BT single NW owing to the lightly doped states, whereas both HDL-NWs (P3BT/Ni and P3BT/Cu) showed bright orange–red light emission, as shown in Fig. 18d. The intensity in the 3D LCM PL image of the P3BT single NW was measured at 22−28 mV. For single HDL-NWs made of P3BT/Ni or P3BT/Cu, the measured voltages of the LCM PL intensities were 1.8−2.3 and 1.5−2.0 V, respectively. The application of the nanoscale Ni or Cu metal coating on the outside of the P3BT NWs led to a 60- to 110-fold increase in the measured voltages of the 3D LCM PL intensities compared with that of the P3BT single NW. Similar results for the HDL-NTs of PTh/metals were reported earlier [64]. Figure 18f shows the averaged LCM PL spectra of corresponding samples. The main LCM PL peak for a single P3BT NW was observed at ~544 nm, corresponding to green light emission. With the nanoscale metal coating, the main LCM PL peaks of the HDL-NWs of P3BT/Ni and P3BT/Cu were red-shifted to ~635 and ~639 nm, respectively, in the range of orange–red light emission. The peak intensity and integrated area of LCM PL spectra significantly increased up to about 80−90 times after hybridization with nanoscale metals [61, 68].

The PL enhancement and color variation of the HDL-NWs are attributed to the energy and charge-transfer effects in SPR coupling. The inset on the right in Fig. 18f
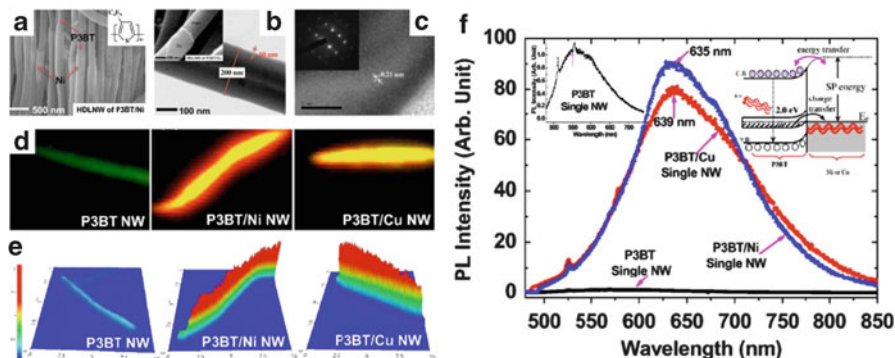
Fig. 18 (**a**) SEM image of HDL-NWs of P3BT/Ni. *Inset*: chemical structure of a P3BT monomer unit. (**b**) TEM image of a single P3BT/Cu HDL-NW. *Inset*: magnified SEM image of the same sample. (**c**) Magnification of HR-TEM image of outside Cu part of a single P3BT/Cu HDL-NW. *Inset*: SAED pattern of the P3BT/Cu HDL-NW. (**d**) Luminescence color CCD images of P3BT NW (*left*) and HDL-NWs of P3BT/Ni (*middle*) and P3BT/Cu (*right*). (**e**) 3D LCM PL images of the corresponding samples. (**f**) LCM PL spectra of an isolated single P3BT NW in the pristine state and HDL-NWs of P3BT/Ni and P3BT/Cu. *Left inset*: magnification of the LCM PL spectrum of a P3BT NW for reference. *Right inset*: energy band diagram explaining the enhancement of PL efficiency and red-shift of the LCM PL peak of the HDL-NWs of P3BT/Ni and P3BT/Cu. (Reproduced with permission from [103]. Copyright 2009 Electrochemical Society.)

illustrates the schematic energy band diagram for HDL-NWs of P3BT/Ni or P3BT/Cu. Because the surface plasmon energies of the nanoscale Ni or Cu were approximately matched by the energy band gap of P3BT ($\sim$2.0 eV), energy transfer occurs between P3BT and the metals owing to SPR coupling, which leads to enhancement of the PL efficiency of the HDL-NWs. For the electrochemically synthesized P3BT NWs with relatively doped states, the Fermi energy (E_F) of the metal and doping-induced bipolaron states of the P3BT NWs matched with each other. Then, charges could be transferred from the bipolaron band of the lightly doped P3BT NWs to the E_F of the metals. This might explain the dedoping effect and the red-shifted LCM PL peaks for the HDL-NWs of P3BT/Ni and P3BT/Cu. In addition to energy transfer, charge transfer also contributed to the increased PL efficiency [6, 64, 65].

Figure 19a shows a magnified SEM image of an isolated single partial HDL-NT of P3MT/Ni in which only the lower half was coated with Ni by controlling the electrochemical deposition time [104]. The diameters of the P3MT NT section and P3MT/Ni HDL-NT section were $\sim$180 and $\sim$200 nm, respectively. Figure 19b shows a 3D LCM PL image of an isolated single partial HDL-NT of P3MT/Ni. The averaged PL intensities of the pristine P3MT NT and P3MT/Ni HDL-NT sections were 12$-$15 and $\sim$600 mV, respectively. Figure 19c compares the normalized LCM PL spectrum of the P3MT/Ni HDL-NT section with that of the pristine P3MT NT section. A broad LCM PL peak was observed in the P3MT/Ni HDL-NT section at 625$-$675 nm. It was $\sim$40 times higher than that of the pristine P3MT NT section, excluding the Raman modes detected at 525 and 570 nm.
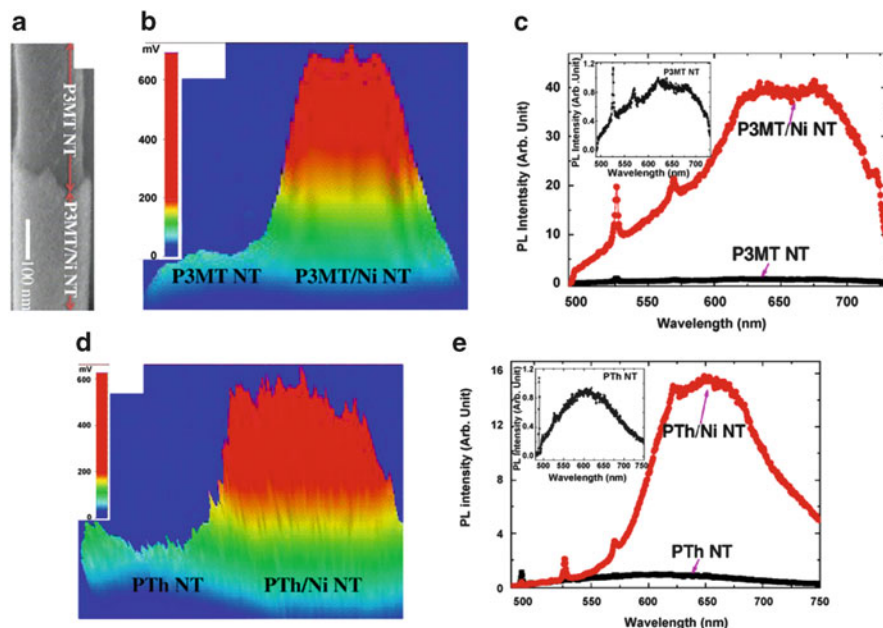
Fig. 19 (**a**) Magnified SEM image of single partial P3MT/Ni HDL-NT. (**b**) 3D LCM PL image of partial P3MT/Ni HDL-NT. (**c**) Comparison of the LCM PL spectra of the pristine and P3MT/Ni HDL-NT sections. *Insets*: magnification of the LCM PL spectrum of the corresponding pristine NTs for reference. (**d**, **e**) Corresponding LCM PL data of PTh/Ni. (Reproduced with permission from [104]. Copyright 2009 Elsevier B.V.)

Enhancement of PL efficiency and variation in light-emitting color attributed to hybridization with metal NTs were also observed by using PTh NTs, as shown in Fig. 19d, e. For the pristine PTh NT section, the measured voltages of the LCM PL intensity and the position of the maximum PL peak were 35−40 mV and ~620 nm, respectively. These values were 540−585 mV and ~650 nm for the PTh/Ni HDL-NT section.

4.4.2 Hybridization with Metal Nanoparticles

Recently, hybrid nanostructures using metal NPs have been intensively studied for improving the physical properties and the efficiencies of optoelectronic devices and biosensors [102, 105–113]. Among the various metals, gold (Au) and silver (Ag) have drawn particular attention owing to their strong SPR effect in the visible spectrum [101, 102, 105]. Kim and coworkers reported PL enhancement in hybrid NPs composed of MEH-PPV NP and Au NPs, which was attributed to the SPR-mediated energy transfer effect [51]. Park and coworkers fabricated a hybrid nanostructure comprising functionalized Au NPs attached to the outer surface of electrochemically synthesized P3MT single NT (denoted as P3MT-NT/Au-NPs) [114].
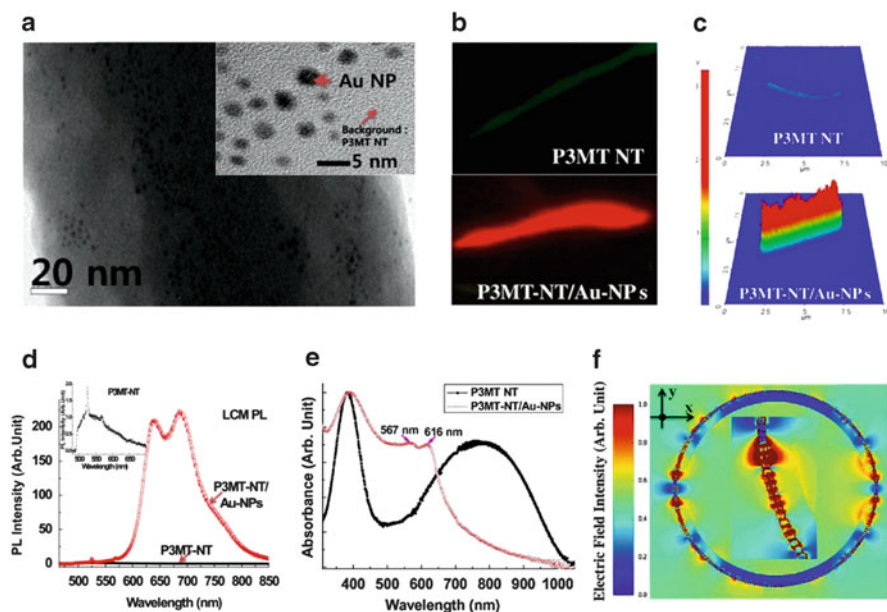
Fig. 20 (**a**) HR-TEM image of single unit of hybrid P3MT-NT/Au-NPs. *Inset*: magnified HR-TEM image of the corresponding sample. The *small black spots* represent the Au NPs. (**b**) Color CCD images of a single P3MT NT (*top*) and the hybrid P3MT-NT/Au-NPs (*bottom*). (**c**) 3D LCM PL image of corresponding samples of (**b**). (**d**) Comparison of the LCM PL spectra of a single strand of the P3MT NT and the hybrid P3MT-NT/Au-NPs. *Inset*: LCM PL spectra of single P3MT NT for reference. (**e**) Normalized UV–vis absorption spectra of the P3MT NT and the hybrid P3MT-NT/Au-NPs. (**f**) Local electric field distribution of 2D nanostructure model of light-emitting polymer with Au NPs attached, based on the FDTD calculation. *Inset*: magnification of local electric field distribution of the 2D nanostructure of polymer/Au-NPs based on the FDTD calculation. (Reproduced with permission from [114]. Copyright 2010 Elsevier B.V.)

Figure 20a shows a magnified HR-TEM image of a single unit of hybrid P3MT-NT/Au-NPs. Small black spots representing the Au NPs were clearly observed on the surface of the P3MT NT, which was evidence for the formation of hybrid nanostructures of P3MT NT with Au NPs. As shown in the inset of Fig. 20a, the fine and periodic stripe patterns of the Au NPs with diameters of 2−3 nm indicate a crystalline structure of the Au material. In addition, nanoscale gaps of 3−20 nm were observed between the Au NPs.

Figure 20b–d shows the results of luminescence color CCD and LCM PL experiments on a single pristine P3MT NT and the hybrid P3MT-NT/Au-NPs. For the pristine P3MT NT, the averaged intensity of the 3D LCM PL image and the peak position of the LCM PL spectrum were 8−10 mV and ~544 nm, respectively. For the hybrid P3MT-NT/Au-NPs, the PL intensity measured at 2.1−2.5 V had increased up to 210−310 times. The PL spectrum was red-shifted, with two characteristic peaks at 640 and 685 nm. These results are consistent with bright red light emission in the

color CCD image. Comparison of the LCM PL spectra showed a PL enhancement estimated at 220-fold, which shows good agreement with the results in the LCM PL images.

Figure 20e shows the normalized UV–vis absorption spectra of the P3MT NTs and hybrid P3MT-NT/Au-NPs. Typical absorption characteristics were observed for the pristine P3MT NTs with doped states. For the hybrid P3MT-NT/Au-NPs, the intensity of the doping-induced bipolaron peak was considerably decreased, and two new absorption peaks were generated at 567 and 616 nm. These new peaks were assigned to the electrical dipole and quadrupole contributions in the surface plasmons, which resulted from the matching of the Fermi energy (E_F) levels between the P3MT NT and the Au NPs.

Figure 20f shows the electric field distributions in hybrid polymer-NT/Au-NPs according to simulation using the finite-difference time-domain (FDTD) method [51]. By choosing experimental values as the simulation parameters [114], a strong local electric field enhancement in the nanogaps between Au NPs was calculated in the background of the light-emitting P3MT [115–117]. This local electric field enhancement, represented by the red color parts in Fig. 20f and its inset, also contributes to the PL enhancement of the hybrid P3MT-NT/Au-NPs. All the results support the occurrence of energy and/or charge transfer attributed to the SPR coupling effects in the hybrid nanostructures of light-emitting polymers and metals.

5 Applications

In this section, various applications of light-emitting polymer nanostructures are introduced. The application of low-dimensional heterojunction NWs to optoelectronics, photonics, and biotechnologies has received considerable attention [118–124]. Inorganic material-based heterojunction NWs have been reported, and their application to optically reflecting barcode NWs has been investigated [118, 119, 125–130]. This section introduces novel organic-based heterojunction NWs, light-emitting color barcode (LECB)-NWs, and quasi-superlattice NWs made using light-emitting polymers. Solid-state and label-free DNA detection is discussed in terms of PL characteristics. Finally, nano-optoelectronic applications of light-emitting polymer nanostructures, such as rectifying, photo-switching, and photovoltaic effects, are presented.

5.1 Barcodes

Conventional black and white barcodes have been used for the identification of commercial products through optical reflection. For effective identification of nanoscale products with complex physical shapes, the identification sensitivity,
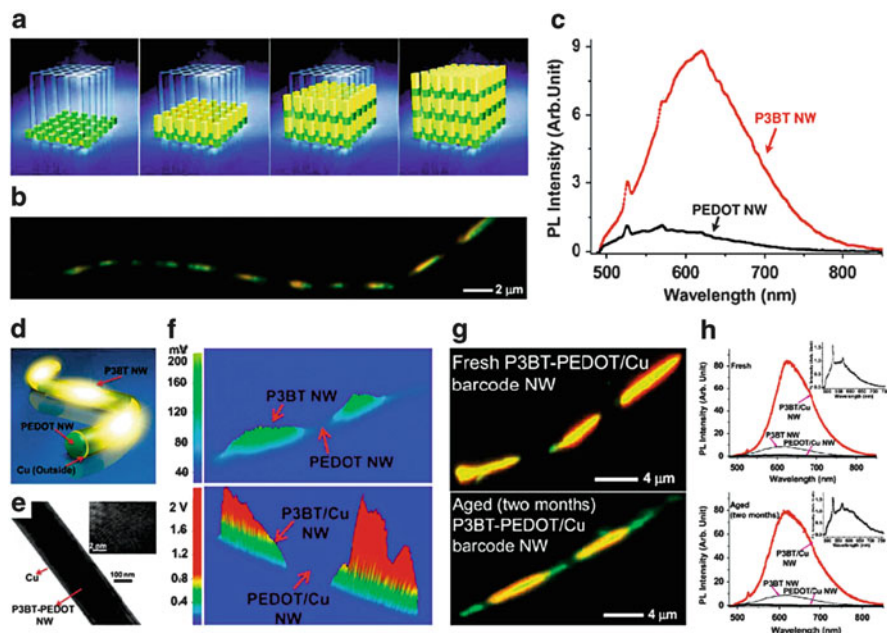
Fig. 21 (**a**) Sequential electrochemical polymerization method for LECB-NWs. (**b**) Color CCD image of single P3BT-PEDOT LECB-NW with 22 sections. (**c**) Comparison of LCM PL spectra of P3BT and PEDOT sections of a single LECB-NW. (**d**) Nanoscale metal coating on LECB-NW. (**e**) HR-TEM image of single P3BT-PEDOT/Cu LECB-NW. *Inset*: magnified HR-TEM image of the outside Cu part of a LECB-NW. (**f**) Comparison of 3D LCM PL images of isolated single LECB-NWs: P3BT-PEDOT (*top*) and P3BT-PEDOT/Cu (*bottom*). (**g**) Color CCD images of fresh (*top*) and 2-month-aged (*bottom*) P3BT-PEDOT/Cu LECB-NWs. (**h**) Comparison of LCM PL spectra of P3BT, P3BT/Cu, and PEDOT/Cu sections of the fresh (*top*) and aged (*bottom*) P3BT-PEDOT/Cu LECB-NWs. *Insets*: normalized LCM PL spectra of the fresh and aged PEDOT/Cu sections for reference. (Reproduced with permission from [131]. Copyright 2010 American Chemical Society.)

accuracy, flexibility, and stability of optical barcode nanomaterials must be improved in combination with the development of appropriate detection tools. Park et al. reported on flexible LECB-NWs synthesized by sequential electrochemical polymerization with distinct light-emitting polymers [131].

Figure 21a shows a schematic illustration of LECB-NWs consisting of two different light-emitting polymer NWs. The length and number of repeated units of the polymer NW code sections were controlled by the polymerization conditions in the electrolyte. As an example, a single strand of other P3BT-PEDOT LECB-NWs having a total of 22 sections is shown in the color CCD image in Fig. 21b. To fabricate the 22 sections of the LECB-NWs, 11 dippings were performed per electrolyte and alternating dipping was employed. The lengths of the P3BT and PEDOT NW sections were controlled to be $1-2$ μm by electrochemical polymerization for $60-90$ s, with an applied current density of 0.6 mA/cm^2 for P3BT and $0.2-0.4$ mA/cm^2 for PEDOT.

Figure 21c shows the LCM PL spectra of the P3BT and PEDOT sections of the same single LECB-NW. The LCM PL peaks for the P3BT and PEDOT sections of the same single NW were detected at ~626 nm (i.e., orange–yellow light emission) and 554 nm (i.e., green light emission), respectively. The LCM PL peak intensity and integrated area of the sections of the P3BT NW were approximately nine times higher than those of the PEDOT NW.

Enhanced luminescence efficiency can be expected for polymer-based light-emitting NWs with a nanoscale metal coating, because of energy transfer via SPR coupling [64, 103]. Figure 21d shows a schematic illustration of an LECB-NW comprising nanoscale Cu metal-coated P3BT-PEDOT (denoted as P3BT-PEDOT/Cu). The formation of the hybrid P3BT-PEDOT/Cu LECB-NWs was confirmed through HR-TEM experiments, as shown in Fig. 21e. From the magnified HR-TEM image, the total diameter of the single P3BTPEDOT/Cu LECB-NW and thickness of the outside Cu NT were found to be ~200 and ~10 nm, respectively. The fine and periodic patterns of the outer tube are attributed to the crystalline structure of the Cu material, as shown in the inset of Fig. 21e.

Figure 21f compares the 3D LCM PL images of isolated single P3BT-PEDOT and P3BT-PEDOT/Cu LECB-NWs under the same LCM experimental conditions. The measured voltages of the LCM PL intensities of the hybrid P3BT/Cu and PEDOT/Cu sections were 1.8−2.0 V and 26−30 mV, whereas those of the P3BT and PEDOT sections without the Cu coating were 140−180 and 22−25 mV, respectively. The measured voltages of the LCM PL intensities for the hybrid P3BT/Cu sections were approximately 10−14 times higher than those of the P3BT sections. The surface plasmon energy (~2.1 eV or 585 nm) of the nanoscale Cu closely matched the emissive photon energy of the P3BT materials. Thus, SPR coupling occurred, which induced energy transfer between the nanoscale Cu and P3BT materials [103]. This explains the considerable enhancement in the PL efficiency for the hybrid P3BT/Cu sections.

Figure 21g shows color CCD images of single P3BT-PEDOT/Cu LECB-NW in the fresh state and after aging by exposure to the atmosphere for 2 months. Green light emission was observed from the PEDOT/Cu sections of the aged LECB-NWs, whereas orange–yellow light emission was dominant for the P3BT/Cu sections of the fresh LECB-NWs. These results imply that the Cu metal-coated P3BT-PEDOT LECB-NWs are promising optical barcode NWs because of their highly sensitive light emission and long-term stability for identification. These results were confirmed by measurements of the LCM PL spectra, as shown in Fig. 21h. The LCM PL peak positions and intensities of the aged samples were found to be comparable with those of the fresh samples because of the protection from oxidation given by the nanoscale Cu coating.

LECB-NWs consisting of three different light-emitting polymers (P3MT, P3BT, and PEDOT) coated with nanoscale Cu were fabricated. Red, orange–yellow, and green luminescence were observed corresponding to the P3MT/Cu, P3BT/Cu, and PEDOT/Cu sections of the same LECB-NW, respectively, as shown in the top image of Fig. 22a. In the color CCD image for the mixture of two different LECB-NWs, the three luminescence colors (red, orange–yellow, and green) of the
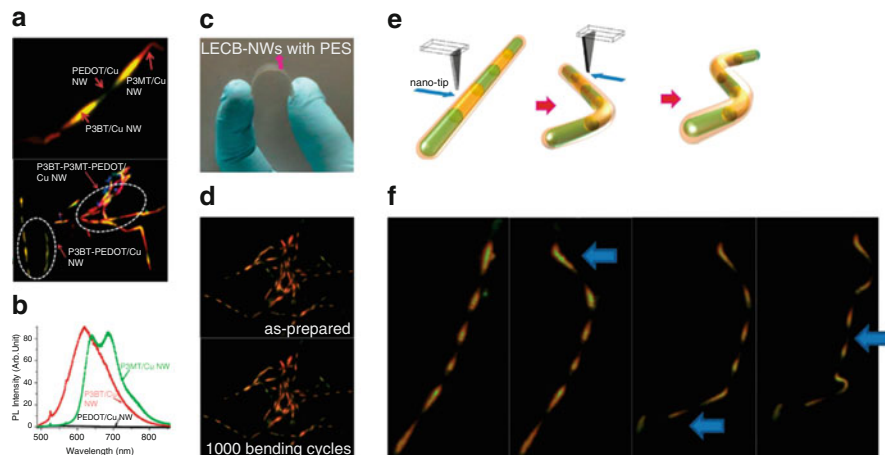
Fig. 22 (**a**) Color CCD images of P3MT-P3BT-PEDOT/Cu single LECB-NW (*top*) and mixture of P3MT-PEDOT/Cu and P3BT-P3MT-PEDOT/Cu LECBNWs (*bottom*). (**b**) LCM PL spectra of P3MT/Cu, P3BT/Cu, and PEDOT/Cu sections of single P3BT-P3MT-PEDOT/Cu LECB-NW. (**c**) Photograph of P3BT-PEDOT/Cu LECB-NWs on bended PES substrate. (**d**) Color CCD images of P3BT-PEDOT/Cu LECB-NWs on PES substrate as-prepared (*top*) and after 1,000 bending cycles (*bottom*). (**e**) Flexibility experiments for LECB-NWs through nanotip impetus. (**f**) Color CCD images of single P3BT-PEDOT/Cu LECB-NW during the applied impetus. The arrows represent the positions of the applied nanotip impetus. (Reproduced with permission from [131]. Copyright 2010 American Chemical Society.)

P3BT-P3MT-PEDOT/Cu LECB-NWs can be selectively distinguished from the two luminescence colors attributed to P3BT-PEDOT/Cu LECB-NWs, as shown in the bottom image of Fig. 22a.

Figure 22b compares the LCM PL spectra of the P3MT/Cu, P3BT/Cu, and PEDOT/Cu sections of the same LECB-NW. The LCM PL peaks for the P3MT/Cu, P3BT/Cu, and PEDOT/Cu sections were detected at 640−685 nm (i.e., red light emission), 620 nm (i.e., orange–yellow light emission), and ~545 nm (i.e., green light emission), respectively. The LCM PL peak intensity and integrated area of the sections of the P3MT/Cu NW and the P3BT/Cu NW were approximately 85 and 90 times higher than that of the PEDOT/Cu NW, respectively.

Figure 22c shows a photograph of the bending of NWs fixed onto a polyethersulfone (PES) flexible substrate. The alternating orange–yellow and green emissions from the P3BT-PEDOT/Cu LECB-NWs on the PES substrate are clearly observed in the color CCD image in Fig. 22d. The flexibility of these NWs was investigated by applying a nanotip impetus to some parts of the NW. Depending on the position of the nanotip impetus (as shown in Fig. 22e), folding and unfolding of the LECB-NW was accomplished, implying that the NW is flexible (as shown in Fig. 22f). These results imply that the P3BT-PEDOT/Cu LECB-NWs can be promising optical barcode NWs that are both durable and flexible.

5.2 Focused E-Beam Treatment: Fine Barcodes and Quasi-superlattice

Focused E-beam irradiation has been used for precisely tailoring the optical and structural properties of organic nanostructures at the nanoscale level [132, 133]. Recently, Hong et al. reported that individual light-emitting P3MT NWs can be tailored successfully to contain multiple 1D serial sections, similar to a quasi-superlattice NW [62]. These sections can have different lengths and characteristics, which can be modified precisely through treatment with a focused E-beam. The spot size of the focused E-beam was adjusted between 50 and 100 nm, and the step size of the focused E-beam irradiation was 2.4 nm, as shown in Fig. 23a.

Figure 23b, c shows the nanoscale optical properties of individual treated P3MT NWs measured by CCD and LCM PL experiments. The PL color of the sections of the pristine P3MT NW remained at the original green with relatively low brightness. When designated positions of the single NW were irradiated with a focused E-beam dose of 7.5×10^{16} electrons/cm^2, the PL color changed from green to yellow, and the emission intensity was clearly enhanced, as shown in the left image of Fig. 23b. The LCM PL intensities of the treated sections (dose of 7.5×10^{16} electrons/cm^2) were approximately 12 times higher than those of the pristine P3MT NW. When the dose was increased to 2.5×10^{17} electrons/cm^2, the PL color of the treated P3MT NW sections changed to bright red (middle image of Fig. 23b), and a significant increase (~31 times) in the light-emission intensity was confirmed from the LCM PL images. When the focused E-beam dose was increased to 2.5×10^{18} electrons/cm^2, the PL intensity of the treated sections decreased and bright yellow–green emission was observed from the pristine sections of the same NW (right images of Fig. 23b, c). The results indicate the existence of a critical E-beam dose (ED_C) for modification of the optical properties of P3MT NWs and for E-beam energy transfer along the NWs. The size of the sections in a P3MT NW treated with a focused E-beam can be controlled on the basis of the designed patterns (including size and position). In the left and middle images of Fig. 23b, the lengths of the treated sections on the NW were 1 and 2 μm, respectively. The lengths of the treated sections were also adjusted to 0.25, 0.5, 1, 2, 3, 4, 5, and 6 μm in the same NW.

The averaged LCM PL intensities of the NW sections, as obtained from the line profile of the 3D LCM PL images, changed considerably with the E-beam dose, as shown in Fig. 23d. The LCM PL intensity of the pristine P3MT NW was six photon counts and those of the pristine sections in the treated P3MT NW were 7, 34 (± 1), 265 (± 5), and 326 (± 14) photon counts for doses of 7.5×10^{16}, 2.5×10^{17}, 2.5×10^{18}, and 1.0×10^{19} electrons/cm^2, respectively. The LCM PL intensities of the treated NW sections were 70 (± 3), 185 (± 6), 24 (± 1), and 3 (± 1), respectively, for these doses.

The LCM PL peak was gradually red-shifted from $520-530$ nm for the pristine NW to approximately 560 and $590-600$ nm for the NW sections treated with doses of 7.5×10^{16} and 2.5×10^{17} electrons/cm^2, respectively, as shown in Fig. 23e. The intensities of the LCM PL peaks of the treated sections with these doses were
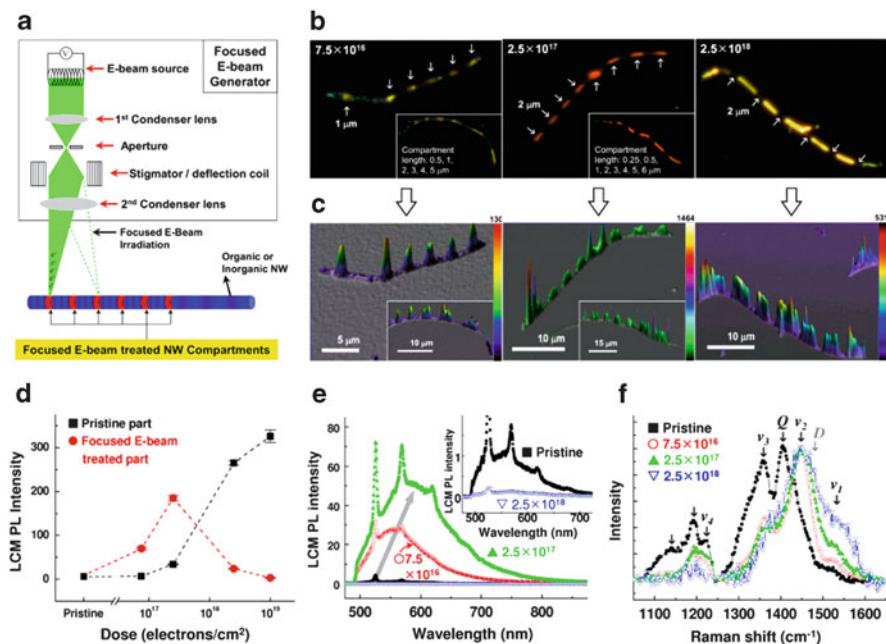
Fig. 23 (**a**) Focused E-beam treatment at designated positions of a single NW. (**b**) Color CCD images of single P3MT NWs treated with focused E-beam doses of 7.5×10^{16} electrons/cm^2 (*left*), 2.5×10^{17} electrons/cm^2 (*middle*), and 2.5×10^{18} electrons/cm^2 (*right*). *Insets*: Images of focused E-beam-treated P3MT NWs with different section lengths. The *arrows* indicate the treated sections. (**c**) 3D LCM PL images of corresponding samples in (**b**) and their *insets*. The color scale bar on the *right* represents the photon counts. (**d**) Averaged LCM PL intensity of P3MT NW sections treated with a focused E-beam as a function of dose. (**e**) LCM PL spectra of the pristine P3MT NW sections and of sections treated with various focused E-beam doses. *Inset*: magnified LCM PL spectra of pristine sections and of the sections treated with a high dose of 2.5×10^{18} electrons/cm^2. (**f**) Normalized micro-Raman spectra for pristine and treated P3MT NW sections at various doses. (Reproduced with permission from [62]. Copyright 2011 Wiley-VCH.)

enhanced up to 25 and 50 times that of the pristine NW, respectively. Below the ED_C, the positions and intensities of the LCM PL peaks were red-shifted and increased with the E-beam dose. However, the emission intensity of the sections treated with a dose higher than the ED_C was considerably lower (inset of Fig. 23e). Therefore, the PL color and intensity of single P3MT NWs can be tailored precisely at the nanoscale level as a function of the focused E-beam dose.

Figure 23f shows the micro-Raman spectra of pristine and treated P3MT NW sections and reveals the structural and doping characteristics. Significant differences in the micro-Raman spectra associated with the focused E-beam treatment were observed in the range of $1,050-1,650$ cm^{-1}. The intensities of the Raman peaks at 1,192, 1,223, and 1,361 cm^{-1}, corresponding to C_β–H bending, antisymmetric C_α–C_α ring stretching, and C_β–C_β ring stretching deformation modes, respectively [67, 68, 134], decreased with increasing E-beam dose [67].
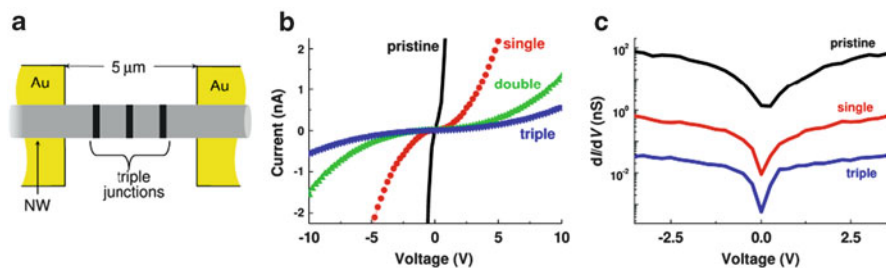
Fig. 24 (**a**) Diagram of NW with triple junctions on Au electrodes. (**b**) Comparison of *I–V* characteristic curves of pristine and treated single P3MT NWs with various numbers of serial junctions. (**c**) Voltage dependence of differential conductance between pristine and treated single P3MT NWs with various numbers of junctions. (Reproduced with permission from [62]. Copyright 2011 Wiley-VCH.)

The intensity of the doping-induced Q mode at 1,404 cm^{-1} decreased gradually with increasing E-beam dose. The intensities, positions, and line widths of the Raman peaks at 1,457 and 1,510 cm^{-1}, corresponding to the disorder mode (D) and the antisymmetric $C_\alpha = C_\beta$ ring stretching mode (ν_1), respectively [67, 134, 135], were increased, up-shifted, and broadened with increasing E-beam dose. The changes in the D and ν_1 vibration peaks indicate structural modifications to the main polymeric chains in the NW. The spectra reveal that focused E-beam irradiation induces conformational changes in the polymer chains at the nanoscale level and causes a decrease in the doping level of the polymer [67].

Figure 24a shows a schematic diagram of multiple 1D serial junctions of a single P3MT NW on Au electrodes through focused E-beam treatment. The dose of the focused E-beam was fixed to 1.0×10^{17} electrons/cm^2. Figure 24b shows a comparison of the current–voltage (*I–V*) characteristic curves of a single pristine P3MT NW and a NW treated with a focused E-beam to form single, double, and triple nanojunctions. As the number of treated sections (i.e., junctions) increased, the current levels of the single P3MT NW decreased dramatically, and the nonlinearity of the *I–V* curves became severe. The results were similar to those reported for heterojunction nanomaterials with multiple 1D serial sections and superlattice structures [125, 136, 137]. The voltage dependence of the differential conductance in the low-bias region was reduced and sharpened when the number of junctions was increased, as shown in Fig. 24c. The results suggest that the treated sections act as tunneling barriers for charge transport [136, 138].

5.3 Biosensing

An efficient method for DNA detection without a fluorescent dye on the nanoscale can be realized through the use of a single light-emitting polymer NW with lightly doped states, as reported by Park and coworkers [139]. Biological materials can be
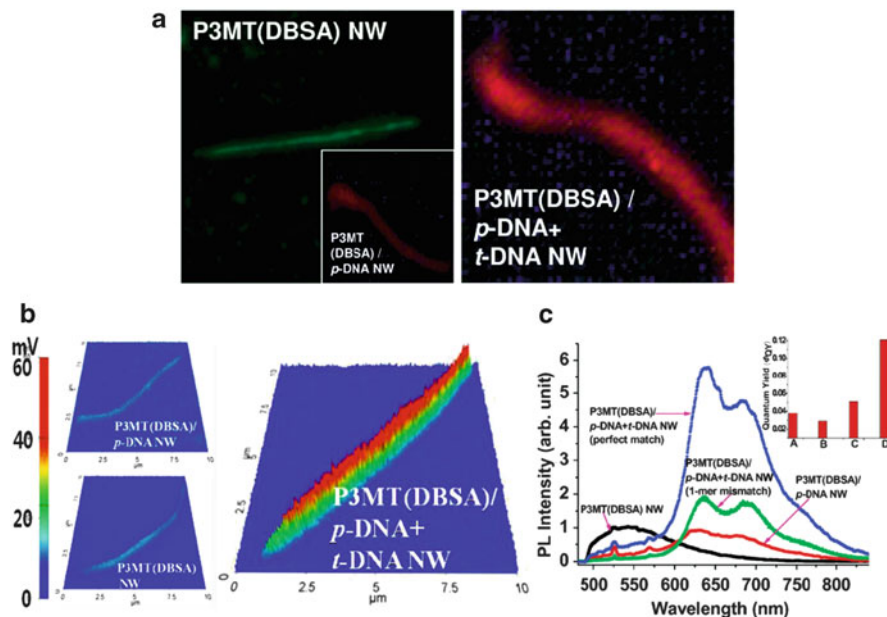
Fig. 25 (**a**) Color CCD images of P3MT(DBSA) (*left*) and P3MT(DBSA)/*p*-DNA + *t*-DNA (*right*) single NWs. *Inset*: color CCD image of a P3MT(DBSA)/*p*-DNA single NW. (**b**) 3D LCM PL images of a P3MT(DBSA) (*left top*), P3MT(DBSA)/*p*-DNA (*left bottom*), and P3MT (DBSA)/*p*-DNA + *t*-DNA single NWs (*right*). (**c**) LCM PL spectra of P3MT(DBSA), P3MT (DBSA)/*p*-DNA, P3MT(DBSA)/*p*-DNA + *t*-DNA (1-mer mismatch), and P3MT(DBSA)/ *p*-DNA + *t*-DNA (perfect match) single NWs. *Inset*: quantum yield of P3MT(DBSA) (*A*), P3MT(DBSA)/*p*-DNA (*B*), P3MT(DBSA)/*p*-DNA + *t*-DNA (1-mer mismatch) (*C*), and P3MT (DBSA)/*p*-DNA + *t*-DNA (perfect match) (*D*) NWs. (Reproduced with permission from [139]. Copyright 2011 Royal Society of Chemistry.)

detected readily through variations in the light-emitting characteristics of the polymer NWs with high signal amplification when the appropriate receptors are linked to the surfaces of the NWs. The light-emitting P3MT material is a promising system to study dopant-mediated DNA detection in fluorescence chain reaction-enhanced PL because of the formation of doping-induced bipolaron (i.e., cationic) states.

Figure 25 shows color CCD images and LCM PL images and spectra of an isolated single P3MT NW with DBSA dopant in the as-prepared, *p*-DNA attached, and *t*-DNA hybridized states. The luminescence color of the single P3MT(DBSA) NW was green with relatively low brightness (left image of Fig. 25a). When coupled with *p*-DNA, the luminescence color changed from green to red (inset of left image of Fig. 25a). This red-shift is attributed to conformational modification of the P3MT main chains by electrostatic interactions between the SO_3^- group of the NW and the NH_3^+ group and the negatively charged phosphate backbone of the wrapping *p*-DNAs. After hybridization with *t*-DNA, the luminescence intensity was enhanced considerably

compared to as-prepared and *p*-DNA-immobilized P3MT(DBSA) NWs, as shown in the right image of Fig. 25a.

Figure 25b shows 3D LCM PL images of the P3MT(DBSA), P3MT(DBSA)/*p*-DNA, and P3MT(DBSA)/*p*-DNA + *t*-DNA single NWs. The average voltages of the LCM PL intensities for the as-prepared P3MT(DBSA), P3MT(DBSA)/*p*-DNA, and P3MT(DBSA)/*p*-DNA + *t*-DNA single NWs were 11 ($\pm$2), 10 ($\pm$1), and 61 ($\pm$3) mV, respectively. The LCM PL intensity of the functionalized P3MT (DBSA)/*p*-DNA + *t*-DNA single NW was about six times higher than that of the as-prepared P3MT(DBSA) single NW.

The LCM PL spectra of the single NWs were compared, as shown in Fig. 25c. The main PL peak of the as-prepared single NW was observed at ~554 nm. When coupled with *p*-DNA, the main PL peak was red-shifted to ~640 nm and its intensity decreased slightly. Upon hybridization of the P3MT(DBSA)/*p*-DNA NW with *t*-DNA, the maximum intensity of the LCM PL peak was enhanced up to about six times compared with that of the as-prepared NW. The change in the luminescence characteristics of P3MT(DBSA) NWs was also studied using 1-mer mismatched *t*-DNAs. When the *p*-DNAs were coupled with the 1-mer mismatched *t*-DNAs (100 nM), the LCM PL intensity of the P3MT(DBSA)/*p*-DNA + *t*-DNA (1-mer mismatch) single NW was much lower than that in the perfect match case, as shown in Fig. 25c. The significant increase in the PL intensity of the P3MT (DBSA)/*p*-DNA + *t*-DNA single NW might be due to the dopant-mediated energy transfer effect in the fluorescence chain reaction between the *t*-DNA and light-emitting P3MT chains. These results highlight the possibility for nanoscale optical detection of DNA without a fluorescent dye using a light-emitting P3MT(DBSA) single NW on the basis of the change in the luminescence color and intensity.

The nanoscale luminescence characteristics of a single P3MT NW with a different dopant, namely, tetrabutylammonium trifluoromethane sulfuric acid (TBACF$_3$SO$_3$), and the DNA-functionalized states were examined to reconfirm the feasibility of dopant-mediated DNA detection. Weak green light emission was observed for the P3MT(TBACF$_3$SO$_3$) single NW (left image of Fig. 26a). When the NWs were coupled with *p*-DNA, the color changed from green to red with a slightly decrease in luminescence intensity, as shown in the inset of the left image of Fig. 26a. The luminescence color CCD image of a P3MT(TBACF$_3$SO$_3$)/*p*-DNA + *t*-DNA single NW showed significantly brighter red light emission than the single NW without *t*-DNA (right image of Fig. 26a). The novel PL enhancement of P3MT(TBACF$_3$SO$_3$) single NWs through hybridization with *t*-DNA was examined as a function of the *t*-DNA concentration from 100 aM to 100 nM, as shown in Fig. 26b. As the concentration of *t*-DNA increased, the LCM PL intensity of the single NW also increased, suggesting that effective energy transfer occurs in the fluorescence chain reaction between the light-emitting NW and *t*-DNAs. The maximum intensity of the LCM PL peak and its integrated area for a single NW hybridized with complementary *t*-DNA (100 nM) increased by a maximum of approximately 30-fold compared with that of the as-prepared and *p*-DNA-functionalized NWs. In addition, the LCM PL intensity of the NW hybridized with *t*-DNA at a concentration of 100 aM increased seven to eightfold compared with that of the NW without *t*-DNA.
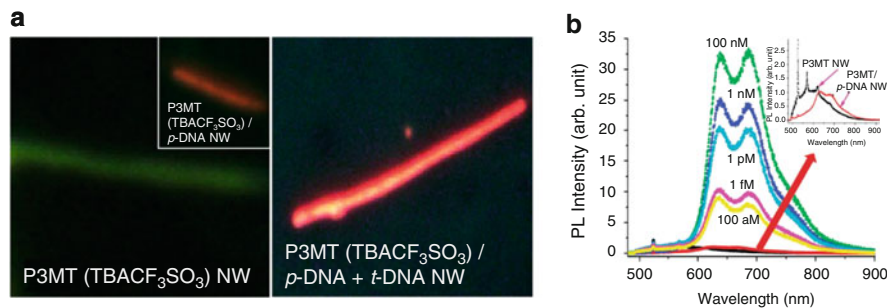
Fig. 26 (**a**) Color CCD images of P3MT(TBACF$_3$SO$_3$) (*left*) and P3MT(TBACF$_3$SO$_3$)/*p*-DNA + *t*-DNA (*right*) single NWs. *Inset*: color CCD image of a P3MT(TBACF$_3$SO$_3$)/*p*-DNA single NW. (**b**) LCM PL spectra of P3MT(TBACF$_3$SO$_3$), P3MT(TBACF$_3$SO$_3$)/*p*-DNA, and P3MT (TBACF$_3$SO$_3$)/*p*-DNA + *t*-DNA single NWs with various concentrations of *t*-DNA (from 100 aM to 100 nM). *Inset*: magnification of LCM PL spectra of P3MT(TBACF$_3$SO$_3$) and P3MT (TBACF$_3$SO$_3$)/*p*-DNA single NWs. (Reproduced with permission from [139]. Copyright 2011 Royal Society of Chemistry.]

5.4 Nano-optoelectronics

Organic photodiodes and phototransistors are fabricated by using photosensitive π-conjugated organic materials, and the photovoltaic properties of these materials have been intensively studied for application to inexpensive and renewable energy sources [140]. The mechanism of charge recombination and dissociation in the *p*–*n* junctions of semiconductors is used in various applications such as diode lasers, LEDs, photodetectors, and photovoltaic cells. With the rapid development of nanotechnology, nanoscale *p*–*n* junctions have been investigated by using low-dimensional nanostructures such as carbon nanotubes (CNTs) and inorganic or organic semiconducting NWs.

A doped Si substrate with as-grown multiwalled (MW) CNTs synthesized through a thermal chemical vapor deposition (CVD) method was attached to a stainless steel working electrode, as shown in Fig. 27a [141]. A P3HT layer with a thickness of ~20 nm was directly deposited on the surface of the MWCNTs using an electrochemical polymerization method. The electrolyte for the electrochemical polymerization consisted of 3-HT monomers, BMIMPF$_6$ as the ionic liquid, and anhydrous acetonitrile as the solvent.

The formation and surface morphology of the coaxial P3HT/MWCNT hybrid NTs were investigated using HR-TEM, as shown in Fig. 27b [141]. The MWCNTs had an outer diameter of 10−30 nm and a wall thickness of 2−8 nm. The total diameter of the hybrid NTs was ~60 nm. The thickness of the P3HT layer deposited on the MWCNTs was ~20 (±10) nm, and the formation of the coaxial-type MWCNTs coated with P3HT was clearly observed.

Figure 27c shows a schematic illustration of the four-probe electrodes on a P3HT/MWCNT hybrid single NT. Two Au/Ti electrodes make contact with the outer P3HT single NT, while the other two make contact with the inner single
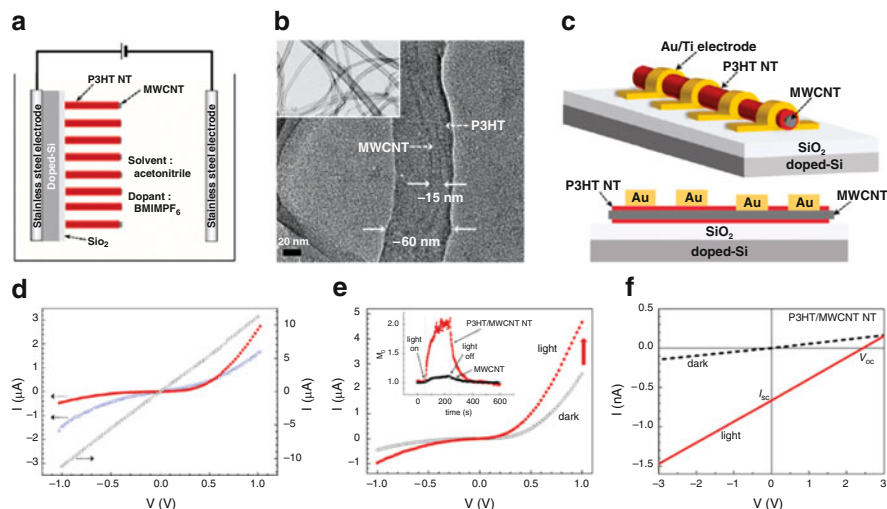
Fig. 27 (**a**) Illustration of electrochemical deposition of P3HT on the MWCNT surface. (**b**) HR-TEM image of P3HT/MWCNT hybrid NT. *Inset*: HR-TEM image of MWCNTs. (**c**) Diagram of single P3HT/MWCNT hybrid NT with four-probe Au/Ti electrodes (*top*) and cross-sectional view of P3HT/MWCNT hybrid NT with electrodes (*bottom*). (**d**) Comparison of *I–V* characteristic curves of a single P3HT NT, MWCNT, and P3HT/MWCNT hybrid NT measured in the dark at room temperature. (**e**) Comparison of *I–V* characteristic curves of P3HT/MWCNT hybrid NT with and without illumination. *Inset*: comparison of normalized currents of P3HT/MWCNT hybrid NT and MWCNT with and without illumination as a function of time. (**f**) *I–V* characteristic curves representing quasi-photovoltaic effect with and without illumination for a single P3HT/MWCNT hybrid NT. (Reproduced with permission from [141]. Copyright 2010 American Chemical Society.)

MWCNT through partial etching of P3HT. Figure 27d shows the $I-V$ characteristic curves of a single NT in the dark at room temperature. The $I-V$ characteristic curve for the outer P3HT single NT in the hybrid NT shows semiconducting behavior, whereas ohmic behavior is observed for the inner single MWCNT, as shown in Fig. 27d. From the slope of the $I-V$ curves for the MWCNT, the conductivity of the single MWCNT was estimated to be 10^3-10^4 S/cm. The current level of the P3HT NT is much smaller than that of the MWCNT. When two electrodes were separately contacted with the MWCNT and the P3HT NT, the $I-V$ characteristic curve of the single P3HT/MWCNT hybrid NT showed rectification behavior (i.e., nanorectifier) owing to the formation of a hybrid junction between the MWCNT and the semiconducting P3HT NT.

Figure 27e shows the photoresponsive $I-V$ characteristics of a P3HT/MWCNT hybrid single NT. Under illumination (100 mW/cm^2), the $I-V$ characteristics of the P3HT/MWCNT hybrid NT also show rectification behavior. The current levels of the hybrid single NT were enhanced through the illumination, as shown in Fig. 27e. The increase in the current level of the P3HT/MWCNT hybrid NT through illumination was relatively higher than that of the MWCNT, as shown in the inset of

Fig. 27e. Figure 27f shows the quasi- photovoltaic effect (i.e., the linear increase in the photocurrent with the applied bias) measured in the P3HT/MWCNT hybrid single NT. In the experiments, the short circuit current (I_{sc}) was measured to be – 0.67 nA, and the open circuit voltage (V_{oc}) was measured to be 2.44 mV. The power conversion efficiency (η) of the P3HT/MWCNT hybrid single NT was estimated to be ~0.42%.

Nanoscale photovoltaic cells are now considered as potentially new types of solar energy harvesting nanosystems. A single coaxial silicon NW with a p-type/intrinsic/n-type (PIN)-doped semiconductor structure has been experimentally realized as a nanoscale electronic power source [142]. Recently, single NW photovoltaic devices using coaxial NWs consisting of ZnO and P3HT were shown to exhibit a η value of 0.036% [143]. The nanoscale photovoltaic cells using the coaxial NWs, composite NWs, or various nanostructures must be studied to fabricate high-efficiency future energy harvesting systems.

Figure 28a shows the fabrication process for the P3HT:PCBM composite NWs through a wetting method by using Al_2O_3 nanoporous templates with a pore size of 100 nm [144]. Figure 28b shows the normalized LCM PL spectra ($\lambda_{ex} = 488$ nm) for single NWs of P3HT, PCBM, and P3HT:PCBM composite (1:1 wt%). For single P3HT NW, the LCM PL peaks corresponding to the 0–0 and 0–1 transitions of P3HT were observed at 650 and 700 nm, respectively. The LCM PL peak of the single PCBM NW was observed at 730 nm, with a shoulder peak at 810 nm. For the single P3HT:PCBM composite NW, the maximum LCM PL peak was observed at 725 nm, with shoulder peaks at 650 and 810 nm, indicating the coexistence of P3HT and PCBM phases in the single NW.

Figure 28c, d shows a schematic illustration and SEM image of a nanodevice comprising a single P3HT:PCBM NW with Au and Al electrodes. The $I-V$ characteristic curve of the single P3HT:PCBM (1:2 wt%) NW in the dark shows diode-like behavior, as shown in Fig. 28e. Under illumination, the current levels were enhanced at a relatively high bias ($V \geq 10$ V), as shown in Fig. 28e. Excitons were created in the major P3HT and minor PCBM components, and they dissociated into electrons and holes under the applied electric field near the interface between P3HT and PCBM.

Recently, Lee and coworkers reported the fabrication and nanoscale physical properties of hybrid P3HT/PCBM NPs and their photovoltaic applications [52]. Figure 29a shows the LCM PL spectra of annealed and non-annealed hybrid NPs of p-type P3HT and n-type PCBM prepared by the mini-emulsion method [46, 50]. From the wide-angle X-ray diffraction patterns, the annealed P3HT NPs had a lager crystalline size (~76.5 Å) than non-annealed NPs (58.8 Å), as shown in the right inset of Fig. 29a. The LCM PL intensities of single annealed and non-annealed hybrid P3HT/PCBM NPs were lower than those of a single annealed P3HT NP, as shown in Fig. 29a, indicating PL quenching.

Figure 29b shows the scheme of a conducting atomic force microscope (c-AFM) experiment using a single hybrid P3HT/PCBM NP. An indium tin oxide (ITO) electrode was used as the cathode because of its relatively low work function (4.8 eV) compared with that (5.1 eV) of the Pt metal used as the anode. Figure 29c
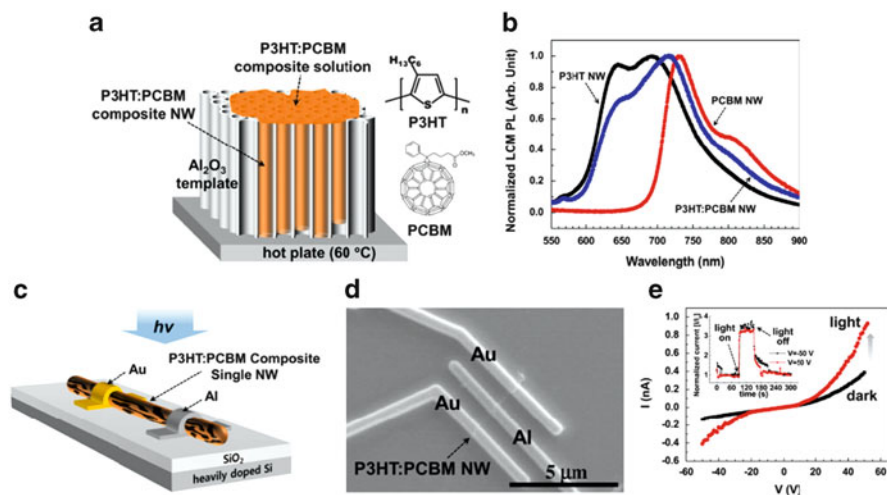
Fig. 28 (**a**) Fabrication process for P3HT:PCBM composite NWs. (**b**) Comparison of normalized LCM PL spectra for single NWs of P3HT, PCBM, and P3HT:PCBM composite. (**c**) Nanodevice with Au and Al electrodes using P3HT:PCBM single NW. (**d**) SEM image of nanodevice using a single NW with Au and Al electrodes. (**e**) *I–V* characteristic curves for single P3HT:PCBM NW with a P3HT:PCBM concentration of 1:2 wt% with and without irradiation. *Inset*: normalized currents of the composite NW with and without illumination as a function of time. (Reproduced with permission from [144]. Copyright 2011 Elsevier B.V.)
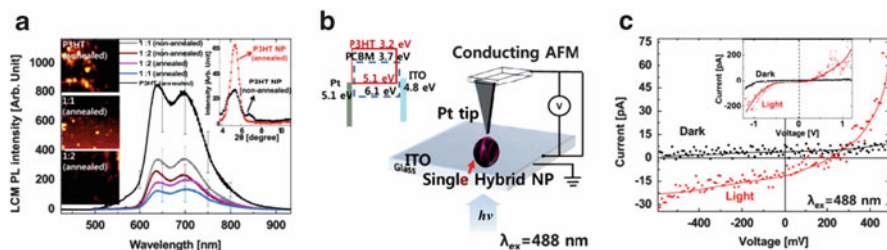
Fig. 29 (**a**) LCM PL intensities of single annealed P3HT NPs and annealed and non-annealed P3HT/PCBM (1:1 and 1:2 wt%) NPs. *Left insets*: LCM PL mapping images of annealed P3HT and hybrid NPs. *Right inset*: wide-angle X-ray diffraction patterns of annealed and non-annealed P3HT NPs. (**b**) Illustration of c-AFM experiment using single hybrid P3HT/PCBM NP. *Inset*: energy band diagram of hybrid NP with Pt and ITO electrodes. (**c**) Photovoltaic *I–V* characteristic curves of single annealed P3HT/PCBM (1:2 wt%) NP. *Inset*: photoresponsive *I–V* characteristic curves of NPs in the full measured range. The *lines* are guides for the eye. (Reproduced with permission from [52]. Copyright 2012 Royal Society of Chemistry.)

shows the photoresponsive $I-V$ characteristic curves in a low-bias regime for a single annealed P3HT/PCBM (1:2 wt%) NP at room temperature. The photovoltaic effect was observed in the single annealed hybrid NP, as shown in Fig. 29c. From the photovoltaic $I-V$ characteristic curves, the open-circuit voltage and short-circuit current were measured to be about 293.15 mV and 11.29 pA, respectively, and the

fill factor was estimated to be about 0.398. The monochromatic η ($\lambda_{ex} = 488$ nm) of the single annealed P3HT/PCBM (1:2 wt%) NP was estimated to be about $1.32 \times 10^{-5}\%$.

6 Conclusions and Outlooks

Nanostructures of light-emitting polymers with π-conjugated structure have been synthesized and used as electronic and optical nanomaterials for nanoscale optoelectronic devices and biosensors. Various synthetic methods such as chemical, electrochemical, reprecipitation, and electrospinning methods with or without nanoporous templates have been developed for the fabrication of polymer nanostructures. The physical sizes and formation of the nanostructures can be controlled by adjusting the synthetic conditions. High-resolution LCM spectroscopy allowed investigation of the light emission characteristics of individual nanostructures. The light absorption and emission efficiencies of the light-emitting polymer nanostructures can be tuned by chemical processing and post-synthetic treatments, as well as by adjusting their physical dimensions. Post-synthetic treatments such as electrochemical doping, E-beam irradiation, hydrothermal processing, and nanoscale metal hybridization were used to modify the intrinsic properties of the polymer nanostructures. The electronic structures of polymer NTs and NWs can be varied through electrochemical doping and E-beam irradiation. The optical properties and formation of NPs are dependent on the hydrothermal temperature. The hybridization of polymer nanostructures with nanoscale metals induces drastic PL enhancement owing to SPR coupling. The light-emitting polymer nanostructures introduced here can be applied to nanoscale identification barcodes, label-free DNA-sensing, nanodiodes, and nanophotovoltaic devices. Industrial applications of light-emitting polymer nanostructures are in their nascent stages. Homogeneous dispersions of nanomaterials must be developed to enable further applications in flexible optoelectronics. In addition, advanced device fabrication techniques using single nanostructures are also required for nano-optoelectronics.

References

1. MacDiarmid AG (2001) Rev Mod Phys 73:701–712
2. Shirakawa H (2001) Rev Mod Phys 73:713–718
3. Heeger AJ (2001) Rev Mod Phys 73:681–700
4. Skotheim TA, Elsenbaumer RL, Reynolds JR (1998) Handbook of conducting polymers. Dekker, New York
5. Perepichka IF, Perepichka DF, Meng H, Wudl F (2005) Adv Mater 17:2281–2305

6. Park DH, Kim MS, Joo J (2010) Chem Soc Rev 39:2439–2452
7. Roth S, Carroll DL (2004) One-dimensional metals, 2nd edn. Wiley, Weinheim
8. Heeger AJ (2002) Synth Met 125:23–42
9. Su WP, Schrieffer JR, Heeger AJ (1979) Phys Rev Lett 42:1698–1701
10. Su WP, Schrieffer JR, Heeger AJ (1980) Phys Rev B 22:2099–2111
11. Heeger AJ, Kivelson S, Schrieffer JR, Su WP (1988) Rev Mod Phys 60:781–850
12. Roothaan CCJ (1951) Rev Mod Phys 23:69–89
13. Anderson PW (1975) Phys Rev Lett 34:953–955
14. Brédas JL, Chance RR, Baughman RH, Silbey R (1982) J Chem Phys 76:3673–3678
15. Brédas JL, Thémans B, André JM (1982) J Chem Phys 78:6137–6148
16. Brédas JL, Elsenbaumer RL, Chance RR, Silbey R (1983) J Chem Phys 78:5656–5662
17. Brédas JL, Thémans B, André JM (1983) Phys Rev B 27:7827–7830
18. Fesser K, Bishop AR, Campbell DK (1983) Phys Rev B 27:4804–4825
19. Brédas JL, Scott JC, Yakushi K, Street GB (1984) Phys Rev B 30:1023–1025
20. Kaufman JH, Colaneri N, Scott JC, Street GB (1984) Phys Rev Lett 53:1005–1008
21. Brédas JL, Street GB (1985) Acc Chem Res 18:309–315
22. Vardeny Z, Ehrenfreund E, Brafman O, Nowak M, Schaffer H, Heeger AJ, Wudl F (1986) Phys Rev Lett 56:671–674
23. Sum U, Fesser K, Büttner H (1988) Phys Rev B 38:6166–6173
24. Sun ZW, Frank AJ (1991) J Chem Phys 94:4600–4608
25. Martin CR (1994) Science 266:1961–1966
26. Feng S, Xu R (2001) Acc Chem Res 34:239–247
27. Joo J, Kim BH, Park DH, Sung JH, Choi HJ (2008) Conducting polymer nanotubes, nanowires, and nanocomposites: synthesis, characteristics, and applications. In: Nalwa HS (ed) Handbook of organic electronics and photonics, vol 1. American Scientific, California, pp 51–83
28. Long YZ, Li MM, Gu C, Wan M, Duvail JL, Liu Z, Fan Z (2011) Prog Polym Sci 36:1415–1442
29. Jones MR, Osberg KD, MacFarlane RJ, Langille MR, Mirkin CA (2011) Chem Rev 111:3736–3827
30. Kim FS, Ren G, Jenekhe SA (2011) Chem Mater 23:682–732
31. Joo J, Kim BH, Park DH, Kim HS, Seo DS, Shim JH, Lee SJ, Ryu KS, Kim K, Jin JI, Lee TJ, Lee CJ (2005) Synth Met 153:313–316
32. Kim BH, Park DH, Joo J, Yu SG, Lee SH (2005) Synth Met 150:279–284
33. Park DH, Kim BH, Jang MK, Bae KY, Lee SJ, Joo J (2005) Synth Met 153:341–344
34. Park JG, Lee SH, Kim B, Park YW (2002) Appl Phys Lett 81:4625–4627
35. Huang J, Kaner RB (2004) J Am Chem Soc 126:851–855
36. Tran HD, Kaner RB (2006) Chem Commun 2006:3915–3917
37. Dan LI, Huang J, Kaner RB (2009) Acc Chem Res 42:135–145
38. Kim K, Jin JI (2001) Nano Lett 1:631–636
39. Sadki S, Schottland P, Brodie N, Sabouraud G (2000) Chem Soc Rev 29:283–293
40. Park DH, Kim BH, Jang MG, Bae KY, Joo J (2005) Appl Phys Lett 86:113116
41. Park DH, Kim M, Kim MS, Kim DC, Song H, Kim J, Joo J (2008) Electrochem Solid State Lett 11:K69–K72
42. Lee SH, Park DH, Kim K, Joo J, Kim DC, Kim HJ, Kim J (2007) Appl Phys Lett 91:263102
43. Park DH, Kim HS, Lee YB, Ko JM, Lee JY, Kim HJ, Kim DC, Kim J, Joo J (2008) Synth Met 158:90–94
44. Parthasarathy RV, Martin CR (1994) Chem Mater 6:1627–1632
45. Horn D, Rieger J (2001) Angew Chem Int Ed 40:4330–4361
46. Kasai H, Nalwa HS, Oikawa H, Okada S, Matsuda H, Minami N, Kakuta A, Ono K, Mukoh A, Nakanishi H (1992) Jpn J Appl Phys 31:L1132–L1134
47. Kong F, Sun YM, Yuan RK (2007) Nanotechnology 18:265707
48. Shimizu H, Yamada M, Wada R, Okabe M (2008) Polym J 40:33–36

49. Landfester K, Montenegro R, Scherf U, GüNTNER R, Asawapirom U, Patil S, Neher D, Kietzke T (2002) Adv Mater 14:651–655
50. Kietzke T, Neher D, Landfester K, Montenegro R, Güntner R, Scherf U (2003) Nat Mater 2:408–412
51. Kim MS, Park DH, Cho EH, Kim KH, Park QH, Song H, Kim DC, Kim J, Joo J (2009) ACS Nano 3:1329–1334
52. Lee YB, Lee SH, Kim K, Lee JW, Han KY, Kim J, Joo J (2012) J Mater Chem 22:2485–2490
53. Reneker DH, Chun I (1996) Nanotechnology 7:216–223
54. Li D, Xia Y (2004) Adv Mater 16:1151–1170
55. Greiner A, Wendorff JH (2007) Angew Chem Int Ed 46:5670–5703
56. Reneker DH, Yarin AL (2008) Polymer 49:2387–2425
57. Lu X, Wang C, Wei Y (2009) Small 5:2349–2370
58. Kim JS, Reneker DH (1999) Polym Eng Sci 39:849–854
59. Li D, Xia Y (2004) Nano Lett 4:933–938
60. Laforgue A (2011) J Power Sources 196:559–564
61. Kim HJ, Kim DC, Kim R, Kim J, Park DH, Kim HS, Joo J, Suh YD (2007) J Appl Phys 101:053514
62. Hong YK, Park DH, Jo SG, Koo MH, Kim DC, Kim J, Kim JS, Jang SY, Joo J (2011) Angew Chem Int Ed 50:3734–3738
63. Kim DC, Kim R, Kim HJ, Kim J, Park DH, Kim HS, Joo J (2007) Jpn J Appl Phys 46:5556–5559
64. Joo J, Park DH, Jeong MY, Lee YB, Kim HS, Choi WJ, Park QH, Kim HJ, Kim DC, Kim J (2007) Adv Mater 19:2824–2829
65. Park DH, Kim HS, Jeong MY, Lee YB, Kim HJ, Kim DC, Kim J, Joo J (2008) Adv Funct Mater 18:2526–2534
66. Yassar A, Roncali J, Garnier F (1989) Macromolecules 22:804–809
67. Hong YK, Park DH, Park SK, Song H, Kim DC, Kim J, Han YH, Park OK, Lee BC, Joo J (2009) Adv Funct Mater 19:567–572
68. Louarn G, Trznadel M, Buisson JP, Laska J, Pron A, Lapkowski M, Lefrant S (1996) J Phys Chem 100:12532–12539
69. Jin S, Xue G (1997) Macromolecules 30:5753–5757
70. Brédas JL, Thémans B, Fripiat JG, André JM, Chance RR (1984) Phys Rev B 29:6761–6773
71. Li Y, Qian R (1988) Synth Met 26:139–151
72. Li Y, Qian R (1993) Synth Met 53:149–154
73. Padmanaban G, Ramakrishnan S (2000) J Am Chem Soc 122:2244–2251
74. Szymanski C, Wu C, Hooper J, Salazar MA, Perdomo A, Dukes A, McNeill J (2005) J Phys Chem B 109:8543–8546
75. Liu C, Kwon YK, Heo J (2008) Chem Phys Lett 452:281–284
76. Di Benedetto F, Camposeo A, Pagliara S, Mele E, Persano L, Stabile R, Cingolani R, Pisignano D (2008) Nat Nanotechnol 3:614–619
77. Lu W, Fadeev AG, Qi B, Smela E, Mattes BR, Ding J, Spinks GM, Mazurkiewicz J, Zhou D, Wallace GG, MacFarlane DR, Forsyth SA, Forsyth M (2002) Science 297:983–987
78. Kim HS, Park DH, Lee YB, Kim DC, Kim HJ, Kim J, Joo J (2007) Synth Met 157:910–913
79. Santos MJL, Brolo AG, Girotto EM (2007) Electrochim Acta 52:6141–6145
80. Garreau S, Louarn G, Buisson JP, Froyer G, Lefrant S (1999) Macromolecules 32:6807–6812
81. Colaneri N, Nowak M, Spiegel D, Hotta S, Heeger AJ (1987) Phys Rev B 36:7964–7968
82. Kros A, Van Hövell SWFM, Sommerdijk NAJM, Nolte RJM (2001) Adv Mater 13:1555–1557
83. Cho SI, Kwon WJ, Choi SJ, Kim P, Park SA, Kim J, Son SJ, Xiao R, Kim SH, Lee SB (2005) Adv Mater 17:171–175
84. Abidian MR, Kim DH, Martin DC (2006) Adv Mater 18:405–409
85. Groenendaal L, Jonas F, Freitag D, Pielartzik H, Reynolds JR (2000) Adv Mater 12:481–494
86. Hong YK, Park DH, Park SK, Joo J (2008) J Korean Phys Soc 53:2627–2631

87. Hong YK, Park DH, Park SH, Park SK, Joo J (2009) Appl Phys Lett 94:053111
88. Kiriy N, Jähne E, Adler HJ, Schneider M, Kiriy A, Gorodyska G, Minko S, Jehnichen D, Simon P, Fokin AA, Stamm M (2003) Nano Lett 3:707–712
89. Cui CX, Kertesz M (1989) Phys Rev B 40:9661–9670
90. Brown PJ, Thomas DS, Köhler A, Wilson JS, Kim JS, Ramsdale CM, Sirringhaus H, Friend RH (2003) Phys Rev B 67:642031–6420316
91. Yu J, Wang W, Cheng B, Su BL (2009) J Phys Chem C 113:6743–6750
92. Zhou Y, Bao Q, Tang LAL, Zhong Y, Loh KP (2009) Chem Mater 21:2950–2956
93. Jung JS, Lee JW, Kim K, Cho MY, Jo SG, Joo J (2010) Chem Mater 22:2219–2225
94. Lee SH, Lee YB, Park DH, Kim MS, Cho EH, Joo J (2011) Sci Technol Adv Mater 12:025002
95. Penn RL, Banfield JF (1999) Geochim Cosmochim Acta 63:1549–1557
96. Hotta S, Rughooputh SDDV, Heeger AJ, Wudl F (1987) Macromolecules 20:212–215
97. Sundberg M, Inganäs O, Stafström S, Gustafsson G, Sjögren B (1989) Solid State Commun 71:435–439
98. Yoshino K, Nakao K, Onoda M (1989) Jpn J Appl Phys 28:323–324
99. Hess BC, Kanner GS, Vardeny ZV, Baker GL (1991) Synth Met 41:1285–1288
100. Clark J, Silva C, Friend RH, Spano FC (2007) Phys Rev Lett 98:206406
101. Barnes WL, Dereux A, Ebbesen TW (2003) Nature 424:824–830
102. Hu M, Chen J, Li ZY, Au L, Hartland GV, Li X, Marquez M, Xia Y (2006) Chem Soc Rev 35:1084–1094
103. Park DH, Kim MS, Cho EH, Park SH, Song H, Kim DC, Kim J, Joo J (2009) Electrochem Solid State Lett 12:K5–K8
104. Park DH, Lee YB, Kim HS, Kim DC, Kim J, Joo J (2009) Synth Met 159:22–25
105. Daniel MC, Astruc D (2004) Chem Rev 104:293–346
106. Tseng RJ, Huang J, Ouyang J, Kaner RB, Yang Y (2005) Nano Lett 5:1077–1080
107. Quinn BM, Dekker C, Lemay SG (2005) J Am Chem Soc 127:6146–6147
108. Wildgoose GG, Banks CE, Compton RG (2006) Small 2:182–193
109. Dong SK, Lee T, Geckeler KE (2006) Angew Chem Int Ed 45:104–107
110. Zhu J, Brink M, McEuen PL (2008) Nano Lett 8:2399–2404
111. Chiu NF, Lin CW, Lee JH, Kuan CH, Wu KC, Lee CK (2007) Appl Phys Lett 91:083114
112. Anker JN, Hall WP, Lyandres O, Shah NC, Zhao J, Van Duyne RP (2008) Nat Mater 7:442–453
113. Kim SS, Na SI, Jo J, Kim DY, Nah YC (2008) Appl Phys Lett 93:073307
114. Park DH, Hong YK, Kim MS, Cho EH, Choi WJ, Kim KH, Park QH, Kim DC, Song H, Kim J, Joo J (2010) Synth Met 160:604–608
115. Schuck PJ, Fromm DP, Sundaramurthy A, Kino GS, Moerner WE (2005) Phys Rev Lett 94:017402
116. Genet C, Ebbesen T (2007) Nature 445:39–46
117. Lassiter JB, Aizpurua J, Hernandez LI, Brandl DW, Romero I, Lal S, Hafner JH, Nordlander P, Hales NR (2008) Nano Lett 8:1212–1218
118. Nicewarner-Peña SR, Freeman RG, Reiss BD, He L, Peña DJ, Walton ID, Cromer R, Keating CD, Natan MJ (2001) Science 294:137–141
119. Gudiksen MS, Lauhon LJ, Wang J, Smith DC, Lieber CM (2002) Nature 415:617–620
120. Tsu R (2005) Superlattice to nanoelectronics. Elsevier, Amsterdam
121. Williams BS (2007) Nat Photonics 1:517–525
122. Qin L, Banholzer MJ, Millstone JE, Mirkin CA (2007) Nano Lett 7:3849–3853
123. Yan R, Gargas D, Yang P (2009) Nat Photonics 3:569–576
124. Wade A, Fedorov G, Smirnov D, Kumar S, Williams BS, Hu Q, Reno JL (2009) Nat Photonics 3:41–45
125. Björ MT, Ohlsson BJ, Sass T, Persson AI, Thelander C, Magnusson MH, Deppert K, Wallenberg LR, Samuelson L (2002) Nano Lett 2:87–89
126. Choi JR, Oh SJ, Ju H, Cheon J (2005) Nano Lett 5:2179–2183

127. Lee JH, Wu JH, Liu HL, Cho JU, Cho MK, An BH, Min JH, Noh SJ, Kim YK (2007) Angew Chem Int Ed 46:3663–3667
128. Algra RE, Verheijen MA, Borgström MT, Feiner LF, Immink G, Van Enckevort WJP, Vlieg E, Bakkers EPAM (2008) Nature 456:369–372
129. Bulbarello A, Sattayasamitsathit S, Crevillen AG, Burdick J, Mannino S, Kanatharana P, Thavarungkul P, Escarpa A, Wang J (2008) Small 4:597–600
130. Caroff P, Dick KA, Johansson J, Messing ME, Deppert K, Samuelson L (2009) Nat Nanotechnol 4:50–55
131. Park DH, Hong YK, Cho EH, Kim MS, Kim DC, Bang J, Kim J, Joo J (2010) ACS Nano 4:5155–5162
132. Krasheninnikov AV, Banhart F (2007) Nat Mater 6:723–733
133. Krasheninnikov AV, Nordlund K (2010) J Appl Phys 107:071301
134. Shi G, Xu J, Fu M (2002) J Phys Chem B 106:288–292
135. Chen F, Shi G, Zhang J, Fu M (2003) Thin Solid Films 424:283–290
136. Devoret MH, Grabert H (1992) Single charge tunneling: coulomb blockade phenomena in nanostructures. Plenum, New York
137. Delsing P, Claeson T, Likharev KK, Kuzmin LS (1990) Phys Rev B 42:7439–7449
138. Aleshin AN, Lee HJ, Jhang SH, Kim HS, Akagi K, Park YW (2005) Phys Rev B 72:1532021–1532024
139. Park DH, Kim N, Cui C, Hong YK, Kim MS, Yang DH, Kim DC, Lee H, Kim J, Ahn DJ, Joo J (2011) Chem Commun 47:7944–7946
140. Facchetti A (2011) Chem Mater 23:733–758
141. Kim K, Shin JW, Lee YB, Cho MY, Lee SH, Park DH, Jang DK, Lee CJ, Joo J (2010) ACS Nano 4:4197–4205
142. Tian B, Zheng X, Kempa TJ, Fang Y, Yu N, Yu G, Huang J, Lieber CM (2007) Nature 449:885–889
143. Briseno AL, Holcombe TW, Boukai AI, Garnett EC, Shelton SW, Fréchet JJM, Yang P (2010) Nano Lett 10:334–340
144. Kim K, Lee JW, Lee SH, Lee YB, Cho EH, Noh HS, Jo SG, Joo J (2011) Org Electron 12:1695–1700

Index